Magneto-Dielectric Wire Antennas

Theory and Design

by

Tom Sebastian

A Dissertation Presented in Partial Fulfillment
of the Requirements for the Degree
Doctor of Philosophy

Approved May 2013 by the
Graduate Supervisory Committee:

Rodolfo Diaz, Chair
George Pan
James Aberle
Michael Kozicki

ARIZONA STATE UNIVERSITY

August 2013

ABSTRACT

There is a pervasive need in the defense industry for conformal, low-profile, efficient and broadband (HF-UHF) antennas. Broadband capabilities enable shared aperture multi-function radiators, while conformal antenna profiles minimize physical damage in army applications, reduce drag and weight penalties in airborne applications and reduce the visual and RF signatures of the communication node. This dissertation is concerned with a new class of antennas called Magneto-Dielectric wire antennas (MDWA) that provide an ideal solution to this ever-present and growing need.

Magneto-dielectric structures $(\mu_r > 1; \epsilon_r > 1)$ can partially guide electromagnetic waves and radiate them by leaking off the structure or by scattering from any discontinuities, much like a metal antenna of the same shape. They are attractive alternatives to conventional whip and blade antennas because they can be placed conformal to a metallic ground plane without any performance penalty.

A two pronged approach is taken to analyze MDWAs. In the first, antenna circuit models are derived for the prototypical dipole and loop elements that include the effects of realistic dispersive magneto-dielectric materials of construction. A material selection law results, showing that: (a) The maximum attainable efficiency is determined by a single magnetic material parameter that we term the hesitivity: Closely related to Snoek's product, it measures the maximum magnetic conductivity of the material. (b) The maximum bandwidth is obtained by placing the highest amount of μ'' loss in the frequency range of operation. As a result, high radiation efficiency antennas can be

obtained not only from the conventional low loss (low μ") materials but also with highly lossy materials ($\tan(\delta_m) \gg 1$).

The second approach used to analyze MDWAs is through solving the Green function problem of the infinite magneto-dielectric cylinder fed by a current loop. This solution sheds light on the leaky and guided waves supported by the magneto-dielectric structure and leads to useful design rules connecting the permeability of the material to the cross sectional area of the antenna in relation to the desired frequency of operation. The Green function problem of the permeable prolate spheroidal antenna is also solved as a good approximation to a finite cylinder.

To my teachers and my family

Ring the bells that still can ring.

Forget your perfect offering.

There is a crack in everything.

That is how the light gets in.

- Leonard Cohen

TABLE OF CONTENTS

Page

CHAPTER

APPENDIX

LIST OF TABLES

LIST OF FIGURES

Chapter 1

INTRODUCTION

An antenna or an “aerial” (term deprecated in 1983 from IEEE Antenna Std. Definitions) has traditionally been considered as a metallic object that radiates energy and is used to send and receive radio signals over large distances. With the increasing use of non-metals in antenna design, the traditional definition of an antenna has been changed to: “that part” of a transmitting or receiving system that is designed to radiate or to receive electromagnetic waves. In the transmitting mode, a conventional metal antenna binds the electromagnetic wave and allows it to propagate close to the speed of light of the external medium. The principal sources of radiation are then the discontinuities at the ends of the antenna. In contrast, a dipole constructed from a penetrable material does not necessarily bind the electromagnetic wave but instead partially guides it, letting it leak off along the length of the structure. Whatever energy is carried to the ends of the antenna radiates at these discontinuities just like a metal antenna. Thus, such antennas make use of two distinct radiation mechanisms. In this report, we examine antennas made up of dielectric ($\epsilon_r > 1$, $\mu_r \sim 1$), permeable ($\mu_r > 1$, $\epsilon_r \sim 1$) or magneto-dielectric ($\mu_r > 1$ and $\epsilon_r > 1$ with $\mu_r \gg \epsilon_r$) materials.

The fundamental sources of radiation in antennas are the electric and magnetic currents supported by the antenna structure. The ‘source’ of any problem in electromagnetic theory or antenna theory is contained within Maxwell’s equations. Maxwells’ original “Treatise on Electricity and Magnetism” contained 20 equations with

20 unknowns represented using quaternions. Twelve of the original twenty were reduced to the set of the now conventional four by Oliver Heaviside. The two curl equations or circuital current equations in its simplest form as stated by Heaviside are:

$$\nabla \times H = J \tag{1-1}$$

$$\nabla \times E = -M \tag{1-2}$$

where, J is the electric current density and M is the magnetic current density. To maintain the symmetry of the curl equations, Heaviside defined these current densities as:

$$J = \frac{\partial D}{\partial t} + J_e \tag{1-3}$$

$$M = \frac{\partial B}{\partial t} + J_m \tag{1-4}$$

where dD/dt and dB/dt are the electric and magnetic displacement current densities respectively and J_e and J_m are the electric and magnetic conduction current densities respectively. By introducing material properties, namely permittivity (ϵ_r) and permeability (μ_r) through the constitutive relations, $D = \epsilon_0 \epsilon_r E$ and $B = \mu_0 \mu_r H,$ the current density equations can be further expanded as:

$$J = \frac{\partial D}{\partial t} + J_e = \varepsilon_0 \frac{\partial E}{\partial t} + \varepsilon_0(\varepsilon_r - 1)\frac{\partial E}{\partial t} + J_e = \varepsilon_0 \frac{\partial E}{\partial t} + \frac{\partial P_e}{\partial t} + J_e \tag{1-5}$$

$$M = \frac{\partial B}{\partial t} + J_m = \mu_0 \frac{\partial H}{\partial t} + \mu_0(\mu_r - 1)\frac{\partial H}{\partial t} + J_m = \mu_0 \frac{\partial H}{\partial t} + \frac{\partial P_m}{\partial t} + J_m \tag{1-6}$$

where, $\partial P_e/\partial t = \varepsilon_0(\varepsilon_r - 1)\partial E/\partial t$ is the electric polarization current density and $\partial P_m/\partial t = \mu_0(\mu_r - 1)\partial H/\partial t$ is magnetic polarization current density. In the case of metallic antennas, the antenna radiation source is the electric current due to J_e. In the case of the most general dielectric antenna, the source of radiation is the electric current due to both J_e and $\partial P_e/\partial t$. In the case of magneto-dielectric antennas with $\mu_r \gg \epsilon_r$ the source of radiation is the the magnetic polarization current density $\partial P_m/\partial t$, since magnetic monopoles don't exist ($J_m = 0$).

The motivation for the analysis of magneto-dielectric antennas comes from the fact that magneto-dielectric materials can be used as wire elements to make efficient conformal antennas over a metal ground plane. The IEEE Standard definition of terms for antennas defines a conformal antenna as an antenna that conforms to a surface whose shape is determined by considerations other than electromagnetic; for example aerodynamic or hydrodynamic. The surface or platform in this case can be part of an aircraft, truck, jeep or any other vehicle. Whip or Blade Antennas are commonly used as VHF/UHF antennas in military vehicles. These off-the-shelf antennas operate over a narrow band of frequency. Therefore, military vehicles often have many such antennas protruding from the body for use in navigation, communication, radars, etc. (Fig. 1-1).

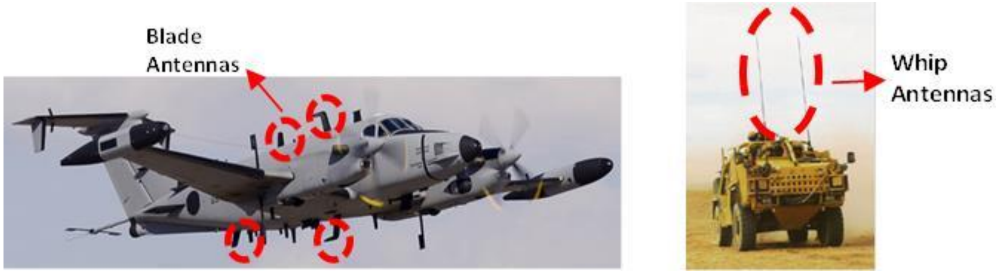

Fig. 1-1Off- the-shelf Whip and Blade Antennas on Military platforms.

Such antennas are usually attached as an afterthought and routinely in locations and orientations that can damage them and expose them to the enemy. In other words, they are not low profile and are conspicuous. They cause considerable drag and increase fuel consumption. The ideal solution would be to replace several such antennas on a military platform with a "<u>Single Conformal Wideband Antenna</u>". An antenna with wideband capabilities enables shared aperture multi-function radiators, while conformal profiles minimize physical damage of the antenna in Army applications, drag and weight penalties in Airborne applications and reduce the visual and RF signatures associated with the communication and RADAR systems.

The traditional approach in designing conformal antennas on a metallic ground plane is to either place the antenna vertically on top of a metallic ground plane (the whip and the blade antennas in Fig. 1-1) or place it horizontally at a height $\lambda_0/4$, λ_0 being the operating wavelength, above the ground plane. According to image theory, the effect of the ground plane can be mimicked by replacing the ground plane with the image current pointing in the appropriate direction. In the case of a vertical metallic antenna, the antenna current and the image current point in the same direction thus ensuring constructive interference of the radiated waves from the two source currents (Fig. 1-2 (a)). A horizontal antenna placed at a height 'h' over ground, on the other hand, has an image current that points in the opposite direction as the antenna current (Fig. 1-2 (b)).

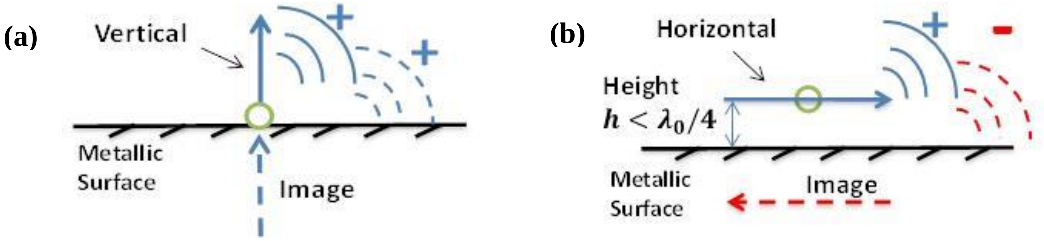

Fig. 1-2 Image effects of (a) Horizontal metallic antenna placed on a metallic ground-plane at height '$h < \lambda_0/4$ '(b) Vertical metallic antenna on a metallic ground plane.

Thus, only if it is placed at a height $h = \lambda_0/4$ will there be constructive interference of the radiated waves from the antenna and its image. Neither a vertical monopole nor a horizontal dipole a quarter wave above ground can be considered to be conformal at VHF and UHF frequencies.

In order to circumvent the image problem faced by horizontal metallic antennas, high impedance metamaterials have been proposed to cover the surface of the metallic ground plane in order to 'flip' the direction of the image current (Fig. 1-3(a)). But, such an approach requires the entire ground plane to be covered by this material. This adds weight and increases the cost of the system. Thus, this approach eventually runs into a problem of diminishing returns. The idea explored in this dissertation is to use the high impedance materials as the antenna itself.

When a "high impedance" magneto-dielectric material is used as an antenna, it can be thought of as a magnetic conductor carrying magnetic currents. Therefore these antennas can be placed right on top of the ground plane (h ~ 0) since the image of a magnetic current on a conducting surface is always collinear with it (Fig. 1-3(b)).

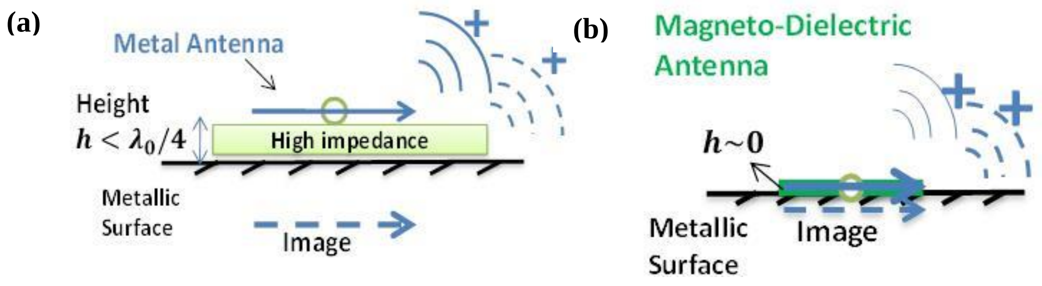

Fig. 1-3 Image effects of a (a) metallic antenna on a metallic ground plane covered with a high impedance material (b) Magneto-dielectric antenna on a metallic ground plane.

It follows that the efficiency of a magneto-dielectric antenna is always enhanced by a nearby electrically conducting surface. As antenna elements, magneto-dielectric wires can replace blade/whip antennas 18" and taller with antennas that are no thicker than 1" over ground and consume a minimum amount of "real estate" on the surface of the vehicle.

The lowest order modes that a magneto-dielectric wire can carry are the HE11 mode and the TE01 mode. The field structure of these modes along with that of a PMC (perfect magnetic conductor) wire are shown in Fig. 1-4.

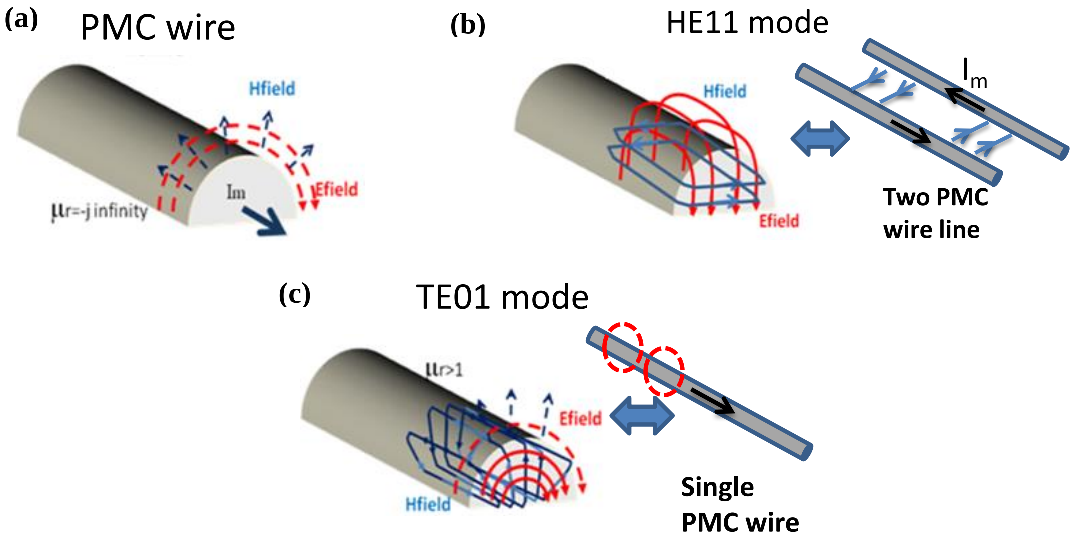

Fig. 1-4 (a) E and H field structure around a PMC wire (b)HE11 mode in a magneto-dielectric material (c) TE01 mode in a magneto-dielectric material.

The HE11 mode shown in Fig. 1-4(b) has no cut-off or onset frequency. That is, the HE11 mode is well guided by the magneto-dielectric wire from dc to daylight. Although it is well supported by the structure, the HE11 mode looks like a two-wire PMC transmission line which we know is a poor radiator. The TE01 mode has a cut-off or onset frequency (f_{cutoff}) given by:

$$f_{cutoff} = \frac{2.4049\ c_0}{2\pi\rho\sqrt{\mu_r\epsilon_r - 1}} \qquad (1\text{-}7)$$

where c_0 is the speed of light in free space and 'ρ' is the radius of the wire. Below the TE01 onset frequency, the wave is loosely guided by the magneto-dielectric wire. The field shape of the TE01 wave outside the wire in this case looks like that of a PMC wire and hence is will radiate off of any discontinuities in the structure. This favorable TE01 mode can be injected into the magneto-dielectric material using an electric current loop with the material place along its axis. This is the feeding mechanism utilized throughout this dissertation.

The outline of the dissertation is shown as flow- chart in Fig. 1-5. Each section in the flow chart is covered in subsequent chapters as labeled.

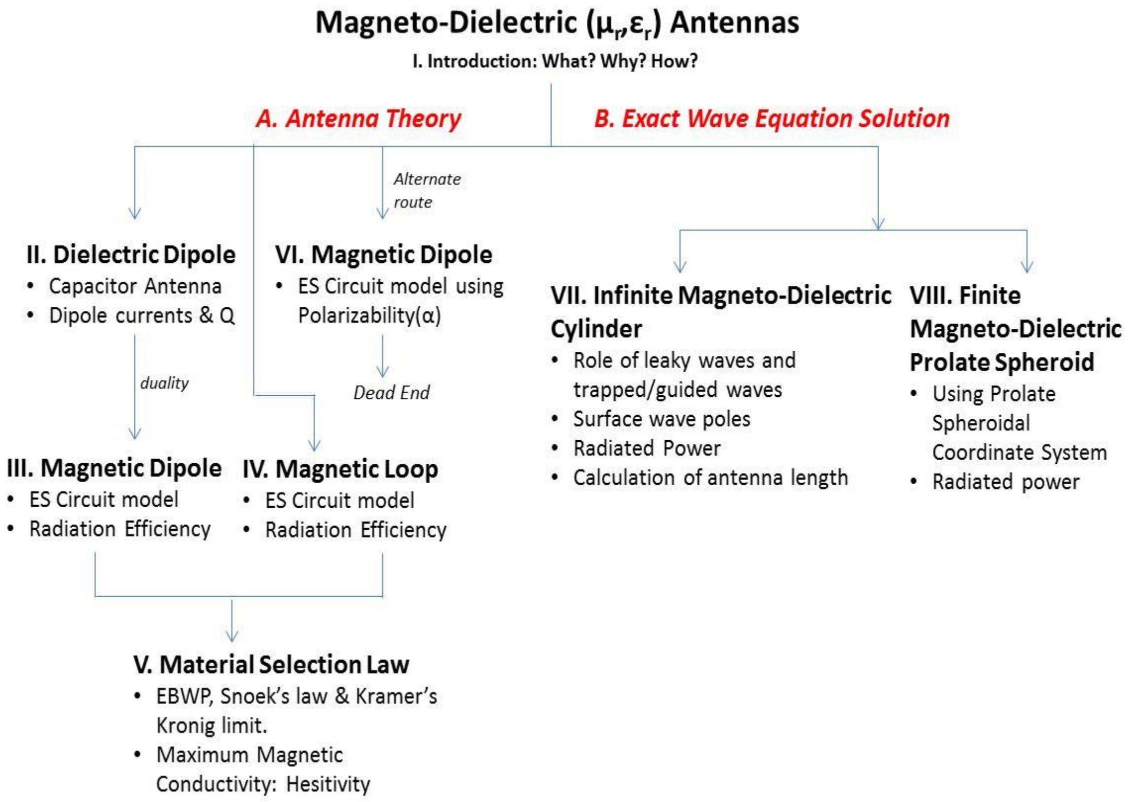

Fig. 1-5 Outline of the dissertation

In Chapter 2, the dielectric capacitor/condenser antenna is re-examined and we point out the efficacy of putting the dielectric material outside the capacitor plates instead of within them as in a condenser. This structure is referred to as a dielectric dipole and its comparison with conventional metallic antennas of the same size is shown. It is demonstrated through simulations that the performance of an electrically small dielectric dipole can approach but never surpass a metallic dipole of the same dimension. A closed form expression of the radiation efficiency of this dielectric dipole using realistic materials is also derived which includes the often omitted loss tangent (tan (δ)) or imaginary part of permittivity i.e. ε” loss. The accuracy of this equation is tested through rigorous full-wave simulations. The results show that high radiation efficiency in dielectric dipoles can be obtained with both low loss and high loss materials which is a deviation from contemporary notion of requiring only low loss materials to achieve the same.

In Chapter 3, the properties of an electrically small dipole antenna constructed from magneto-dielectric media ($\mu_r > 1$, $\varepsilon_r \geq 1$) are derived in closed form by following Schelkunoff’s original development for electrically small metallic antennas and exploiting duality. Such dipoles are attractive alternatives to vertical monopoles because they can be placed conformal to a metallic ground plane without performance degradation. The closed form expression of the radiation efficiency derived includes the often neglected imaginary part of permeability i.e. μ'' loss. This analysis shows that it is possible to construct high radiation efficiency antennas out of not only the traditional or conventional low loss (low μ'') materials but also with highly lossy materials ($tan(\delta_m) \gg 1$). This is a noteworthy conclusion given the fact that most magnetic materials exhibit loss beyond VHF or sometimes even beyond the HF range. A magneto-dielectric dipole using commercially available NiZn ferrite absorber tile material was constructed and tested in an anechoic chamber demonstrating significant efficiency . Finally, the duality between a magneto-dielectric dipole and the dielectric dipole of Chapter 2 is explored analytically and numerically.

In Chapter 4, the properties of a magneto-dielectric electrically small loop antenna are derived in closed form using the same approach as that followed for the magneto-dielectric dipole in Chapter 3. A magneto-dielectric loop is an ideal alternative to vertical monopoles because they have same radiation pattern as the monopole and yet can be placed conformal to a metallic ground plane without performance degradation. Similar to Chapter 3, the results here also show that it is possible to construct high efficiency loops using lossy materials. An application to the case of a body wearable antenna is also discussed.

In Chapter 5, a material selection law for selecting the most appropriate permeable material to design magneto-dielectric antennas is postulated. This selection law is derived within the bounds of three fundamental physical limits, namely, 1) the Gain-Bandwidth product limit, 2) Snoek's product limit for magnetically permeable materials and 3) the restrictions imposed on the permeability function by the Kramers-Krönig relations. Within these constraints it is shown that one dominant parameter with the units of magnetic conductivity characterizes the performance of the material. The validity and applicability of the selection law is demonstrated by full-wave simulations of conformal magneto-dielectric dipoles using both fictitious and realistic magneto-dielectric materials.

In Chapter 6, a simpler three element RLC circuit model for a magneto-dielectric dipole is postulated where the capacitance 'C' is proportional to the polarizabilty of the object. The proportionality factor that relates the two accounts for the morphology of the magnetic field structure and is found to be a single pole Debye function in the morphology variable ($u = 1/(\mu_r - 1)$). The inductance and the radiation resistance are then derived by duality from the case of the electric dipole. Although this approach extends the magneto-dielectric dipole model beyond the regime of the electrically small circuit models of Chapter 3, it implicitly assumes that the magnetic current distribution on the antenna is triangular. As is shown in Chapter 7 this is only true for a narrow range of frequencies and values of permeability that result in operation close to the onset of guided mode propagation.

In Chapter 7, the Green function problem of a cylindrical magneto-dielectric rod of infinite length excited by an electric current loop current is solved. The magnetic current wave excited in a magneto-dielectric infinite rod is shown to go through a succession of fast wave-slow wave transitions as a function of frequency. Below the first mode and in between modes the fast wave regions exhibit leaky wave behavior with decaying amplitude and phase velocities faster than the speed of light. Every time we approach the onset of guidance of a mode, there is a band of frequencies over which the magneto-dielectric rod behaves very much like a PMC metal rod. Given the predominantly leaky wave behavior exhibited by these antennas in their most common application (low frequencies, electrically small elements) it is possible to calculate the minimum length of material required to get the same amount of radiated power as that of an infinite magneto-dielectric cylinder of the same cross-section.

In Chapter 8, the Green function problem of a finite prolate spheroidal magneto-dielectric antenna fed by a current loop is solved. The electric and magnetic fields calculated are shown to agree well with full-wave simulations. An expression for the total radiated power from this finite dipole is also derived and compared to simulations.

At the end of every chapter, suggestions are given for follow-on work that could extend the results presented. Three Appendices are included covering the impact to the model of the skin effect in magneto-dielectric cylinders, an alternative derivation of the efficiency of a permeable dipole, and details of the solution of the Helmholtz wave equation in Prolate spheroidal coordinates.

Chapter 2

DIELECTRIC DIPOLE ANTENNA

2.1 Introduction

Ever since the idea of accelerated charges radiating energy was first conceived, scientists and engineers have extensively used conductors or metals as antenna elements due to the abundance of free charges available in them. It was also known that dielectric materials can guide waves in them. But, it was an accepted fact that since dielectric materials guide waves, they have the tendency to trap these waves and hence do not promote radiation. Nevertheless, one of the first variants from the conventional metallic antennas was the capacitor/condenser antenna. Such a design employing dielectric materials was implemented but was immediately disregarded by prominent engineers like S. Schelkunoff [1] and H. A. Wheeler [2] [3] (Fig. 2-1(a) & Fig. 2-1(b)).

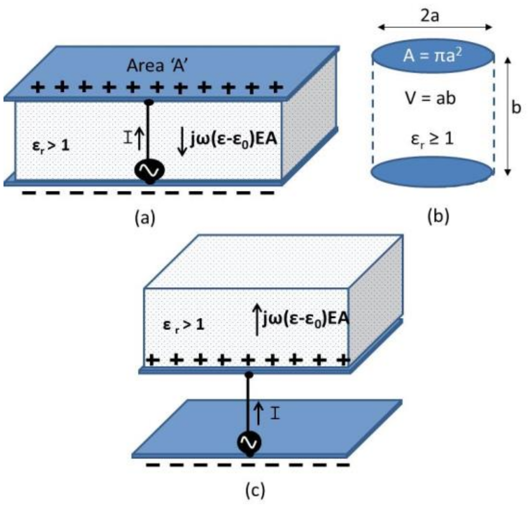

Fig. 2-1 a) Schelkunoff's dielectrically loaded antenna [1] (b) Wheeler's capacitor antenna [2] [3] (c) Dielectric Dipole antenna

They pointed out that such an electrically small antenna would actually result in a decrease in net radiation compared to its bare metallic counterpart. Wheeler described its ineffectiveness using his ‘radiation power factor (p)’ which happens to be the inverse of antenna Q. The dielectric in the capacitor decreases the radiation power factor thereby decreasing the bandwidth of the antenna from its unloaded metallic case. On the other hand, Schelkunoff explained that the density of the polarization current (or displacement current in the medium minus the displacement current in free space) in the dielectric is in the direction opposite to that of the current in the dipole that feeds it. The polarization current produces fields just as conduction currents do but in this case they weaken the field of the conducting current. Thus, the effective radiating current is reduced as it is inversely proportional to ‘ε’.

But now along the same lines if the dielectric were to be placed outside the capacitor as shown in Fig. 2-1(c), then the polarization current would be in the same direction as the dipole feed current and hence aid radiation. We can immediately see that the capacitor will setup or pump energy into the TM mode in the dielectric that will leak out along the length of the antenna when operated below the cut-off frequency or onset frequency of the mode. Thus, the material and the dimensions are chosen to encourage leakage of the TM waves that are partially guided by it. Such an antenna can be truly called a dielectric antenna since the dielectric material is the most significant part of the radiating system.

The analysis and comparison of this dielectric antenna and the capacitor antenna is shown in this chapter. Wheeler was quick to point out that the antenna with the dielectric outside will be considerable larger in size. Hence in order to evaluate the performance of the “dielectric dipole”, comparison is done with a metallic dipole of the same length and cross-section. We show that in the electrically small limit we can never do better than a metallic small antenna with dielectric materials.

A comprehensive summary of theoretical analysis and experimental data on electrically small and moderate dielectric loaded antennas done up to 1977 was presented by Smith [4]. Three distinct cases were considered and it was shown that i) a dielectrically loaded electrically small antenna always led to reduction in efficiency and bandwidth. ii) Metal monopoles are superior to antennas of moderate lengths with a thin dielectric coating and iii) dipole with thick dielectric coatings are intrinsically narrowband.

Since the 1980s the focus of design of antennas that use dielectric materials shifted to another class of such antennas called ‘dielectric resonator antennas’. The term was first coined by Richtmyer [5] in 1939, however such antennas were first analyzed in detail in the eighties starting with Long et al. [6]. A detailed summary of research on this subject is given in [7]. These antennas have found widespread use in mobile phone handsets. These can also be called dielectric antennas but because they operate at frequencies past or around the resonance of the dielectric object, they are intrinsically narrowband. Their usual operating frequency range is anywhere between 1GHz-40GHz with the antenna length being greater than $\lambda/4$. In this chapter, we shall concentrate on dielectric antennas operated in the electrically small regime (length$\ll \lambda/4$).

Another sub-class of antennas employing dielectric materials is the dielectric rod antenna or polyrod antenna [8-10]. These are typically fed from a dielectric filled metallic waveguide that launches the lowest order surface wave into the dielectric rod several wavelengths long. Such antennas also rely on leakage along the length of the structure. As they are many wavelength’s long, these antennas also do not fall under the category that we are interested in.

Although there are many variations of the dielectric dipole as listed above, we are going to restrict our analysis to the most fundamental case: a monopole over a ground plane. We start our analysis in Section 2.2 with the classic capacitor antenna and prove via simulations, Wheeler and Schelkunoff’s heuristic reasoning as to why they are not beneficial. This is followed by the dielectric dipole antenna analysis in Section 2.3 which showing how a dielectric material can aid the radiation process. In Section 2.4, the radiation efficiency of a realistic dielectric antenna with lossy material is derived based on the electrically small antenna circuit model. The result shows that unlike the classical notion that all materials ought to have very low loss for high radiation efficiency, an extremely lossy dielectric can also give high radiation efficiency. Section 2.5 contains the summary of the chapter, some notable conclusions and possible future work on this subject.

The purpose of this chapter is to explain why and how small dielectric dipoles work the way they do and derive some simple expressions and antenna models that agree with simulations. It serves as an introduction to a much more useful and practical antenna: the magneto-dielectric dipole antenna.

2.2 Capacitor/ Condenser Antenna

The HFSS simulation geometry for the capacitor antenna of Fig. 2-1(a) is shown below in Fig. 2-2(a). It's a 10cm tall and 2cm diameter monopole over ground terminated in a top plate filled with a dielectric ε_r, with the center conductor extending all the way to the top plate. In order to prove Schelkunoff's assessment, the conduction current 'Ic' in the center conductor and the total radiation current 'Itotal' (sum of conduction current in the center conductor and the displacement current in the dielectric) in the monopole are measured using two Amperean loops shown in Fig. 2-2(b).

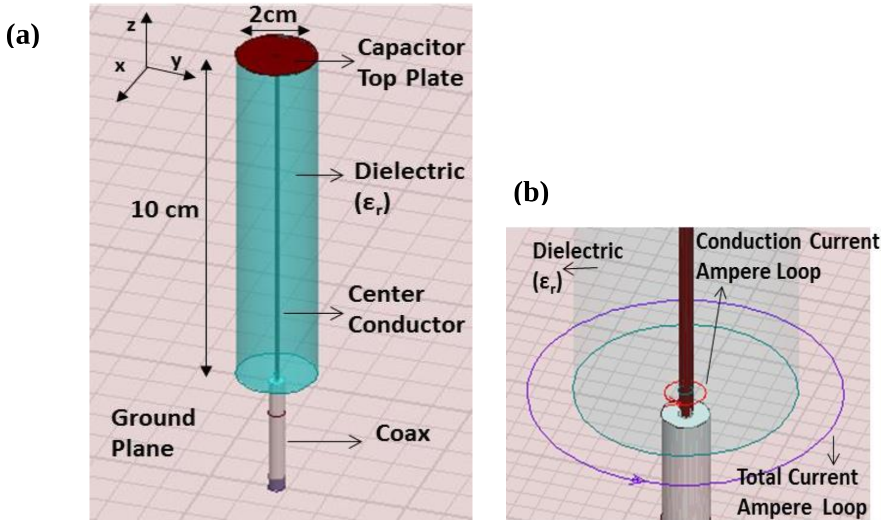

Fig. 2-2 (a) Simulation geometry of the capacitor antenna. (b) Ampere's loop in the simulator to measure the conduction current in the center conductor and the total radiation current of the monopole.

The dielectric constant ε_r of the material is swept from unity which is the basic metallic monopole over ground to ε_r=1000. The ratio of the total radiating current to the conduction current at 100MHz is shown in Fig. 2-3.

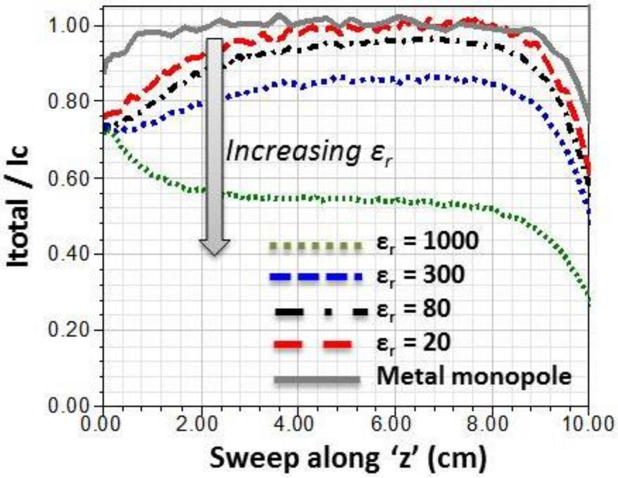

Fig. 2-3 The ratio of the total radiated current (Itotal) to the conduction current (Ic) in the center conductor @ 100MHz plotted along the length of the loaded monopole for different values of ϵ_r.

For the metallic monopole, this ratio should be unity. The slight drop seen around the origin and around 10cm is due to the turbulence near the feed and the end discontinuity respectively. Clearly, as Schelkunoff envisioned the net current that accounts for radiation drops as the dielectric constant of the material increases. The input impedance of the capacitor antenna is shown in Fig. 2-4.

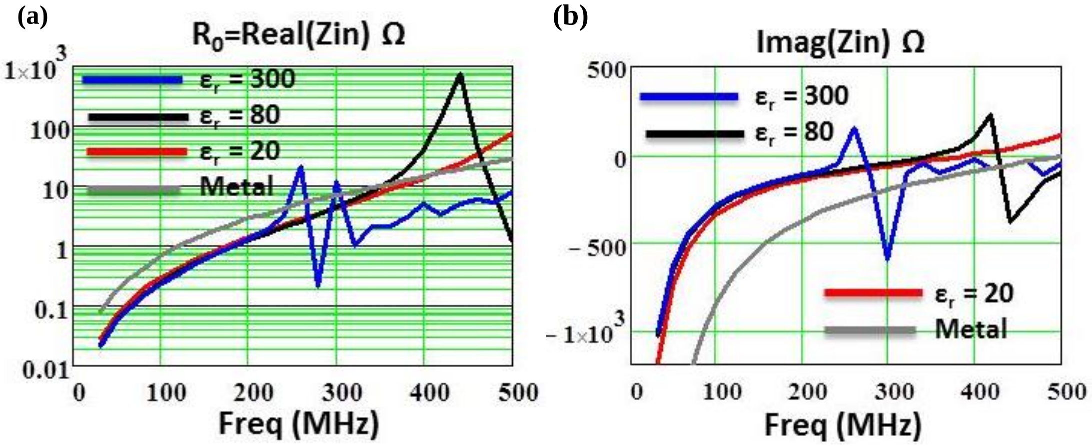

Fig. 2-4 (a) Real and (b) Imaginary part of input impedance of the capacitor antenna for different values of ε_r.

Loading the dipole with a dielectric material has resulted in a drop in the real part of input impedance indicating a drop in radiation resistance due to the reduction in net radiating current as seen in Fig. 2-3. The added dielectric has also clearly shifted the dipole resonance to a much lower value. The resonance frequency decreases with increasing ε_r due to an increase in capacitance. The antenna Q can be now calculated using the equation below given by Best et al. [11].

$$Antenna\ Q = \frac{\omega_0}{2R_0}|Z_0'(\omega_0)| \tag{2-8}$$

The antenna Q calculated from the input impedance of the antenna is a convenient approximation and can have errors in cases where there are closely spaced resonances. For all the dielectrically loaded cases, the antenna Q is higher than that of the metal monopole (as seen in Fig. 2-5. It is not that significant but it still is higher than the metal for this particular geometry) and therefore the bandwidth is reduced. Also, the radiation efficiency of a capacitor antenna will always be lower than that of a pure metallic dipole assuming negligible conductor losses. Therefore the efficiency bandwidth product which is sometimes used as a figure of merit for antennas will always decrease when the capacitor antenna is loaded with a dielectric. Hence we can see that dielectrically loading a monopole is not useful in the electrically small regime.

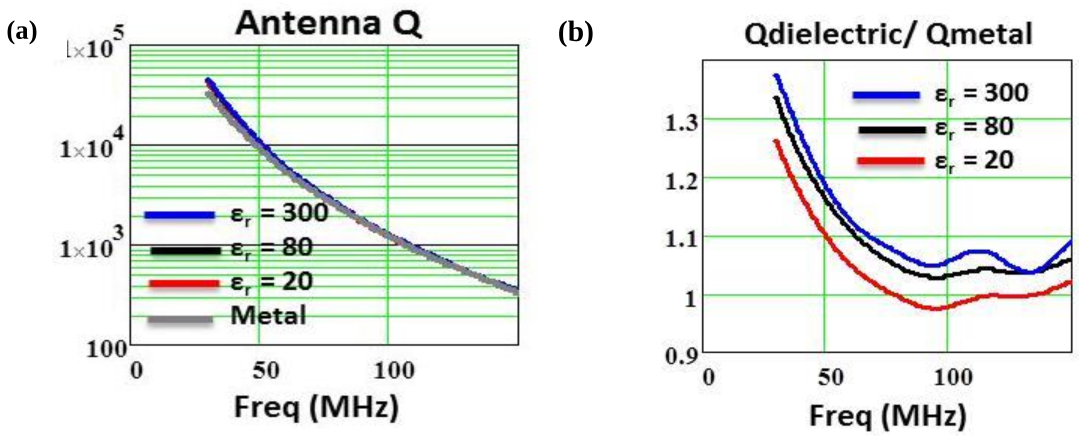

Fig. 2-5(a) Antenna Q calculated from input impedance using (1) and (b) Ratio of the Antenna Q of the dielectric capacitor to the Q of the metallic monopole. The dielectric Q is higher than the metallic monopole throughout the band.

2.3 Dielectric Monopole (Capacitive Feed)

Now, consider a dielectric monopole postulated before, with the dielectric placed outside the capacitor similar to Fig. 2-1(c). The simulation geometry is shown below in Fig. 2-6.

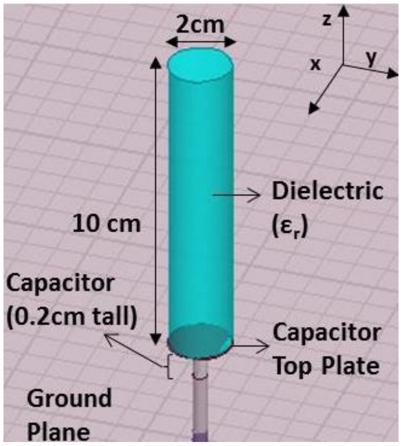

Fig. 2-6 Simulation geometry of the dielectric monopole.

The dielectric constant ϵ_r of the material is swept from unity which is the capacitive feed gap (a short monopole) by itself all the way to $\epsilon_r = 1000$. In order to make a fair comparison with its metallic counterpart, a metallic monopole is also simulated of the same dimensions (i.e. height =10cm and 2cm diameter). The capacitive feed injects TM like modes (circulating H_ϕ and longitudinal E_z) into the dielectric material supported by it which when below the onset of guidance (i.e. below the cutoff frequency) will leak out of the material. The cutoff frequency of the TM modes depends on the antenna cross-section and the dielectric constant. For this geometry and set of dielectric constants the lowest order TM01 mode onset/cutoff frequencies are given below in Table 2-1.

Dielectric Constant (ε_r)	**TM01 Onset Frequency (MHZ)**
20	2632.5
80	1291
300	663.6
1000	363

Table 2-1 TM01 onset/cutoff frequency for a 1cm radius dielectric cylinder for different ϵ_r.

The simulation frequency range is 30MHz-500MHz. Note that in this range, ε_r=1000 is the only case where the onset frequency is crossed. Figure 7 below gives the shape of the mode inside the dielectric material for different dielectrics at two different frequencies (100MHz and 500MHz). Figure 7(a) and (b) show the strength of the circulating magnetic field H_ϕ, at a height $z = 4cm$ above the feed as a function of tranverse position ('x' in cm). The black vertical lines at $x = \pm 1cm$ indicate the boundary of the rod. At 100MHz (Fig. 2-7(a)) the TM mode launched into the dielectric is strongly cutoff. At 500MHz (Fig. 2-7(b)) we see evidence of the onset of guided waves particularly in the case of $\epsilon_r = 1000$ where we can clearly see more than one transverse wavelength fit inside the dielectric. Outside the cylinder, the field drops exponentially as expected. As the wave becomes more and more trapped due to guidance, its energy migrates to the interior of the rod i.e H_ϕ increases inside the cylinder and the next higher order mode(TM02) starts to appear.

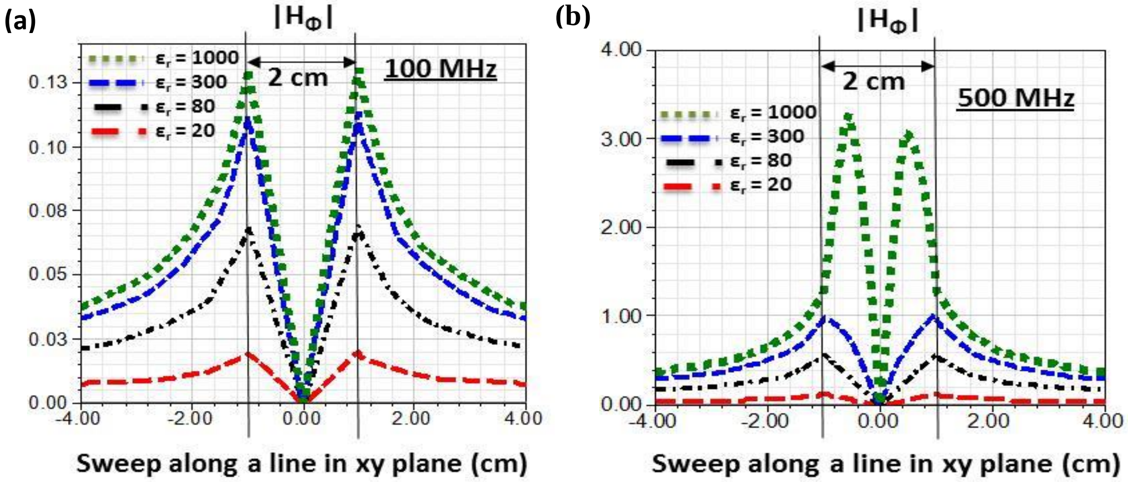

Fig. 2-7 (a) & (b) are plots of H_ϕ along a line in the XY plane (@ z=4cm) indicating TM Mode structure inside the dielectric material at 100MHz and 500MHz respectively (c) Plot of displacement current density 'D_z' plotted along the axis of the dielectric cylinder.

In Fig. 2-8, the ratio of the total radiating current to the conduction current is plotted. The conduction current in this case is the current at the coaxial feed. As expected in a clear contrast with the capacitor antenna, the net radiating current in the dielectric increases with increasing values of the dielectric constant ϵ_r.

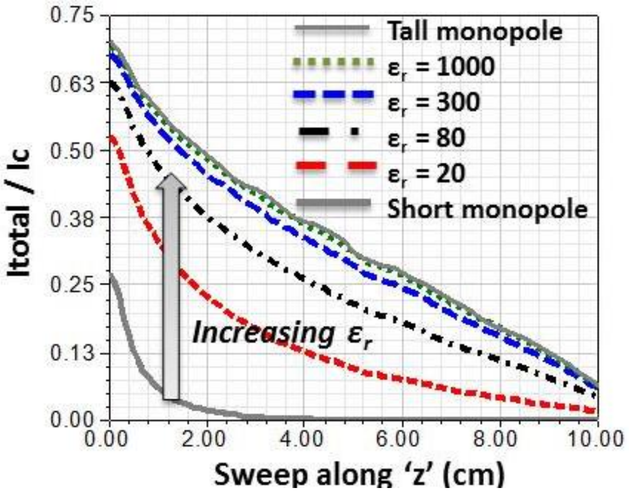

Fig. 2-8 The ratio of the total radiated current (Itotal) to the average conduction current (Ic) in the center conductor of the feed capacitor@ 100MHz plotted along the length of the dielectric monopole for different values of ϵ_r.

The input impedance and the antenna Q of this antenna is given in Fig. 2-9. The input resistance (Fig. 2-9(a)) increases with ε_r since the wave is now partially guided over a longer distance along the material dipole as ε_r rises. This apparent increase in the length of the antenna increases the net leaky radiation and therefore also increases the radiation resistance. The input reactance (Fig. 2-9(b)) drops as ε_r increases because the external capacitance of the antenna increases with its apparent size.

The short monopole feed has the highest Q (or smallest bandwidth) and as the dielectric constant increases the antenna Q improves as well (Fig. 2-9(c)). Note that no matter how high the permittivity is, the Q of a dielectric monopole never drops lower than that of a metallic monopole of the same dimension. The physical size of the antenna is one of the fundamental factors that should be taken into consideration when comparing two different small antennas. Therefore, as Wheeler pointed out [3] it is unfair to claim that the dielectric monopole is better than its metallic counterpart by referring to its performance w.r.t the short monopole or the capacitive feed.

Also, the radiation efficiency of the tall monopole will always be higher than the dielectric dipole assuming negligible conductor losses because on a metallic surface the wave always uses the full length of the antenna (i.e. no leakage occurs). Therefore, the efficiency bandwidth product of the metallic dipole will always be greater than the dielectric dipole of same dimensions. Thus, the antenna performance of a dielectric dipole can never surpass that of a metallic dipole of the same size.

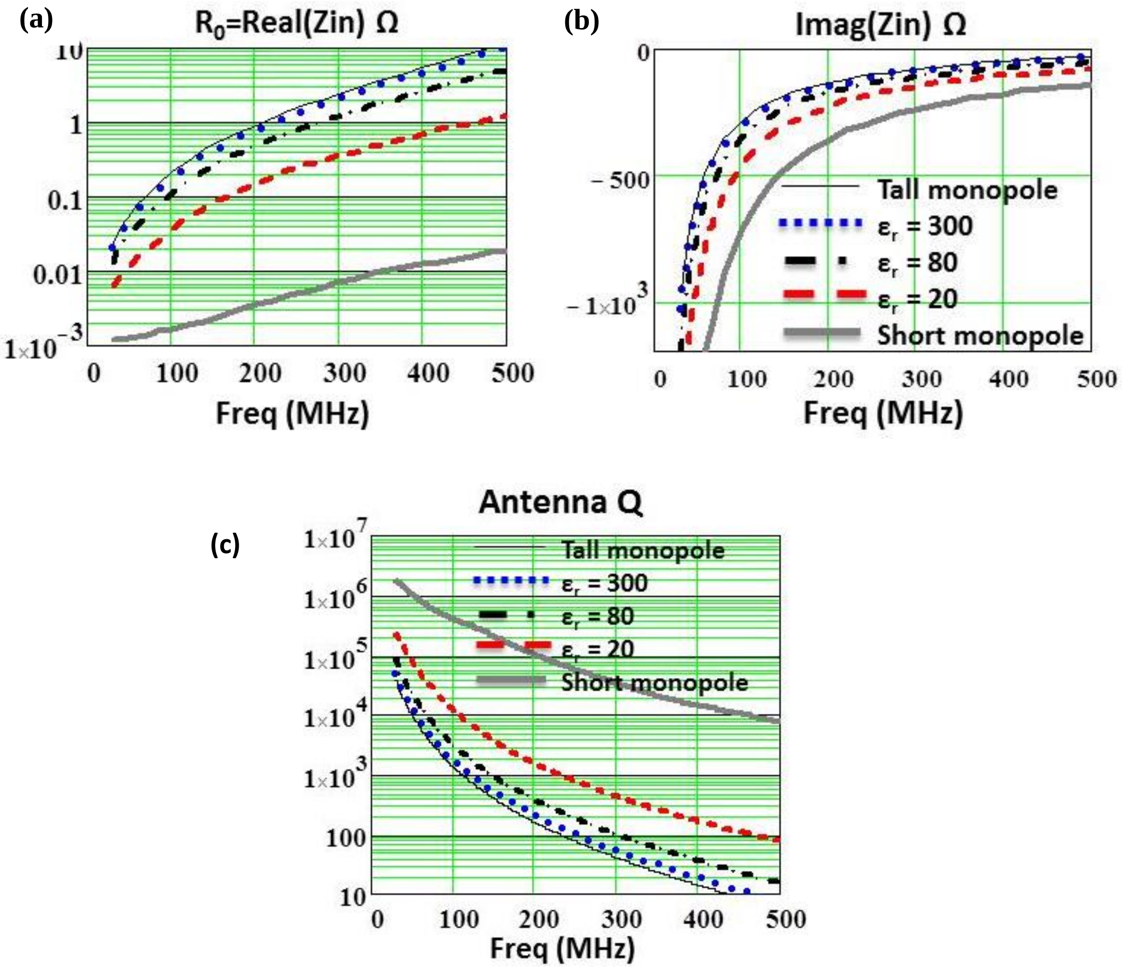

Fig. 2-9 (a) Real and (b) Imaginary part of input impedance of the dielectric monopole for different values of ε_r. (c) Antenna Q calculated from input impedance.

2.4 Radiation Efficiency of a Lossy Dielectric Dipole

The goal of this section is to determine in closed form an equation for the radiation efficiency of a dielectric dipole antenna. There are two definitions of efficiency for antennas: the radiation efficiency and the antenna efficiency. The radiation efficiency computes efficiency of radiation in the presence of antenna material losses (conductor losses or dielectric losses). The antenna efficiency is the total efficiency of the system which includes the feed mismatch loss. Since all realistic materials have some amount of loss in them (i.e. $\epsilon = \epsilon' - j\epsilon"$ or $\epsilon = \epsilon'(1 - jtan(\delta))$ where $\epsilon"$ or loss tangent $\tan(\delta)$ signifies the loss), we will start our analysis with the radiation efficiency. The radiation efficiency is defined as

$$Eff_{rad} = \frac{Prad}{Prad + Plost} = \frac{1}{1 + \frac{Plost}{Prad}} \tag{2-9}$$

where, 'Prad' is the power radiated by the antenna and 'Plost' is the power lost in the antenna material.

Starting from Schelkunoff's circuit model for electrically small metallic antennas [2]; a dielectric dipole antenna can be modeled by including the material properties in series with it i.e. with a series internal complex capacitance C_{diel} (due to complex permittivity $\epsilon = \epsilon' - j\epsilon"$). This term accounts for the internal energy in the material. The circuit model is shown in Fig. 2-10.

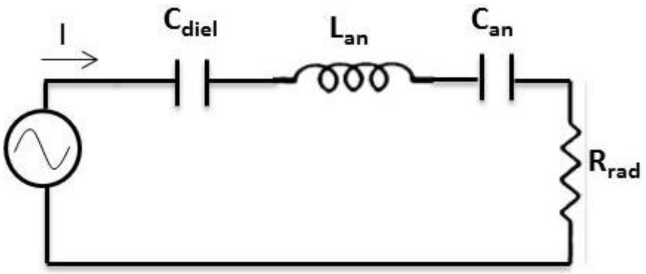

Fig. 2-10 Dielectric dipole electrically small dipole model based on Schelkunoff’s model of electrically small metallic antennas.

The elements from Schelkunoff’s model are defined as:

$$C_{an} = \frac{\pi\varepsilon_0 \frac{l}{2}}{\ln\left(\frac{l/2}{\rho}\right)} \tag{2-10}$$

$$L_{an} = \frac{\mu_0 \frac{l}{2}}{3\pi} \ln\left(\frac{l/2}{\rho}\right) \tag{2-11}$$

$$Rrad = 20\pi^2 \left(\frac{l}{\lambda}\right)^2 = 5(kl)^2 \tag{2-12}$$

Therefore, the input impedance of this dielectric dipole is:

$$Zin_{diel} = \frac{1}{j\omega C_{diel}} + j\omega \frac{\mu_0 \frac{l}{2}}{3\pi} \ln\left(\frac{l/2}{\rho}\right) + \frac{1}{j\omega \frac{\pi\varepsilon_0 \frac{l}{2}}{\ln\left(\frac{l/2}{\rho}\right)}} + 5(kl)^2 \tag{2-13}$$

The current distribution in the antenna is assumed to be triangular (just like a small metallic dipole). The internal reactance due to the complex capacitance for a triangular current distribution can be shown to be:

$$Z_{mat} = \frac{1}{j\omega C_{diel}} = \frac{1}{j\omega\left(3\frac{\varepsilon_0(\varepsilon_r - 1)\pi\rho^2}{l}\right)} = \frac{1}{j\omega\left(3\frac{\varepsilon_0\varepsilon'\pi\rho^2}{l}\right) + \omega\left(3\frac{\varepsilon_0\varepsilon''\pi\rho^2}{l}\right)} \tag{2-14}$$

where, $C_{diel} = 3\left(\frac{\varepsilon_0(\varepsilon_r-1)\pi\rho^2}{l}\right)$. The factor of ‘3’ shows up due the triangular distribution. This factor is unity for uniform current distribution which would be a simple capacitor equation. C_{diel} is derived by equating the electric energy integral to the circuital capacitor energy equation Free space is subtracted from the internal capacitance (i.e. dielectric constant $(\varepsilon_r - 1)$) since when $\varepsilon_r = 1$ we must be left with just the feed. This internal reactance can be further expanded as,

$$Z_{mat} = \frac{\omega\left(\frac{\varepsilon_0\varepsilon"\pi\rho^2}{l}\right) - j\omega\left(\frac{\varepsilon_0(\varepsilon' - 1)\pi\rho^2}{l}\right)}{\left(\omega\left(\frac{\varepsilon_0(\varepsilon' - 1)\pi\rho^2}{l}\right)\right)^2 + \left(\omega\left(\frac{\varepsilon_0\varepsilon"\pi\rho^2}{l}\right)\right)^2}$$

$$=> Z_{mat} = \frac{1}{j\omega 3\frac{\varepsilon_0\pi\rho^2}{l}\frac{|\varepsilon_r - 1|^2}{\varepsilon'}} + \frac{1}{3\frac{\omega\varepsilon_0\pi\rho^2}{l}}\frac{\varepsilon"}{|\varepsilon_r - 1|^2} \tag{2-15}$$

The loss in the antenna comes from the frequency dependent “loss resistance” or the terms with $\epsilon"$. Therefore, the power lost in the antenna carrying a current ‘I’ can be defined as,

$$Plost = \frac{1}{2}I^2R_{loss} = \frac{1}{2}I^2\left(\frac{l}{3\omega\varepsilon_0\pi\rho^2}\frac{\varepsilon"}{|\varepsilon_r - 1|^2}\right) \tag{2-16}$$

Now the radiated power ‘Prad’ is defined as

$$Prad = \frac{1}{2}I^2Rrad = \frac{1}{2}I^2 5(kl)^2 \tag{2-17}$$

From (2-16) and (2-17),

$$\frac{Plost}{Prad} = \left(\frac{l}{3\omega\varepsilon_0\pi\rho^2}\frac{\varepsilon"}{|\varepsilon_r - 1|^2}\right)\frac{1}{5(kl)^2}\ \frac{c_0 l}{c_0 l} \tag{2-18}$$

We know that k=ω/c0 , $c_0 = 1/\sqrt{\mu_0\varepsilon_0}$ and $\eta_0 = \sqrt{\mu_0/\varepsilon_0} = 120\pi$. Also, $c_0\varepsilon_0 = 1/\eta_0$ & $c_0\mu_0 = \eta_0$.

Therefore,

$$\frac{Plost}{Prad} = \frac{\varepsilon"}{|\varepsilon_r - 1|^2}\frac{8}{\left(\frac{\rho}{l}\right)^2 (kl)^3} \tag{2-19}$$

Or the radiation efficiency can be defined as:

$$Eff_{diel\_\Delta lar} = \frac{1}{1 + \frac{8}{\left(\frac{\rho}{l}\right)^2 (kl)^3}\frac{\varepsilon"}{|\varepsilon_r - 1|^2}} \tag{2-20}$$

According to (2-20) there are two ways to get low power loss or high radiation efficiency: either by using a material with $\epsilon" \ll \epsilon'$ OR by using a material with $\epsilon" \gg \epsilon'$. The second conclusion, that we need a material that's highly lossy shouldn't come as a surprise since we know that a metal is a dielectric with $\epsilon" \gg \epsilon'$. Therefore as seen in (2-20) when this condition is true, the radiation efficiency tends to unity which is the radiation efficiency of a perfectly conducting metallic dipole. Figure 11 below gives the contour plot of (2-20) with respect to ϵ' and $\epsilon"$ and also with respect to ϵ' and $\tan(\delta)$ at a single frequency of 100MHz. The dipole radius $\rho = 1" = 2.54cm$ and the length is $l = 2m$.

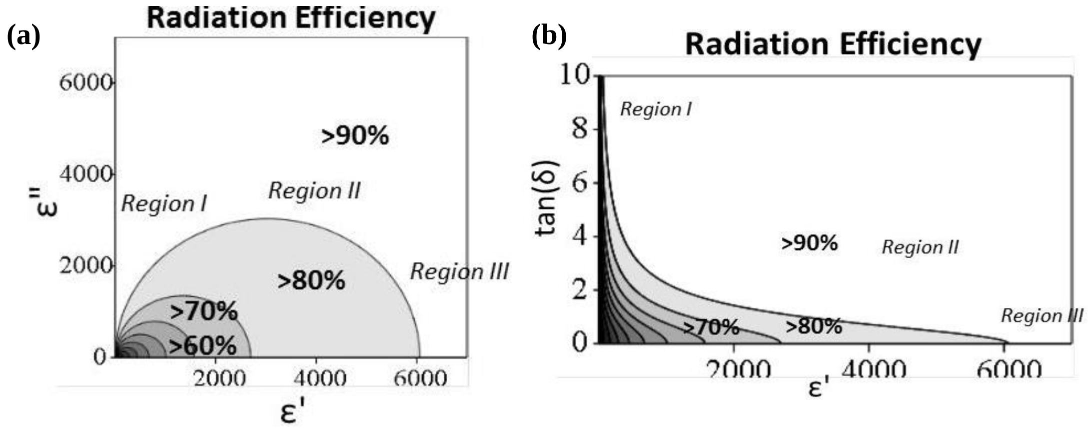

Fig. 2-11 Efficiency equation (2-20) contour plot (a) versus ϵ' and $\epsilon"$ and (b) versus ϵ' and $\tan(\delta)$. The three regions indicate region of high loss, moderate loss and low loss

Fig. 2-11 is in greyscale with the efficiency going from highest to lowest as the shade goes from light to dark. The contours are divided in tens i.e the lightest region has efficiency greater than 90%, the next, greater than 80% and so on. Region I, II and III stands for regions of high loss ($\epsilon" \gg \epsilon'$) or metal-like materials, moderate loss (where ϵ' is comparable to $\epsilon"$) and low loss ($\epsilon" \ll \epsilon'$) or what researchers call good dielectrics, respectively. The figure reiterates the comment made before that there are different ways to get low power loss-to-power radiated ratios. The figure also shows a third region of high efficiency where both $\epsilon"$ and ϵ' are sufficiently high and comparable to each other. It is obvious that the 'good dielectrics' of Region I will have high radiation efficiency due to low dielectric loss. In the metal-like Region I and Region II, the material skin-depth is very small compared to the antenna cross-section and hence all the fields are pushed out to the surface of the antenna. Therefore, the dielectric dipole tends to act more like the conventional metal dipole and therefore exhibit high radiation efficiency.

Now if the assumed current distribution is uniform then,

$$C_{diel} = \frac{\varepsilon_0(\varepsilon_r - 1)\pi\rho^2}{l} \tag{2-21}$$

$$Rrad = 80\pi^2\left(\frac{l}{\lambda}\right)^2 = 20(kl)^2 \tag{2-22}$$

Therefore, the radiation efficiency assuming a uniform current distribution can be derived the same way as before to be:

$$Eff_{diel\_uniform} = \frac{1}{1 + \frac{6}{\left(\frac{\rho}{l}\right)^2 (kl)^3} \frac{\varepsilon"}{|\varepsilon_r - 1|^2}} \tag{2-23}$$

In [3], Wheeler showed that the radiation power factor of a capacitor antenna (or inductor antenna) is somewhat greater than a factor p_{min} given below:

$$p_{min} = \frac{1}{6\pi} Abk^3 \tag{2-24}$$

where, ‘k’ is the wave number in free space and ‘Ab’ is the cylindrical volume ‘V’ occupied by the antenna with A=area of cross-section=$\pi\rho^2$ and b: length of the antenna ‘l’. Re-writing (2-23) in terms of this quantity we see that:

$$Eff_{diel\_uniform} = \frac{1}{1 + \frac{1}{p_{min}} \frac{\varepsilon"}{|\varepsilon_r - 1|^2}} = \frac{p_{min}}{p_{min} + \frac{\varepsilon"}{|\varepsilon_r - 1|^2}} = \frac{p_{min}}{p_{min} + p_{loss}} \tag{2-25}$$

The term in the denominator is the “loss power factor” [3] of this material antenna, i.e.

$$p_{loss} = \frac{\varepsilon"}{|\varepsilon_r - 1|^2} = \frac{\varepsilon"}{(\varepsilon' - 1)^2 + (\varepsilon")^2} \tag{2-26}$$

This quantity can be measured using a Wheeler cap/ Radiation shield [12]. For the triangular current distribution, the radiation efficiency equation in terms of p_{min} will look like:

$$Eff_{diel\_\Delta lar} = \frac{p_{min}}{p_{min} + \frac{4}{3}\, p_{loss}} \tag{2-27}$$

The term in front of ‘p_{loss}’ can be construed as a current distribution shape factor ‘f_c’. Therefore in general we can define the efficiency of a cylindrical dielectric dipole as

$$Eff_{dielectric} = \frac{p_{min}}{p_{min} + f_c p_{loss}} \tag{2-28}$$

$$where, f_c = \begin{cases} 1 & : uniform\ distribution \\ \frac{4}{3} & : triangular\ distribution \end{cases},$$

$$and \quad p_{min} = \frac{Vk^3}{6\pi} \quad and \quad p_{loss} = \frac{\varepsilon"}{|\varepsilon_r - 1|^2}$$

Simulations were run for the same set of dielectric constants ϵ_r as the lossless case but now with a loss tangent of 0.05. The comparison between the simulation and the analytical equation (2-20) is shown below in Fig. 2-12.

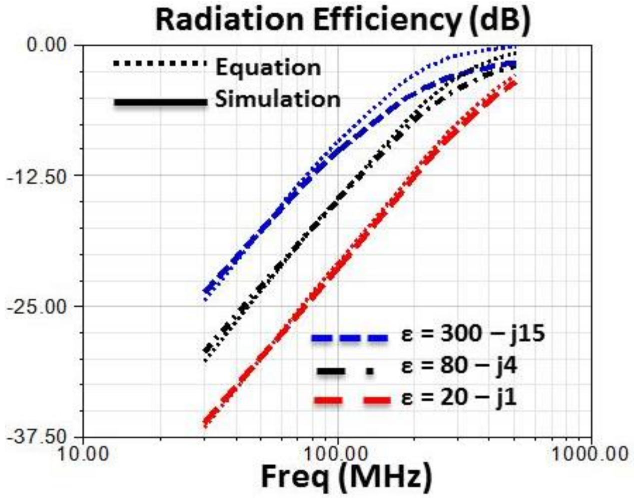

Fig. 2-12 Comparison of simulated results and analytical equation (2-20) of the Radiation Efficiency (dB) of a lossy dielectric dipole.

The agreement between the simulated result and (2-20) is very good at the low end (upto $k_0 l/2 = 1$) for all ε_r. As in the lossless case, it is clear that increasing the permittivity of a low loss dielectric dipole results in higher radiation efficiency. The appropriateness of the assumption made regarding the current distribution is verified in Fig. 2-13. The assumption has limited validity but the effects of it are not drastic in this case.

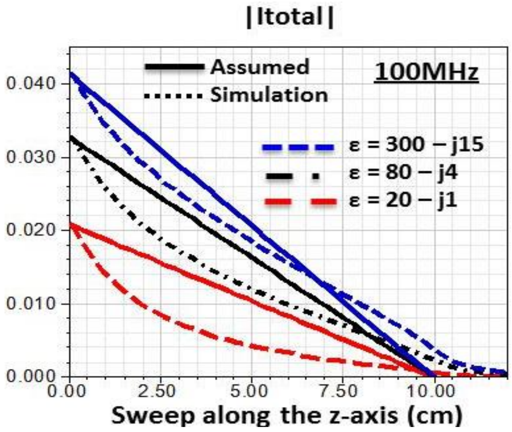

Fig. 2-13 Assumed and Simulated current distribution in the lossy dielectric monopole

Because of the leaky nature of these antennas, the shape of the current distribution is a decaying exponential away from the TM01 mode onset frequency and eventually becomes more and more triangular as the onset is approached. Therefore, along with the physical size of the antenna, the current distribution is a function of both frequency and permittivity. To prove unequivocally the accuracy of the radiation efficiency equation (2-23) (and therefore also (2-20)) a dielectric dipole antenna with multiple capacitive feeds was simulated as shown in Fig. 2-14.

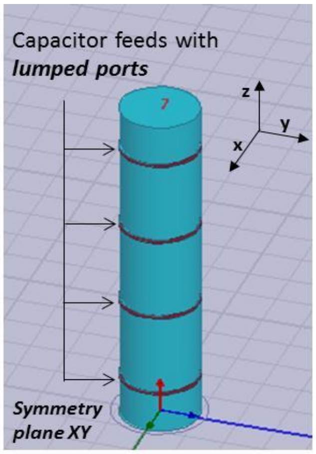

Fig. 2-14 Dielectric dipole antenna with multiple capacitive feeds simulated using lumped ports

The multiple capacitive feed forces the dipole current distribution to be more uniform. The multiple feeds were implemented using lumped ports in the fullwave simulator. The resulting current distribution and the radiation efficiency comparison with (2-25) are shown in Fig. 2-15.

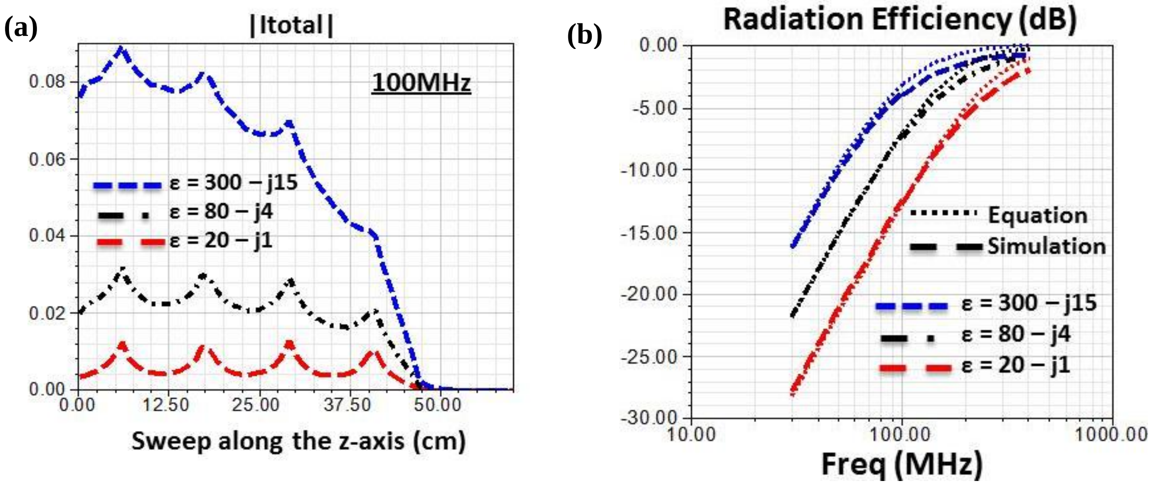

Fig. 2-15 (a) Current distribution of the multiple feed 1m long dielectric dipoles using dielectrics with$\tan(\delta) = 0.05$. (b) Radiation Efficiency as compared to (2-23).

The 'Λ' notches in Fig. 2-15(a) for all the cases are due to the calculation of the Amperean current at the lumped ports where there is no dielectric material. These notches are therefore non-radiating and can be ignored. The current distribution is significantly uniform and the comparison between simulated and calculated radiation efficiency shows better agreement as expected. These simulations were repeated for highly lossy materials i.e. with loss tangent $\tan(\delta) = 1$. The radiation efficiency for this case is shown in Fig. 2-16.

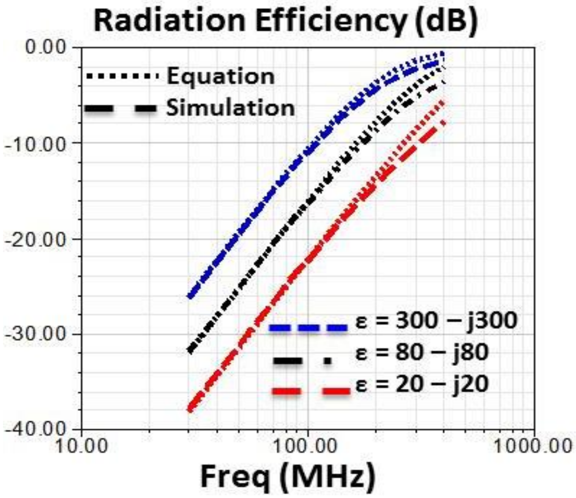

Fig. 2-16 Radiation Efficiency as compared to (2-23) of the multiple capacitive feed 1m long dipole using dielectrics with tan(δ)=1.

The current distribution is also uniform and the match between simulated efficiency and the analytical equation is still excellent. Thus the equation for radiation efficiency of (2-28) for a dielectric dipole is valid for all realistic materials.

2.5 Summary, Conclusions and Future Work

At the beginning of this chapter, the capacitor antenna conceived in the early part of last century was re-examined. It was shown through full-wave simulations that it is indeed true that adding a dielectric material is detrimental to radiation as envisioned by Wheeler and Schelkunoff. It was also shown that if the same dielectric material is placed outside the capacitor plates i.e. if the air capacitor is made to excite TM modes into a dielectric placed outside it, then we see an improvement in antenna Q and efficiency with increasing permittivity. But such a dipole can never surpass the performance of a metallic dipole of the same dimension. A closed form expression for radiation efficiency of a dielectric dipole with complex permittivity was derived (2-20),(2-23) and shown to be accurate using full-wave simulations. The equation shows that there are three possible ways to get maximum radiation efficiency out of a material dipole: (a) use a material with very low loss (b) use a material with very high loss but low real part of permittivity and (c) using a dielectric with both high loss and high real part of permittivity. The efficiency equation was also written in terms of the radiation power factor described by Wheeler explicitly showing the radiation power factor and the loss power factor for the antenna.

Based on the analysis in this chapter, it is seen that the electrically small dielectric dipole or monopole is an ineffectual antenna when compared to the metal alternative. That is, for electrically small monopoles we have access to materials with extraordinarily high ε'', namely metals, and the high efficiency that it entails. This is true at microwave frequencies but at optical frequencies, metals no longer have high ϵ'' [13]. They behave more or less like a low loss dielectric material. Thus, the concepts learned in this chapter can be directly applied in design of optical dielectric antennas.

However at microwave frequencies, when we consider low profile conformal antennas tangent to a ground plane, metallic antennas are not the answer and neither would be dielectric dipoles. In these antennas the primary radiating current is always fighting the opposing image current. Thus for conformal applications we require magnetic current radiators. Since magnetic conductors do not exist this leads us to the pragmatic choice of the permeable dipole, the electromagnetic dual of the dielectric dipole considered in this chapter. Such an antenna can be analyzed in the same way as the dielectric dipole by invoking duality.

Chapter 3

MAGNETO-DIELECTRIC DIPOLE ANTENNA: CIRCUIT MODEL & RADIATION EFFICIENCY

3.1 Introduction

In Chapter 1, we developed an electrically small circuit model for a realistic dielectric dipole antenna where the primary radiator is a pure dielectric material of complex permittivity $\varepsilon_r = \varepsilon' - j\varepsilon''$. We concluded that as long as we have materials with extraordinarily high ε'', namely metals, the dielectric dipole will be inferior in performance to a metallic dipole of the same size in the microwave regime. However, when it comes to low profile conformal antennas, both metallic & dielectric dipoles are not the answer. In this chapter we develop an electrically small circuit model for a magneto-dielectric dipole that is suited for such conformal applications. Such an antenna is analyzed the same way as the dielectric dipole in Chapter 1 by invoking duality.

Antennas made up of ideal magnetic conductors can be placed on a metallic ground plane without any adverse effect on their impedance or radiation efficiency because, unlike conventional metallic antennas, their primary radiating magnetic current is aided by the image current due to the ground plane. Since magnetic conductors do not exist, the more practical choice is to use permeable materials (with permeability: $\mu_r \gg 1$). Given that both natural and engineered permeable materials are often accompanied with a permittivity (ε_r) greater than 1, realistic magnetic materials are magneto-dielectrics i.e. they are materials with $\mu_r, \varepsilon_r > 1$. In this chapter we analyze a dipole antenna constructed from magneto- dielectric materials with $\mu_r \gg \varepsilon_r > 1$. A unique feature of these magneto-dielectric dipole antennas is that the main radiating current is the displacement current in the material rather than the conduction current used in conventional metallic antennas. Such an antenna is the ideal candidate for practical low profile conformal antenna applications.

The permeable dipole antenna is the electromagnetic dual of the dielectric dipole antenna described in Chapter 1 and hence radiates in the same two ways: end discontinuity and wave leakage along the structure. The desired magnetic dipole mode, the TE mode, is generated using an electric feed loop. In Section 3.2, we briefly review the classic and recent work on permeable and permeable core augmented radiators. In Section 3.3, starting with the electrically small circuit model of a dielectric dipole, we use the principle of duality to develop the model for the magneto-dielectric dipole and obtain a radiation efficiency equation that incorporates the material constitutive properties (complex μ_r and ε_r). This analysis encompasses the classic work on ferrite rod antennas and extends it to the development of efficient low frequency conformal radiators. In Section 3.4, full-wave simulations are used to verify the correctness of the results. And in Section 3.5, experimental results of a magneto-dielectric dipole constructed out of NiZn ferrite tiles are shown that confirm the value of the closed-form formulation. In Section 3.6, the duality between the magnetic dielectric dipole is shown via simulation and equations. Section 3.7 contains the summary of the chapter, some notable conclusions and possible future work on this subject.

3.2 Historical Development of Permeable Antennas

Throughout most of the 20^{th} century, the most common kind of permeable dipole antenna that was investigated was the ferrite rod antenna [1-2], [14-16]. It is an electrically small loop antenna (usually a multi-turn loop or solenoid) with a ferrite core. They were generally used in AM broadcast receivers due to its high Signal to Noise Ratio (SNR) and compact size as opposed to a metallic monopole. Schelkunoff [1] showed that for a given current in the winding, the field, hence the radiated power and therefore the radiation resistance, is increased by the ferrite core. Wheeler [2] also showed that the radiation power factor ‘p’ (which is the inverse of Quality factor ‘Q’) of such an inductor antenna is increased by the addition of the core thereby increasing the bandwidth of the antenna as well. The radiation efficiency of an electrically small ferrite loaded multi-turn loop antenna was first derived by Rumsey et al. [14] using the reaction concept [16]. Apart from ignoring permittivity they assumed that the ferrite had low loss i.e. $\mu' \gg \mu"$. The derived efficiency in [14] is:

$$Eff_{Rumsey} = \frac{1}{1 + \frac{1-D}{\frac{4/3\pi^2(\pi\rho^2 l)}{\lambda^3}} \frac{\mu"}{(\mu')^2}} \tag{3-1}$$

where, $'l'$ is the length of the ferrite rod, $'\rho'$ is the radius of the rod/solenoid, $\mu = \mu' - j\mu"$ is the complex permeability of the ferrite, $'\lambda'$ is the wavelength in free space and $'D'$ is the demagnetization factor. Using the same low loss ferrite assumption and ignoring permittivity, DeVore et al. [15] derived the radiation resistance R_{rad} and loss resistance R_{loss} of a multi-turn magnetically loaded loop antenna. Using R_{rad} and $R_{loss}$the radiation efficiency hence reads,

$$Eff_{DeVore} = \frac{1}{1+\frac{R_{loss}}{R_{rad}}} = \frac{1}{1+\frac{\omega\mu_0 \frac{n^2}{l}(\pi\rho^2)\frac{\mu"}{\left(1+D(\mu'-1)\right)^2}}{20k^4(n\pi\rho^2)^2\left(1+\frac{(\mu'-1)}{1+D(\mu'-1)}\right)^2}} \tag{3-2}$$

where, $'n'$ is the number of turns of the loop and $'k'$ is the wave number. For large aspect ratio (length/diameter) ferrite rods, the demagnetization factor is approximately zero. For such a case, both (3-1) and

(3-2) reduce to:

$$Eff_{Rumsey} = Eff_{DeVore} = \frac{1}{1+\frac{6}{(kl)^3\left(\frac{\rho}{l}\right)^2}\frac{\mu"}{(\mu')^2}} \tag{3-3}$$

Equation (3-3) leads us to two important conclusions:

(a) The radiation efficiency improves if the real part of the complex permeability (μ') is increased.

(b) High values of the imaginary part of the permeability (μ'') reduce the antenna efficiency.

Ever since these conclusions were reached, researchers appear to have believed that the only way to get efficient ferrite rod antennas was to use low loss materials; and since those were not readily available the interest in such antennas dwindled. The fact is that both Rumsey [14] and DeVore [15] assumed in their derivation that all they had were low loss materials i.e. $\mu' \gg \mu"$. Therefore, it was and still is unfair to come to the conclusion that lossy materials are detrimental to radiation efficiency solely based on (3-3). We show in this chapter, using a circuit model of the antenna in the electrically small regime, that it is possible to get high radiation efficiency using highly lossy materials.

Lately there has been a renewed interest in antennas that utilize magneto-dielectric materials, due to the availability of considerably lower loss materials than what was available a decade or two ago. Stuart et al. [17] designed an electrically small electric dipole antenna surrounded by a high permeability material that has very low antenna Q (quality factor). Another example is the use of magneto-dielectric materials as the core in a spherical TE mode wire antenna [18], to reduce its Q [19-21]. The high permeability core excludes the magnetic field from within the spherical antenna thereby reducing the stored internal magnetic energy and reducing Q. This fact is true only when there are no internal resonances within the sphere since resonances would increase the internal stored energy and therefore would reduce Q. Thus the onset of internal resonances imposes a restriction on the size and value of permeability that can be used.

Since all materials have some loss, the case of a lossy magneto-dielectric core was analyzed numerically in [22] and analytically in [23]. In [23], the authors showed that it is possible to get high radiation efficiency in a spherical wire antenna with a highly lossy magneto-dielectric core which goes against the conventional notion of requiring only low loss materials to get high efficiency. The magnetically loaded spherical antenna although attractive owing to its low Q is not a low-profile or conformal structure. In this chapter, we restrict the analysis to linear magneto-dielectric dipoles that can be placed tangential to a metallic ground plane. A purely numerical analysis of an array of lossy magneto-dielectric dipoles was shown in [24] in which the radiation efficiency was seen to increase as the loss tangent was increased beyond unity. We prove this observation analytically for a single magneto-dielectric dipole.

3.3 Radiation Efficiency of an Electrically Small Magneto-dielectric Dipole Antenna

The radiation efficiency of an antenna is defined as:

$$Eff_{rad} = \frac{Prad}{Prad + Plost} = \frac{1}{1 + \frac{Plost}{Prad}} \tag{3-4}$$

where, ‘$Prad$’ is the power radiated by the antenna and ‘Plost’ is the power lost in the antenna material.

In this section, the radiation efficiency of a magneto-dielectric dipole is derived starting from Schelkunoff’s circuit model for electrically small antennas. The ultimate goal is to estimate the material properties required to build a conformal magneto-dielectric antenna that can meet a given target efficiency requirement. We will use the concept of duality to derive the equations for the magnetic dipole antenna starting from the circuit model of a dielectric antenna from Chapter 1.

In the dielectric dipole model, the material properties are represented by a series internal impedance $'Z_{mat}'$ term which is composed of a complex internal capacitance $'C_{diel}'$ to represent permittivity $'\varepsilon_r'$ and a complex internal inductance $'L_{diel}'$ to represent permeability $'\mu_r'$. This Z_{mat} term accounts for the internal energy in the material. For a rod of radius, $'\rho'$, the internal capacitance is defined by assuming a uniform E-field (TM like fundamental mode) in the material thus yielding a simple capacitor of area $A = \pi\rho^2$ and separation $'l'$ which is the length on the dipole. The internal inductance is the inductance of a wire with uniform current $'I'$. The current distribution is assumed uniform. The circuit model is shown in Fig. 3-1.

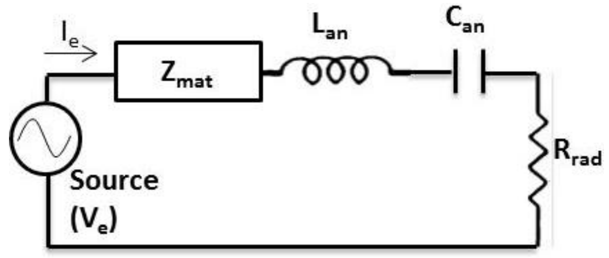

Fig. 3-1 Dielectric dipole model based on Schelkunoff's model of electrically small metallic antennas. The permeability of the dielectric material is also included.

where,

$$Z_{mat} = \frac{1}{j\omega C_{diel}} + j\omega L_{diel}$$

i.e.

$$Z_{mat} = \frac{1}{j\omega\left(\frac{\varepsilon_0(\varepsilon_r - 1)\pi\rho^2}{l}\right)} + \frac{j\omega\mu_0(\mu_r - 1)l}{8\pi} \tag{3-5}$$

Free space is subtracted from the internal capacitance (i.e. dielectric constant $(\varepsilon_r - 1)$) and internal inductance (i.e. permeability $(\mu_r - 1)$) since when $\varepsilon_r = \mu_r = 1$ we must be left with just the source. In such a case, the internal inductance is shorted out and the internal capacitance is open as expected.

The rest of the elements are components of Schelkunoff's electrically small metallic dipole model for uniform current distribution and are defined as:

$$C_{an} = \frac{\pi\varepsilon_0 \frac{l}{2}}{\ln\left(\frac{l/2}{\rho}\right)} \tag{3-6}$$

$$L_{an} = \frac{\mu_0 \frac{l}{2}}{3\pi} \ln\left(\frac{l/2}{\rho}\right) \tag{3-7}$$

$$Rrad = 80\pi^2 \left(\frac{l}{\lambda}\right)^2 = 20(kl)^2 \tag{3-8}$$

In Chapter 1, we did not include the effect of skin depth 'δ' since the majority of dielectric materials have $\mu_r \sim 1$ (L_{diel} was ignored). This is not true about the relative permittivity of realistic magnetic materials i.e. ε_r can be much greater than unity. For a plane wave, the skin depth can be calculated as:

$$\delta = \frac{1}{Im(k_0\sqrt{\mu_r \varepsilon_r})} \tag{3-9}$$

where, $'k_0'$ is the wave number in free space. For small ε_r, the calculated skin depth is usually larger than the radius 'ρ' of the material i.e. a very significant amount of the field pervades the entire material. For such cases 'δ' is set equal to 'ρ'. In magnetic materials with large ε_r, the electromagnetic skin depth of the material will force the magnetic flux to flow closer to the surface and therefore has the effect of decreasing the internal capacitance and internal inductance.

Since we are concerned with TM like modes in the dielectric dipole, the internal complex capacitance as seen in the first term of (3-5) can be corrected to account for skin depth (due to the permeability in this case) with an Area Factor (AF) in front of it. This factor is given by

$$AF = \frac{\pi\rho^2 - \pi(\rho - \delta)^2}{\pi\rho^2} = \frac{2\rho\delta - \delta^2}{\rho^2} \tag{3-10}$$

The correction to the inductance term is ambiguous since the shape of the φ-directed H-field in the transverse *'r'* direction is a function of frequency, size of the cross-section and the material properties μ_r and ε_r. A simple and good approximation to this rapidly changing field structure and the corresponding equation of the H_φ-field due to a current 'I' in the electrically small regime is shown below in Fig. 3-2.

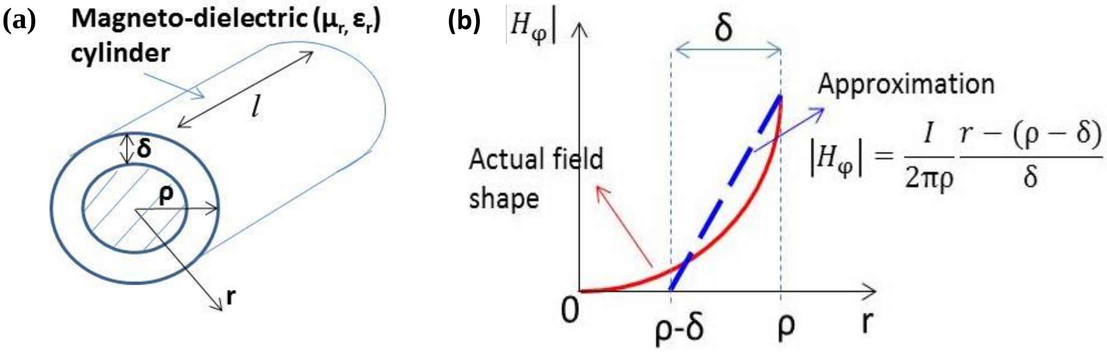

Fig. 3-2 (a) Skin depth in a cylindrical dipole (b) The transverse field shape for 0<δ<ρ of the TM mode dielectric dipole. The solid line is the actual field shape and the dashed line is the closest approximation

The resulting internal Field Shape Factor (FSF) correction term to the complex internal inductance term is given below:

$$FSF = \frac{1}{\left(\frac{\delta}{\rho}\right)^2}\left[1-\frac{8}{3}\left(1-\frac{\delta}{\rho}\right)+2\left(1-\frac{\delta}{\rho}\right)^2-\frac{1}{3}\left(1-\frac{\delta}{\rho}\right)^4\right] \tag{3-11}$$

This factor is derived by equating the magnetic energy integral to the circuital inductor energy equation and is shown in Appendix A. The input impedance of the dielectric dipole is therefore:

$$Zin_{dielectric} = \frac{1}{j\omega\left(\frac{\varepsilon_0(\varepsilon_r-1)\pi\rho^2}{l}AF\right)}+\frac{j\omega\mu_0(\mu_r-1)l}{8\pi}FSF$$
$$+j\omega\frac{\mu_0 l/2}{3\pi}\ln\left(\frac{l}{2}/\rho\right)+\frac{1}{j\omega\frac{\pi\varepsilon_0 l/2}{\ln\left(\frac{l}{2}/\rho\right)}}+20(kl)^2 \tag{3-12}$$

Using the concept of duality, we can obtain the magnetic input impedance (in mhos) of the dual antenna by:

$$Zin^{m}_{permeable}(mhos) = \frac{Zin^{e}_{dielectric}(ohms)}{\eta_0^2} \tag{3-13}$$

where, the superscript 'm' and 'e' represent magnetic and electric impedances, respectively. However, this dual problem maps a dielectric dipole with PEC feed lines and electric voltage source (V_e) to a permeable dipole with PMC feed line and magnetic voltage source (V_m) as shown in Fig. 3-3(a) and (b). Since we don't have PMC wires and a magnetic voltage source, the simplest way to feed a permeable dipole is to use an electric loop as shown in Fig. 3-3(c). The cross section of this electric loop fed permeable dipole at the feed loop is shown in Fig. 3-4.

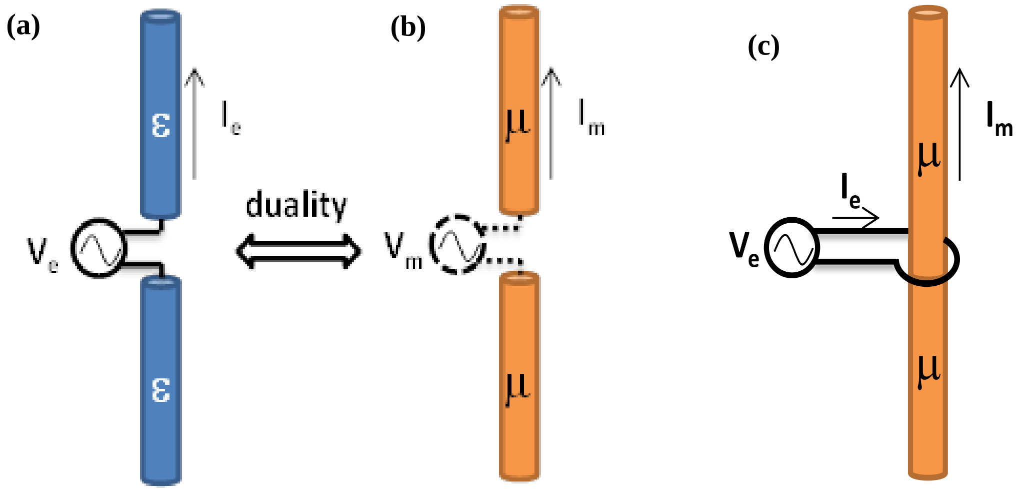

Fig. 3-3 (a) A dielectric dipole carrying an electric current 'Ie' fed with an electric voltage source 'Ve' and PEC feed lines (solid lines) such that $Zin_{dielectric} = Ve/Ie$ (b) Dual magnetic dipole carrying magnetic current 'Im' fed with a magnetic voltage source 'Vm' and PMC feed lines (dashed lines) such that $Zin_{dual\_dielectric} = Vm/Im$ (c) Permeable or magnetic dipole carrying magnetic current 'Im' fed with an electric loop.

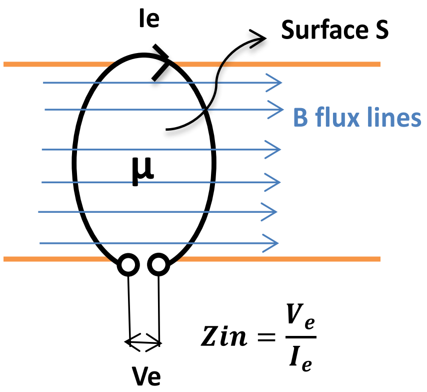

Fig. 3-4 Cross-section of the permeable material dipole of Fig. 3-3(c) at the electric feed loop. The mode of operation is TE like with the B-field along the axis of the dipole.

The magnetic current (Im) is defined as the surface integral of dB/dt or jωB passing through the surface ‘S’ and the magnetic voltage (Vm) is the line integral of the H-field around the closed contour of the surface. Now, according to Faraday’s law, the surface integral of jωB is equal to the line integral of the E-field along the closed contour of the surface ‘S’ (c(S)), which by definition is the electric voltage ‘Ve’. In other words,

$$I_m = -\int_S^{\cdot} \frac{\partial \boldsymbol{B}}{\partial t} \cdot dS = \oint_{c(S)}^{\cdot} \boldsymbol{E} \cdot dl = V_e \tag{3-14}$$

Also according to Ampere’s circuit law, the line integral of the H field along the closed contour formed by surface ‘S’ (c(S)), is the electric current Ie or in the dual world the magnetic voltage Vm. In other words,

$$I_e = \oint_{c(S)}^{\cdot} \boldsymbol{H} \cdot dl = V_m \tag{3-15}$$

Therefore,

$$Yin^{e}_{permeable}(mhos) = \frac{I_e}{V_e} = \frac{V_m}{I_m} = Zin^{m}_{permeable}(\,mhos) \tag{3-16}$$

From (3-13) and (3-16) the input admittance of a permeable dipole antenna fed by an electric loop is given by:

$$Yin_{permeable}^{e} = \frac{Zin_{dielectric}^{e}}{\eta_0^2} = Zin_{dielectric}^{e}\frac{\varepsilon_0}{\mu_0}\bigg|_{swap\ \varepsilon_r \leftrightarrow \mu_r} \tag{3-17}$$

Since we are interested in a magneto-dielectric dipole and not just a permeable one, we will call the input admittance of the magneto-dielectric circuit $Yin_{magnetic}$. Therefore from

(3-12) and (3-17), the input admittance of the magneto-dielectric dipole can be written as

$$Yin_{magnetic} = Y_{mat} + \frac{j\omega\varepsilon_0 l/2}{3\pi} ln\left(\frac{l/2}{\rho}\right) + \frac{1}{\frac{j\omega\pi\mu_0 l/2}{\ln\left(\frac{l/2}{\rho}\right)}} + \frac{20(kl)^2}{\eta_0^2} \tag{3-18}$$

$$= Y_{mat} + j\omega C + \frac{1}{j\omega L} + G_{rad}$$

where,

$$Y_{mat} = \frac{1}{j\omega\mu_0(\mu_r - 1)\frac{\pi\rho^2}{l}AF} + \frac{j\omega\varepsilon_0(\varepsilon_r - 1)l}{8\pi}FSF \tag{3-19}$$

$Yin_{magnetic}$ is the admittance of the following circuit shown in Fig. 3-5.

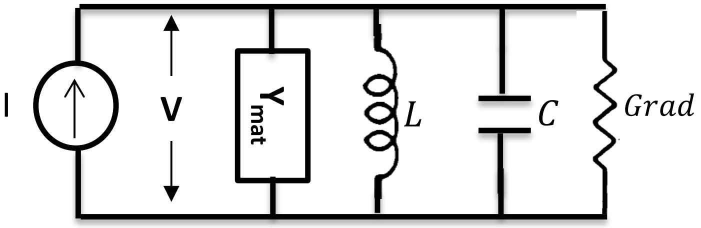

Fig. 3-5 Electrically small magnetic dipole antenna circuit model.

Now since $\mu_r = \mu' - j\mu"$ and $\varepsilon_r = \varepsilon' - j\varepsilon"$, Y_{mat} can be expanded to get

$$Y_{mat} = \frac{1}{j\omega \frac{\mu_0 \pi \rho^2}{l} \frac{|\mu_r - 1|^2}{\mu' - 1} AF} + \frac{1}{\frac{\omega \mu_0 \pi \rho^2}{l} AF} \frac{\mu"}{|\mu_r - 1|^2} \tag{3-20}$$

$$+ \frac{j\omega\varepsilon_0(\varepsilon' - 1)l}{8\pi} FSF + \frac{\omega\varepsilon_0\varepsilon" l}{8\pi} FSF$$

As in the case of the dielectric dipole, the losses in the antenna arise from the two frequency dependent “loss conductance” terms above (real terms with $\varepsilon"$ and $\mu"$).

$$G_{mat} = \frac{l}{\omega\mu_0\pi\rho^2 AF} \frac{\mu"}{|\mu_r - 1|^2} + \frac{\omega\varepsilon_0\varepsilon" l}{8\pi} FSF \tag{3-21}$$

Therefore, the power lost in the antenna with a voltage ‘V’ across its terminals is defined as:

$$Plost = \frac{1}{2}|V|^2 G_{mat} \tag{3-22}$$

while the radiated power (using *Grad* from (3-18)) is defined as:

$$Prad = \frac{1}{2}|V|^2 Grad \tag{3-23}$$

From (3-4), (3-18), (3-21), (3-22) and (3-23) after some algebraic manipulation knowing that $k = \omega/c_0$, $c_0 = \frac{1}{\sqrt{\mu_0\varepsilon_0}}$ and $\eta_0 = \sqrt{\mu_0/\varepsilon_0} = 120\pi$ the Radiation Efficiency of a magneto-dielectric antenna (Eff_{mag}) having uniform current distribution is given by:

$$Eff_{mag} = \frac{1}{1 + \frac{\mu"}{|\mu_r - 1|^2} \frac{6}{AF\left(\frac{\rho}{l}\right)^2 (kl)^3} + \frac{3}{4}\frac{\varepsilon"}{(kl)} FSF} \tag{3-24}$$

Now if the assumed current distribution is triangular and not uniform then,

$$C_{diel} = 3\left(\frac{\varepsilon_0 \varepsilon_r \pi \rho^2}{l}\right) AF \tag{3-25}$$

$$L_{diel} = \frac{1}{3}\left(\frac{\mu_0 \mu_r l}{8\pi}\right) FSF \tag{3-26}$$

$$Rrad = 20\pi^2 \left(\frac{l}{\lambda}\right)^2 = 5(kl)^2 \tag{3-27}$$

Therefore, the radiation efficiency assuming a triangular current distribution can be derived in the same way as before to be:

$$Eff_{mag\,\Delta lar} = \frac{1}{1 + \frac{\mu"}{|\mu_r - 1|^2} \frac{8}{AF\left(\frac{\rho}{l}\right)^2 (kl)^3} + \frac{\varepsilon"}{(kl)} FSF} \tag{3-28}$$

Now for a purely magnetic material i.e. $\varepsilon_r = 1$, for $\delta > \rho$ which implies AF = FSF = 1, (3-24) simplifies to

$$Eff_{purely\,mag} = \frac{1}{1 + \frac{\mu"}{|\mu_r - 1|^2} \frac{6}{\left(\frac{\rho}{l}\right)^2 (kl)^3}} \tag{3-29}$$

This equation is the exact dual of the radiation efficiency of a dielectric dipole in Chapter 1. Equation (3-29) can be re-written in terms of Wheeler’s loss power factor and minimum power factor as

$$Eff_{purely\,mag} = \frac{1}{1 + \frac{1}{p_{min}} \frac{\mu"}{|\mu_r - 1|^2}} = \frac{p_{min}}{p_{min} + \frac{\mu"}{|\mu_r - 1|^2}} = \frac{p_{min}}{p_{min} + p_{loss}} \tag{3-30}$$

where,

$$p_{min} = \frac{1}{6\pi} Abk^3 \; and \; p_{loss} = \frac{\mu"}{|\mu_r - 1|^2} = \frac{\mu"}{(\mu' - 1)^2 + (\mu")^2} \qquad (3\text{-}31)$$

(3-29) and (3-30) tell us that there are <u>two ways</u> to get low power loss (and therefore high radiation efficiency) using magnetic materials with $\mu'' << \mu'$ OR with $\mu'' >> \mu'$. The second conclusion that we need a material that is highly lossy should not come as a surprise since we know that a perfect magnetic conductor is a magnetic material with $\mu'' >>> \mu'$. Therefore when this condition is true we see that the efficiency tends to unity which is the radiation efficiency of a PMC dipole. The contour plot of the efficiency equation of (3-29) for a 1 inch radius cylinder is shown in Fig. 3-6. It is clear from Fig. 3-6 that this particular conformal magnetic dipole will have approximately the same radiation efficiency as a purely metallic dipole for three different kinds of material: a) the well-known extremely low loss material with $\mu' > 1000$ which is labeled region III b) the unconventional extremely lossy material ($\mu" > 200$) with low $\mu' < 10$ or $\tan(\delta) > 5$ which is labeled region I and c) a region where both μ' and $\mu"$are moderately high labeled region II.

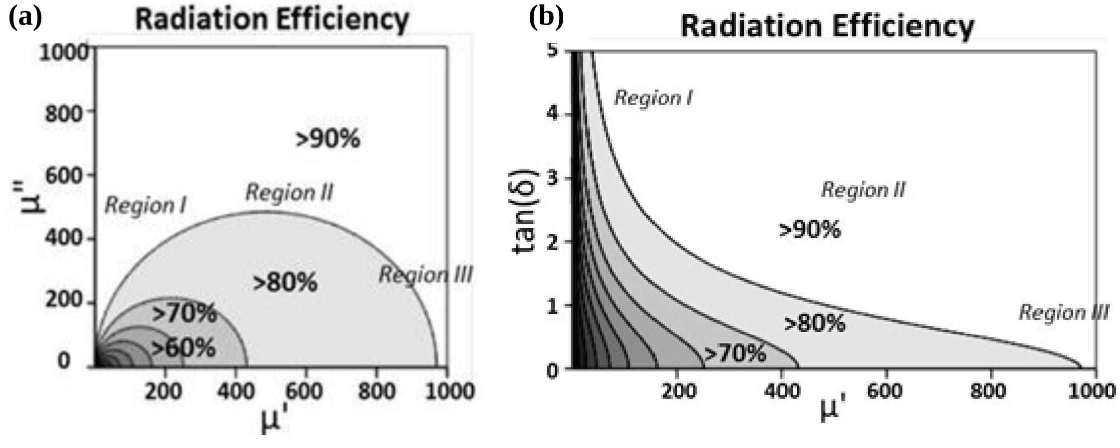

Fig. 3-6 (a) Efficiency equation (3-29) contour plot (a) versus μ' and μ" and (b) versus μ' and tan(δ). The three regions indicate region of high loss, moderate loss and low loss.

In Region I and Region II, the material skin-depth is so small that all the fields are pushed out of the antenna. Therefore, the material dipole tends to act more like the conventional metal dipole and therefore exhibit high radiation efficiency. The same conclusions were obtained for the dielectric dipole.

3.4 Full-wave Simulations of the Magneto-dielectric Dipole Antenna

Full wave simulations of the magneto-dielectric dipole were carried out using a variety of magneto-dielectric material parameters in order to ascertain the accuracy of (3-24) and (3-28). Two simulation cases are shown in Fig. 3-7. In Fig. 3-7(a) a magnetic dipole is fed with a single current loop and in Fig. 3-7(b) a magnetic dipole is fed with eight current loops. The single loop simulation results will be compared with (3-28) in which the magnetic current distribution was assumed to be triangular. However, due to the leaky nature of radiation from a material antenna, this assumption will be true only for a small range of frequencies. The current distribution for a material dipole is not only a function of the antenna size but also of the material properties. Also, this leaky behavior implies that the entire length of the antenna will not contribute to radiation at all frequencies. The energy will leak out sooner when operated well below the TE01 guidance frequency.

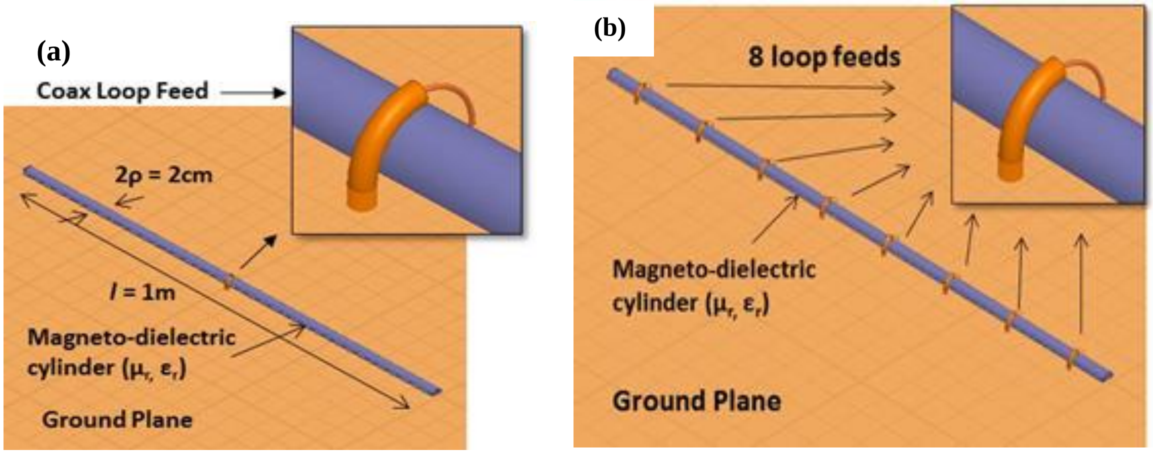

Fig. 3-7(a) Simulation geometry of a magneto-dielectric dipole fed by a single electric feed loop and (b) eight feed loops

One way to ensure that all the material available contributes to radiation is to employ multiple feed loops. By doing so, we force the magnetic current distribution to be more uniform for which we have derived (3-24). The magneto-dielectric dipole simulated is 1m long (extending from -50cm to 50cm on the simulation axis) with a radius of 1cm.The magnetic current distribution $'I_m'$ (volts) along the dipole length for the single feed loop case is shown in Fig. 3-8.

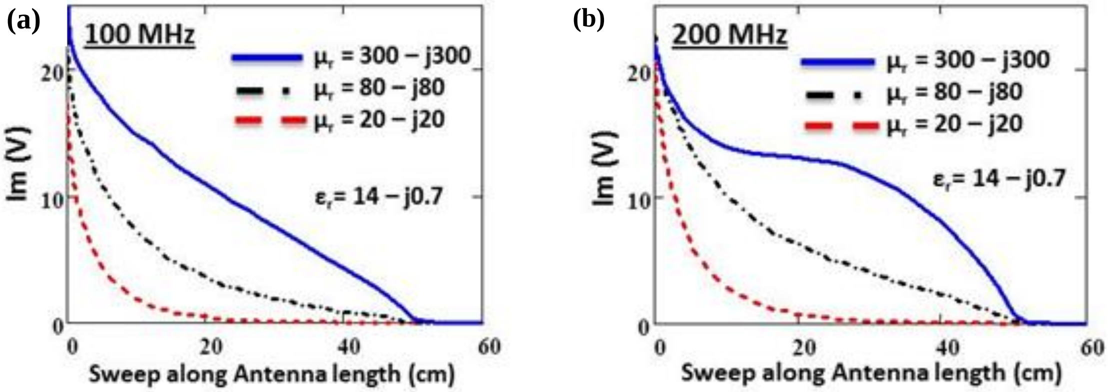

Fig. 3-8(a) Magnetic current distribution along the length of the dipole at two frequencies (a) 100MHz ($k_0 l/2 = 1.05$) (b) 200MHz ($k_0 l/2 = 2.1$)

The radiation efficiency comparison with the triangular current distribution equation (3-28) is shown in Fig. 3-9. As expected from Fig. 3-8(a) the agreement is excellent throughout the electrically small regime for the high permeability case ($\mu_r = 300 - j300$) and degrades from there as the current becomes more exponentially damped.

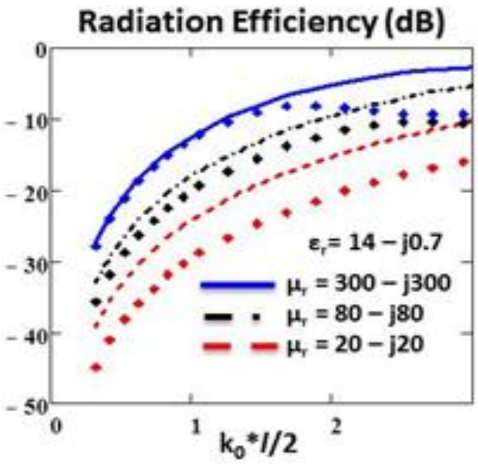

Fig. 3-9 Simulated Radiation Efficiency (symbols) comparison with (3-28) (solid curves) for a single loop fed magneto-dielectric dipole.

As mentioned before, one way to obviate the problem of the exponentially damped (leaky) current is to employ multiple feed loops along the length of the antenna. This is tantamount to using a solenoid feed ensuring that the B-field or the magnetic current is uniform throughout the length of the dipole. A solenoid would work fine in the electrically small limit but, as the antenna becomes electrically large, there would be a considerable phase difference in the electric current along the length of the solenoid which can cause destructive interference in radiation. Therefore in order to minimize this effect, it is better to use multiple individual feed loops each fed in phase as shown in Fig. 3-7(b).

The magnetic current distribution plots of a multi-loop fed 1m long (extending from -50cm to 50cm on the simulation axis) magnetic dipole are shown in Fig. 3-10. The current distribution is nearly uniform except for the spikes seen in the figure. These spikes/notches result from the calculation of the current as the closed line integral of the electric field when we get too close to the feed loops. Very close to the loops we capture in the integral near field flux lines (higher order modes) that are not part of the assumed magnetic current in the material.

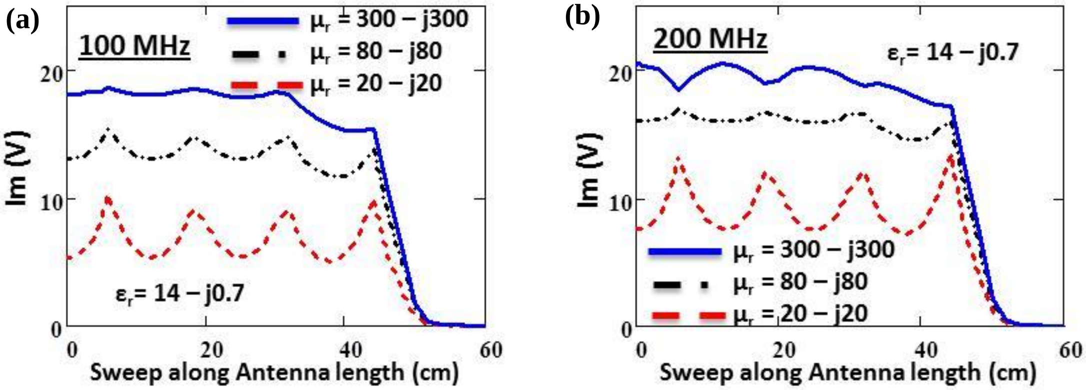

Fig. 3-10 Uniform magnetic current distribution along the length of the dipole at two frequencies (a) 100MHz ($k_0 l/2 = 1.05$) (b) 200MHz ($k_0 l/2 = 2.1$)

The simulated results for radiation efficiency and the comparison with equation (3-28) are shown in Fig. 3-11. The cases studied vary from low permeability to high permeability cases where the permittivity is also varied as $\varepsilon_r = 10 - j\varepsilon"$ to validate the calculation of skin depth in equation (3-28). Even though the above model was derived assuming the dipole is electrically small, it behaves properly all the way to the half-wave resonance ($k_0 l = \pi$). For low loss materials the validity extends further as seen in Fig. 3-11(a).

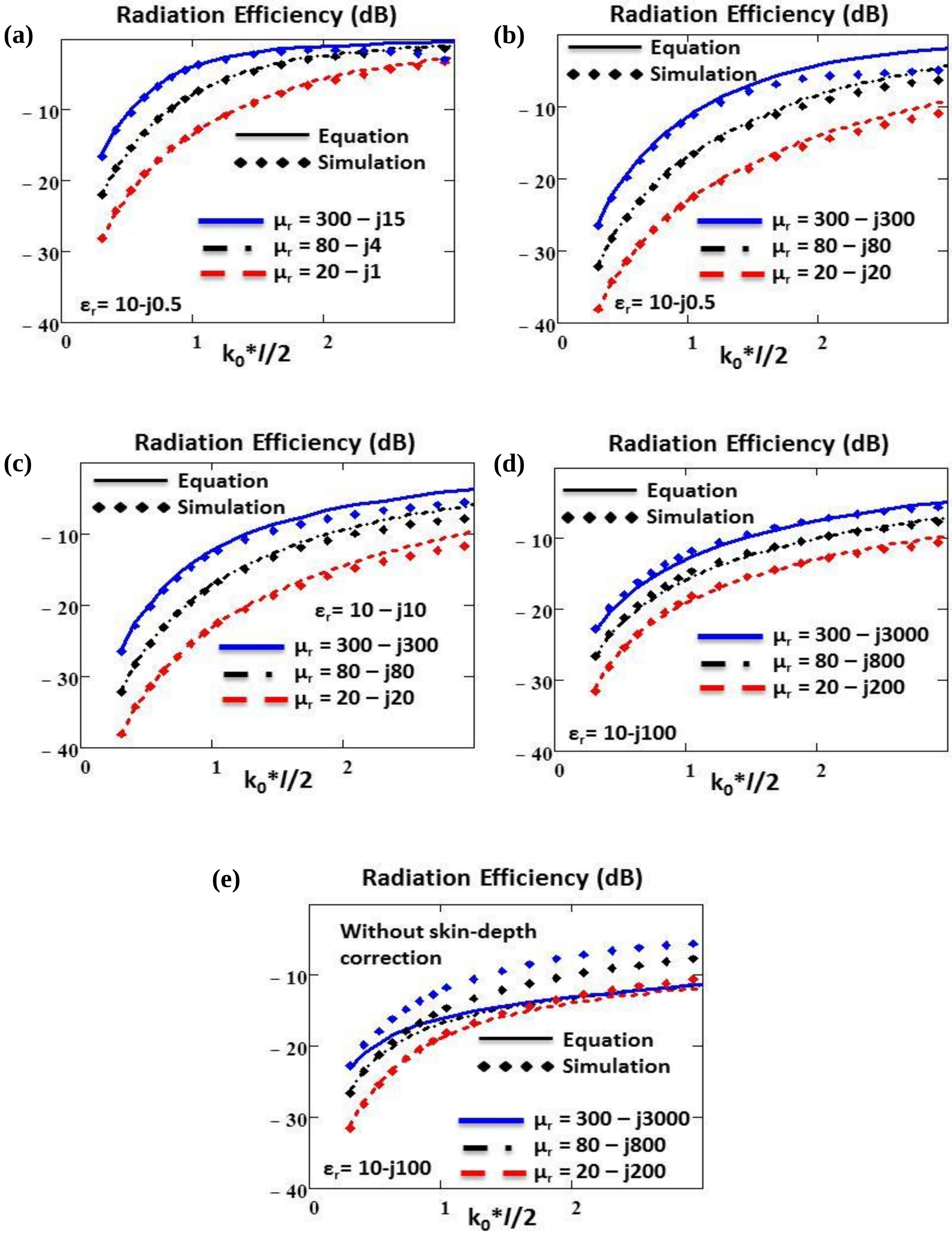

Fig. 3-11 Radiation Efficiency comparison of (3-28) with full-wave simulations of a multi-loop fed magnetic dipole made of (a) low loss ($tan(\delta_m) = tan(\delta_e) = 0.05$), (b) high magnetic but low electric loss ($tan(\delta_m) = 1$ & $tan(\delta_e) = 0.05$) (c) high loss($tan(\delta_m) = tan(\delta_e) = 1$) (d) extremely high loss ($tan(\delta_m) = tan(\delta_e) = 10$) and (e) extremely high loss materials but neglecting skin depth effects in the efficiency calculation.

For the low and moderate loss in permittivity or permeability or both, the inclusion of skin depth effect i.e. the area factor AF and the internal field shape factor have negligible effects on efficiency as skin depth ‘δ’ is almost always greater than radius ‘ρ’. But for the extremely high loss case i.e. for $\tan(\delta_m) = \tan(\delta_e) = 10$, the correction factors make a huge impact to retain the validity of the equation over a broader band of frequency. (Compare the results in Fig. 3-11(d) with those in Fig. 3-11(e) where the skin depth effect is neglected).

3.5 Magneto-dielectric Dipole Prototype

A magneto-dielectric dipole was constructed using commercially available NiZn ferrite tiles from FairRite by *JEM Engineering LLC* (Fig. 3-12). The antenna is 40” long, 4” wide and 1.5” tall above the ground plane. The dipole was fed with four symmetric feed loops.

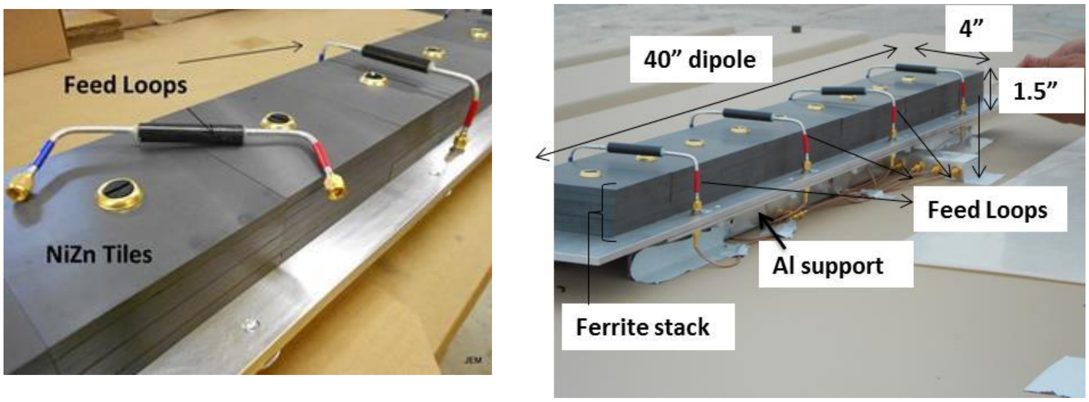

Fig. 3-12 Magneto-dielectric dipole constructed using the NiZn ferrite tiles.

Fig. 3-13(a) shows the material properties of the FairRite tiles used in the design. Note that in the frequency range of interest (VHF) the material is lossy with the magnetic loss tangent $\tan(\delta_m) > 2$. Fig. 3-13(b) shows the comparison between full-wave simulation radiation efficiency and the two closed form equations: (3-24) and the one derived by Rumsey et al. ignoring permittivity and assuming low material loss (3-3). As expected, since Rumsey's equation was for only low loss materials ($\tan(\delta_m) << 1$) the curve deviates significantly from simulation results whereas, equation (3-24)'s agreement is excellent up to $l/\lambda = 0.4$ that is well beyond the electrically small antenna assumption.

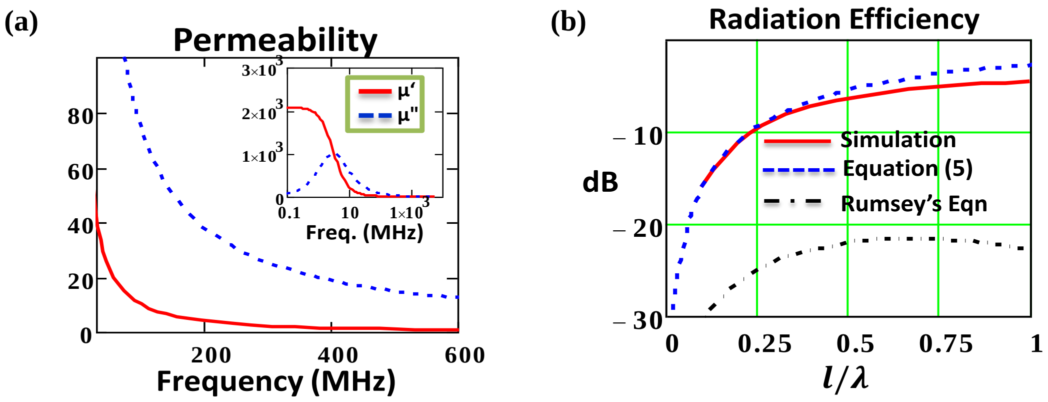

Fig. 3-13 (a) NiZn FairRite tile material permeability. Permittivity of the ferrite is $\varepsilon_r = 14 - j0.14$. (b)Comparison of simulated Radiation Efficiency of the magneto-dielectric dipole with two closed form equations.

The magneto-dielectric antenna gain was measured in JEM's anechoic chamber. The comparison between measured and simulated gain is shown in Fig. 3-14(b). Since the model assumes an infinite ground plane the measurement is compared to full wave simulations. Their gains agree well over the entire range of measured frequencies. This suggests that the circuit model works well in the electrically small limit since the measured gain agreed with the simulations and the simulated radiation efficiency matches the analytical equation.

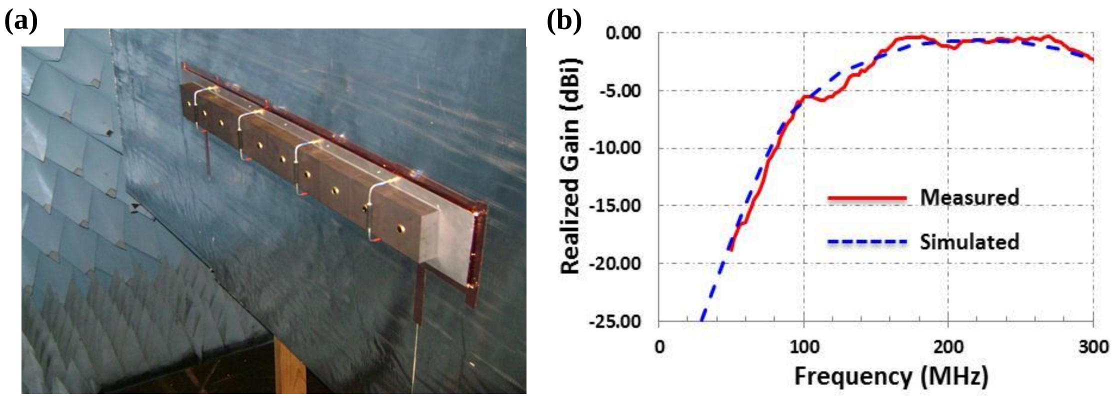

Fig. 3-14 (a) Magneto-dielectric dipole antenna mounted in the anechoic chamber (b) Comparison of simulated realized gain & antenna gain measured in the chamber.

The lossy magneto-dielectric dipole antenna performance was also compared to a conventional whip antenna mounted on top of a HUMVEE. The two antennas were mounted as shown in Fig. 3-15(a). Fig. 3-15(b) shows the comparison of raw gain measurements of two perpendicular planes (90^0 & 270^0).

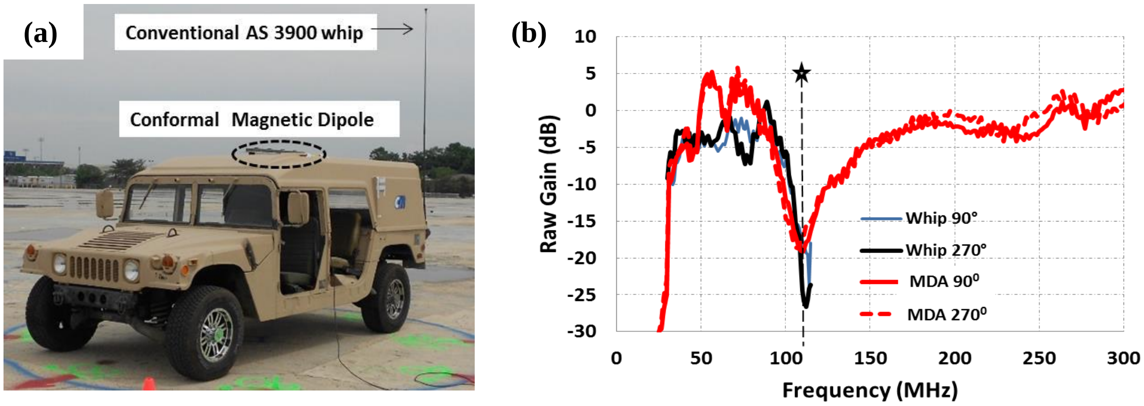

Fig. 3-15 (a) Conformity of a Magneto-dielectric dipole as compared to a conventional Whip antenna (b) Magneto-dielectric dipole raw measured gain comparison with the standard whip antenna on a Humvee.

In the operational frequency range of the whip, the lossy MD antenna excels in performance compared to the standard whip between 30-88MHz. Any variations in gain in this range are due to structural resonances being setup in the HUMVEE by the antenna under test. The star marker (110MHz) indicates the whip antenna's roll-off above 88MHz. At the same frequency the conformal antenna is half wavelength away from the ground causing a null in the gain.

3.6 A Note on the Duality between Material Dipoles

We have always known that a PMC dipole fed by a magnetic voltage generator is the dual of a PEC dipole fed with an electric voltage generator. In the same way, a material dipole made up of a dielectric material fed using an electric voltage source must be the dual of dipole made up of magnetic material fed with magnetic voltage source. We used this principle while deriving the equation of radiation efficiency of a magneto-dielectric dipole in the preceding section. We pointed out in that section that the analytic efficiency equations of a dielectric and magnetic dipole are perfectly dual. In this section, we prove this conjecture via simulations. Consider the two cases shown in Fig. 3-16. Fig. 3-16(a) is a dielectric dipole fed with eight voltage ports to ensure uniform current distribution and (b) is the magnetic dipole of the previous section with eight metallic loops as feeds. The two dipoles are of the same length (1 m) and have the same cross-section (radius =1").

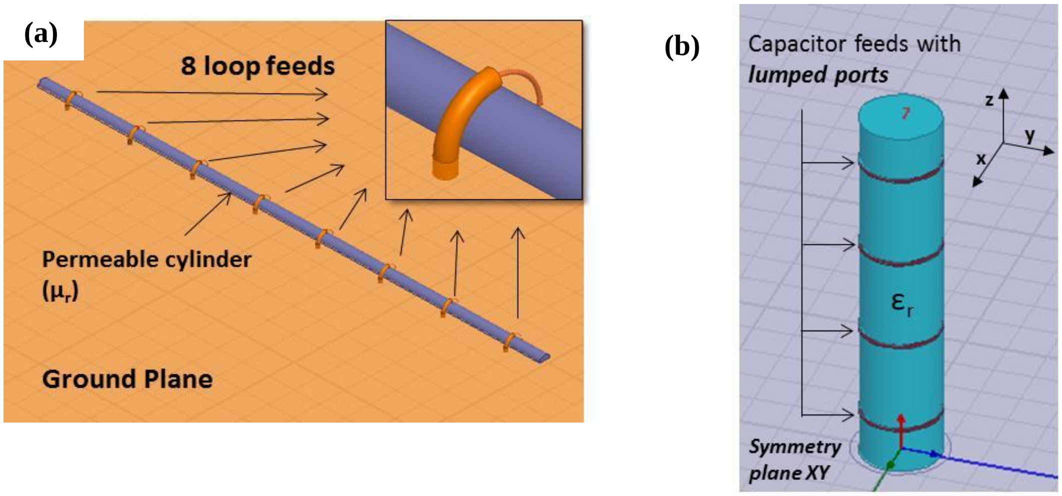

Fig. 3-16 (a) Magnetic dipole with 8 electric feed loops. (b) Dielectric Dipole with 8 lumped port feeds.

Fig. 3-17 shows the comparison of the radiation efficiency of the two cases. They are on top of each other which confirm our assertion that the dielectric dipole from Chapter 1 and the magnetic dipole presented in this chapter are perfect duals of each other. But, there is a basic fundamental difference between the two that makes the magnetic dipole much more valuable. The dielectric dipole due to its electric displacement currents cannot be placed conformal to a metallic ground plane as it would short out and is not the best replacement of metallic dipoles. Whereas the magnetic dipole, due to the fact that the dB/dt magnetic displacement current is the only source of radiation, can be placed perfectly conformal to any metallic surface without sacrificing performance. Assuming that area is not the limiting factor, magnetic dipoles are ideal candidates for low profile conformal antenna applications since their radiation performance can approximate that of its dual counterpart (a vertical electric monopole).

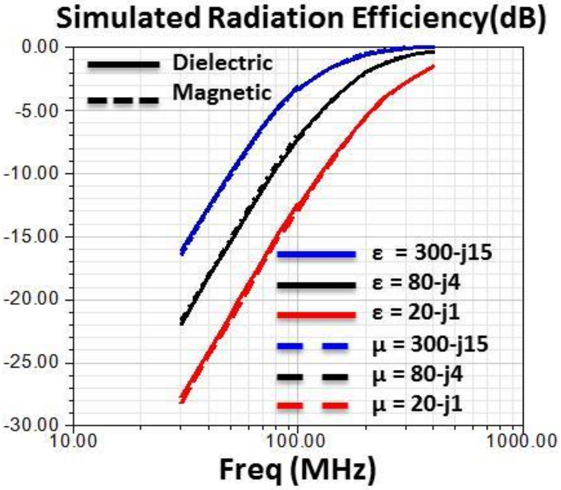

Fig. 3-17 Radiation Efficiency comparison of a dielectric and magnetic dipole of the same length and cross-section but with dual material properties.

3.7 Summary, Conclusions and Future Work

A closed form equation for the radiation efficiency equation was developed for a small magneto-dielectric dipole. The equation is derived from the electrically small circuit model of a conventional metallic dipole by adding additional elements (L for permeability and C for permittivity) to take into account the material properties. The equation shows that maximum radiation efficiency of a material dipole can be obtained not only by using a material with very low loss but also with a material that has very high loss.

Two equations were derived, one for uniform magnetic current distribution generated by using multiple feed loops and the other for a triangular current distribution assumed with a single feed loop. It is hard to maintain a triangular current distribution across the length of a magneto-dielectric dipole due to the leaky nature of radiation mechanism and hence the validity of the radiation equation for this case is limited. On the other hand, fairly uniform current distribution can be maintained with multiple loops and hence the radiation efficiency equation for uniform current distribution matches the full-wave simulations accurately.

The circuit model presented here does not include the details of the feed structure. Once the feed is included we would have a complete model that can be used to calculate the input impedance of the antenna. This will enable us to calculate the Antenna Q and hence the bandwidth of the antenna; thus yielding in one formulation the radiation efficiency and antenna bandwidth, the two parameters that completely characterize a given material dipole antenna.

The next logical extension to this development is to analyze a loop or a toroid made up of a magneto-dielectric material. Although such an antenna would occupy more area over ground than the linear dipole it would offer unequivocal vertical polarization for all azimuth directions which can therefore replace a vertical metallic dipole antenna. Since there is a closed form model for the electrically small metallic loop antenna with uniform current distribution, we can use the same steps used in this chapter to arrive at the radiation efficiency equation of a magneto-dielectric toroid. This is the subject of the next chapter.

Chapter 4

MAGNETO-DIELECTRIC LOOP/TOROID ANTENNA: CIRCUIT MODEL & RADIATION EFFICIENCY

4.1 Introduction

The magneto-dielectric dipole in Chapter 3 has a broadside ‘figure of 8’ pattern just like a metallic dipole. However, often conformal low-profile antenna applications demand omnidirectional antenna coverage. In fact this is one of the reasons why a vertical metallic monopole is preferred over a horizontal metallic dipole, apart from the obvious problem of destructive image effect in the horizontal dipole. A magneto-dielectric loop antenna has a radiation pattern that is identical to a vertical electric dipole. It has an omnidirectional pattern in the azimuth plane and it comes with the added advantage of being low profile and conformal without any adverse effects due to a conventional metallic ground plane. Therefore, it is quintessential to model the magneto-dielectric loop antenna.

The steps followed in the derivation of the model and the radiation efficiency equation is identical to that of the magneto-dielectric dipole. In Section 4.2, we will start with the electrically small circuit model of a metallic loop and introduce the material properties as a series impedance to come up with a model for a dielectric loop antenna. Then, similar to the derivation in Chapter 3, we will use the principle of duality and obtain an admittance circuit model of the magneto-dielectric loop which will then be used to derive the radiation efficiency. In Section 4.3, we will examine design trade-offs based on the radiation efficiency equation between a magneto-dielectric loop and a magneto-dielectric dipole. In Section 4.4, a practical application of the admittance circuit model of the loop: design of a Body Wearable Belt Antenna will be discussed. Section 4.5 contains the summary of the chapter, some notable conclusions and possible future work on this subject.

4.2 Circuit model

In this section, the radiation efficiency of a magneto-dielectric loop is derived starting from the circuit model for an electrically small metallic loop antenna. The ultimate goal is to estimate the material properties required to build a conformal magneto-dielectric antenna that can meet a given target efficiency requirement. As in Chapter 2, the material properties are introduced by a series internal impedance $'Z_{mat}'$ term which is composed of a complex internal capacitance $'C_{diel}'$ to represent permittivity $'\varepsilon_r'$ and a complex internal inductance $'L_{diel}'$ to represent permeability $'\mu_r'$. This Z_{mat} term accounts for the internal energy in the material. For a loop of radius $'a'$ and wire radius, $'\rho'$, the internal capacitance is defined by assuming a uniform E-field (TM like fundamental mode) in the material thus yielding a simple capacitor of area $A = \pi\rho^2$ and separation $'2\pi a'$ which is the circumference of the loop. The internal inductance is the inductance of a wire of length equal to the circumference of the loop with a uniform current $'I'$. The current distribution is assumed uniform. The circuit model is shown in Fig. 4-1.

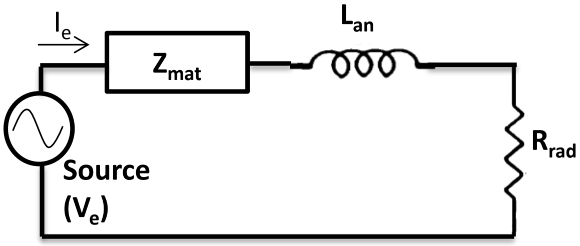

Fig. 4-1 Electrically small dielectric loop antenna model.

where,

$$Z_{mat} = \frac{1}{j\omega C_{diel}} + j\omega L_{diel}$$

i.e.

$$Z_{mat} = \frac{1}{j\omega\left(\frac{\varepsilon_0(\varepsilon_r - 1)\pi\rho^2}{2\pi a}\right)} + \frac{j\omega\mu_0(\mu_r - 1)(2\pi a)}{8\pi} \tag{4-1}$$

Free space is subtracted from the internal capacitance (i.e. dielectric constant $(\varepsilon_r - 1)$) and internal inductance (i.e. permeability $(\mu_r - 1)$) since when $\varepsilon_r = \mu_r = 1$ we must be left with just the source. In such a case, the internal inductance is shorted out and the internal capacitance is open as expected.

The rest of the elements are components of the electrically small metallic loop model for uniform current distribution and are defined as:

$$L_{an} = \mu_0 a\left(\ln\left(\frac{8a}{\rho}\right) - 2\right) \tag{4-2}$$

$$Rrad = 320\pi^4\left(\frac{\pi\rho^2}{\lambda^2}\right)^2 = 20\pi^2(ka)^4 \tag{4-3}$$

To account for skin depth, the same correction factors as in Chapter 3 can be used. The internal complex capacitance is corrected by the area factor ‘AF’ (3-10).

$$AF = \frac{\pi\rho^2 - \pi(\rho - \delta)^2}{\pi\rho^2} = \frac{2\rho\delta - \delta^2}{\rho^2}$$

The internal complex inductance is corrected by the Field Shape Factor ‘FSF’ (3-11).

$$FSF = \frac{1}{\left(\frac{\delta}{\rho}\right)^2}\left[1 - \frac{8}{3}\left(1 - \frac{\delta}{\rho}\right) + 2\left(1 - \frac{\delta}{\rho}\right)^2 - \frac{1}{3}\left(1 - \frac{\delta}{\rho}\right)^4\right]$$

The input impedance of the dielectric loop is therefore:

$$Zin_{dielectric} = \frac{1}{j\omega\left(\frac{\varepsilon_0(\varepsilon_r - 1)\pi\rho^2}{l}AF\right)} + \frac{j\omega\mu_0(\mu_r - 1)l}{8\pi}FSF$$

$$+ j\omega\mu_0 a\left(\ln\left(\frac{8a}{\rho}\right) - 2\right) + 20\pi^2(ka)^4 \tag{4-4}$$

Using the concept of duality as explained in Chapter 3, using (3-13),(3-16) and (3-17), the input admittance of the magneto-dielectric loop ($Yin_{magnetic}$) can be written as,

$$Yin_{magnetic} = Y_{mat} + j\omega\varepsilon_0 a\left(ln\left(\frac{8a}{\rho}\right) - 2\right) + \frac{20\pi^2(ka)^4}{\eta_0^2} \tag{4-5}$$

$$= Y_{mat} + j\omega C + G_{rad}$$

where,

$$Y_{mat} = \frac{1}{j\omega\mu_0(\mu_r - 1)\frac{\pi\rho^2}{2\pi a}AF} + \frac{j\omega\varepsilon_0(\varepsilon_r - 1)(2\pi a)}{8\pi}FSF \tag{4-6}$$

$Yin_{magnetic}$ is the admittance of the following circuit shown in Fig. 3-52.

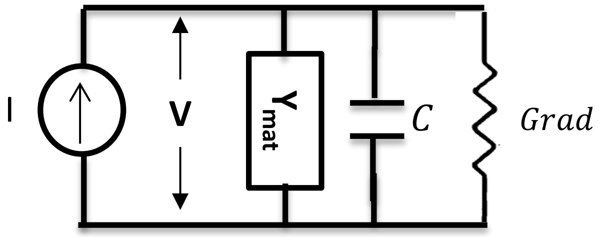

Fig. 4-2 Electrically small magneto-dielectric loop antenna circuit model.

Now since $\mu_r = \mu' - j\mu"$ and $\varepsilon_r = \varepsilon' - j\varepsilon"$, Y_{mat} can be expanded to get

$$Y_{mat} = \frac{1}{j\omega \frac{\mu_0 \pi \rho^2}{2\pi a} \frac{|\mu_r - 1|^2}{\mu' - 1} AF} + \frac{1}{\frac{\omega \mu_0 \pi \rho^2}{2\pi a} AF} \frac{\mu"}{|\mu_r - 1|^2} \tag{4-7}$$
$$+ \frac{j\omega\varepsilon_0(\varepsilon' - 1)(2\pi a)}{8\pi} FSF + \frac{\omega\varepsilon_0\varepsilon" l}{8\pi} FSF$$

As in the case of the magneto-dielectric dipole, the losses in the antenna arise from the two frequency dependent "loss conductance" terms in (4-7) above (real terms with $\varepsilon"$ and $\mu"$).

$$G_{mat} = \frac{2\pi a}{\omega \mu_0 \pi \rho^2 AF} \frac{\mu"}{|\mu_r - 1|^2} + \frac{\omega\varepsilon_0\varepsilon"(2\pi a)}{8\pi} FSF \tag{4-8}$$

Therefore, the power lost in the antenna with a voltage 'V' across its terminals is defined as:

$$Plost = \frac{1}{2}|V|^2 G_{mat} \tag{4-9}$$

while the radiated power (using *Grad* from (3-18)) is defined as:

$$Prad = \frac{1}{2}|V|^2 Grad \tag{4-10}$$

From (3-4), (4-5), (4-8),(4-9) and (4-10) after some algebraic manipulation knowing that $k = \omega/c_0$, $c_0 = \frac{1}{\sqrt{\mu_0\varepsilon_0}}$ and $\eta_0 = \sqrt{\mu_0/\varepsilon_0} = 120\pi$ the Radiation Efficiency of a magneto-dielectric antenna ($Eff_{magloop}$) having uniform current distribution is given by:

$$Eff_{magloop} = \frac{1}{1 + \frac{\mu"}{|\mu_r - 1|^2} \frac{12/\pi}{AF\left(\frac{\rho}{a}\right)^2 (ka)^5} + \frac{3}{2\pi} \frac{\varepsilon"}{(ka)^3} FSF} \tag{4-11}$$

Now for a purely magnetic material i.e. $\varepsilon_r = 1$, for $\delta > \rho$ which implies AF = FSF = 1, (4-11) simplifies to

$$Eff_{purely\ mag} = \frac{1}{1 + \frac{\mu"}{|\mu_r - 1|^2} \frac{12/\pi}{\left(\frac{\rho}{a}\right)^2 (ka)^5}} \tag{4-12}$$

(4-11)and (4-12) tell us that there are <u>two ways</u> to get low power loss (and therefore high radiation efficiency) using magnetic materials with μ”<<μ’ OR with μ”>>μ’. The second conclusion that we need a material that is highly lossy should not come as a surprise since we know that a perfect magnetic conductor is a magnetic material with μ”>>>μ’. Therefore when this condition is true we see that the efficiency tends to unity which is the radiation efficiency of a PMC loop. This conclusion was corroborated in Chapter 3 by the contour plot of the radiation efficiency equation of the magneto-dielectric dipole versus μ' and $\mu"$. Here, let us plot the radiation efficiency of the magneto-dielectric loop as a function of the loss tangent ($\tan(\delta) = \mu"/\mu'$) for different fixed μ' ranging from 5 to 5000 (Fig. 4-3) and different electrical size of the antenna by varying $k_0 a$ from 0.1 to 1.

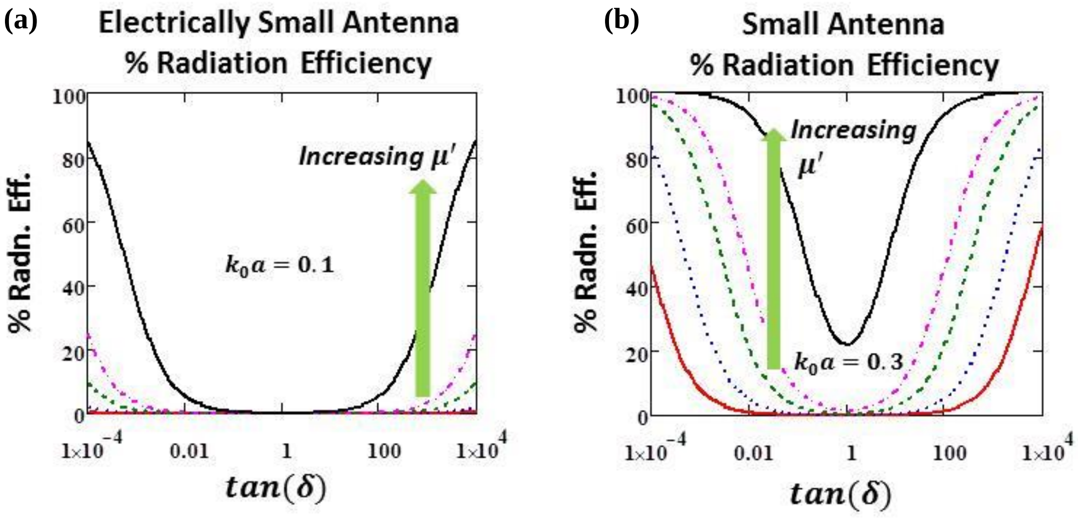

(c)

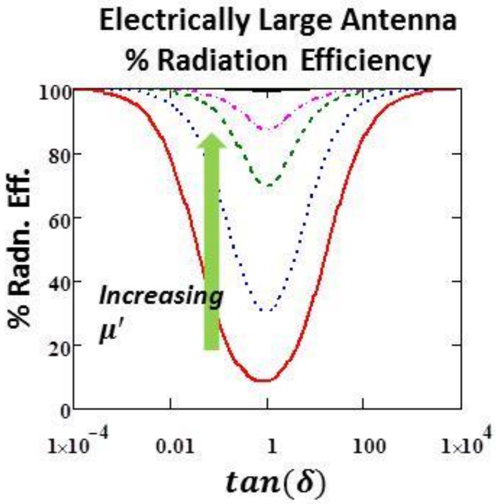

Fig. 4-3 (a) Efficiency equation (4-12) plot versus $tan(\delta)$for (a) electrically small antenna $k_0a = 0.1$ (b) small antenna $k_0a = 0.3$ and (c) electrically large antenna $k_0a = 1$. The radiation efficiency is the lowest at $\tan(\delta) = 1$ for any μ'.

Fig. 4-3 shows that for low loss materials i.e. $\tan(\delta) \ll 1$, the radiation efficiency is high as expected from the conventional notion of highly efficient antennas. The radiation efficiency then drops as $\tan(\delta)$ is increased till it reaches a minimum at $\tan(\delta) = 1$. Beyond unity loss tangent, the radiation efficiency starts to rise back up again for all the three cases. In this region, the material skin-depth is so small that all the fields are pushed out of the antenna. Hence, the magneto-dielectric antenna tends to act more like the conventional metal loop and therefore exhibit high radiation efficiency.

4.3 Full-wave Simulations of the Magneto-dielectric Loop Antenna

Full wave simulations of the magneto-dielectric loop were carried out using a variety of magneto-dielectric material parameters in order to ascertain the accuracy of (4-11). Consider a 12cm radius magneto-dielectric toroid/loop with a wire radius of $\rho = 0.5'' = 1.27cm$ symmetrically fed by four electric feed loops as shown in Fig. 4-4. Since $a = 12cm$, the circumference of the loop is 1λ at ~400MHz or $k_0 a = 1$ at 400MHz. Different magneto-dielectric materials are considered by varying the permeability and permittivity ($\mu_r = \mu' - j\mu''\ and\ \epsilon_r = \epsilon' - j\epsilon''$). The cases studied vary from low permeability to high permeability cases where the permittivity is also varied as $\varepsilon_r = 10 - j\varepsilon''$.

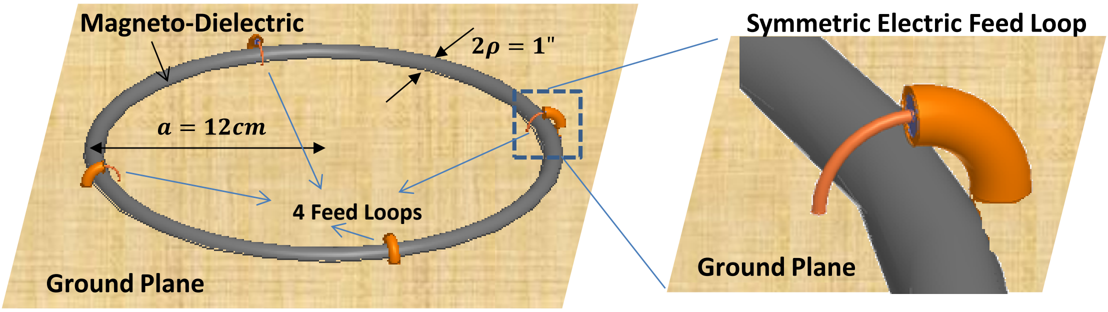

Fig. 4-4 Magneto-dielectric loop HFSS simulation geometry

The electric feed loop injects TE modes (circulating E_ϕ and longitudinal H_z) into the magneto-dielectric material which when below the onset of guidance (i.e. below the cutoff frequency) will leak out of the material. The cutoff frequency of the TE modes depends on the antenna cross-section and the relative permeability and permittivity. For this wire radius and set of relative constants the lowest order TE01 mode onset/cutoff frequencies are given below in Table 4-1.

Real Permeability (μ')	**Real Permittivity (ε')**	**TE01 Onset Frequency (MHz)**	**$k_0 a$ value at the TE01 Onset**
20	10	640	1.61
80	10	320	0.8
300	10	165	0.42

Table 4-1 TE01 onset/cutoff frequency for a 0.5" wire radius magneto-dielectric cylinder for different μ_r and ϵ_r.

The magnetic current distribution plots at two different frequencies (100MHz and 200MHz) of the multi-loop fed magneto-dielectric loop for different materials are shown in Fig. 4-5. The current distribution is nearly uniform except for the spikes seen in the figure. These spikes/notches result from the calculation of the current as the closed line integral of the electric field when we get too close to the feed loops. Very close to the loops we capture in the integral the near field flux lines (higher order modes) that are not part of the assumed magnetic current in the material.

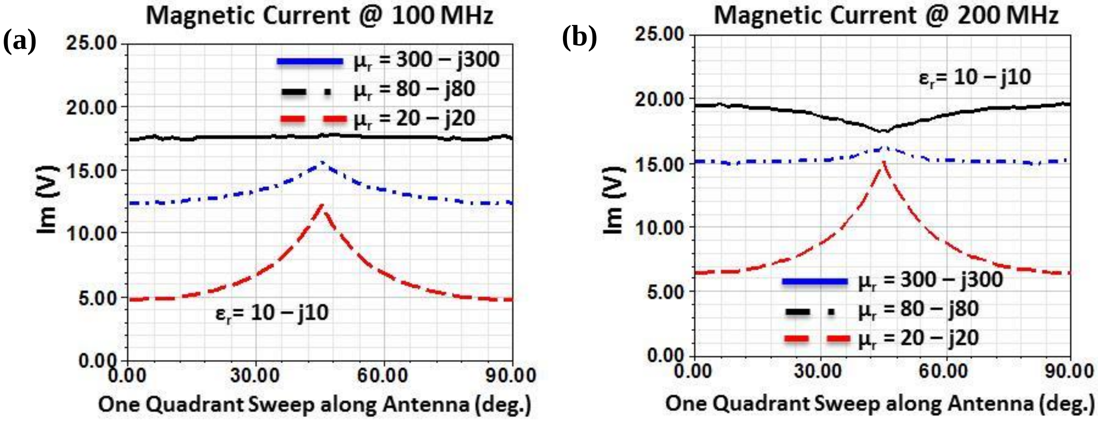

Fig. 4-5 Uniform magnetic current distribution along the length of the loop at two frequencies (a) 100MHz ($k_0 a = 0.25$) (b) 200MHz ($k_0 a = 0.5$)

The simulated results for radiation efficiency and the comparison with equation (4-11) are shown in Fig. 4-6. Even though the above model was derived assuming the dipole is electrically small, it behaves properly all the way to the loop resonance ($k_0a = 1$). Note that in Fig. 4-6(a), which is the low loss case, near the onset frequency of the TE01 guidance ($k_0a = 0.42$ for $\mu' = 300$ (black curve) and $k_0a = 0.8$ for $\epsilon' = 80$ (blue curve)), the simulated efficiency curve starts to plateau and deviate from the curve that is generated using (4-11). There reaches a point beyond the onset frequency where the efficiency drops to a minimum (at $k_0a = 0.65$ for $\mu' = 300$ (black curve)) and then it rises again. This phenomenon occurs because once the onset frequency is crossed majority of the wave that the magneto-dielectric loop supports is trapped inside the loop and very little extends outside it. Therefore, it becomes progressively difficult to 'leak off' the structure due to just the curvature discontinuity of the toroid and you reach a minima in the efficiency curve. However beyond that point, the electric feed loop starts to favor the excitation of the next higher order TE mode which is the TE02 inside the magneto-dielectric loop. Hence, the radiation efficiency starts to climb up again due to TE02 mode radiation. As we keep going higher in frequency, this phenomenon keeps repeating and successive higher order TE modes appear and fade away just like the TE01 mode. A detailed analysis of this phenomenon is done in Chapter 6. This effect is not seen in the lossy material cases, because the supported electromagnetic wave is never truly guided in the lossy structure, the wave always leaks off the structure.

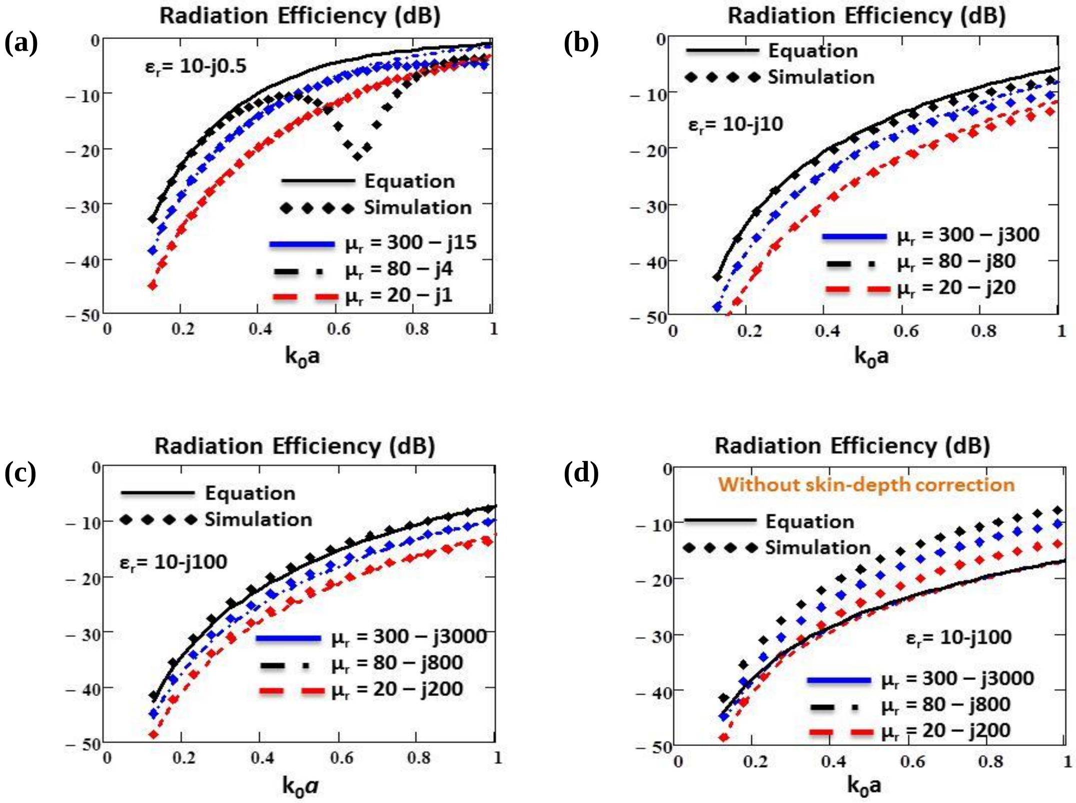

Fig. 4-6 Radiation Efficiency comparison of (4-11) with full-wave simulations of a multi-loop fed magnetic dipole made of (a) low loss ($tan(\delta_m) = tan(\delta_e) = 0.05$), (b) high loss($tan(\delta_m) = tan(\delta_e) = 1$) (c) extremely high loss ($tan(\delta_m) = tan(\delta_e) = 10$) and (d) extremely high loss materials but neglecting skin depth effects in the efficiency calculation.

For the low and moderate loss in permittivity or permeability or both, the inclusion of skin depth effect i.e. the area factor AF and the internal field shape factor have negligible effects on efficiency as skin depth 'δ' is almost always greater than radius 'ρ'. But for the extremely high loss case i.e. for $\tan(\delta_m) = \tan(\delta_e) = 10$, the correction factors has a huge effect in retaining the validity of the equation over a broader band of frequency. (Compare the results in Fig. 4-6(c) with those in Fig. 4-6 (d) where the skin depth effect is neglected).

4.4 Practical Application of the Circuit Model: Body Wearable Belt Antenna

In this section, we will discuss a practical application of the circuit model of the magneto-dielectric loop antenna described in Section 3.3. The circuit model will be used to evaluate the radiation efficiency of a Body Wearable Belt Antenna (BWBA) shown in Fig. 4-7. The antenna design is targeted towards use by the communication personnel in a battlefield. The goal is to replace the tall whip antennas carried around by these soldiers with a low observable body wearable antenna (Fig. 4-7). The performance of the new antenna must be better or at least the same as the standard antennas currently used for this purpose.

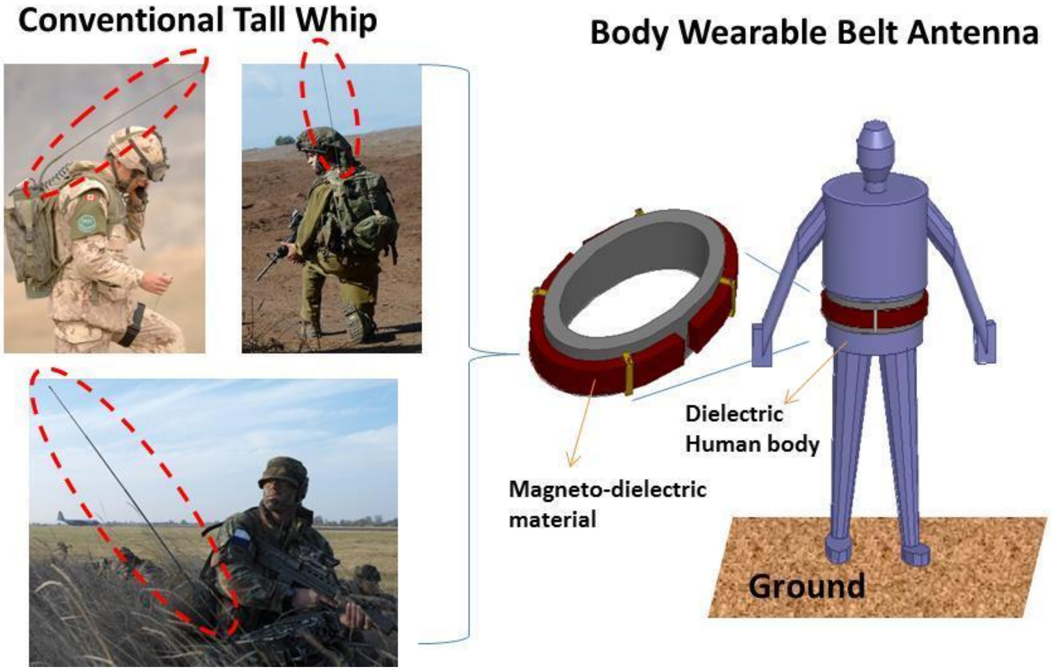

Fig. 4-7 Body Wearable Belt Antenna designed to replace tall whip antennas carried by foot soldiers for interpersonal communication

The operational frequency band for the antenna design is from 30MHz to 500MHz. But in particular, we want to maximize the efficiency of the antenna in the 30MHz to 100MHz band in order to beat the conventional whip antennas, used in this range, convincingly. At the same time we want to minimize the manufacturing cost of these antennas so that they can be mass produced and distributed. Also, this antenna will be worn by the soldier, therefore we also want minimize the overall weight of the antenna as well. Therefore, the most appropriate approach to tackle this problem is to find an analytic circuit model of the system and then play 'what if' games with the volume of material used.

The BW antenna system not only consists of the body wearable antenna made up of some magneto-dielectric material but also the "dielectric" human body. These are the two primary sources of radiation. Therefore, to model the system, we first simulate a dielectric cylinder representing the human body fed with an ideal lumped port source in the full-wave simulator. The human body is then 'modeled' as circuit impedance in the frequency range of interest. Next, the source is replaced by the body wearable belt antenna circuit model to complete the complete antenna model.

Consider a dielectric cylinder having the frequency dependent permittivity of a human torso fed by a capacitive feed (lumped port in the simulator) over a ground plane (Fig. 4-8). A foot soldier does not stay stationary and moves his arms and legs during combat or in other words the shape of the dielectric human body radiator is constantly changing. A cylinder is a good statistical average for the shape of the human body. The dimensions of the cylinder soldier are 6 feet height and 32" waist.

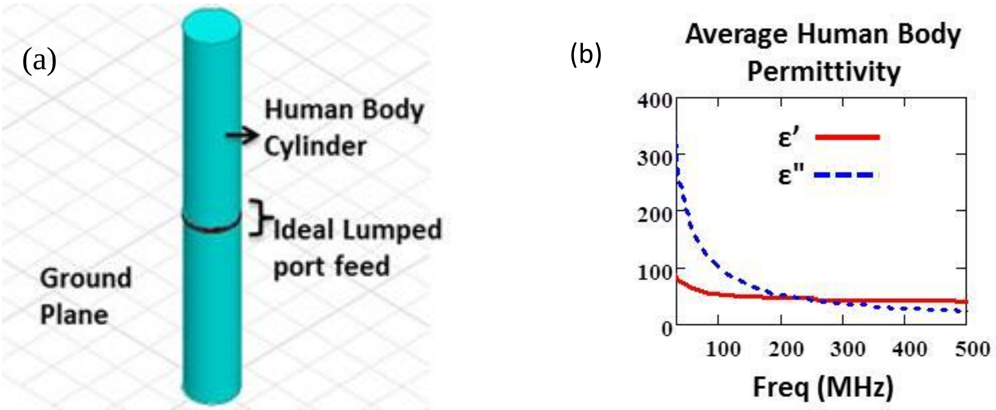

Fig. 4-8 (a) Human body cylinder fed with an ideal lumped port at the same location as the eventual position of the BWA belt. (b) Frequency dependent permittivity of the human body.

Full-wave simulation of the geometry above yields the curves in Fig. 4-9(a) for radiated power ($\mathrm{Prad_b}$) and power loss ($\mathrm{Ploss_b}$). The input voltage (Vfeed) measured at the lumped port is shown in Fig. 4-9(b). Fig. 4-9(c) shows the real and imaginary part of the input impedance.

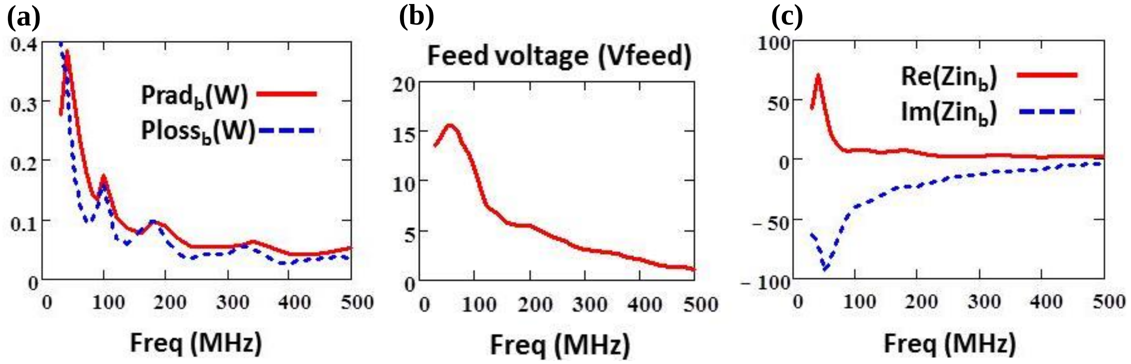

Fig. 4-9 Simulation results of the geometry in Fig. 4-8(a) where (a) Radiated power and Power loss, (b) Feed Voltage and (c) Input impedance.

Given these simulation data we can calculate the radiation resistance ($\mathrm{Rrad_b}$) and loss resistance ($\mathrm{Rloss_b}$) the following way:

$$Rrad_b = \frac{2Prad_b}{\left(\frac{Vfeed}{|Zin_b|}\right)^2} \quad and \quad Grad_b = \frac{Rrad_b}{|Zin_b|^2} \tag{4-13}$$

$$Rloss_b = \frac{2Ploss_b}{\left(\frac{Vfeed}{|Zin_b|}\right)^2} \quad and \quad Gloss_b = \frac{Rloss_b}{|Zin_b|^2} \tag{4-14}$$

The resulting radiation resistance and loss resistance is shown in Fig. 4-10(a). Fig. 4-10(b) show that the sum of $Rrad_b$ and $Rloss_b$ is equal to the real part of the input impedance as expected. The radiation efficiency of this dielectric cylinder fed with the ideal capacitive lumped port feed is shown in Fig. 4-10(c). This is the maximum radiation efficiency that can be achieved by this antenna system. Any addition of lossy materials to the system by replacing the ideal feed with a permeable material feed will bring down the radiation efficiency below this maximum value.

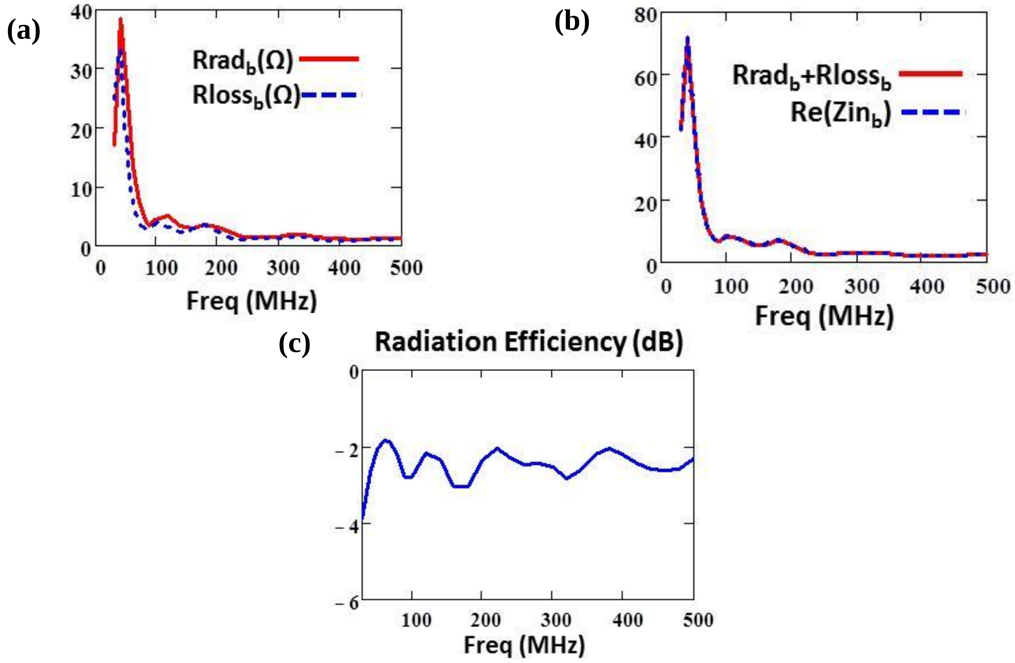

Fig. 4-10 (a) Radiation resistance and loss resistance calculated from the simulation data (b) the sum of which equals the real part of input impedance. (c) Radiation Efficiency of the dielectric human body cylinder fed with an ideal lumped capacitive port feed

Therefore, the circuit model for the human body is now reduced to the one shown in Fig. X+4. The imaginary part of input impedance is left as it is and the real part has been separated into radiation and loss resistance.

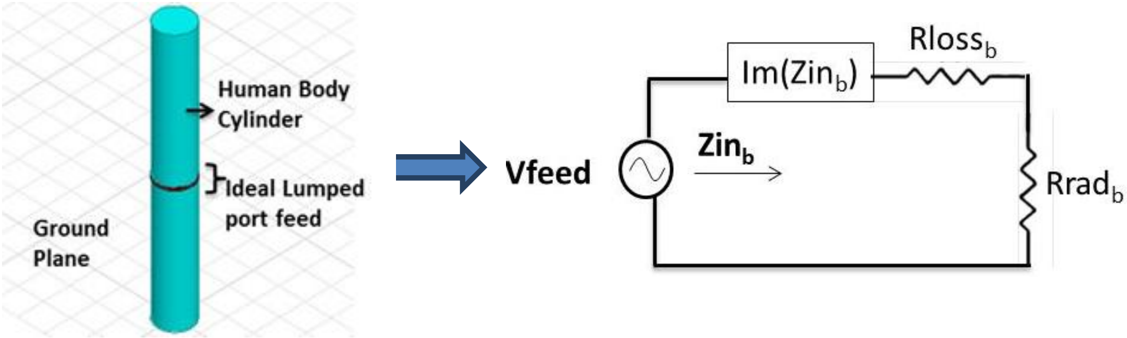

Fig. 4-11 Circuit model of the dielectric human body cylinder fed with a capacitive feed.

The next step is to replace the ‘Vfeed’ with the magneto-dielectric loop circuit model from Fig. 4-2. The resulting model is shown in Fig. 4-12.

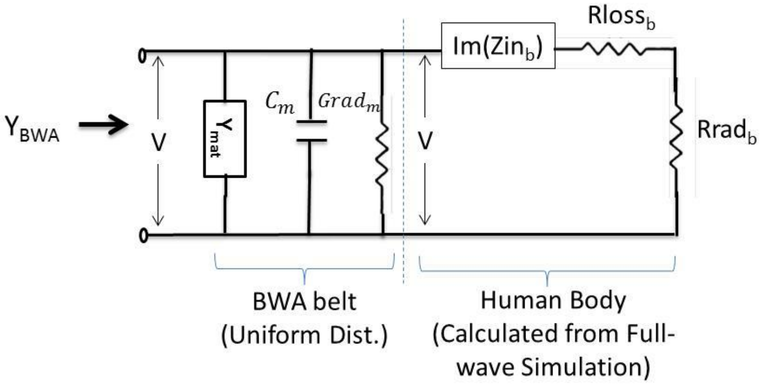

Fig. 4-12 The circuit model of the BWA system that takes into account the ground plane.

Now let us compare the model to full-wave simulations. The simulation geometry is shown in Fig. 4-13 where the lumped port of Fig. 4-8(a) has been replaced by the body wearable toroid belt of minor radius of 4cm (ρ=4cm). It also has its own finite metallic ground plane. We will use quarter symmetry to simplify the simulations. The circuit element equations for the permeable toroid are the same as before except that we observed thorough simulation of the toroid by itself that we need to add a correction factor (2/5) to the Gloss$_m$. This factor comes from the fact that the model was developed for a toroid in free space. The problem at hand has a finite ground plane and a dielectric core. This factor accounts for this change in geometry. Since the ground plane and the core properties are fixed the factor will always be the same 2/5. The same factor is also applied to the radiation resistance. Thus,

$$Gloss_m = \frac{1}{\frac{\omega\mu_0\pi\rho^2}{2\pi a}\left(\frac{2}{5}\right)}\frac{\mu'}{(\mu')^2+(\mu")^2} \quad ; \quad Grad_m = \frac{20\pi^2(k_0 a)^2}{\eta_0^2\left(\frac{2}{5}\right)} \tag{4-15}$$

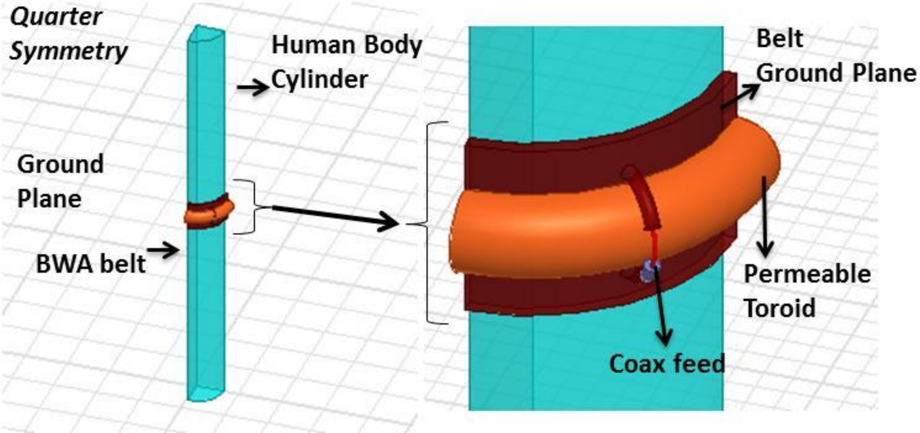

Fig. 4-13 Simulation geometry of the body wearable antenna system with quarter plane

The permittivity of the human body is the same as in Fig. 4-8(b). To start with, different dispersion-less permeability was simulated and the comparison to the model is shown in Fig. 4-14.

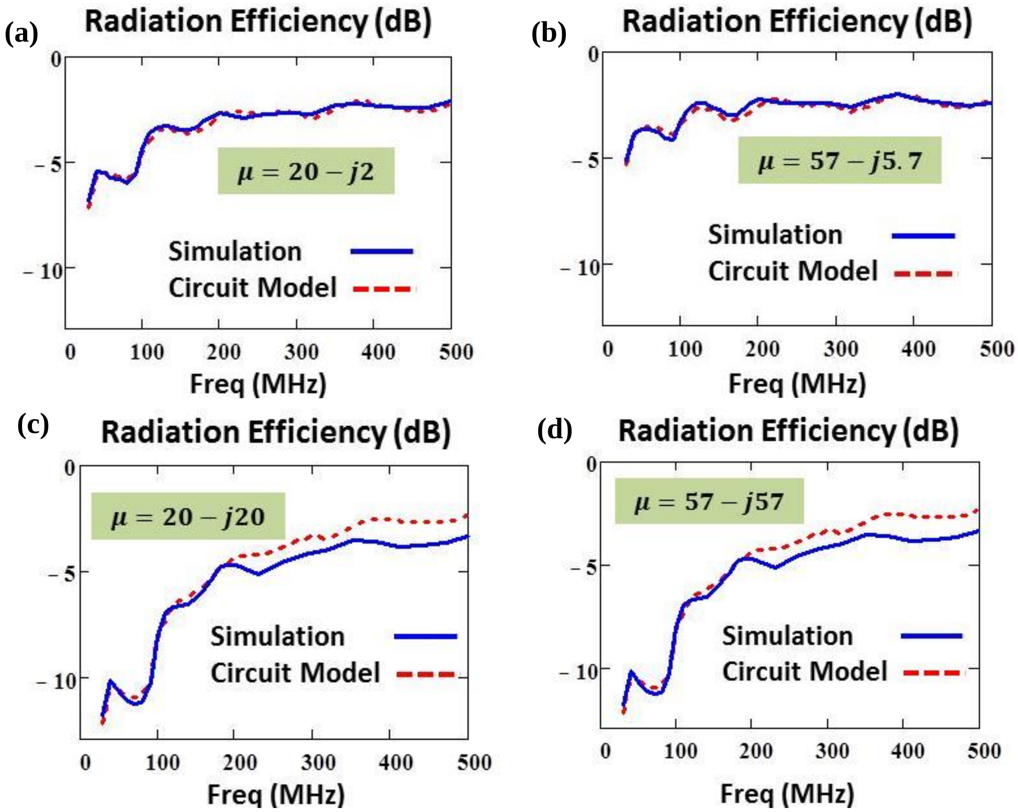

Fig. 4-14 Radiation Efficiency comparison of the BWA system circuit model and full-wave simulations for different values of permeability of the belt with (a),(b) having a loss tangent of tan(δ)=0.1 and (c)(d) with high tan(δ)=1.

As seen in Fig. 4-14(c) and (d) the model works well for extremely lossy μ_r values as well. Next let us test the validity for different volume of the permeable material i.e. for different toroid radii ‘ρ’. Fig. 4-15 is for ρ=3cm and Fig. 4-16 is for ρ=6cm.

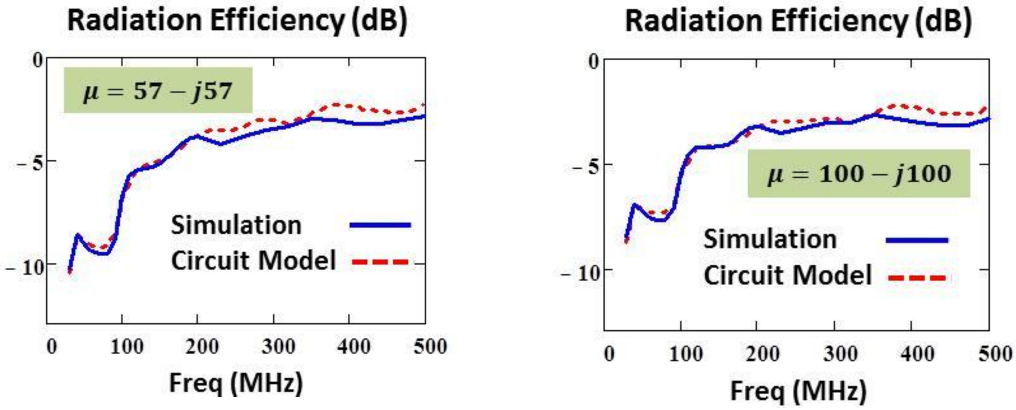

Fig. 4-15 Radiation efficiency comparison for different permeability values for a toroid minor radius of 3cm.

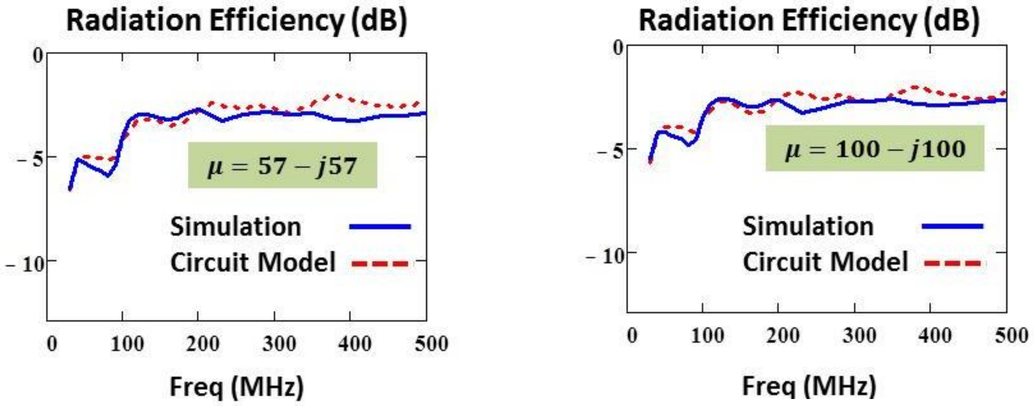

Fig. 4-16 Radiation efficiency comparison for different permeability values for a toroid minor radius of 6cm.

Fig. 4-14, Fig. 4-15 and Fig. 4-16 show that the circuit model is valid for different constant permeability values and for different belt radii. Now we are ready to play ‘what if’ games with the permeability and the amount of material to determine how far we are from the ideal radiation efficiency curve of Fig. 4-10(c). We know that the resulting radiation efficiency will always be below the curve of Fig. 4-10(c). Let us use a frequency dispersive magneto-dielectric material (Fig. 4-17(a)) and see the effect of changing the radii of the toroid. Fig. 4-17(b) show the radiation efficiency curves for different ‘ρ’. Clearly as the radii of the belt increases, the radiation efficiency of the BWA system increases as well, but the price we pay is the increase in the amount of material required which corresponds to the increase in the overall cost of the belt. Table next to Fig. 4-17(b) also gives the volume of material used in cubic centimeters. Also beyond a certain radii (8cm in this case), any additional increase of the radius doesn’t show any appreciable increase in radiation efficiency.

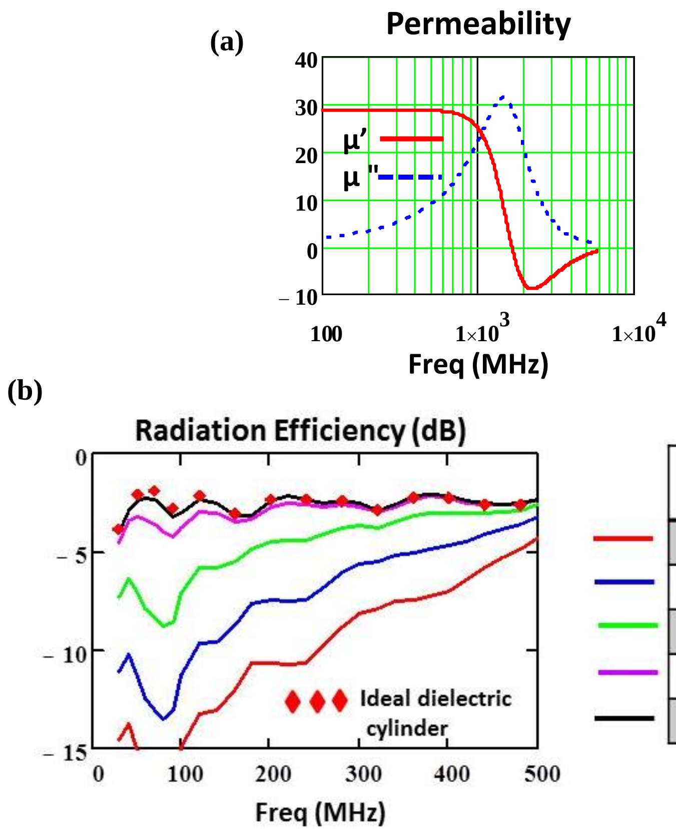

	ρ(cm)	Volume (cm³)
🟥	0.005	**79**
🟦	0.008	**202.13**
🟩	0.01	**315.83**
🟪	0.04	**5,053**
⬛	0.08	**20,210**

Fig. 4-17 (a) Magneto-dielectric material permeability used in the belt(b) Radiation efficiency of the BWA using the circuit model for different radii of the loop belt.

Another consequence of the circuit model for this body wearable antenna system is that we can clearly isolate the contribution towards radiation from the two sources, the human body and the permeable toroid. From the circuit model in Fig. 4-12, we can see that the voltage ‘V’ at the toroid feed is the same as voltage fed to the human body circuit model. Therefore, the contribution to the radiated power from the toroid and that from the human body can be defined as $Prad_m = 0.5V^2Grad_m$ and $d_b = 0.5V^2Grad_b$, respectively. Thus the same voltage ‘V’ implies we can directly compare the two radiation conductance to see their individual effects. Fig. 4-18 below shows the plot of $Grad_b$ and $Grad_m$.

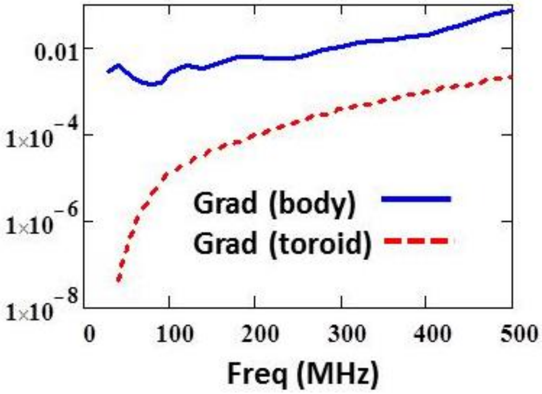

Fig. 4-18 Contribution to the total radiation from the two sources of radiation: the human body and the permeable toroid.

The human body is clearly the greater source of radiation than the toroid belt. Therefore, we can say for a fact that the permeable toroid belt is the magnetic frill current feed for the dielectric human body.

4.5 Summary, Conclusions and Future Work

A closed form equation for the radiation efficiency equation was developed for a small magneto-dielectric loop. The equation is derived from the electrically small circuit model of a conventional metallic loop by adding additional elements (L for permeability and C for permittivity) to take into account the material properties. The equation shows that maximum radiation efficiency of a material loop can be obtained not only by using a material with very low loss but also with a material that has very high loss.

The main reason behind analyzing the Magneto-dielectric Loop antenna geometry is the fact that it has an omnidirectional pattern unlike the Magneto-dielectric Dipole. Just by examining the radiation efficiency equations of the two ((3-24) and (4-11)) the dipole is superior in the electrically small limit because the efficiency drops as a factor of $(kl)^3$ in its case as opposed to the $(ka)^5$ in the loop.

The circuit model presented here does not include the details of the feed structure. Once the feed is included we would have a complete model that can be used to calculate the input impedance of the antenna. This will enable us to calculate the Antenna Q and hence the bandwidth of the antenna; thus yielding in one formulation the radiation efficiency and antenna bandwidth, the two parameters that completely characterize a given material dipole antenna.

Chapter 5

MATERIAL SELECTION RULE FOR MAGNETO-DIELECTRIC ANTENNA DESIGNS

5.1 Introduction

In Chapter 3 and 4, the two fundamental magneto-dielectric antenna designs, the magneto-dielectric dipole and the magneto-dielectric loop was analyzed. A simple small antenna equivalent circuit model was postulated using which the radiation efficiency equation for such antennas was derived and validated in the small antenna limit using full-wave simulations. The radiation efficiency equation is a function of the antenna geometry and the material properties (μ_r, ϵ_r). Purely based on antenna geometry and operational frequency range, i.e. for the same magneto-dielectric material, the magneto-dielectric dipole has higher radiation efficiency than the magneto-dielectric loop in the small antenna limit. In this chapter, it is shown that for either of the two fundamental geometries, for a given size constraints of the antenna, the desired operation frequency range and the desired efficiency in this range we can unequivocally identify the magneto-dielectric material that can meet the required specifications. The analysis that follows is under the assumption that the frequency range of operation is below the onset frequency of the principal wave mode supported by the material antenna structure, theTE01 mode.

There are numerous books written and countless papers published on magnetic materials each with its unique characteristics. The most basic classification of such materials based on its magnetic properties is quite literally done based on whether a material is “magnetic” or not in the presence or absence of an external magnetic field. Materials are broadly classified as being diamagnetic, paramagnetic, ferromagnetic, ferrimagnetic or anti-ferromagnetic. This classification is briefly described in Section 5.2. Of these, ferromagnetic and ferromagnetic materials are most useful for antenna applications as they have sufficiently high frequency dispersive permeability in the frequencies of interest for antenna designs. In Section 5.3 we show three fundamental physical limits that dictate the eventual choice of magneto-dielectric material. These are: 1) Gain Bandwidth Product limit 2) Snoek’s Product limit and 3) Kramers Krönig relation restriction on the permeability dispersion. Within these constraints it is shown that one single parameter which we call ‘hesitivity’ (h_m) with the units of magnetic conductivity (Ω/m) characterizes the performance of the material. In Section 5.4, the relationship between Hesitivity and antenna radiation efficiency is derived. The relationship shows that materials that have the same hesitivity will have the same antenna radiation efficiency. Hence, the parameter hesitivity is used to identify a family of materials that satisfy the design requirements. It is shown that, higher the hesitivity of the material family, the higher is the radiation efficiency over the frequency range of operation. In Section 5.5, we narrow down the choice of material from the family with a unique hesitivity to a single material based on the Gain-Bandwidth Product limit. We show that any loss in the material (μ'') improves the bandwidth of the antenna. Therefore we state the material selection law based on hesitivity (h_m) and the magneto-dielectric material loss (μ''). In Section 5.6, the material selection law is applied to realistic magneto-dielectric materials obtained from the literature. Section 5.7 contains the summary of the chapter, some notable conclusions and possible future work.

5.2 Classification of Magnetic Materials: Dia, Para, Ferro, Ferri and Anti-Ferro

The origin of magnetism is directly related to the motion of electrons in an atom. Without delving deep into quantum physics, the two most significant sources of an electron's magnetic properties are the orbital motion of the electron around the atom's nucleus and the electron spinning around its own axis (Fig. 5-1). The electron orbiting the nucleus can be thought of as a small current loop generating a small magnetic field with a magnetic moment along its axis of rotation. The electron spinning on its axis has a spin magnetic moment associated with it whose vector direction depends on the direction of spin (up for right spin and down for left spin based on the right hand rule). Each atom therefore acts like a tiny magnet carrying an intrinsic or net magnetic dipole moment which is a superposition of the moments from these two sources. The type of magnetism is determined by how these elementary dipole moments are ordered and are broadly classified into diamagnetic, paramagnetic, ferromagnetic, ferrimagnetic or anti-ferromagnetic.

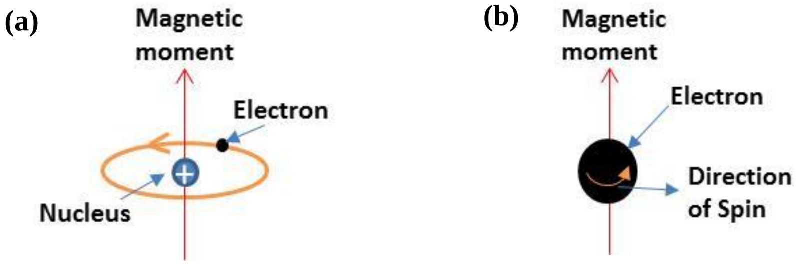

Fig. 5-1 Two sources of atomic magnetic dipole moments a) an orbiting electron and (b)a spinning electron

Most of the materials that exist on earth fall under the category of Diamagnetic materials. They do not have a net dipole moment i.e. the orbital and spin magnetic moments cancel out within an atom. The application of an external magnetic field results in an induced magnetic moment which is in the opposite direction to the applied field. Thus, the relative permeability is less than unity (i.e. less than that of vacuum or free space) and hence the magnetic susceptibility ($\chi_m = \mu_r - 1$) is negative. Hence they are not useful for antenna applications.

The individual atoms in a paramagnetic material on the other hand, have a net magnetic dipole moment. But they are randomly oriented such that the bulk material has no net magnetic dipole moment (Fig. 5-2(a)). When an external field is applied, the magnetic moments align preferentially in the direction of the applied field. This results in a relative permeability μ_r that is slightly greater than 1. These materials are also not useful in designing magnetic antennas.

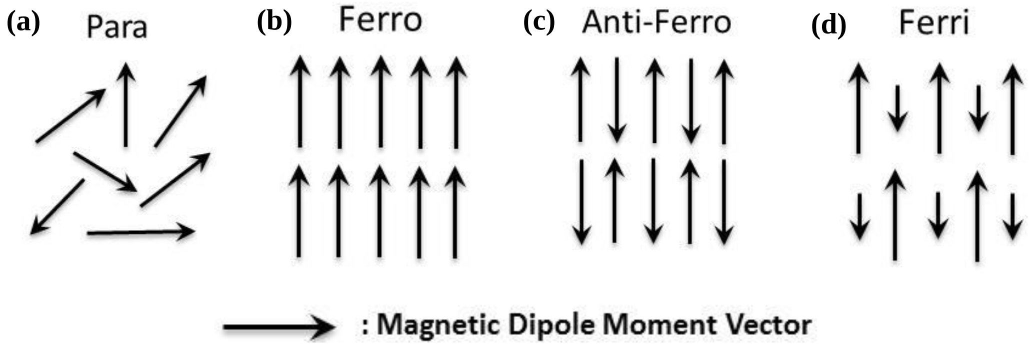

Fig. 5-2 Intrinsic magnetic dipole moments in (a) Paramagnetic material (b) Ferromagnetic material (c) Anti-ferromagnetic material and (d) Ferrimagnetic materials

Ferromagnetic materials possess a net magnetic dipole moment even in the absence of an external field (Fig. 5-2(b)). Such a permanent magnetic moment results from alignment of individual atomic moments (mostly spin moments) in a preferred direction. The mutual alignment of spins exists over relatively large volumes regions of the materials called domains. There could be several domains within a bulk structure each with a magnetic moment vector that point in some random direction. This phenomenon in which the magnetic moments within a domain are bound to a preferred direction is said to be caused by an internal effective anisotropy field (H_a). On the application of an external d.c field, the domains most closely oriented with the direction of the applied field grows at the expense of other domains, eventually occupying the material’s whole volume. When this happens, the material is said to be saturated with a saturation magnetization ‘M_s’ (units: Gauss in CGS) which is equal to the maximum magnetic flux density within the material. Any further increase in the strength of the external field will not result in an increase in the magnetic flux density in the material. Also, on the application of an external field ‘H’, the spinning electron starts to precess about the direction of H at a frequency ‘f_0’ or ‘ω_0’. This frequency is called the Larmor frequency or ferromagnetic resonance frequency.

Some examples of ferromagnetic materials are iron, nickel, cobalt, rare earth metals, etc. They have a large relative permeability and are hence one of the candidate material category in antenna applications. The only drawback with ferromagnetic materials is that they have very high electrical conductivity (therefore high ϵ''). Apart from the obvious disadvantage seen just from the radiation efficiency equations ((3-24) and (4-11)), on the application of an external high frequency magnetic field, the high electrical conductivity results in creation of eddy currents in the material, which in turn creates a field in opposition to the external applied field. The opposition to the applied field results in the fields being pushed out from within the material. Thus, electromagnetic waves only penetrate to a certain depth, called the skin depth (seen in Chapter 3, Section 3.3), within the material. Therefore, only a fraction of the volume of the bulk material will contribute towards radiation if used as a bulk material in magneto-dielectric antenna designs. Furthermore, the skin depth loss dampens the effective permeability of the material and reduces the radiation efficiency of the antenna. Two possible workarounds to this problem are given in Fig. 5-3.

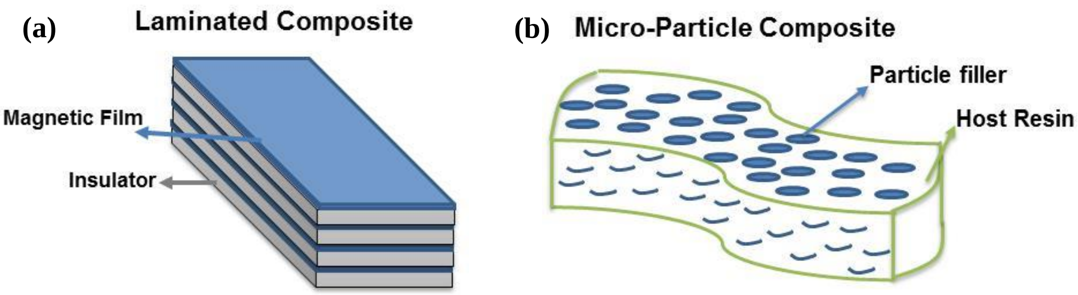

Fig. 5-3 Possible solutions to negate eddy current effects in ferromagnetic materials (a) Lamination of thin films of material with an insulator in between and (b) Micro-particles/ Flakes of ferromagnetic materials mixed in with an insulating resin

One solution is to form a laminate with thin layers or thin ferromagnetic films ($\leq \sim 1 \mu m$), as thin as skin depth and interleaving them with equally thin insulating layers, to form a bulk structure. This is the standard technique used to make low loss transformer cores. This prevents formation of large eddy current loops that reduces the antenna efficiency. Another solution is to make a bulk composite by mixing micro-particles or flakes of a ferromagnetic material with an insulating resin. Although these two methods negate eddy current effects, the effective permeability of the resulting composite is reduced.

The next category is Anti-ferromagnetic materials. They have anti-parallel atomic magnetic moment alignment (Fig. 5-2(c)) which again results in a zero net magnetic moment. They are therefore not useful for antennas.

Ferrimagnetic materials or Ferrites have anti-parallel atomic magnetic moments as well, but they are not of equal strengths and hence do not cancel out in the bulk structure (Fig. 5-2(d)).They are generally oxides of iron combined with one or more mixtures of bivalent transition metals 'Me' of the form "$MeFe_2O_4$". The prototypical ferrite, with just iron in it, is magnetite (Fe_3O_4), most commonly known as lodestone. Other examples are NiZn ferrite, MnZn ferrite, NiZnCo, CoZ Hexaferrites, etc. Their permeability spectra is similar to ferromagnetic materials i.e. they have a relatively high relative permeability (usually lower than ferromagnetic materials) but they come with an added advantage of high electrical resistivity due to the presence of insulating oxides. Therefore, eddy current or skin depth losses are not an issue unlike ferromagnetic metals and hence, it is also a candidate material category for antenna applications.

To summarize this section, the two candidate magnetic material categories for use in magneto-dielectric antenna designs are ferromagnetic materials and ferrimagnetic materials or ferrites. The next criterion for narrowing down the candidate magneto-dielectric material is the frequency dispersion of the relative permeability, both its real and imaginary components. The selection will depend on the three fundamental limits in the design of magneto-dielectric material antennas described in the next section.

5.3 Fundamental Physical Limits in Designing Low Profile & Conformal Electrically Small Magneto-dielectric Material Antennas

Electrically small antennas constitute the primary component of the physical layer in a large percentage of wireless communication systems. Whether the application is commercial or scientific the benefits afforded by miniaturization of these systems continually drives the size of the antenna down. Frequently absent from many of these intriguing proposals is an examination of the fundamental limits of performance to which electromagnetic radiators are subjected.

5.3.1 Gain-Bandwidth or Efficiency-Bandwidth Product Limit

The first of these limits is the Gain-bandwidth Product(GBWP) limit. It is a known fact that an antenna performance is best described by the product of gain and bandwidth. Since the antenna Q is inversely proportional to the bandwidth (BW) of the antenna ($Q \sim 1/BW$), some researchers and authors prefer to state the Gain/Antenna Q limit [25] [26]. To reduce it a step further, since we are concerned with electrically small antenna whose directive gain is constant (approximately 1.5), we prefer to fix the Directive gain to unity (or ignore it in other words) and call it the Efficiency Bandwidth Product (EBWP) limit. Now, traditionally since a vast majority of radiators were metallic with unity radiation efficiency, the main concern was to estimate the minimum Q limit. The antenna Q is defined as the ratio of the energy stored per unit cycle in the near field of the antenna ($W_{e,m}$) to the power radiated by the antenna (P_{rad}). The minimum Q equation for a resonant electrically small radiator that is completely enclosed in a sphere of radius ‘a’ was first given by Chu in 1948 [25]. Since then, there have been numerous modifications and re-derivations to this equation but the most simple and accepted equation for the minimum Q (Q_{min}) of the lowest order mode (TE or TM) for an electrically small antenna is the one derived my McLean [27].

$$Q = \frac{2\omega W_{e,m}}{P_{rad}} \geq Q_{min} \; = \; \frac{1}{(k_0 a)^3} + \frac{1}{(k_0 a)} \tag{5-1}$$

Here, $k_0 = 2\pi/\lambda_0$ is the propagation constant, λ_0 is the free space wavelength and ‘a’ is the radius of the enclosing sphere. The limiting equation (5-1) gives us the maximum limit of the Efficiency bandwidth Product of an electrically small metallic antenna. This limit is extremely stringent and difficult to achieve with realistic metallic antennas as only fields outside the sphere ‘a’ were considered in deriving the equation. By including the fields inside the sphere, Thal [28] showed that the lowest achievable Q is about three times the value given by (5-1).

Now, for magneto-dielectric antennas, Wheeler [2] showed that it is possible to come close to (5-1) limit using an infinitesimally small spherical permeable (μ_r) antenna. Hansen [29], Kim et al [23] have given equations for a spherical antenna with a lossless and lossy magneto-dielectric core for any size of the sphere. They showed that even with magneto-dielectric materials, the minimum Q that could be achieved is always greater than the equation given in (5-1). Since the radiation efficiency of realistic magneto-dielectric antennas will always be less than unity, it is safe to assume that the maximum unassailable EBWP is given by $1/Q_{min}$.

The actual Antenna Q for any given antenna (metallic or magneto-dielectric) can be calculated from its input impedance ($Z(\omega)$) in closed form using the equation given by

Best et al [11] ((2-8) given in Chapter 2). In the same paper, a better and more accurate expression for the Fractional bandwidth (FBW) of the antenna, than the 1/Q approximation, is given which depends on the allowable amount of reflection coefficient (Γ_{BW}).

$$Q = \frac{\omega}{2R(\omega)}|Z'(\omega)| \quad ; \quad \beta = \frac{|\Gamma_{\mathrm{BW}}|^2}{1-|\Gamma_{\mathrm{BW}}|^2} \quad ; \quad FBW(\omega) = \frac{2\sqrt{\beta}}{Q(\omega)} \tag{5-2}$$

where, $R(\omega) = Re(Z(\omega))$. The equation assumes that the antenna is perfectly matched at every frequency at which the FBW is calculated. That is, at every matched frequency, the reflection coefficient, $\Gamma = 0$ and antenna efficiency (Ant Eff.) is equal to the radiation efficiency (Radn Eff.) since, $Ant\,Eff = Radn\,Eff(1-|\Gamma|^2)$. Therefore, using (3-24), (4-11) and (5-2) we can calculate the EBWP of a small magneto-dielectric antenna dipole or loop.

The most important consequence of the antenna Q and EBWP calculation is the following:

The magneto-dielectric antenna will radiate with the highest possible radiation efficiency given by (3-24) and (4-11) only if it operates within the FBW given by (5-2). This is also true for metallic radiators in the sense that the theoretical close to 100% radiation efficiency can only be attained if operated in the FBW given by (5-2). The only way to increase the bandwidth in either case is to sacrifice antenna efficiency by adding loss in the system. This trade-off between efficiency (or gain) and bandwidth does not affect or change the EBWP curve (or GBWP curve).

5.3.2 Snoek's Law Limit

The second limiting factor in the design of antennas using magnetic materials is the limit imposed by Snoek's Law which was first postulated by J.L. Snoek in 1948 [30]. He observed a general trend in ferrites; the higher the dc permeability (μ_i or μ_{DC}) the lower the ferromagnetic resonance frequency. He made the theoretical connection between the two by realizing that, while the ferromagnetic resonance frequency is proportional to the internal anisotropy field 'H_a', the initial dc permeability (or initial susceptibility $\chi_{DC} = \mu_{DC} - 1$) is inversely proportional to 'H_a', and therefore, the product of these two quantities, which is now called Snoek Product (SP), is a constant that is dependent only on the saturation magnetization (M_s) of the material. The Snoek's Law for a bulk polycrystalline ferrite is:

$$\mu_0(\mu_{DC} - 1) = \left(\frac{2}{3}\right)\frac{4\pi M_s}{H_a} \quad and \quad \omega_0 = \mu_0 \gamma H_a \tag{5-3}$$

$$\rightarrow \quad SP = \omega_0 \mu_0 (\mu_{DC} - 1) = \omega_0 \chi_{DC} = \mu_0 \gamma \frac{2}{3} 4\pi M_s \tag{5-4}$$

All the members in a particular family of magnetic materials have roughly the same Snoek product value. An example is the $Ni_\delta Zn_{1-\delta} Fe_2 O_4$ ferrite family given in Smit and Wijn [31] (Page 269) Fig. 5-4. The Snoek Product for all the members in this family is ~30,000.

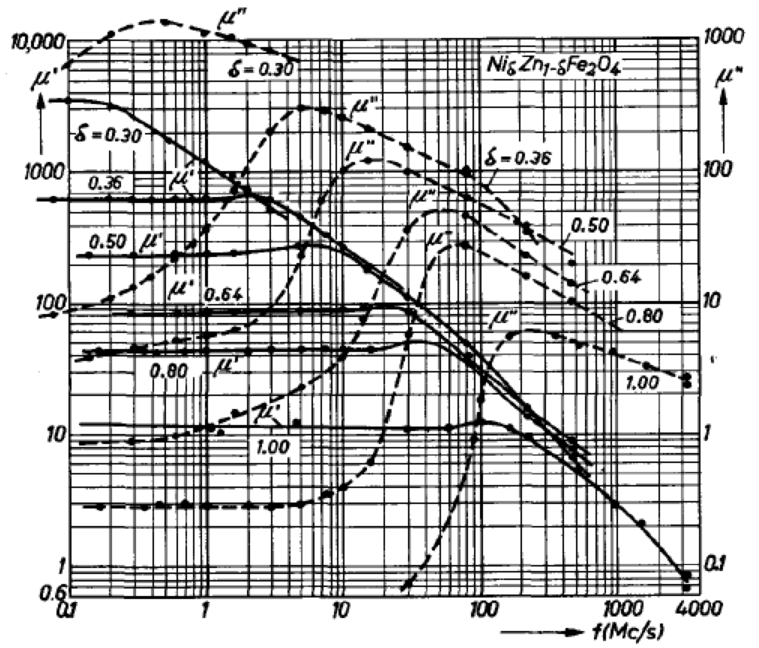

Fig. 50.1. Frequency dependence of the real and the imaginary parts of the initial permeability, μ' and μ'' repsectively, for polycrystalline specimens of ferrites having chemical compositions which are determined by the different values of the parameter δ in the formula $Ni_\delta Zn_{1-\delta} Fe_2O_4$. Note the scale shift by a factor of 10 between the μ' and the μ'' scale.

Fig. 5-4 Complex permeability of the NiZn family from [31]

Since the Snoek product is constant for members of the same family and since it is only a function of ‘M_s’, we can say that chemical composition of such materials primarily alters the anisotropy field ‘H_a’. Therefore, Snoek’s law implies that to increase the resonance frequency of a member of a material family, the price paid is a drop in initial susceptibility. This has been an important limit in the development of magnetic materials for radiofrequency applications over the last half century because most designers look for materials with low loss ($\mu' \gg \mu''$) at ever increasing frequencies. From Snoek’s law this means pushing the resonance frequency up past the desired operating frequency range and accepting a lower permeability.

5.3.3 Limit imposed by the Kramer’s Krönig relations

The third limit is the recognition that the requirements of causality, linearity, passivity and energy conservation force the frequency dependent permeability and permittivity of all materials to be an analytic function of a very precise nature that obeys the Kramers-Krönig relations [32]. Two classic examples of analytic functions that obey these relations are a Debye function and a Lorentz function.

$$Debye\ Susceptibility = \chi_{Debye} = \frac{\chi_{DC}}{1 + j\dfrac{\omega}{\omega_0}} \tag{5-5}$$

$$Lorentz\ Susceptibility = \chi_{Lor} = \frac{\chi_{DC}}{1 + j\dfrac{\omega}{\omega_0}\alpha - \left(\dfrac{\omega}{\omega_0}\right)^2} \tag{5-6}$$

where, ‘χ_{DC}’ is the DC susceptibility, ‘ω_0’ is the relaxation frequency (or resonance frequency) and ‘α’ in the Lorentz function is the damping factor.

An example of these two susceptibility functions is given in Fig. 5-5 with $\chi_{DC} = 75$, $\omega_0 = 2\pi(1.6GHz)$ and $\alpha = 0.8$ for the Lorentz function.

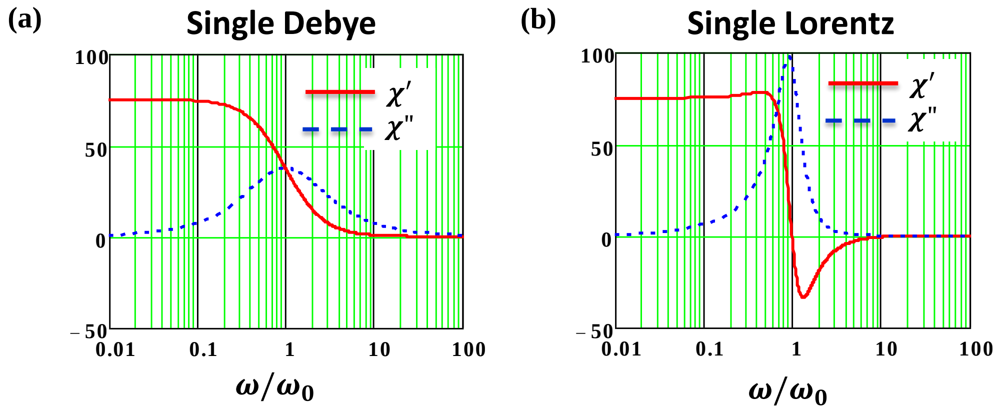

Fig. 5-5 (a) A single Debye susceptibility function (b) A single Lorentz susceptibility function

Almost all material frequency dependent permittivity and permeability functions are either Debye or Lorentz or a linear combination of many single Debye and/or Lorentz functions. In the case of the dispersive permittivity function it can be shown these analytic functions can always be reduced to the form of an electric circuit consisting of a parallel sum of series Inductor- Capacitor-Resistor (LCR) circuits [33] [34]. Given the duality of Maxwell's equations, the LCR circuit model also holds for the magnetic permeability function. Thus, the typical spin resonance of a single Debye permeable material and a single Lorentz material is represented by the LCR circuit of Fig. 5-6 (a) and (b) respectively, resulting in the dispersive permeability with a ferromagnetic resonance frequency ω_0. In this representation, the complex permeability $\mu(\omega) = \mu'(\omega) - j\mu''(\omega)$ is the magnetic capacitance of the RLC circuits. Any physically realizable magnetic material must, at the very least, be described by a single Debye relaxation or a single Lorentz resonance circuit.

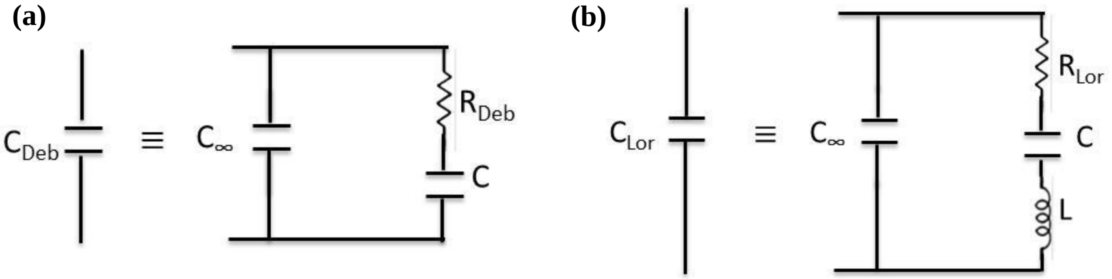

Fig. 5-6 (a) Single Debye equivalent RC circuit and (b) Single Lorentz equivalent RLC circuit

$$C_{Deb} = C_\infty + \frac{C}{1 + j\omega RC} \tag{5-7}$$

$$C_{Lor} = C_\infty + \frac{C}{1 + j\omega RC - \omega^2 LC} \tag{5-8}$$

Here, $C_\infty = \mu_0,\ C = \mu_0(\mu_{dc} - 1)$ and $L = 1/(\omega_0^2 C)$. The two resistors are given by,

$$R_{Deb} = \frac{1}{\omega_0 \mu_0 (\mu_{DC} - 1)} \tag{5-9}$$

$$R_{Lor} = \frac{\alpha}{\omega_0 \mu_0 (\mu_{DC} - 1)} \tag{5-10}$$

A little algebra recovers the usual form of the Debye and Lorentz permeability dispersion given by,

$$\mu_{Deb} = \mu_0 \left\{ 1 + \frac{\mu_{dc} - 1}{1 + j\dfrac{\omega}{\omega_0}} \right\} \tag{5-11}$$

$$\mu_{Lor} = \mu_0 \left\{ 1 + \frac{\mu_{dc} - 1}{1 + j\dfrac{\omega}{\omega_0}\alpha - \left(\dfrac{\omega}{\omega_0}\right)^2} \right\} \tag{5-12}$$

Now, a closer look at (5-9) and (5-10), reveals that the units of the inverse of this Debye and Lorentz circuit resistance is that of magnetic conductivity (Ω/m). Heaviside first introduced the concept of magnetic conductivity when he postulated a completely symmetric form of Maxwell's curl equations which some call Heaviside's duplex equations [35]. By introducing the complex permittivity and permeability functions into his equations, Heaviside's version of Maxwell's equations is reduced to:

$$\begin{aligned} \nabla \times H &= j\omega D = j\omega\epsilon_0 E + j\omega\epsilon_0(\epsilon' - 1)E + \omega\epsilon_0\epsilon'' E \\ &= j\omega\epsilon_0 E + j\omega P + \sigma_e E \end{aligned} \tag{5-13}$$

$$\begin{aligned} \nabla \times E &= -j\omega B = -j\omega\mu_0 H - j\omega\mu_0(\mu' - 1)H + \omega\mu_0\mu'' H \\ &= j\omega\mu_0 H + j\omega M + \sigma_m H \end{aligned} \tag{5-14}$$

From (5-14), Heaviside's magnetic conductivity is defined as $\sigma_m = \omega\mu_0\mu''$. The plot of the magnetic conductivity for the two susceptibility examples given in Fig. 5-5 is shown in Fig. 5-7.

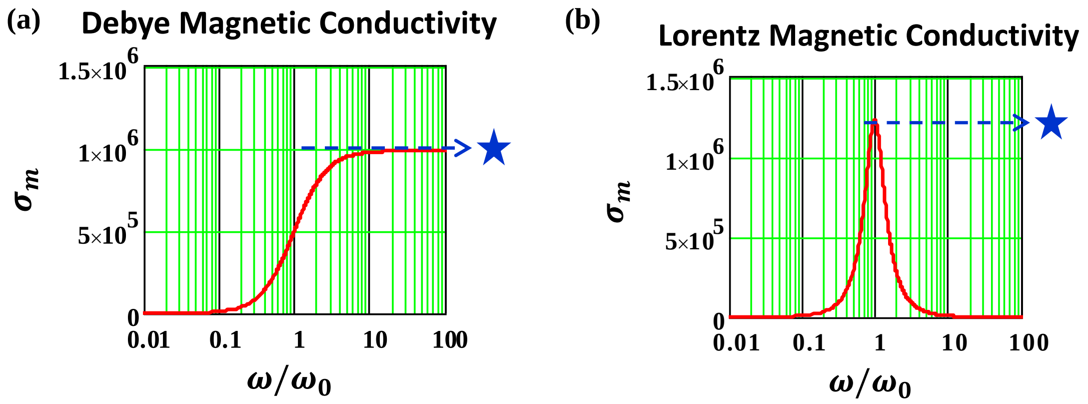

Fig. 5-7 Magnetic conductivity of the (a) Debye and (b) Lorentz examples in Fig. 5-5

The star marker represents the 'maximum magnetic conductivity' in both the Debye and Lorentz curve. For a Debye equation, this maximum value is twice the magnetic conductivity at the resonance frequency i.e. $2\sigma_m(\omega_0)$ and for the Lorentz function, this value is equal to the magnetic conductivity at resonance i.e. $\sigma_m(\omega_0)$.We have given the term "hesitivity" (h_m) to this maximum conductivity. In the Debye and Lorentz circuit equivalent (Fig. 5-6), the hesitivity is equal to the inverse of the circuit resistor (R). Therefore,

$$h_m(Debye) = \frac{1}{R_{Deb}} = 2\sigma_m(\omega_0) = \omega_0\mu_0(\mu_{DC} - 1) \tag{5-15}$$

$$h_m(Lorentz) = \frac{1}{R_{Lor}} = \sigma_m(\omega_0) = \frac{\omega_0\mu_0(\mu_{DC} - 1)}{\alpha} \tag{5-16}$$

As will be shown momentarily, this quantity h_m determines the radiation efficiency of a magnetic antenna constructed from a permeable material. We should point out immediately that the hesitivity is proportional to the Snoek's Product (5-4) and therefore is also a fundamental quantity that characterizes families of magnetic materials. Materials that belong to the same family have the same Hesitivity. For Debye materials, hesitivity and Snoek Product is identical. Table 5-1shows typical hesitivities of some magnetic material families.

Material	**Hesitivity h_m (Ω/m)**
Air	0
Bulk NiZn ferrite	30,000
Co_2Z Hexaferrite(aligned)	280,000
CoFeSiNoB ferromagnetic metal alloy	2,175,000
CoZrNb ferromagnetic metal alloy	5,000,000

Table 5-1 Typical Hesitivities of Microwave materials

5.4 Hesitivity and Magneto-Dielectric Antenna Radiation Efficiency

In this section, we derive the radiation efficiency equations of a magneto-dielectric dipole and the magneto-dielectric loop antenna in terms of hesitivity, the new term that we coined in Section 5.3 for maximum magnetic conductivity. We will show that the radiation efficiency equation is identical for both a single Debye permeability material and a single Lorentz permeability material in terms of hesitivity. The radiation efficiency of a magneto-dielectric dipole and magneto-dielectric loop was derived in Chapters 3, (3-24), and Chapter 4, (4-11), respectively. The terms that contain permeability components ($\mu'$and μ") which are common to both these efficiency equations can be written together as $f(\mu)$:

$$f(\mu) = \frac{\mu"}{|\mu_r - 1|^2} = \frac{\mu"}{(\mu' - 1)^2 + (\mu")^2} \tag{5-17}$$

Let, $\mu' - 1 = \chi' = x$ and $\mu" = \chi" = y$. Therefore,

$$f(\mu) = \frac{y}{x^2 + y^2} \tag{5-18}$$

$$x^2 + \left(y - \frac{1}{2f(\mu)}\right)^2 = \left(\frac{1}{2f(\mu)}\right)^2 \tag{5-19}$$

which is the equation of a circle with center at $\left(0, \frac{1}{2f(\mu)}\right)$ and radius '$\frac{1}{2f(\mu)}$'.

Now for the Debye susceptibility function in (5-5), the real and imaginary parts of the function can be separated as

$$\chi'_{Debye} = x = \frac{\chi_{DC}}{1 + \left(\frac{\omega}{\omega_0}\right)^2} \quad and \quad \chi''_{Debye} = y = \frac{\chi_{DC}\left(\frac{\omega}{\omega_0}\right)}{1 + \left(\frac{\omega}{\omega_0}\right)^2} \tag{5-20}$$

Therefore,

$$y = x\left(\frac{\omega}{\omega_0}\right) \tag{5-21}$$

Substituting (5-21) in (5-19), we get

$$x^2 + x^2\left(\frac{\omega}{\omega_0}\right)^2 - \frac{1}{f(\mu)}x\left(\frac{\omega}{\omega_0}\right) = 0$$

Therefore, $x = 0$ or

$$x = \frac{1}{f(\mu)}\frac{\left(\frac{\omega}{\omega_0}\right)}{1 + \left(\frac{\omega}{\omega_0}\right)^2} \tag{5-22}$$

Comparing (5-22) and (5-20) we get

$$\chi_{DC} = \frac{1}{f(\mu)}\left(\frac{\omega}{\omega_0}\right) \quad or \quad \omega_0\chi_{DC} = \frac{\omega}{f(\mu)} \tag{5-23}$$

Now, the Hesitivity of a single Debye material is defined in (5-15) as:

$$h_m(Debye) = \omega_0 \mu_0 \chi_{DC}$$

Substituting in (5-23) we get:

$$f(\mu) = \frac{\omega \mu_0}{h_m(Debye)} \tag{5-24}$$

Now, let us consider the single Lorentz material, the real and imaginary parts of susceptibility can be separated as

$$\chi'_{Lorentz} = x = \frac{\chi_{DC}\left(1 - \left(\frac{\omega}{\omega_0}\right)^2\right)}{\left(1 - \left(\frac{\omega}{\omega_0}\right)^2\right)^2 + \left(\frac{\omega}{\omega_0}\alpha\right)^2} \;\; ;$$

$$\chi''_{Lorentz} = y = \frac{\chi_{DC}\left(\frac{\omega}{\omega_0}\right)\alpha}{\left(1 - \left(\frac{\omega}{\omega_0}\right)^2\right)^2 + \left(\frac{\omega}{\omega_0}\alpha\right)^2} \tag{5-25}$$

Therefore,

$$y = x\frac{\left(\frac{\omega}{\omega_0}\right)\alpha}{1 - \left(\frac{\omega}{\omega_0}\right)^2} \tag{5-26}$$

Substituting (5-21) in (5-19), we get

$$x^2 + x^2\left(\frac{\left(\frac{\omega}{\omega_0}\right)\alpha}{1 - \left(\frac{\omega}{\omega_0}\right)^2}\right)^2 - \frac{1}{f(\mu)}x\frac{\left(\frac{\omega}{\omega_0}\right)\alpha}{1 - \left(\frac{\omega}{\omega_0}\right)^2} = 0$$

Therefore, $x = 0$ or

$$x = \frac{1}{f(\mu)}\frac{\left(\frac{\omega}{\omega_0}\right)\alpha\left(1 - \left(\frac{\omega}{\omega_0}\right)^2\right)}{\left(1 - \left(\frac{\omega}{\omega_0}\right)^2\right)^2 + \left(\frac{\omega}{\omega_0}\alpha\right)^2} \tag{5-27}$$

Comparing (5-22) and (5-20) we get

$$\chi_{DC} = \frac{1}{f(\mu)} \alpha \left(\frac{\omega}{\omega_0}\right) \quad or \quad \frac{\chi_{DC}\omega_0}{\alpha} = \frac{\omega}{f(\mu)} \tag{5-28}$$

Now, the Hesitivity of a single Lorentz material is defined in (5-15) as:

$$h_m(Lorentz) = \frac{\omega_0 \mu_0 \chi_{DC}}{\alpha}$$

Substituting in (5-23) we get:

$$f(\mu) = \frac{\omega \mu_0}{h_m(Lorentz)} \tag{5-29}$$

From (5-23) and (5-23), we see that for both a single Debye and a single Lorentz, the relationship between the function $f(\mu)$ and h_m is the same, i.e.

$$f(\mu) = \frac{\omega \mu_0}{h_m(Debye)} = \frac{\omega \mu_0}{h_m(Lorentz)} = \frac{\omega \mu_0}{h_m} \tag{5-30}$$

Substituting (5-23) back into the equations of the radiation efficiency of the magneto-dielectric dipole and the loop antenna we get the following two equations:

$$Eff_{dipole} = \frac{1}{1 + \frac{\omega \mu_0}{h_m} \frac{6}{\left(\frac{\rho}{l}\right)^2 (k_0 l)^3}} = \frac{1}{1 + \frac{\eta_0^2}{20\, h_m\, Vol_d\, k_0^2}} \tag{5-31}$$

$$Eff_{loop} = \frac{1}{1 + \frac{\omega \mu_0}{h_m} \frac{12}{\pi \left(\frac{\rho}{a}\right)^2 (k_0 a)^5}} = \frac{1}{1 + \frac{\eta_0^2}{20\, h_m\, Vol_l\, k_0^2} \frac{4}{(k_0 a)^2}} \tag{5-32}$$

where, $Vol_d = \pi \rho^2 l$ is the volume of the cylindrical dipole and $Vol_l = (\pi \rho^2)(2\pi a)$ is the volume of the loop.

Therefore, the efficiency of a cylindrical magneto-dielectric dipole and a magneto-dielectric loop carrying a uniform current is uniquely determined by a single parameter for the material, its hesitivity, which is only a function of the d.c.

susceptibility, the resonance frequency and the damping constant (for the Lorentz). These results are readily shown to be true using a full-wave simulator like Ansoft HFSS.

Fig. 5-8 shows a 1 meter long dipole of 0.5" radius fed with eight electric feed loops, placed directly on a conducting surface. The eight feed loops are used to strictly enforce the uniform current distribution assumption.

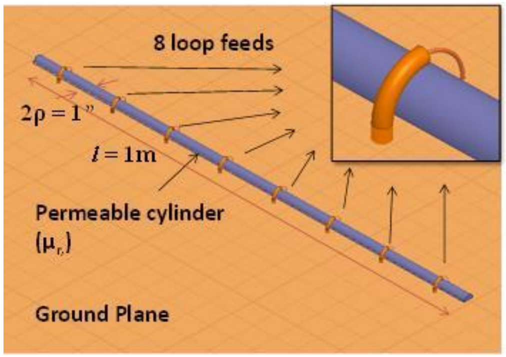

Fig. 5-8 Magneto-dielectric dipole antenna geometry used to test the radiation efficiency equations in terms of hesitivity

Fig. 5-9(a) and (b) shows three different Debye materials and four different Lorentz materials, respectively, considered in the numerical experiment. All the Debye materials and the all the Lorentz materials have exactly the same hesitivity but with relaxation frequencies ranging from 300 MHz to 2 GHz as seen in the magnetic conductivity plots.

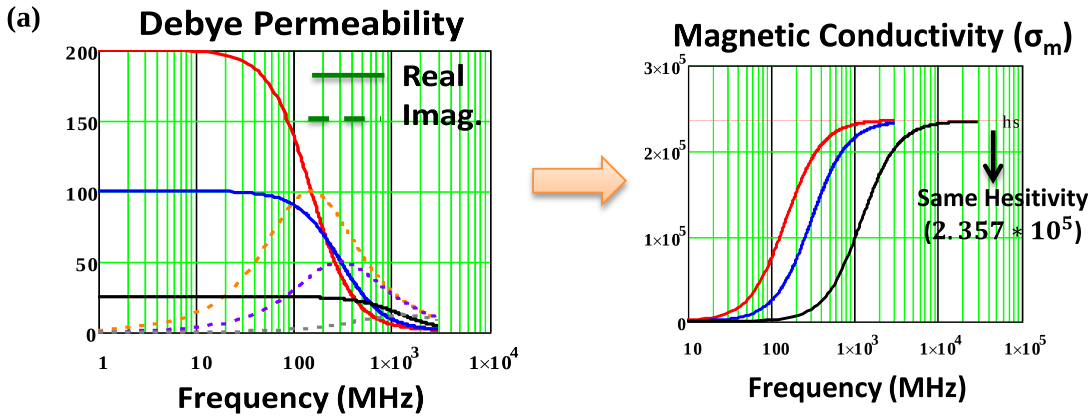

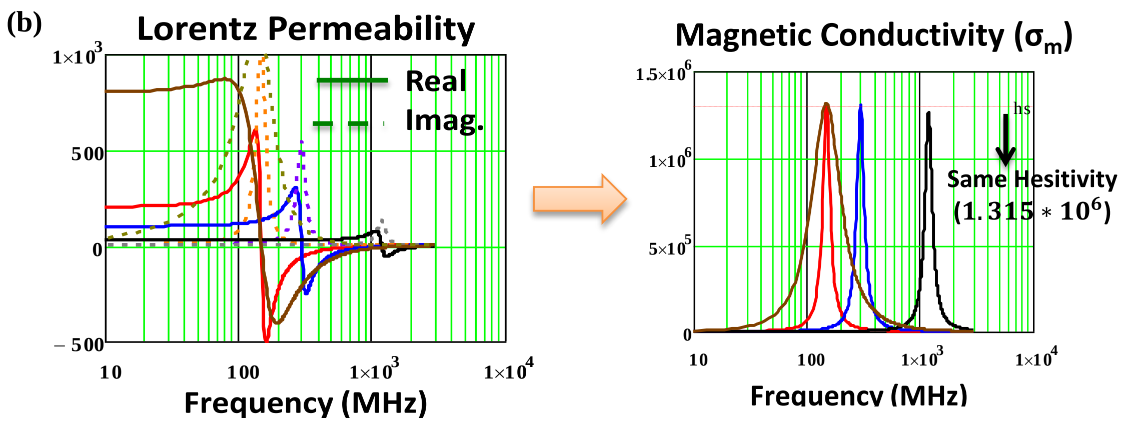

Fig. 5-9 Different (a) Debye and (b) Lorentz materials permeability and magnetic conductivity plots, used in the verification of the radiation efficiency equation (5-31). The hesitivity of the three seemingly different Debye materials is the same and the same is true for the four Lorentz materials.

They clearly exhibit very different loss tangents across the frequency range that was simulated: 30MHz to 300MHz. Nevertheless as Fig. 5-10 shows that the efficiency computed by the full-wave solver is the same for all three Debye materials and also for the four Lorentz materials, and lies right on top of the result of equation (5-31) in the entire small antenna range.

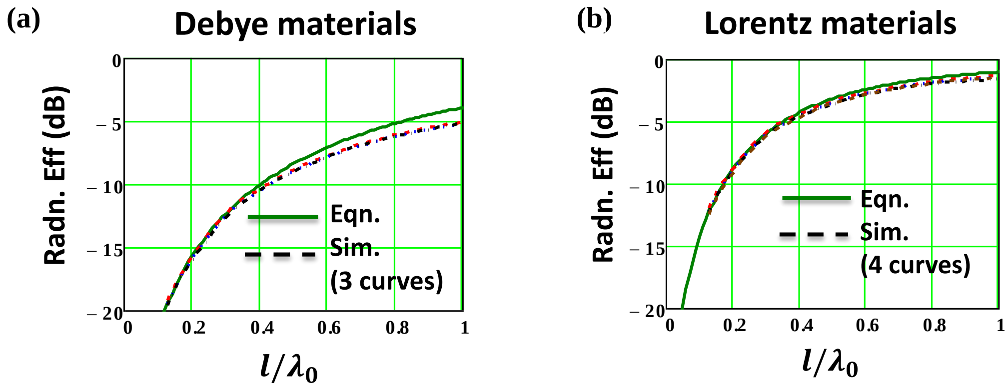

Fig. 5-10 The Radiation Efficiency of (a) single Debye materials and (b) single Lorentz materials shown in Fig. 5-9. The solid curve is using (5-31).

Therefore, using (5-31) and (5-31), given the real estate available and a minimum efficiency requirement to design a low profile conformal magneto-dielectric material antenna, we can determine to which family of magnetic materials the candidate antenna material will belong to. That is, we can estimate the hesitivity of the family of the candidate magneto-dielectric material.

In a different scenario, in antenna designs where we know beforehand the material that we intend to use, we can estimate the radiation efficiency at any frequency within the small antenna limit without having to measure the permeability of the material at the said frequencies because we would know the hesitivity of the material.

The next obvious question is whether we can narrow down the choice of material further, by picking an optimum one within the family of same hesitivity materials. The answer lies within the first fundamental physical limit EBWP that was described in section 5.3 of this chapter: Antenna Bandwidth.

5.5 Material Selection Law in the design of magneto-dielectric antennas

The radiation efficiency equations of (5-31) and (5-32) show that higher the hesitivity of the material used in the design of magneto-dielectric antennas, higher will be the radiation efficiency. But it is always possible to have more than one material with the same hesitivity, which is true of materials that belong to the same family, an example being the NiZn family in Fig. 5-4. The parameter that can aid us in the final choice of material is the antenna bandwidth. We have already described in Section 5.3 how the product of Efficiency and Bandwidth, EBWP, is a fundamental physical limit in antenna designs. Let us calculate the bandwidth for the Debye and Lorentz materials that were simulated in Section 5.4 (Fig. 5-9) using the fractional bandwidth equations given by Best et al. [11] (5-2). In order to use this equation, the input impedance of the antenna (Z_{in}) is calculated by using ideal power splitters/dividers to form a single feed line. Since the efficiency for these materials is the same, the EBWP is essentially a plot of the antenna bandwidth.

The Efficiency Bandwidth Product along with the loss tangent of the Debye materials shown in Fig. 5-9(a), is shown in Fig. 5-11. The material with the highest μ'' in the frequency band that was simulated gives the highest Efficiency Bandwidth Product. This is not a surprising result. We know that adding any kind of loss to the antenna system improves the bandwidth of the antenna. In contrast to some traditional methods to increase bandwidth like additional elements like a resistor in series to the input of the antenna, etc. the loss in the magneto-dielectric material itself is performing the function of raising antenna bandwidth.

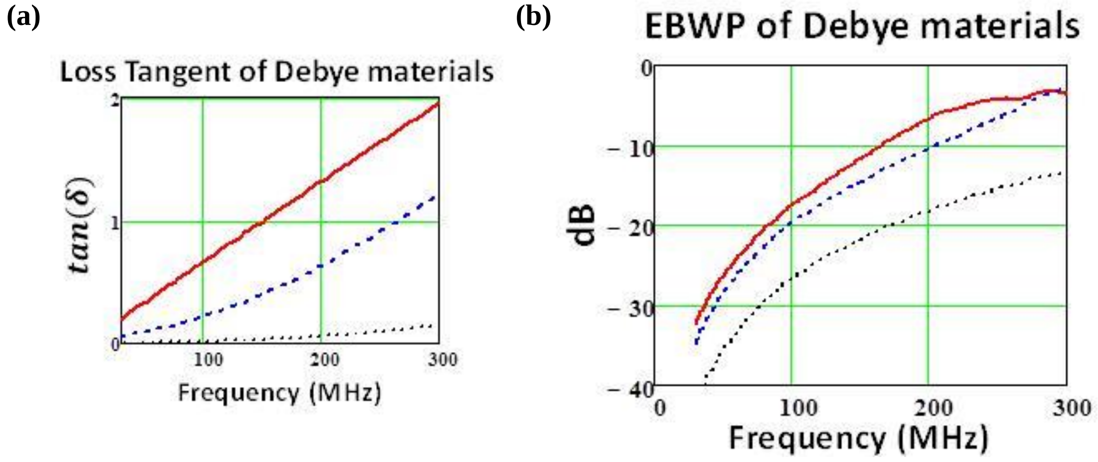

Fig. 5-11 (a) Loss tangent of the simulated Debye materials and (b) Efficiency Bandwidth Product (EBWP) curves for the same.

Following the same steps as above, the Efficiency Bandwidth Product along with the loss tangent of the Lorentz materials shown in Fig. 5-9(b), is shown in Fig. 5-11. Again, among the different materials in the same hesitivity family, the material with the highest loss gives the highest Efficiency Bandwidth Product.

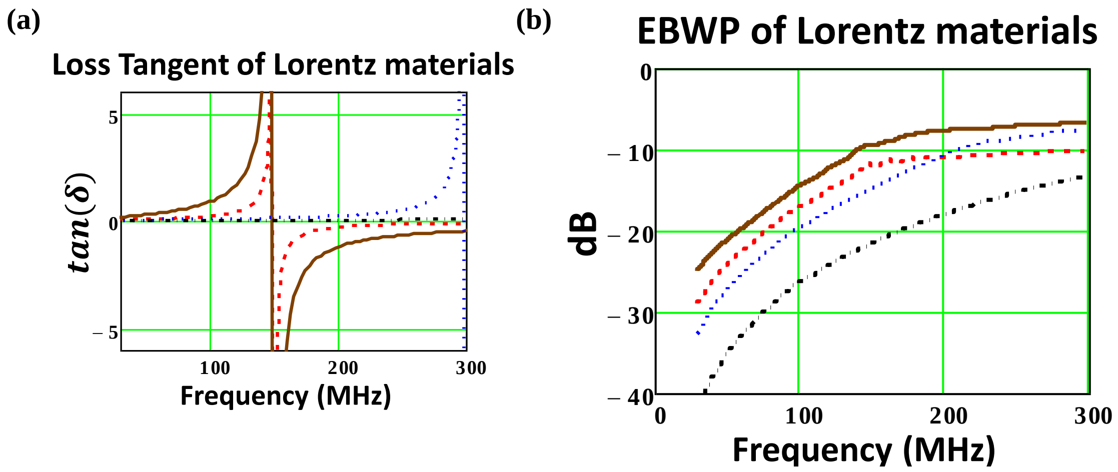

Fig. 5-12 (a) Loss tangent of the simulated Lorentz materials and (b) Efficiency Bandwidth Product (EBWP) curves for the same.

Therefore, from the radiation efficiency equations in Section 5.4, we see that we need a magneto-dielectric material with high hesitivity for high radiation efficiency. From the EBWP calculations in this section, we have realized that we need materials that have high μ'' within the frequency band of interest to get high antenna bandwidth. Therefore, by combining these two statements we state the material selection law to choose the optimum magneto-dielectric antenna material as:

“The candidate material to design efficient broadband low profile conformal magneto-dielectric antenna will belong to the material family with the highest hesitivity and among that family; it will be the one that has the most μ'' loss in the targeted frequency band of operation”.

Since the loss or the imaginary part of permeability (μ") peaks at the ferromagnetic resonance frequency (ω_0), a useful rule of thumb or extension to the material selection law is to ensure that the ferromagnetic resonance frequency of the material that is selected is within band of interest.

5.6 Some Realistic and Almost Realistic Magneto-dielectric materials Evaluated using the Material Selection Law

In this section, the material selection law that was postulated in the previous section will be used to evaluate some of the existing magneto-dielectric material found in the literature. The permeability data obtained from these sources was fit to an analytic function (Debye or Lorentz) whenever it was possible to do so. The following materials were considered:

a) **NiZn:** Bulk NiZn ferrite produced by FairRite [36]. The permeability data was obtained from the same reference.

b) **Co2Z:** Unaligned Cobalt Hexaferrite (permeability data from the book by Smit and Wijn [31]. This material is also produced by Transtech Inc.)

c) **Bek12:** Bekaert CZN film sheets (12 μm Kapton substrate thin film) laminated to form a bulk composite (as in Fig. 5-3). The data sheet was provided by the manufacturer Bekaert Specialty Films.

d) **Bek7p5:** Bekaert CZN assuming that it is deposited on 7.5 μm insulating substrate; many such thin films are then assumed to be laminated to form the bulk structure.

e) **Bek7p5_500:** Similar to d) but with the ferromagnetic resonance frequency artificially shifted to 500MHz while keeping the same hesitivity. Although this material doesn't exist, it is used here to re-iterate the need to move the materials high loss (μ") region into the frequency range of interest.

f) **CoB7p5:** Cobalt Boron thin film from [37] assuming that it is deposited on a 7.5micron Kapton substrate and laminated to form the bulk composite.

Using the permeability dispersion data of a single film we can calculate the effective permeability of this composite. The frequency dispersive effective permeability of the bulk structure for each material is shown in Fig. 5-13.

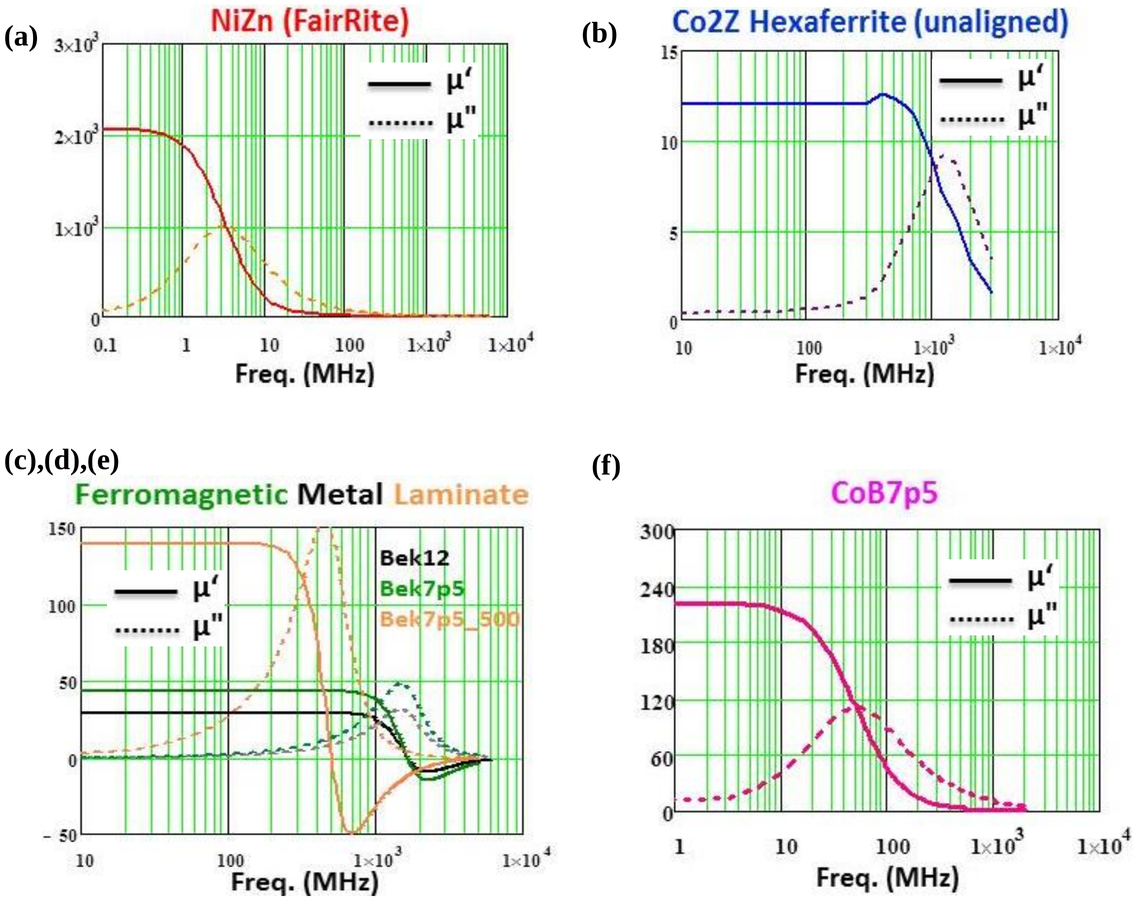

Fig. 5-13 Frequency dispersive permeability (Solid: Real and Dashed: Imaginary) of different magnetic materials that were considered for evaluation.

The hesitivity of the individual thin films and the hesitivity of the bulk sample are tabulated in Table 5-2.

Magnetic Material	**Hesitivity (Ω/m) (Single Film)**	**Hesitivity (Ω/m) (Bulk Sample)**
NiZn	na	$5.524*10^4$
Co2Z	na	$1.042*10^5$
Bek12	$6.511 * 10^6$	$3.951*10^5$
Bek7p5	$6.511 * 10^6$	$5.01*10^5$
Bek7p5_500	$6.511 * 10^6$	$5.01*10^5$
CoB7p5	$2.720 * 10^6$	$8.646*10^4$

Table 5-2 Hesitivity of the materials being evaluated using the material selection rule

As expected, upon lamination the permeability of the single film gets diluted and the hesitivity drops. Notice that the hesitivity of the CoB drops significantly after lamination because the individual film found in the literature has a thickness of 300nm which is significantly thinner than the assumed dielectric substrate. Therefore, if it is possible to deposit thicker films while maintaining the same permeability dispersion, then the bulk hesitivity of this material will approach that of the Bekaert's films.

The materials arranged in the ascending order of hesitivity is therefore,

$$Bulk\ Hesitivity\colon\ NiZn < CoB7p5 < Co2Z < Bek12 < Bek7p5 = Bek7p5\_500$$

Also, among the two high hesitivity materials, Bek7p5 and Bek7p5_500, Bek7p5_500 has the highest amount of loss (μ'') in the frequency range of interest. Therefore, according to the Material Selection Law, the optimum choice among the materials above must be Bek7p5_500. This conclusion is easily validated by using a full-wave simulator.

Full-wave simulations of a 1m long cylindrical dipole of 0.5” radius fed with four feed loops were performed using these materials. This geometry was fixed for all the materials listed above for direct comparison. The frequency range of simulation was 30MHz to 300MHz. The impedance seen at each feed port was combined using an ideal power divider netwrok as in Section 5.6, to find the total input impedance Z_{in}. The bandwidth (BW) was again calculated using (5-2). The radiation efficiency, bandwidth (for Γ = -10dB) and Efficiency-Bandwidth Product (EBWP)’ for all these cases are shown in Fig. 5-14.

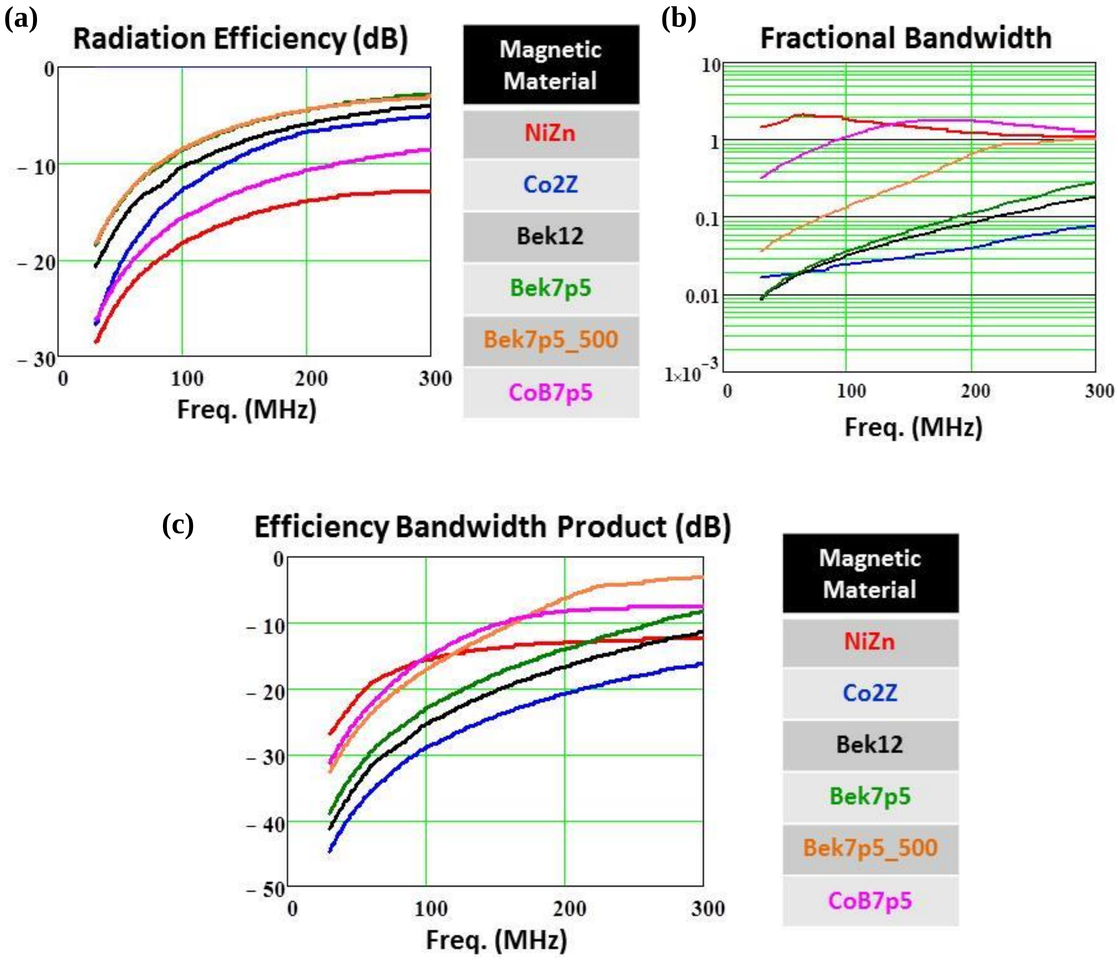

Fig. 5-14 a) Radiation Efficiency (b) Fractional Bandwidth (c) Efficiency Bandwidth product for different materials for a 1m long, 0.5” radius dipole.

From Fig. 5-14(a), it is clear that the radiation efficiency of the magneto-dielectric dipole increases with hesitivity. And also as expected, two different materials with different permeability dispersion but with the same hesitivity, have the same radiation efficiency (Orange: Bek7p5_500 curve is on top of the Green: Bek7p5 curve).

The fractional bandwidth (FBW) curve, on the other hand (Fig. 5-14(b)), has a different trend. As we saw in Section 5.6, the highest FBW is obtained using the NiZn and CoB materials that are extremely lossy at these frequencies.

Fig. 5-14(c) shows that at low frequencies, for this structure, the NiZn ferrite has the highest EBWP. The loss in this material makes it very easy to match the antenna and hence the boost in bandwidth overcomes the drop in efficiency as seen in Fig. 5-14(a) and Fig. 5-14(b). A similar result is observed in the case of CoB7p5 material. But, as frequency goes up, we see that the Bek7p5_500 material has the highest EBWP. The high hesitivity of this material results in high efficiency and as the ferromagnetic resonance of this material is close to the band of operation (ferromagnetic resonance f_0=500MHz), the high μ" loss gives it higher FBW. The difference is clearly seen when compared to Bek7p5 which is a material from the same 'family' (same hesitivity). Although Bek7p5_500 and Bek7p5 have the same radiation efficiency, Bek7p5 has a lower bandwidth (and therefore lower EBWP) as it has low μ" in the frequency range of operation.

These results validate the material selection law that was stated in Section 5.6. The laminated Bek7p5_500 material has the highest EBWP throughout the band of interest. Therefore, it is the right choice of material as predicted by the Material Selection Law.

5.7 Conclusions and Future Work

Using a closed form model of an electrically small magneto-dielectric antenna that satisfies automatically the Fano-Chu Gain bandwidth Product limit, and including in that model a dispersive permeability consistent with the Kramers Kronig relations, we obtain a material selection rule that states that given a fixed volume of material, maximum efficiency is obtained by choosing the material to have the largest possible hesitivity, a quantity commensurate with Snoek’s Product, and which has the largest amount of μ'' loss in the desired frequency range of operation. This material selection rule enables the rapid design of magneto dielectric antennas for conformal applications.

Future work on this subject will include extending the material selection law to multi-Debye and multi-Lorentz materials.

Chapter 6

MAGNETO-DIELECTRIC DIPOLE ANTENNA CIRCUIT MODEL USING POLARIZABILITY

6.1 Introduction

In Chapters 3 and 4, we developed an electrically small magneto-dielectric antenna model by adding circuit elements (L & C) that are functions of the magneto-dielectric material constitutes (permeability (μ_r) and permittivity (ε_r) respectively) to the electrically small RLC circuit model of a conventional metallic antenna. The additional elements accounted for the penetration of fields into the material. The external field structure were assumed to be the same as that of a metallic (or PEC) electrically small antenna and hence they were modeled by Schelkunoff's electrically small antenna circuit elements. In this chapter, we take a different approach in modeling a magneto-dielectric dipole antenna in which we use only three basic elements (R, L and C) to come up with a much simpler (less circuit elements) equivalent magnetic circuit model, with the magnetic capacitor being a function of permeability. The permeability is incorporated into the antenna capacitance using polarizability (α) of the object. The polarizability equation enables us to model both the external and internal magnetic field morphology using a single magnetic capacitor. The analysis is done for a purely magnetic material before extending it to a more general realistic lossy magneto-dielectric material.

Any dipole or loop like antenna in the electrically small regime can be modeled as an RLC circuit where R is the radiation resistance ($R = 5(k_0 l)^2$ for a small dipole with triangular current distribution). For a PEC dipole, a series resonant circuit is the best model (Fig. 6-1(a)), the equations for L and C given by Schelkunoff [38] are,

$$L_{PEC\_dipole} = \frac{\frac{\mu_0 l}{2}}{3\pi}\left(ln\left(\frac{l}{a}\right) - \frac{11}{6}\right) \tag{6-1}$$

$$C_{PEC\_dipole} = \frac{\pi \varepsilon_0 l/2}{ln(l/a) - ln2} + 2\varepsilon_0 a \tag{6-2}$$

The equations above are for a PEC dipole. For a magneto-dielectric antenna fed by either a frill magnetic current or an electric voltage gap, the L and C equations need to be a function of its constitutive properties namely μ_r and ε_r. Therefore, given the properties of the magneto-dielectric material we want to find the total antenna capacitance and inductance of the circuit model Fig. 6-1.

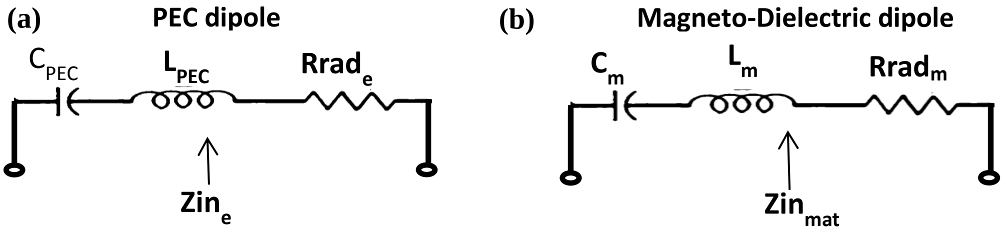

Fig. 6-1 ESA circuit model of (a) PEC dipole (b) the proposed model for a Magneto-dielectric Dipole

In Section 6.2, the relationship between the magnetic capacitance of the magneto-dielectric antenna magnetic circuit model and polarizability is established. The two are related by a proportionality factor which is calculated in Section 6.3. In Section 6.4, the complete circuit model is compared with full-wave simulations. It is shown that the agreement between the circuit model and the full wave simulations is good only in the electrically small limit. The summary and some notable conclusions of the chapter are outlined in Section 6.5.

6.2 Polarizability and Antenna Capacitance

Let us complete the magnetic circuit model by starting with the antenna capacitance. Now we need a parameter that connects capacitance to its constituents. One such quantity is Polarizability (α). Suppose a uniform electric field (E) is impressed on a conducting sphere of radius ‘a’ (Fig. 6-2(a)).The induced dipole moment (p) of the sphere in the presence of this uniform E-field is given by

$$p = 4\pi\varepsilon_0 a^3 E = \alpha_{PECsphere} * E\;;\quad where\ \alpha = Polarizability \tag{6-3}$$

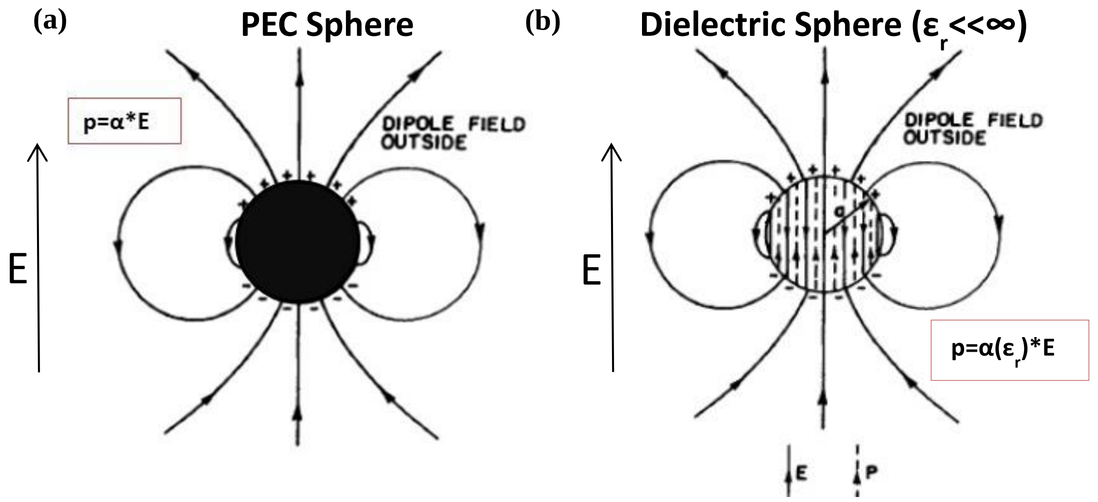

Fig. 6-2 (a) PEC sphere with external flux lines and a (b) Dielectric sphere with internal and external flux lines created in the presence of a uniform ambient E field(E).

Now suppose, the sphere is not made up of PEC but a material say of finite dielectric constant ($\varepsilon_r \neq \infty$) (Fig. 6-2(b)), then the Polarizability, $\alpha_{material}$, is that of a PEC sphere de-rated by the *factor*, $(\varepsilon_r - 1)/(\varepsilon_r + 2)$. The dipole moment is still p= α_{material} E. Note that the PEC sphere has only external flux lines while the material object has both internal and external flux lines. Now, if we consider a PEC sphere and wrap it with a magnetic ring current and make a spherical antenna (Fig. 6-3) we know that its near field looks like the field of a dipole and we can calculate its dipole moment. Therefore, is there a relation between the antenna capacitance (from the flux lines) and Polarizability? Let us assume that

$$C_{PECsphere} = \alpha_{PECsphere}/factor \qquad (6\text{-}4)$$

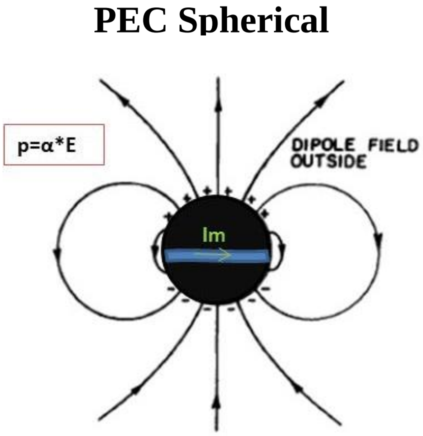

Fig. 6-3 PEC spherical antenna excited by a magnetic ring current

The antenna susceptance of different spherical modes of the metallic sphere is given by [38]:

$$Bn = j\omega C_n = \frac{1}{60} * \frac{2n+1}{2n^2(n+1)} \varepsilon_0 \beta_0 a \left(\frac{n!}{2^{n-1}\left\{\left[\frac{n-1}{2}\right]!\right\}^2} \right)^2$$

Since we are interested in the electrically small domain; for the lowest order mode or principal wave (TM01), n=1,

$$C_1 = C_{PECsphere} = \frac{3\pi}{2}\varepsilon_0 a \tag{6-5}$$

From (6-3), (6-4) & (6-5) :

$$C_{PECsphere} = \frac{\alpha_{PECsphere}}{\frac{8}{3}a^2} \qquad \text{or} \quad factor = \frac{8}{3}a^2 \tag{6-6}$$

Thus, (6-6) relates Polarizability to capacitance of a PEC sphere. This can be extended to a magneto-dielectric sphere by using its polarizability $\alpha_{material}$ from above. But here we are interested in linear cylindrical objects as antennas that can be placed conformal to ground. We can always approximate a cylinder by a prolate spheroid of large aspect ratio (Fig. 6-4). The reason for considering a prolate spheroid is that unlike a cylinder, we know the Polarizability of a prolate spheroid in closed form [39].

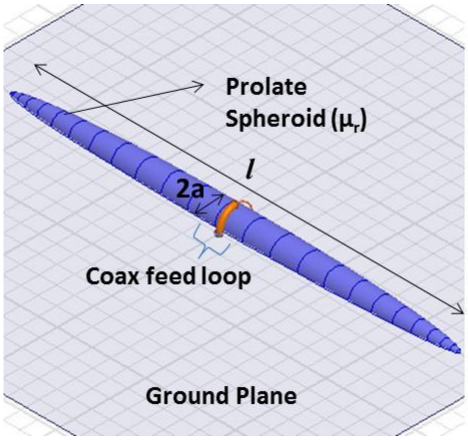

Fig. 6-4 Prolate Spheroidal Magneto-Dielectric Antenna fed by an electric loop (Approximates a Cylinder)

If 'k1' and 'k2' represent the constitutive properties of the external and the internal medium and k0 = ε_0 or μ_0 (depending on the type of material):

$$\varphi = \cos^{-1}\left(\frac{1}{AspectRatio}\right)$$

$$M = \frac{\varphi - \frac{1}{2}sin(2\varphi)}{sin^3(\varphi)} cos(\varphi)$$

$$\beta = \frac{1}{3}\left[\frac{2}{1+\left(\frac{k2}{k1}-1\right)\frac{M}{2}} + \frac{1}{1+\left(\frac{k2}{k1}-1\right)(1-M)}\right]\left(\frac{k2}{k1}-1\right)$$

$$Polarizability = \alpha = \beta \cdot k0 \cdot Vol \tag{6-7}$$

where, *Aspect Ratio* = (*l*/2)/a, a = Minor axis radius and *l/2* = Major axis radius (See Fig. 6-4). Our next task is to find the factor that relates the Polarizability of a prolate spheroid and the total magneto-dielectric prolate spheroidal antenna capacitance.

6.3 Factor Relating Polarizability and Antenna Capacitance of a Permeable Prolate Spheroid Antenna

We begin our analysis, by simulating prolate spheroidal antennas (in HFSS) of different Aspect Ratios ($AR = (l/2)/a$) going from 1 which is a sphere to 50 which looks like a needle (Fig. 6-5) and different μ_r (lossless i.e. $\mu'' = 0$) from $\mu' = 1$ to $\mu' = 10^8$ (a PMC) in the electrically small regime (30MHz to 100MHz).

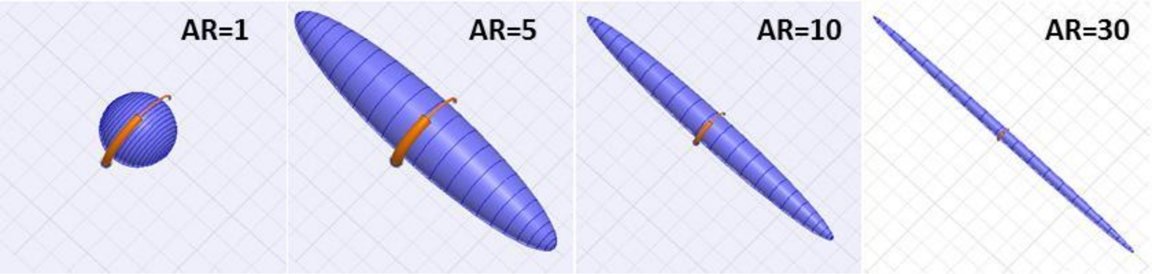

Fig. 6-5 Simulation model of a Prolate Spheroidal Antenna of different aspect ratios (AR) in the full wave simulator (Ansoft HFSS).

The circuit model assumed is shown in Fig. 6-1(b), but since we are working in the electrically small regime, we will ignore the inductance (L_m) for now. In HFSS we measure the input impedance of the loop which is electric impedance Zin_e. We want the dual impedance Zin_m. We saw in Chapter 3 that the magnetic input impedance is equivalent to the electric input admittance. Thus, we can find the magnetic input impedance of the ESA equivalent circuit model by taking the inverse of the input impedance measured in the full wave simulator.

Note, that although we said that the inductance of the equivalent circuit will be ignored, what we were talking about was the internal inductance. The antenna would always see the inductance of the feed loop itself. Hence, this extra inductance should be subtracted out of our antenna capacitance calculation. Therefore, before we analyze the magneto-dielectric case, let us analyze the electric feed loop by itself (μ'=1) in order to find out its self-inductance. Jeffimenko [40] gives us the static solution of the self-inductance of a thin circular wire ring (circle radius 'R' and wire radius 'ρ'):

$$Jeffimenko\_L_{loop} = \mu_0 R \left(\ln \left(\frac{8R}{\rho} \right) - \frac{7}{4} \right) \tag{6-8}$$

On the other hand, Schelkunoff [41] also gives us the inductance of a small loop by integrating around the loop the inductance per unit length of the principal wave:

$$Schelkunoff\_L_{loop} = \mu_0 R \left(\ln \left(\frac{R}{\rho} \right) \right) \tag{6-9}$$

Surprisingly, the two equations are different. The comparison of the two equations along with the HFSS result for different loop radii is shown in Fig. 6-6. We can clearly see that Schelkunoff's Loop equation agrees well with simulation for all the cases considered keeping in mind that the simulation curves can go lower as we go deeper into the electrically small domain. Therefore, we will use his equation to subtract out the inductance of the loop in our antenna capacitance calculation.

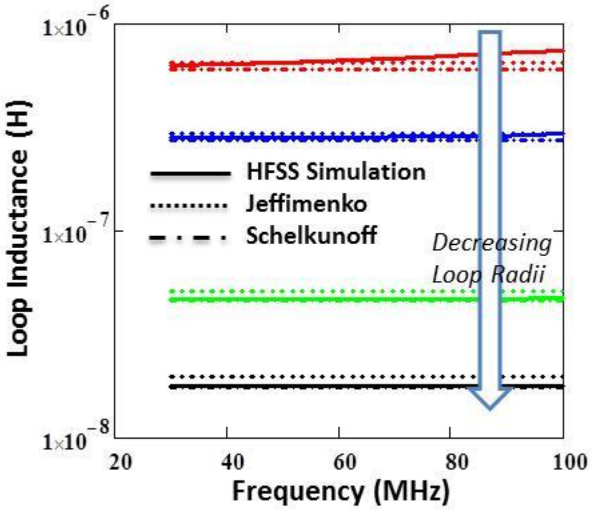

Fig. 6-6 Inductance of feed loop vs Frequency for different loop radii

Therefore, the antenna capacitance calculated from HFSS is given by

$$\frac{1}{j\omega Cm_{HFSS}} = Im(Zin_m) = \frac{1}{2} Im\left(\frac{1}{Zin_e}\right)$$

$$=> \qquad Cm_{HFSS} = \frac{2}{\omega * Im\left(\frac{1}{Zin_e}\right)} - Schelkunoff_{L_{loop}} \tag{6-10}$$

The factor of ‘2’ is to account for the fact that the antenna was placed on top of a PEC ground plane. Fig. 6-7 below shows this HFSS magnetic capacitance compared with the magnetic capacitance calculated from the polarizability for two different values of μ_r.

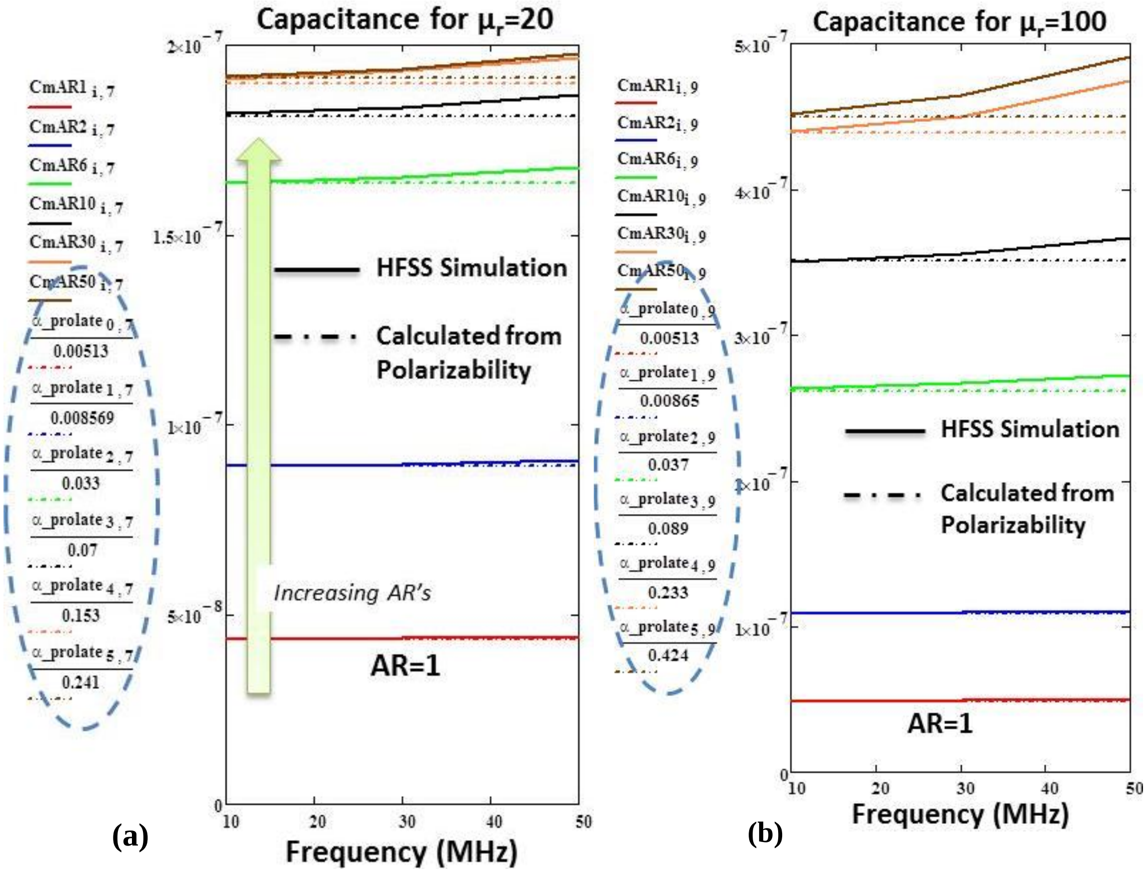

Fig. 6-7 Magnetic Capacitance of the ESA magneto-dielectric dipole Simulated and Calculated from Polarizability for (a) $\mu' = 20$ (b) $\mu' = 100$.

The capacitance calculated from the polarizability is encircled in Fig. 6-7. The factor for Aspect ratio of '1' is the same for both the cases. In other words for a sphere (AR=1), the factor is independent of material properties i.e the polarizability takes into account the change in the shape of the fields inside and outside the spherical structure. In fact, from (6-6), the factor for a PEC (or PMC) was estimated to be 8/3 times the square of the radius of the sphere. That value for the simulated sphere is 0.0053. The value using the polarizability equation is 0.00513 for AR=1 (Fig. 6-7). In other words, the capacitance factor of a spherical magneto-dielectric antenna is the same as that of a spherical PEC or PMC antenna.

Also note that the in each plot the factor is different for different aspect ratio's and at the same time the factor in Fig. 6-7(a) and (b) are different for a fixed aspect ratio except AR=1. This implies that the factor that relates polarizability and magnetic capacitance for a prolate spheroidal antenna is a function of both the Aspect ratio (AR) and the material property of the magneto-dielectric (μ'). The proportionality factor is plotted versus the Aspect ratio for different μ's and vice versa in Fig. 6-8 below.

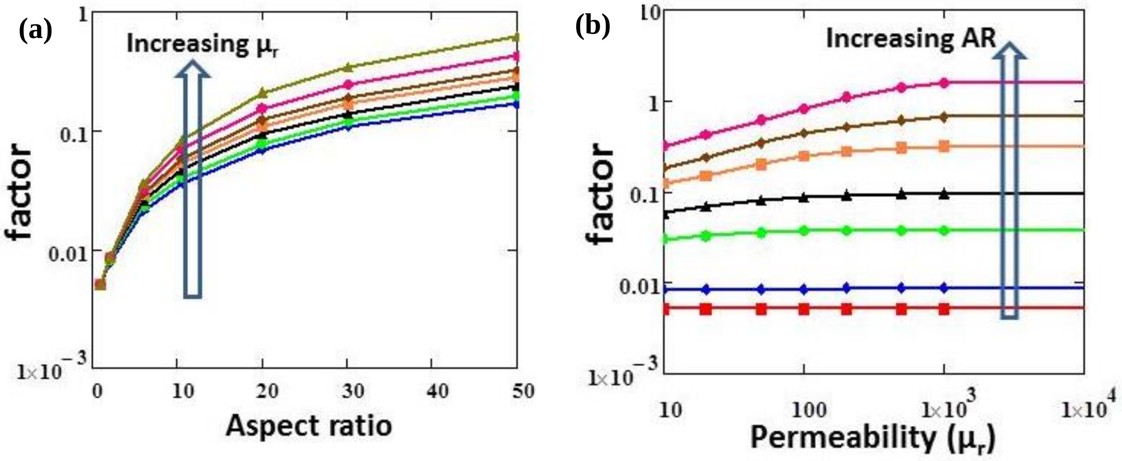

Fig. 6-8 Magnetic Capacitance and Polarizability proportionality factor (a) versus Aspect Ratio and (b) versus Permeability

The constant curve in Fig. 6-8(b) is for the sphere (AR=1) which as mentioned before is a constant w.r.t μ_r. Fig. 6-8 clearly shows the variation of the proportionality factor with aspect ratio and μ_r. Therefore, we are left with the task of finding a function for the factor which is a function of AR and μ_r. Based on Diaz et. al. [42], since the problem at hand is that of finding the capacitance factor in the electrically small regime, Laplace's equation must be satisfied. Thus, the equation of this capacitance factor that accounts for the morphology of the field structure as a function of μ_r will be of a Debye equation form:

$$factor = \left(facDia + \frac{facPMC - facDia}{1 + \frac{u}{upoles}} \right) \tag{6-11}$$

where, 'facPMC' is the factor for PMC, 'facDia' is the factor at the diaphanous limit (assuming μ=1.1 since μ=1 makes the polarizability zero), $u = 1/(\mu_r - 1)$ and 'upoles' are the estimated poles of this function. Thus we have in effect separated the two possible sources of variation of the factor function into 'facPMC', 'facDia' and upoles that vary only with aspect ratio and 'u' that is a function of just the permeability μ_r. The comparison between simulated factor and equation (6-11) for two different cross-sectional radius of the prolate spheroid is shown in Fig. 6-9.

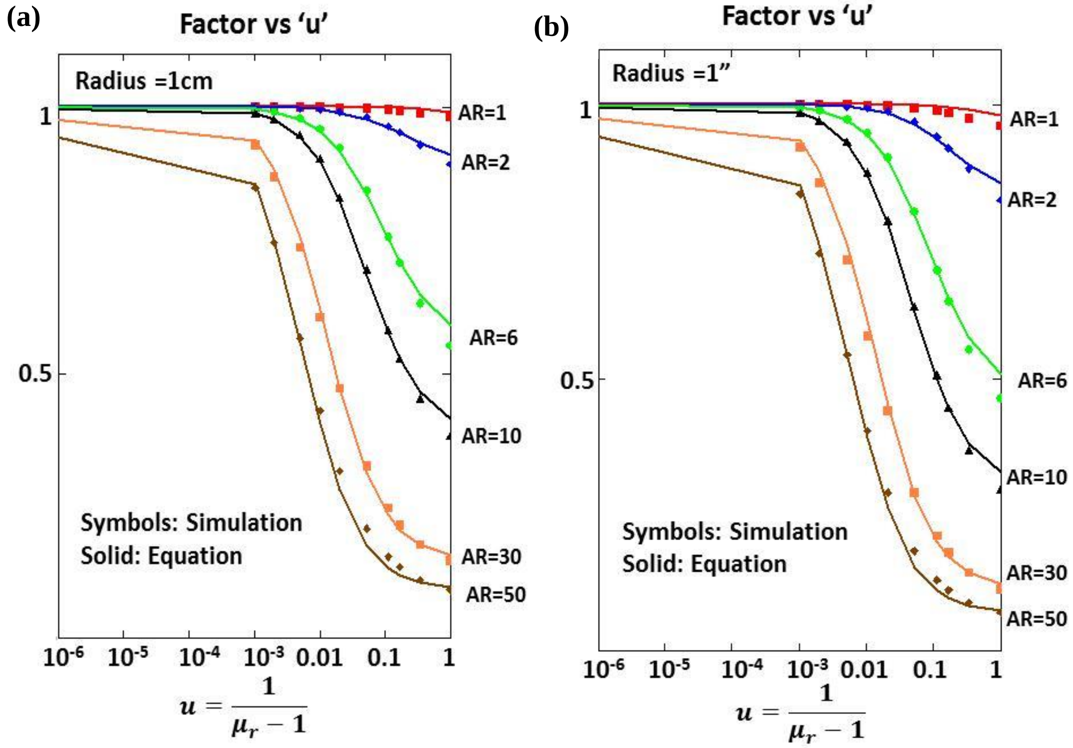

Fig. 6-9 Single pole Debye factor function (6-11) compared to full-wave simulation extraction from polarizability for cross sectional radius (a) 1cm and (b) 1inch=2.54cm.

The plot of the terms of the factor function that depend on the aspect ratio is shown in Fig. 6-10.

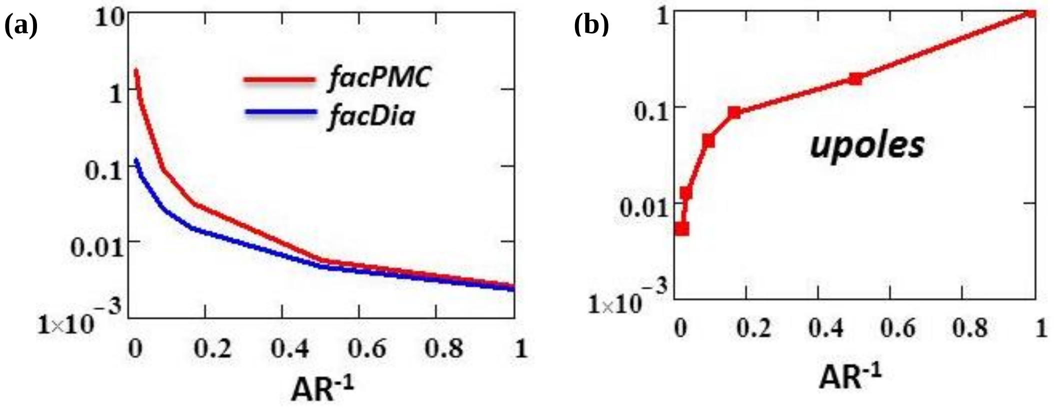

Fig. 6-10 a) Plot of factor for PMC dipole ‘facPMC’ and factor at the diaphanous limit ‘facDia’ versus invers of the aspect ratio. (b) Plot of the poles of (6-11).

As this function (6-11) is analytic; although it was derived for purely real μ_r, its validity extrapolates to the entire complex plane of permeability. For a few complex values of μr, HFSS simulations were run to find the magnetic capacitance as before. Note that since we have a complex μ_r, the Polarizability calculated from (6-4) and (6-11) will be complex and therefore we end up with a Complex magnetic capacitance with the imaginary part corresponding to the magnetic loss resistance. In order to preserve the complex data from our HFSS ‘Zin’ measurement, we have to subtract out the Radiation resistance due to the magnetic current flowing in the magneto-dielectric dipole. Since we are operating in the electrically small regime it is safe to assume a triangular current distribution due to the leaky nature of the wave in this structure. Therefore, the magnetic radiation resistance of this dipole using duality is given by:

$$Rrad_m = \frac{5(k_0 l)^2}{\eta_0^2} \tag{6-12}$$

where η_0 is the impedance of free space, i.e. 377Ω.

Fig. 6-11shows the resulting calculated and HFSS simulated magnetic capacitance for different cases. There is an excellent agreement between simulation and the calculated magnetic capacitance from polarizability using the factor calculated before. The agreement is good not only in the real part of capacitance but also the imaginary term, which goes to show that the polarizability can also accurately account for the magnetic loss resistance incurred due to the complex permeability. Therefore we have determined a closed form expression for the magnetic capacitance C_{mat} in the circuit model of Fig. 6-1(b). Now all that is left is the inductance.

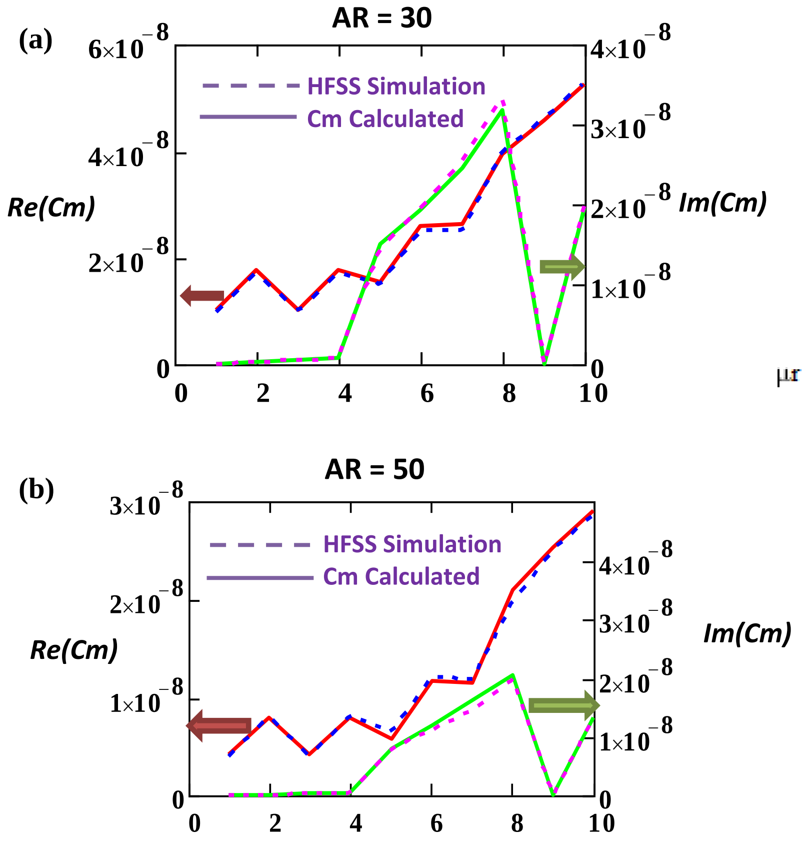

(c)

μr =

1	10-0.1i
2	20-0.2i
3	10-0.5i
4	20-i
5	10-20i
6	20-40i
7	10-50i
8	20-100i
9	100-0.5i
10	100-100i

Fig. 6-11 Simulated and Calculated complex magnetic capacitance for AR=30(a) & AR=50(b), (c) List of complex μ_r used (numbered 1-10 => x-axis)

The antenna magnetic inductance, to first order, is the dual of (6-2). Therefore the zeroth order equations for the electrically small magnetic circuit model of a permeable prolate spheroidal dipole (Fig. 6-1 (b)) fed by a single electric loop are summarized as follows:

From (6-12), $Rrad_m = \frac{5(k_0 l)^2}{\eta_0^2}$

From (6-4), (6-7) and (6-11), $C_m = \frac{Polarizability}{facDia + \frac{facPMC - facDia}{1 + \frac{u}{upoles}}}$

Using duality on (6-2) $L_m = \frac{\varepsilon_0 l}{6\pi}\left(\ln\left(\frac{l}{a}\right) - \frac{11}{6}\right)$

6.4 Circuit Model Comparison with Full-Wave Simulations

Consider a 21 inch long and 2inch cross-section prolate spheroid permeable antenna. Note that the TE01 mode onset frequency for a cylinder of this cross section for the different permeability values simulated are: $\mu_r = 2$ => 4.5GHz; $\mu_r = 10$ => 1.5GHz; $\mu_r = 50$ => 645MHz and $\mu_r = 500$ => 202MHz which corresponds to l/λ_0 of 8, 2.7, 1.15 and 0.36 respectively. The comparison of input impedance and the proposed circuit model is shown in Fig. 6-12.

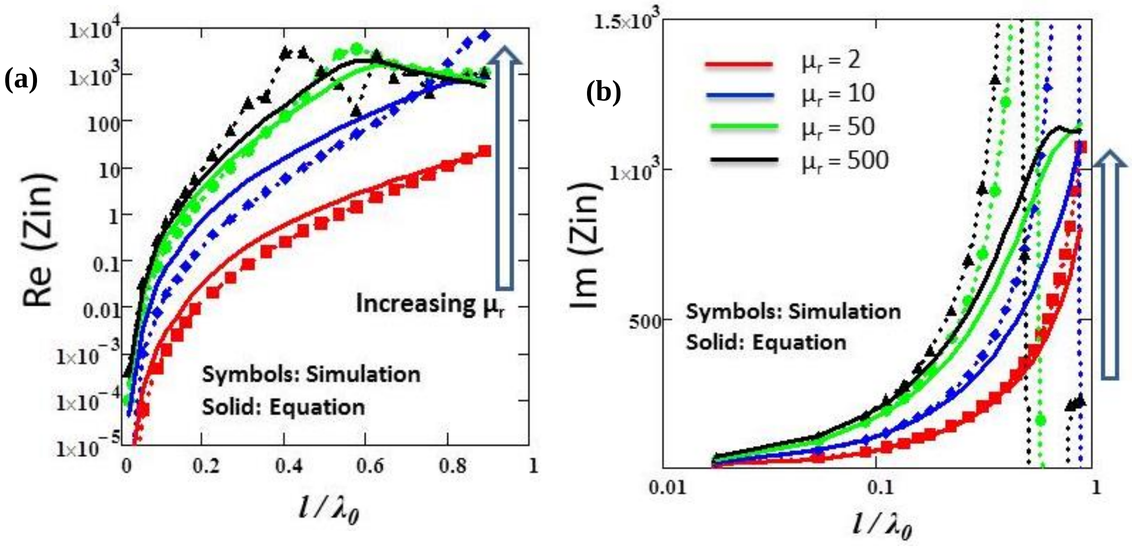

Fig. 6-12 Input impedance comparison of circuit model and simulation of a 21” long, 1” radius antenna (a) Real part (b) Imaginary part of input impedance.

The imaginary part of the input impedance matches well in the electrically small limit (antenna $\sim 0.2\lambda_0$ long). The real part does not agree well even at the low end. All signs point towards the fact that our assumption of triangular current distribution is not accurate for all the values of μ_r. Let us take a closer look at the magnitude of current distribution on the antenna (Fig. 6-13).

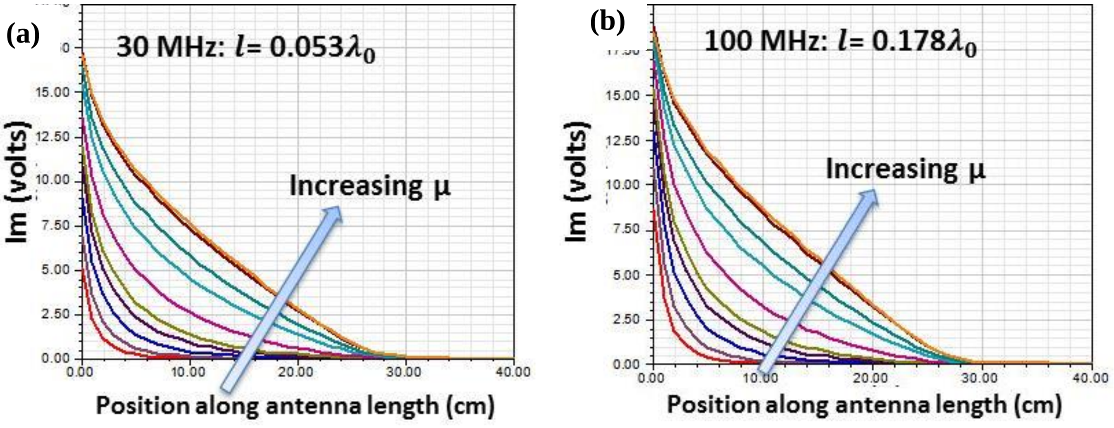

(c)

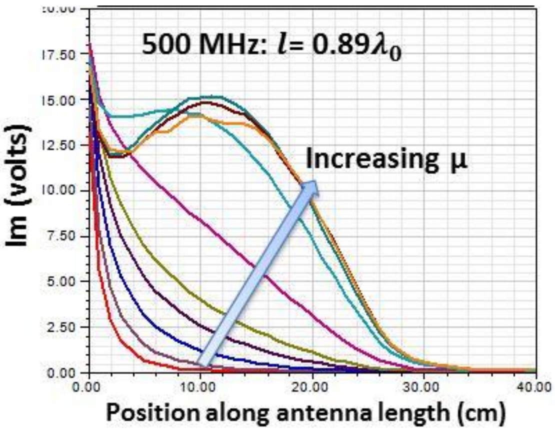

(d)

μr =

1	1.1
2	2
3	4
4	7
5	10
6	20
7	50
8	100
9	500
10	$1 \cdot 10^8$

Fig. 6-13 The magnetic current 'Im' (in volts) plotted along the length of the antenna (a) 30MHz (b) 100MHz and (c) 500MHz. (d) List of permeability μ_r simulated.

At 30MHz (Fig. 6-13(a)), for low values of permeability, the current magnitude drops extremely fast along the antenna length. The antenna is well below the TE01 mode onset frequency of the structure and hence the wave quickly leaks off the material. The antenna does not use the entire length of material available and therefore the apparent length of the antenna (effective length 'l_{eff}') is much shorter than the physical length and there is less radiation. Thus the red simulation curve of the real part of input impedance in Fig. 6-12(a) is lower than the model. As the permeability increases, the structure guides the wave longer and therefore the effective length is longer and hence the radiation resistance is higher. Note that the black curves in Fig. 6-12(a) almost match at l/λ=0.05 since the current distribution for $\mu_r = 500$ is almost triangular. Now as frequency increases, the effective length of the antenna increases faster as permeability increases and approaches the actual physical length. Thus, the current distribution is closer to being triangular and the simulation matches the model better (green curves in Fig. 6-12). But as the frequency increases even more, the structure starts guiding the wave all the way to the ends of the antenna and hence deviates further away from the triangular distribution assumption (Fig. 6-13(c)). Hence the circuit model devised in this chapter is valid for only a narrow range of combination of frequency and permeability where the distribution is close to being triangular.

6.5 Summary and Conclusions

In this chapter, we tried to come up with a simple three element (R,L and C) circuit model for an electrically small magneto-dielectric antenna. We were successful in calculating one of the three elements accurately, namely the magnetic capacitance C_m , by relating polarizability and antenna capacitance through a proportionality factor. This factor for a prolate spheroid antenna magneto-dielectric is a function of both the aspect ratio and the permeability of the material used. The prolate spheroid was analyzed as opposed a more conventional cylindrical geometry as we have a closed form equation of the polarizability of prolate spheroid. A high aspect ratio prolate spheroid is a good approximation for a cylinder. The inductance and the radiation resistance were assumed to be the dual of the electric dipole. By doing so, the current distribution on the antenna was fixed to triangular which on hindsight resulted in the final circuit model to be valid only for a narrow range of frequencies and value of permeability.

Chapter 7

INFINITELY LONG MAGNETO-DIELECTRIC CYLINDER AS A MAGNETIC RADIATOR

7.1 Introduction

In Chapters 3, 4, 5 & 6 we developed an electrically small magneto-dielectric antenna circuit model. The individual circuit elements were functions of the geometry and the magneto-dielectric material constitutes (permeability (μ_r) and permittivity (ε_r)) . We determined the radiation efficiency of the antenna and the input impedance sans the feed circuit. But the circuit model did not and cannot tell us anything about the electric and magnetic field structure inside and around the antenna object, nor did it give us any insight on the kind of wave guided by this structure. The conventional approach to tackle this problem is to solve the wave equation for the antenna structure and apply the appropriate boundary conditions. However, it is difficult to obtain the wave equation solution for a finite cylinder because of the complexities involved in matching the boundary conditions at the finite ends of the cylinder. Therefore, we will start with the 'slightly easier' problem of solving the wave equation for an infinite magneto-dielectric cylinder placed on the axis of a single electric feed loop source which will inject the desired TE-like modes into the cylinder. Depending on the frequency of operation and the radius of the cylinder, the injected TE waves either 'leaks' off the structure or is guided by it. Although such a structure is physically not realizable, the analysis gives us insight into how magneto-dielectric materials guide or partially guide the TE modes.

A material with a high enough real constitutive can provide a wave-guiding boundary, similar to conductors, as long as the modes excited in the structure is of the form of the TE (for magnetic structures) or TM (for dielectric structures) modes. If the frequency of operation is below the cut-off (or onset) frequency of the modes, the electromagnetic wave excited in the material is loosely (or poorly) guided and radiates by leaving the antenna structure or if the structure is finite, by scattering off the ends of the antenna structure in a way similar to a wave guided by a metal antenna of the same shape. The magneto-dielectric antenna, being penetrable, exhibits intrinsic frequency dependent behavior. As frequency increases the wave on the penetrable rod becomes more and more tightly bound until the onset of the TE01 and TM01 modes, when it is formally a guided wave. Clearly, once the mode is well above this onset frequency, and trapped by the material, it will not be available to be radiated by scattering off the ends of the antenna.

The purpose of this chapter is to elucidate partially guided or leaky wave and guided wave propagation in magneto-dielectric cylinders or wires. In Section 7.2, the equations for electric and magnetic fields everywhere in space is derived starting from Helmholtz vector wave equation and applying appropriate boundary conditions to arrive at the particular solution. The magnetic current (‘I_m’ in Volts) along the length of the structure is calculated by performing the circulation integral of the E-field around the rod. The magnetic current amplitude and phase plots versus length along the antenna clearly show us whether the wave is guided or is leaky at a particular frequency. Using the electric and magnetic field equations, the power radiated by this structure is calculated by integrating the complex Poynting vector over a cylindrical surface enclosing the antenna. Using this equation, in Section 7.3, given the predominantly leaky wave behavior exhibited by these antennas in their most common application (low frequencies, electrically small elements), a method to calculate the minimum length of material required to get the same amount of radiated power as that of an infinite magneto-dielectric cylinder of the same cross-section is described. This effective length calculation is a quick and easy method to design magneto-dielectric dipoles where a particular ‘dB’ radiated power design specification has to be met. Section 7.4 contains the summary of the chapter, some notable conclusions and possible future work.

7.2 Infinite Magneto-Dielectric Cylinder Wave Equation Solution

Following the paper by Islam [43], the problem is to find the field equations at an observation point in space due to a semi-infinite magnetically loaded loop antenna as shown in Fig. 7-1.

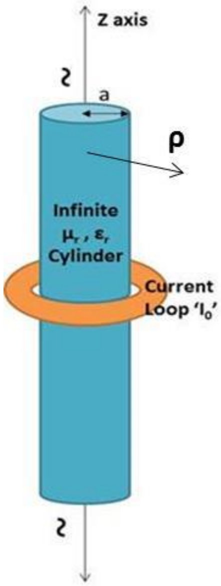

Fig. 7-1 Infinite Magneto-Dielectric cylinder of radius ‘a’

It is a homogenous and isotropic semi-infinite (along the z-axis) permeable core of radius ‘a’ coaxial with a current loop also of radius ‘a’ located at a point ‘z_0=0’ i.e. the origin on the z-axis. The approach is to solve the homogenous wave equation in terms of the vector potential ‘A’ and then apply the appropriate boundary conditions.

$$\nabla^2 A + k^2 A = 0 \tag{7-1}$$

The dimensions of the feed loop antenna itself are very small compared to the wavelength. The current ‘I’ through the loop is assumed to be uniform. The symmetry of the problem demands that we can only excite TE modes, since the source current, being I_φ, can only create a φ-directed vector potential A_φ and only φ-directed E-fields i.e. $A_\rho = A_z = 0$ and there will be no variation with φ, i.e. ∂/∂φ=0. Therefore (7-1) can be expanded as

$$\frac{\partial^2 A_\varphi}{\partial \rho^2} + \frac{1}{\rho}\frac{\partial A_\varphi}{\partial \rho} - \frac{A_\varphi}{\rho^2} + \frac{\partial^2 A_\varphi}{\partial z^2} + k^2 A_\varphi = 0 \tag{7-2}$$

Now we can employ the classic separation of variables method by letting

$A_\varphi = R(\rho)Z(z) = R * Z.$

$$\rightarrow \quad Z\frac{\partial^2 R}{\partial \rho^2} + \frac{1}{\rho}Z\frac{\partial R}{\partial \rho} - \frac{RZ}{\rho^2} + R\frac{\partial^2 Z}{\partial z^2} + k^2 RZ = 0$$

Dividing throughout by R*Z, we get

$$\frac{1}{R}\frac{\partial^2 R}{\partial \rho^2} + \frac{1}{\rho R}\frac{\partial R}{\partial \rho} + \frac{1}{Z}\frac{\partial^2 Z}{\partial z^2} + k^2 - \frac{1}{\rho^2} = 0$$

Let ‘k_z’ be the separation constant. Therefore,

$$\frac{1}{R}\frac{\partial^2 R}{\partial \rho^2} + \frac{1}{\rho R}\frac{\partial R}{\partial \rho} + k^2 - k_z^2 - \frac{1}{\rho^2} = 0\ ;$$

$$=>\ \ \rho^2\frac{\partial^2 R}{\partial \rho^2} + \rho\frac{\partial R}{\partial \rho} + \{(k^2 - k_z^2)\rho^2 - 1\}R = 0 \tag{7-3}$$

And

$$\frac{1}{Z}\frac{\partial^2 Z}{\partial z^2} = -k_z^2 \quad OR \quad \frac{\partial^2 Z}{\partial z^2} = -Zk_z^2 \tag{7-4}$$

Since there are two regions, inside the magneto-dielectric i.e. $\rho < a$ and outside i.e. $> a$, the solution can be written as

$$A_\varphi^{[1]} = C * J_1(k_{\rho 1}\rho)e^{-jk_z z} \qquad ;\ \rho \leq a \tag{7-5}$$

$$A_\varphi^{[2]} = D * H_1^{(2)}(k_{\rho 0}\rho)e^{-jk_z z} \qquad ;\ \rho \geq a \tag{7-6}$$

Where, $k_{\rho 1} = \sqrt{k_1^2 - k_z^2}$ and $k_{\rho 0} = \sqrt{k_0^2 - k_z^2}$. The $e^{-jk_z z}$ term implies a wave travelling along the +ve z-axis with a propagation constant k_z.

Here, C and D are unknown constants to be determined by applying the boundary conditions, $J_1(k_{\rho 1}\rho)$ is the Bessel function of the first kind and $H_1^{(2)}(k_{\rho 0}\rho)$ is the Hankel function of the second kind.

Since the solution extends to infinity radially i.e. there are no cylindrical boundaries that might impose restrictions on $R(\rho)$, there are correspondingly no restrictions on k_z and the solution involves integral over all k_z. Therefore,

$$A_\varphi^{[1]} = \int_{-\infty}^{\infty} C(k_z) * J_1(k_{\rho 1}\rho)e^{-jk_z z}dk_z \qquad ;\ \rho \leq a \tag{7-7}$$

$$A_\varphi^{[2]} = \int_{-\infty}^{\infty} D(k_z) * H_1^{(2)}(k_{\rho 0}\rho)e^{-jk_z z}dk_z \qquad ;\ \rho \geq a \tag{7-8}$$

Now, the two boundary conditions to be enforced at the boundary of the two regions I and II are

$$\hat{n} \times (E_{II} - E_I) = 0$$

$$\hat{n} \times (H_{II} - H_I) = the\ surface\ current\ at\ the\ boundary$$

These two equations can be rewritten in terms of the vector potential A ($\nabla \times A = B$) as

$$A_\varphi^{[2]} = A_\varphi^{[1]} \tag{7-9}$$

$$\frac{1}{\mu_0 \rho} \frac{\partial}{\partial \rho}\left(\rho A_\varphi^{[2]}\right) - \frac{1}{\mu_r} \frac{\partial}{\partial \rho}\left(\rho A_\varphi^{[1]}\right) = surface\ current\ at\ the\ boundary \tag{7-10}$$

Substituting (7-5) and (7-6) in (7-9) at $\rho = a$ we get,

$$C * J_1(k_{\rho 1} a) = D * H_1^{(2)}(k_{\rho 0} a)$$

Or

$$D = C \frac{J_1(k_{\rho 1} a)}{H_1^{(2)}(k_{\rho 0} a)} \tag{7-11}$$

Now, since the only surface current is at the feed loop located at the origin, the current can be represented by the Dirac Delta function $= I\delta(z)$. This Delta function can be expanded into an infinite set of current waves travelling along the z-axis each using the Fourier Integral theorem:

$$\delta(z) = \frac{1}{2\pi} \int_{-\infty}^{\infty} e^{-jk_z z} dk_z \tag{7-12}$$

Substituting (7-7), (7-8) and (7-12) in (7-10) and keeping in mind that the integrands alone should satisfy this condition we get,

$$\frac{1}{\mu_0 \rho} D \frac{\partial}{\partial \rho}\left(\rho H_1^{(2)}(k_{\rho 0} \rho)\right) - \frac{1}{\mu_r} C \frac{\partial}{\partial \rho}\left(\rho J_1(k_{\rho m} \rho)\right)\Big|_{\rho = a} = \frac{I}{2\pi} \tag{7-13}$$

The derivative of the Bessel or the Hankel function (let's call it $Y_1(px)$) is given by

$$Y_1'(px) = pY_0(px) - \frac{1}{x}Y_1(px)$$

Also

$$\frac{\partial}{\partial x}\big(xY_1(px)\big) = xY_1'(px) + Y_1(px) = pxY_0(px) - x\frac{1}{x}Y_1(px) - Y_1(px)$$

$$=> \qquad \frac{\partial}{\partial x}\big(xY_1(px)\big) = pxY_0(px)$$

Substituting in (7-13) we get,

$$\frac{k_{\rho 0}a}{\mu_0 a} D H_0^{(2)}\big(k_{\rho 0}a\big) - \frac{k_{\rho 1}a}{\mu a} C J_0\big(k_{\rho 1}a\big) = \frac{I}{2\pi} \tag{7-14}$$

Substituting (11) in (14) we get

$$\frac{k_{\rho 0}}{\mu_0} C \frac{J_1\big(k_{\rho 1}a\big)}{H_1^{(2)}\big(k_{\rho 0}a\big)} H_0^{(2)}\big(k_{\rho 0}a\big) - \frac{k_{\rho 1}}{\mu_0 \mu_r} C J_0\big(k_{\rho 1}a\big) = \frac{I}{2\pi}$$

Therefore, C(k$_z$) is given by

$$C(k_z) = \frac{I\mu_0}{2\pi} \frac{\mu_r H_1^{(2)}\big(k_{\rho 0}a\big)}{\mu_r k_{\rho 0} J_1\big(k_{\rho 1}a\big) H_0^{(2)}\big(k_{\rho 0}a\big) - k_{\rho 1} J_0\big(k_{\rho 1}a\big) H_1^{(2)}\big(k_{\rho 0}a\big)}$$

Or

$$C(k_z) = \frac{I\mu_0 a}{2\pi} \frac{\mu_r H_1^{(2)}\big(k_{\rho 0}a\big)}{\mu_r \big(k_{\rho 0}a\big) J_1\big(k_{\rho 1}a\big) H_0^{(2)}\big(k_{\rho 0}a\big) - \big(k_{\rho 1}a\big) J_0\big(k_{\rho 1}a\big) H_1^{(2)}\big(k_{\rho 0}a\big)} \tag{7-15}$$

And

$$D(k_z) = \frac{I\mu_0 a}{2\pi} \frac{\mu_r J_1\big(k_{\rho m}a\big)}{\mu_r \big(k_{\rho 0}a\big) J_1\big(k_{\rho 1}a\big) H_0^{(2)}\big(k_{\rho 0}a\big) - \big(k_{\rho 1}a\big) J_0\big(k_{\rho 1}a\big) H_1^{(2)}\big(k_{\rho 0}a\big)} \tag{7-16}$$

Substituting (7-15)and (7-16)in (7-7) and (7-8) we get

$$A_{\varphi}^{[1]} = \frac{I\mu_0 a}{2\pi}\int_{-\infty}^{\infty}\frac{\mu_r H_1^{(2)}\left(k_{\rho 0}a\right)J_1\left(k_{\rho 1}\rho\right)e^{-jk_z z} \quad dk_z}{\mu_r\left(k_{\rho 0}a\right)J_1\left(k_{\rho 1}a\right)H_0^{(2)}\left(k_{\rho 0}a\right) - \left(k_{\rho 1}a\right)J_0\left(k_{\rho 1}a\right)H_1^{(2)}\left(k_{\rho 0}a\right)} \tag{7-17}$$

$$, for\ \rho \leq a$$

$$A_{\varphi}^{[2]} = \frac{I\mu_0 a}{2\pi}\int_{-\infty}^{\infty}\frac{\mu_r J_1\left(k_{\rho 1}a\right)H_1^{(2)}\left(k_{\rho 0}\rho\right)e^{-jk_z z} \quad dk_z}{\mu_r\left(k_{\rho 0}a\right)J_1\left(k_{\rho 1}a\right)H_0^{(2)}\left(k_{\rho 0}a\right) - \left(k_{\rho 1}a\right)J_0\left(k_{\rho 1}a\right)H_1^{(2)}\left(k_{\rho 0}a\right)} \tag{7-18}$$

$$;\ for\ \ \rho \geq a$$

Now the individual field components can be derived using $E = -j\omega A$ and $H = \frac{1}{\mu}\nabla \times A$. Therefore, using the two equations above we get the E and H fields in the two regions as:

For $\rho < a$ (inside the magneto-dielectric)

$$E_{\varphi}^{[1]} = \frac{-j\omega I\mu_0 a}{2\pi}\int_{-\infty}^{\infty}\frac{\mu_r H_1^{(2)}\left(k_{\rho 0}a\right)J_1\left(k_{\rho 1}\rho\right)e^{-jk_z z} \quad dk_z}{\mu_r\left(k_{\rho 0}a\right)J_1\left(k_{\rho 1}a\right)H_0^{(2)}\left(k_{\rho 0}a\right) - \left(k_{\rho 1}a\right)J_0\left(k_{\rho 1}a\right)H_1^{(2)}\left(k_{\rho 0}a\right)} \tag{7-19}$$

And

$$H_{z}^{[1]} = \frac{I\mu_0 a}{\mu_r\mu_0 2\pi}\int_{-\infty}^{\infty}\frac{\mu_r k_{\rho 1} H_1^{(2)}\left(k_{\rho 0}a\right)J_0\left(k_{\rho 1}\rho\right)e^{-jk_z z} \quad dk_z}{\mu_r\left(k_{\rho 0}a\right)J_1\left(k_{\rho 1}a\right)H_0^{(2)}\left(k_{\rho 0}a\right) - \left(k_{\rho 1}a\right)J_0\left(k_{\rho 1}a\right)H_1^{(2)}\left(k_{\rho 0}a\right)} \tag{7-20}$$

And

$$H_{r}^{[1]} = \frac{jI\mu_0 a}{\mu_r\mu_0 2\pi}\int_{-\infty}^{\infty}\frac{\mu_r k_z H_1^{(2)}\left(k_{\rho 0}a\right)J_1\left(k_{\rho 1}\rho\right)e^{-jk_z z} \quad dk_z}{\mu_r\left(k_{\rho 0}a\right)J_1\left(k_{\rho 1}a\right)H_0^{(2)}\left(k_{\rho 0}a\right) - \left(k_{\rho 1}a\right)J_0\left(k_{\rho 1}a\right)H_1^{(2)}\left(k_{\rho 0}a\right)} \tag{7-21}$$

For $\rho > a$,

$$E_\varphi^{[2]} \tag{7-22}$$

$$= \frac{-j\omega I\mu_0 a}{2\pi}\int_{-\infty}^{\infty}\frac{\mu_r J_1(k_{\rho 1}a)H_1^{(2)}(k_{\rho 0}\rho)e^{-jk_z z}\quad dk_z}{\mu_r(k_{\rho 0}a)J_1(k_{\rho 1}a)H_0^{(2)}(k_{\rho 0}a)-(k_{\rho 1}a)J_0(k_{\rho 1}a)H_1^{(2)}(k_{\rho 0}a)}$$

And

$$H_z^{[2]} = \frac{Ia}{2\pi}\int_{-\infty}^{\infty}\frac{\mu_r k_{\rho 0}J_1(k_{\rho 1}a)H_0^{(2)}(k_{\rho 0}\rho)e^{-jk_z z}\quad dk_z}{\mu_r(k_{\rho 0}a)J_1(k_{\rho 1}a)H_0^{(2)}(k_{\rho 0}a)-(k_{\rho 1}a)J_0(k_{\rho 1}a)H_1^{(2)}(k_{\rho 0}a)} \tag{7-23}$$

And

$$H_\varphi^{[2]} = \frac{Ia}{2\pi}\int_{-\infty}^{\infty}\frac{\mu_r k_z J_1(k_{\rho 1}a)H_1^{(2)}(k_{\rho 0}\rho)e^{-jk_z z}\quad dk_z}{\mu_r(k_{\rho 0}a)J_1(k_{\rho 1}a)H_0^{(2)}(k_{\rho 0}a)-(k_{\rho 1}a)J_0(k_{\rho 1}a)H_1^{(2)}(k_{\rho 0}a)} \tag{7-24}$$

Upon some manipulations we note that all fields have in common the following term in the denominator:

$$\left\{1-\frac{k_{\rho 1}\mu_0}{k_{\rho 0}\mu_1}\frac{H_1^{(2)}(k_{\rho 0}a)J_0(k_{\rho 1}a)}{H_0^{(2)}(k_{\rho 0}a)J_1(k_{\rho 1}a)}\right\}$$

When this is zero we have a pole. Rearranging the terms:

$$H_0^{(2)}(k_{\rho 0}a)J_1(k_{\rho 1}a)\frac{\mu_r}{k_{\rho 1}} = \frac{1}{k_{\rho 0}}H_1^{(2)}(k_{\rho 0}a)J_0(k_{\rho 1}a)$$

We recognize this as precisely the transcendental equation for the propagation constant of the TE01 mode in a permeable rod. Thus during the calculation of the spatial fields we will have to deal with these surface wave poles. These poles can only arise in the range:

$$k_0 < k_z < k_1$$

Because in this range, $k_{\rho 0} = \sqrt{k_0^2 - k_z^2} = -jk_0\sqrt{k_z^2 - k_0^2}$; $k_{\rho 0}$ is a negative imaginary number while $k_{\rho 1} = \sqrt{k_1^2 - k_z^2}$ is a positive number. Now since:

$$K_0(x) = -j\frac{\pi}{2}H_0^{(2)}(-jx)\,;\; K_1(x) = -\frac{\pi}{2}H_1^{(2)}(-jx)\,;$$

The quantity

$$\frac{H_1^{(2)}(-jx)}{H_0^{(2)}(-jx)} = -j\frac{K_1(x)}{K_0(x)}$$

is known as the logarithmic derivative of $K_0(x)$ and is well behaved. In fact, the quantity

$$\frac{1}{(-jx)}\frac{H_1^{(2)}(-jx)}{H_0^{(2)}(-jx)}$$

is purely real and negative while in the same range the quantity

$$\left\{\frac{(k_{\rho 1}a)J_0(k_{\rho 1}a)}{J_1(k_{\rho 1}a)}\right\}$$

is also purely real, so only in this range can the denominator vanish. Said another way: we know guided slow waves travel slower than free space but no slower than the rod medium, therefore it is only in this range between k_0 and k_1 that the k_z spectrum waves can match in speed the slow wave modes and it is then that they can couple strongly to them.

When we are concerned with the onset of surface waves as a function of frequency in the source-less solution of the penetrable rod, this onset is controlled by the argument of the Bessel functions $k_m a$. In the case of the spectrum excited by the current band, this onset is a function of $k_\rho$in the rod medium; and k_ρ is at its largest, namely equal to k_m, at the horizon when k_z approaches k_0:

$$k_{\rho 1} = \sqrt{k_1^2 - k_0^2} \approx k_1$$

Therefore, if the rod is internally electrically large enough to trap the wave, this pole will first appear in the spectrum at the horizon.

Now we are interested in the current wave (guided displacement current dB/dt wave). We obtain this by integrating the circulating E-field at the surface of the rod:

$$\oint \vec{E} \cdot \overrightarrow{dl} = \int -\frac{\partial \vec{B}}{\partial t} \cdot d\vec{S} = I_m = 2\pi a E_{\varphi}^{[2]}$$

$$I_m(z) = -j\omega\mu_0 a^2 I_0 \int_{-\infty}^{+\infty} \frac{\mu_r J_1(k_{\rho 1}a) H_1^{(2)}(k_{\rho 0}a) e^{-jk_z z} \quad dk_z}{\mu_r (k_{\rho 0}a) J_1(k_{\rho 1}a) H_0^{(2)}(k_{\rho 0}a) - (k_{\rho 1}a) J_0(k_{\rho 1}a) H_1^{(2)}(k_{\rho 0}a)} \tag{7-25}$$

the magnetic current is in Volts.

To perform the integration numerically, we deform the integration path in the vicinity of the surface wave poles. Fig. 7-2 shows the amplitude (a) and phase(b) of the current wave from 30MHz to 170MHz every 20MHz versus distance in wavelengths for a permeable rod of $\mu_r = 80$, $\epsilon_r = 2$ and radius a = 2 inches. Fig. 7-2(c) shows the structure of the mode inside the permeable rod (Plot of the E_φ field). In Fig. 7-2(a), it is clear that for frequencies far below cutoff the current is not guided at all and we see a precipitous drop in amplitude. Therefore, far below cutoff the noise in the calculation makes determination of the phase velocity ambiguous for the black and gray curves in Fig. 7-2 (b) (30MHz and 50MHz). Nevertheless it is clear that they start below the light line and then all we see above one wavelength is noise. Above 70MHz the phase plots are well behaved and we clearly see fast wave behavior with phase velocities that approach the light line (31.4^{c} over 5 wavelengths) at 170MHz.The amplitude and phase plots show that as 170MHz is approached, the approaching surface wave onset tends to flatten the amplitude of the current wave and brings its speed close to light, thus the magneto-dielectric rod behaves more and more like a Perfect Magnetic Conductor antenna.

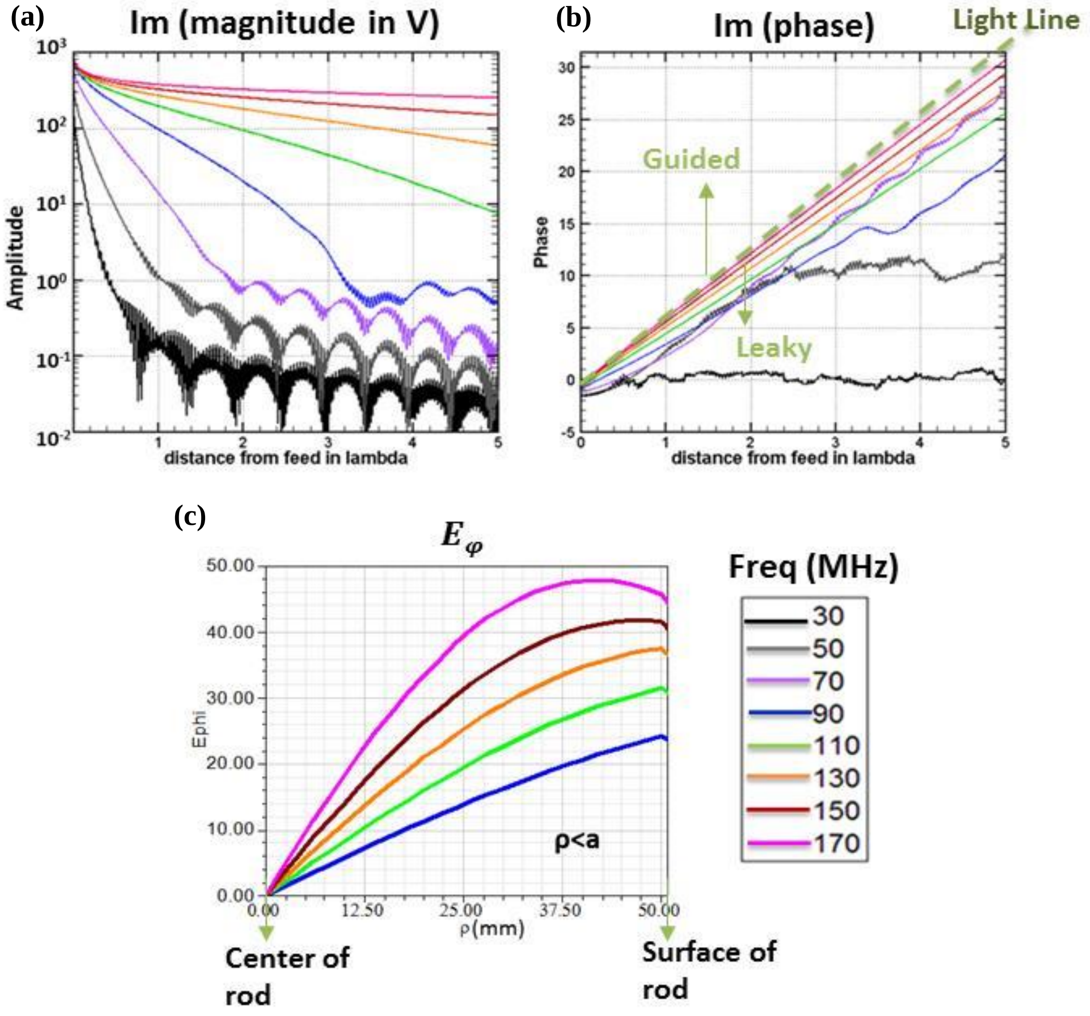

Fig. 7-2 Amplitude (a),Phase (b) as a function of distance from the feed for a 2” radius $\mu_r = 80$, $\varepsilon_r = 2$ rod from 30MHz to 170MHz (c) Mode Structure (E_φ)

Fig. 7-3show the results from 190MHz to 330MHz every 20MHz again plotted versus distance from the feed in wavelengths. We are now in the region of the guided TE01 mode.

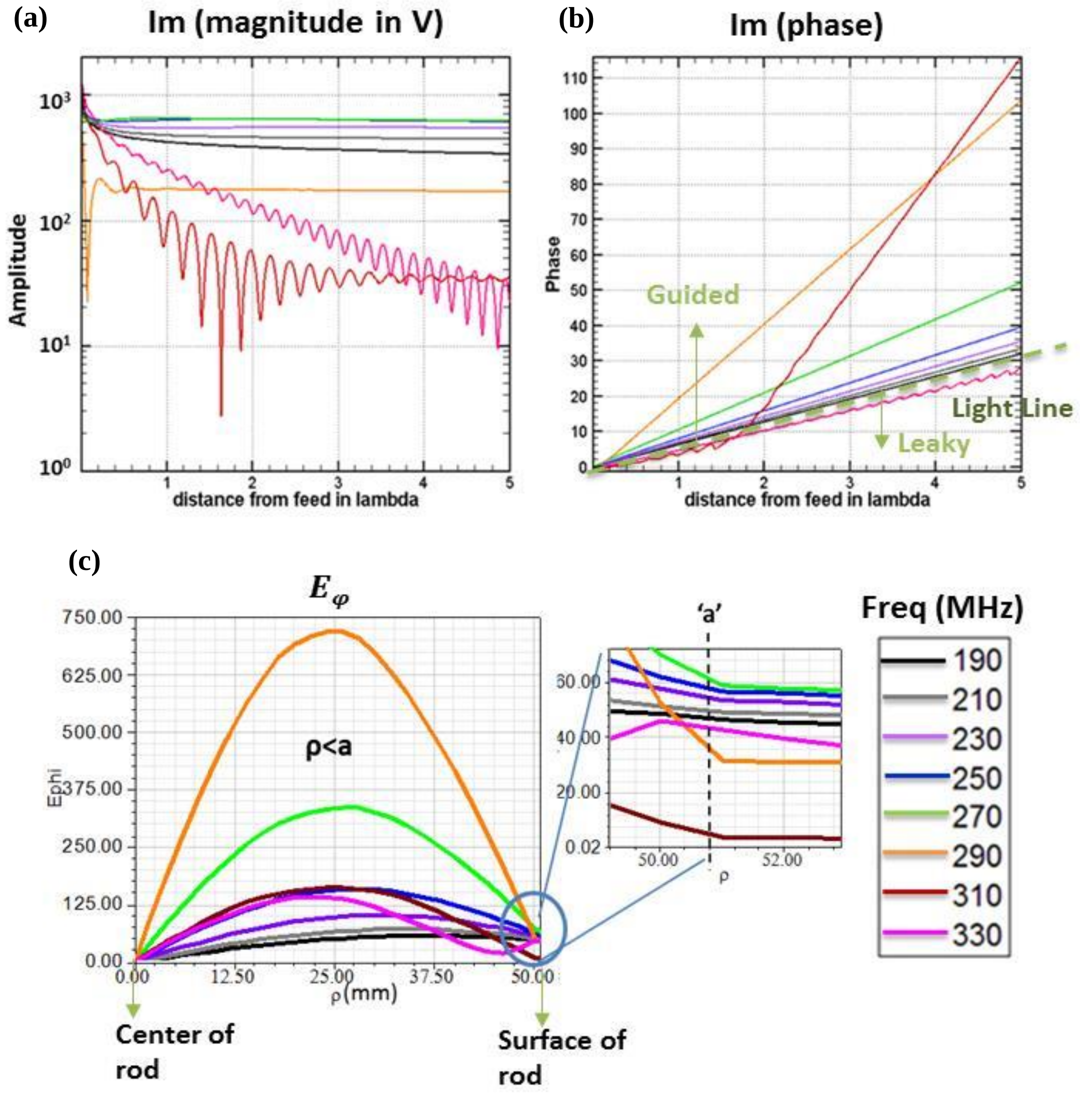

Fig. 7-3 Amplitude (a),Phase (b) as a function of distance from the feed for a 2” radius $\mu_r = 80$, $\varepsilon_r = 2$ rod from 190MHz to 330MHz (c) Mode Structure (E_φ)

At 190MHz, just above onset of the guided wave shows amplitude behavior very much like a PMC rod ($log(1/|z|)$). It also shows a phase velocity very close to that of light. As the frequency continues to increase the current becomes more uniform indicating a better guided wave with the accompanying phase velocity becoming slower than light (slope of phase lines greater than the light line). From 250MHz to 270MHz the wave slows down even more and the amplitude, though flat is stationary. There is a sudden change between 270MHz and 290 MHz and this corresponds to the frequency above which the surface wave pole starts losing strength (In Fig. 7-3(c), the magnitude of E_φ drops from 270MHz to 290MHz). The wave becomes very slow and the amplitude of the current drops dramatically. This behavior is a result of exciting the rod at the surface. As the wave becomes more and more trapped its energy migrates to the interior of the rod i.e E_φ increases inside the rod (Fig. 7-3(c)) and its surface field drops (E_φ at ρ=a), reducing the reaction between the electric field and the exciting current.

Thus above this frequency the TE01 mode becomes increasingly hard to excite and the next mode, the TE02 is beginning to appear. As a result the excited current wave reverts to the rapidly attenuated fast wave (310MHz), with a plateau far from the feed. The phase curve reveals that this plateau is a very slow wave, probably the last time we can excite the TE01 mode from the surface of the rod. At 330MHz, the TE01 mode is out of reach and the TE02 has not hit onset and thus we are back to the leaky current mode (magenta curve) traveling just faster than light.

Fig. 7-4 shows the same plots from 350MHz to 490MHz. Around 410 MHz (the TE02 cutoff frequency) the amplitude becomes much like a PMC antenna and the phase velocity crosses the light line. Above that frequency the wave continues to become better bound again, this time as TE02 (Fig. 7-4 (c)), in complete analogy to what we saw above already.

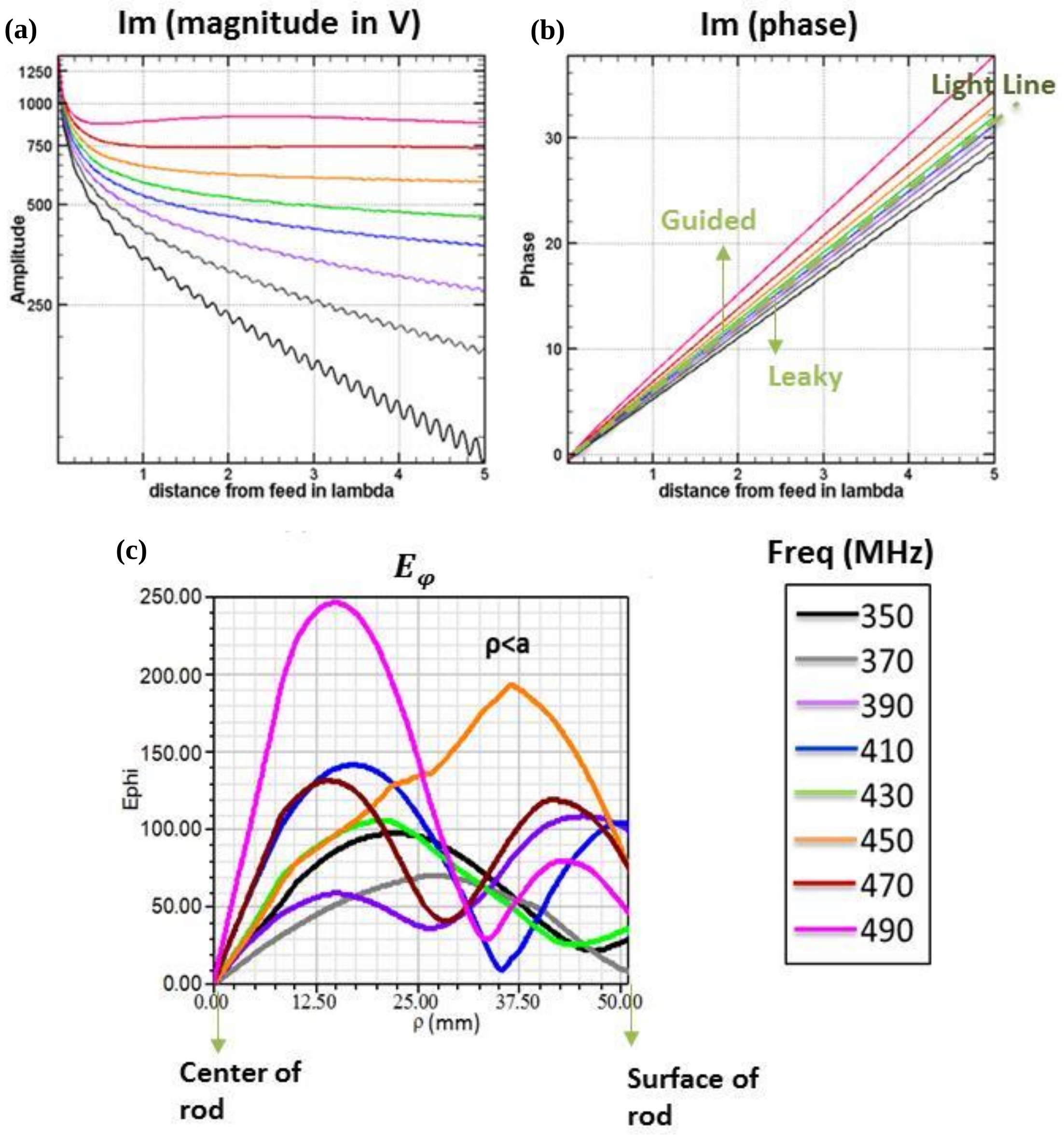

Fig. 7-4 Amplitude (a),Phase (b) as a function of distance from the feed for a 2” radius $\mu_r = 80$, $\varepsilon_r = 2$ rod from 350MHz to 490MHz (c) Mode Structure (E_φ)

Fig. 7-5 below shows the Radiated power (Prad) versus frequency. Prad is calculated by integrating the complex Poynting vector over a cylindrical surface enclosing the antenna. The red lines indicate the cut-off frequencies of the TE0n modes.

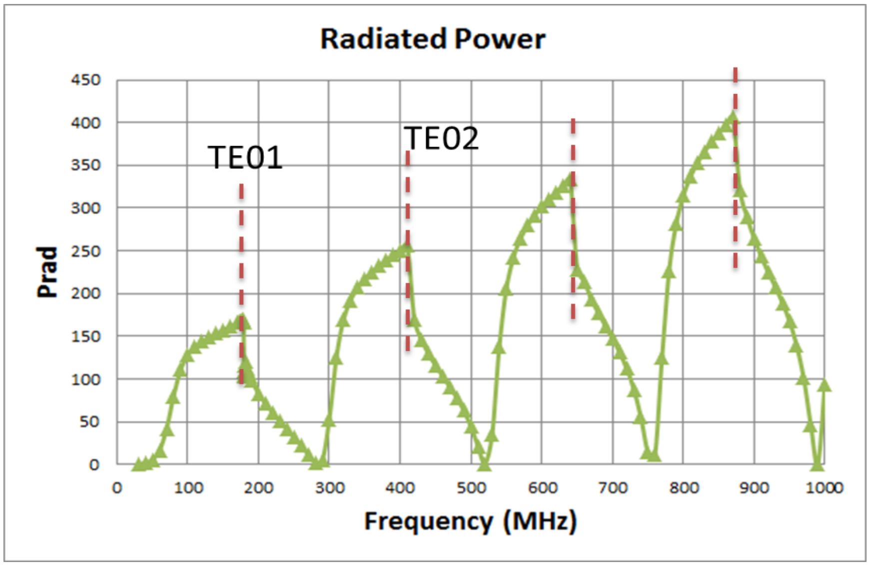

Fig. 7-5 Radiated Power (Prad) vs Frequency(MHz) for a 2” radius $\mu_r = 80$, $\varepsilon_r = 2$ rod

The Radiated power and hence the Radiation Resistance drops right after every TE0n cutoff as the mode is well guided. Prad continues to drop until the loop feed starts exciting the next higher order mode.

7.3 Effective Length for a Finite Magneto-dielectric Dipole Based on the Radiated Power of an Infinite Magneto-dielectric cylinder

We know that the magneto-dielectric antenna radiates by leaking off energy off its structure. In Section 7.3, we calculated the magnetic current distribution of an infinite cylindrical antenna. Since we can’t make an infinite structure can we design a realistic finite magneto-dielectric antenna using what we have learned so far?

Let us start by looking at the current distribution at a fixed frequency for different values of permeability μ_r. A fixed radius (a=3cm) infinite magneto-dielectric rod was simulated and the permeability varied from $\mu_r = 40$ to 160 (permittivity $\varepsilon_r = 1$). The frequency was fixed to 100MHz which is well below the TE01 mode cut-off frequency for even the highest μ_r considered ($\mu_r = 160, f_{cutoff} = 303\ MHz$). The magnetic current I_m is shown below in Fig. 7-6.

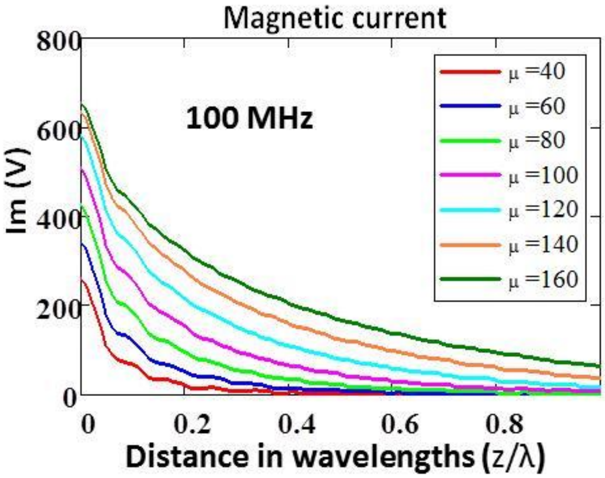

Fig. 7-6 Magnetic current (I_m) of a semi-infinite cylindrical magento-dielectric antenna (a = 3cm) vs antenna length measured from the feed loop.

The ripples seen in the results are due to the numerical noise when solving the equations from Section 7.2. The magnetic current shows an exponential tail (leaky wave behavior) away from the feed, however, close to it we can clearly see a logarithmic drop in magnitude (ln(1/L)).

Now, a closer look at the current curves shows that it is possible to fit the exponential tail of the magnetic current with a single exponential term (dashed black curves in Fig. 7-7).

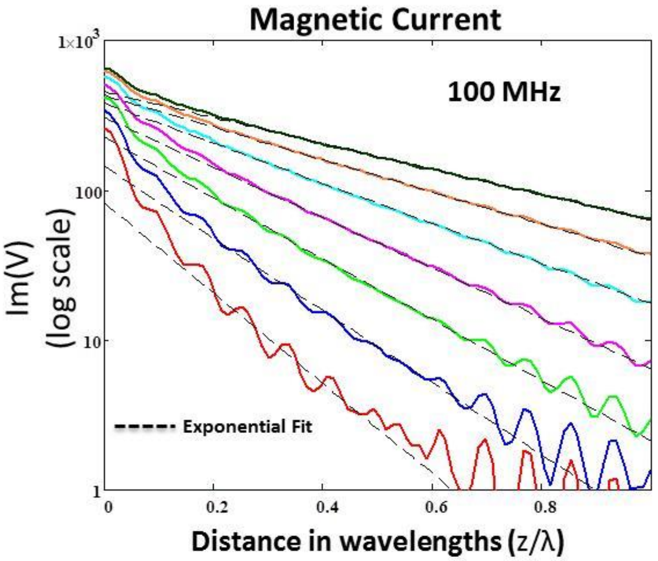

Fig. 7-7 Magnetic current (I_m) of a semi-infinite magneto-dielectric antenna fit to an exponential (dashed black curves).

If we now subtract these exponential fits from the magnetic current, I_m, we get the following curves for different values of μ_r (Fig. 7-8).

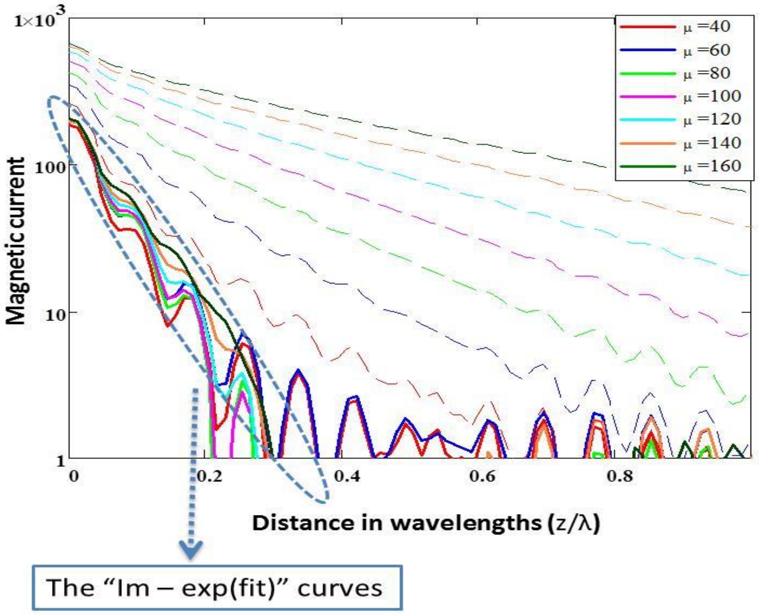

Fig. 7-8 'I_m' and 'I_m – exp(fit)' current curves for different μ_r vs antenna length.

Fig. 7-8 shows that the magnetic current I_m of a semi-infinite magneto-dielectric antenna is the sum of a constant perturbation current (Im-exp(fit) curves in Fig. 7-8) and an exponential leaky wave current of the TE01 mode below its cutoff. The constant perturbation current is due to all the higher order modes that are extremely leaky that can get coupled into the magneto-dielectric material.

Now if we ask the question at what length should we truncate the antenna so that we can get as much radiated power as possible? For an exponential current distribution it is natural to choose the 1/e point as my effective length (L_{eff}). Table 7-1 lists L_{eff} for different μ_r.

μ_r	**Leff (in)**	**Leff (cm)**
40	17.02	43.18
60	21.29	54.07
80	25.55	64.9
100	30.46	77.36
120	38.32	97.33
140	47.57	120.84

Table 7-1 L_{eff} values for different μ_r

Now let us see how well did we do in choosing the length by comparing the radiated power of the finite dipole of length = 2 L_{eff} (Fig. 7-9) with that of an infinite dipole of same cross-section and permeability.

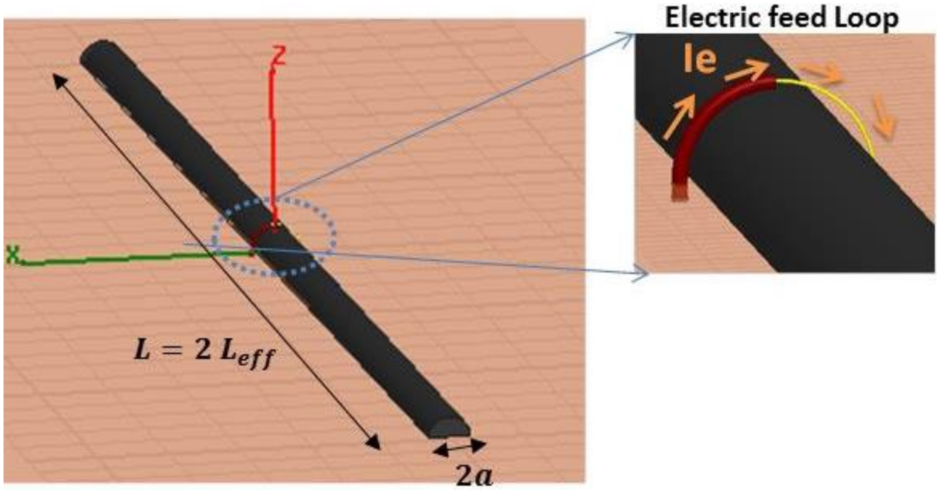

Fig. 7-9 Finite cylindrical magneto-dielectric rod with circular feed loop.

As shown in Fig. 7-9, the outer conductor of the coaxial feed of the circular loop is extended out of the ground plane all the way to the center of the loop. This removes the asymmetry of the loop and maintains the unidirectional electric current flow. Fig. 7-10 shows the electric current in the feed loop for this new configuration.

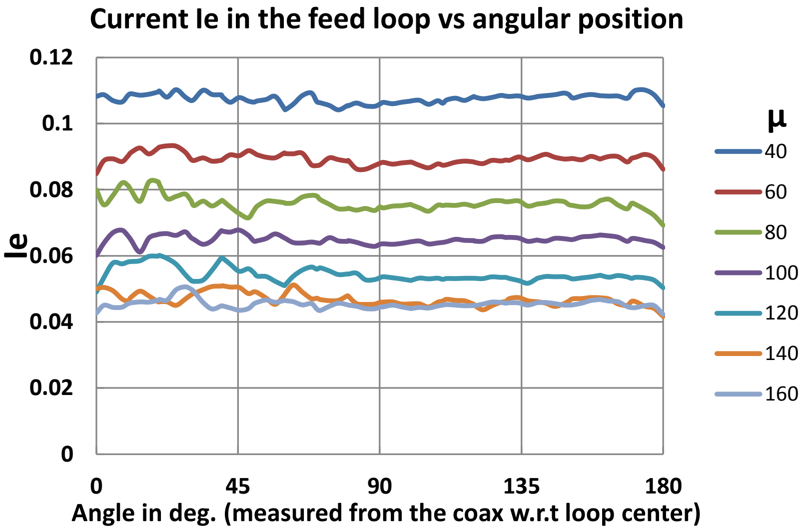

Fig. 7-10 Electric Current ‘I_e’ in the feed loop vs angular position for different μ_r.

The circular loop has a uniform constant current distribution. Now we compare the analytical Prad of an infinite magneto-dielectric cylinder with the simulated Prad of a finite magneto-dielectric cylindrical dipole over ground vs μ_r (Fig. 7-11).

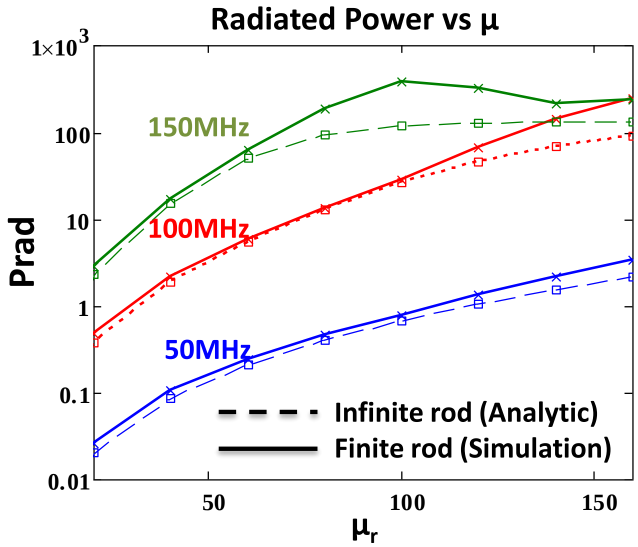

Fig. 7-11 Radiated Power vs μ_r (Analytic: Infinite rod versus Simulated Finite cylindrical rod)

The L_{eff} simulated was calculated from f=100MHz magnetic current curves. The length was kept the same for the other two frequencies. If we consider just the f=100MHz case, the analytic and simulation results match fairly well for small ‘μ’. As the value of ‘μ_r’ goes up, we keep getting closer and closer to the guided domain i.e. the waves are better guided by the PC rod. Hence, we can see that there is a deviation between analytic and simulated results for higher μ_r due to the fact that in the case of the finite rod there is an additional radiation effect from the end discontinuities. Therefore, we get a higher Prad in our finite rod simulations. In the 50MHz case, Prad is higher because we have started with a longer L_{eff} than what would be required, as the 100MHz L_{eff} was chosen.

So far, a finite magneto-dielectric antenna with different permeability at a fixed frequency was analyzed. In Fig. 7-11, the simulation and calculations at 50MHz and 150MHz were done using the effective length values obtained from the 100MHz case. Therefore, in order to prove the validity of the method conclusively, the above approach was now repeated for a single value of μ_r (=60) analyzed at different frequencies. Since we are interested in the leaky domain operation of these antennas; for 3cm magneto-dielectric cylinder as before, 50MHz to 400MHz is the frequency range considered as the TE01 mode cutoff frequency for these values is 500MHz. Fig. 7-12 shows the Prad curves obtained analytically and from simulation along with the plot of the effective length calculated from the procedure outlined above w.r.t frequency.

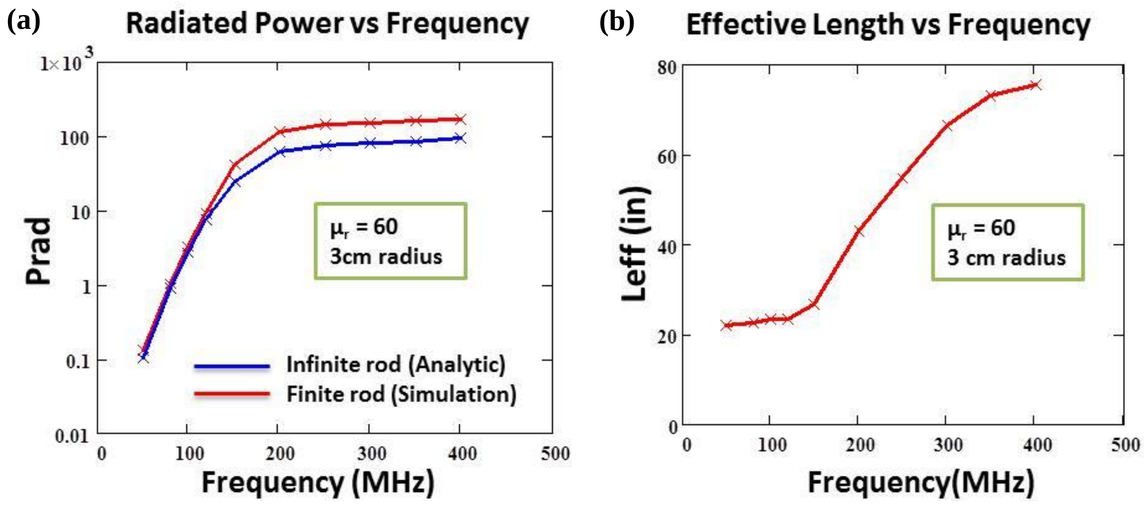

Fig. 7-12 a) Radiated power, (b) Effective (Half) Length of Finite 3cm radius magneto-dielecric cylinder vs Frequency for $\mu_r = 60$

Fig. 7-12(a) shows that the Prad curves has the same behavior as the case where different μ's were analyzed. At low frequency, the analytic and simulated curves are on top of each other. As the frequency increases, the magneto-dielctric cylinder starts guiding the wave longer along its axis resulting in a stronger radiation from the two end discontinuities. Thus, we see around a factor of two increase in radiated power at higher frequencies close to cut-off.

Similar analysis was done for two other magneto-dielectric cross-sections. The results are shown below in Fig. 7-13. For a 0.75cm radius magneto-dielectric cylinder, the TE01 cut-off frequency for $\mu_r = 60$ is 2GHz and for a 6cm radius magneto-dielectric cylinder, the TE01 cut-off frequency is 249MHz.

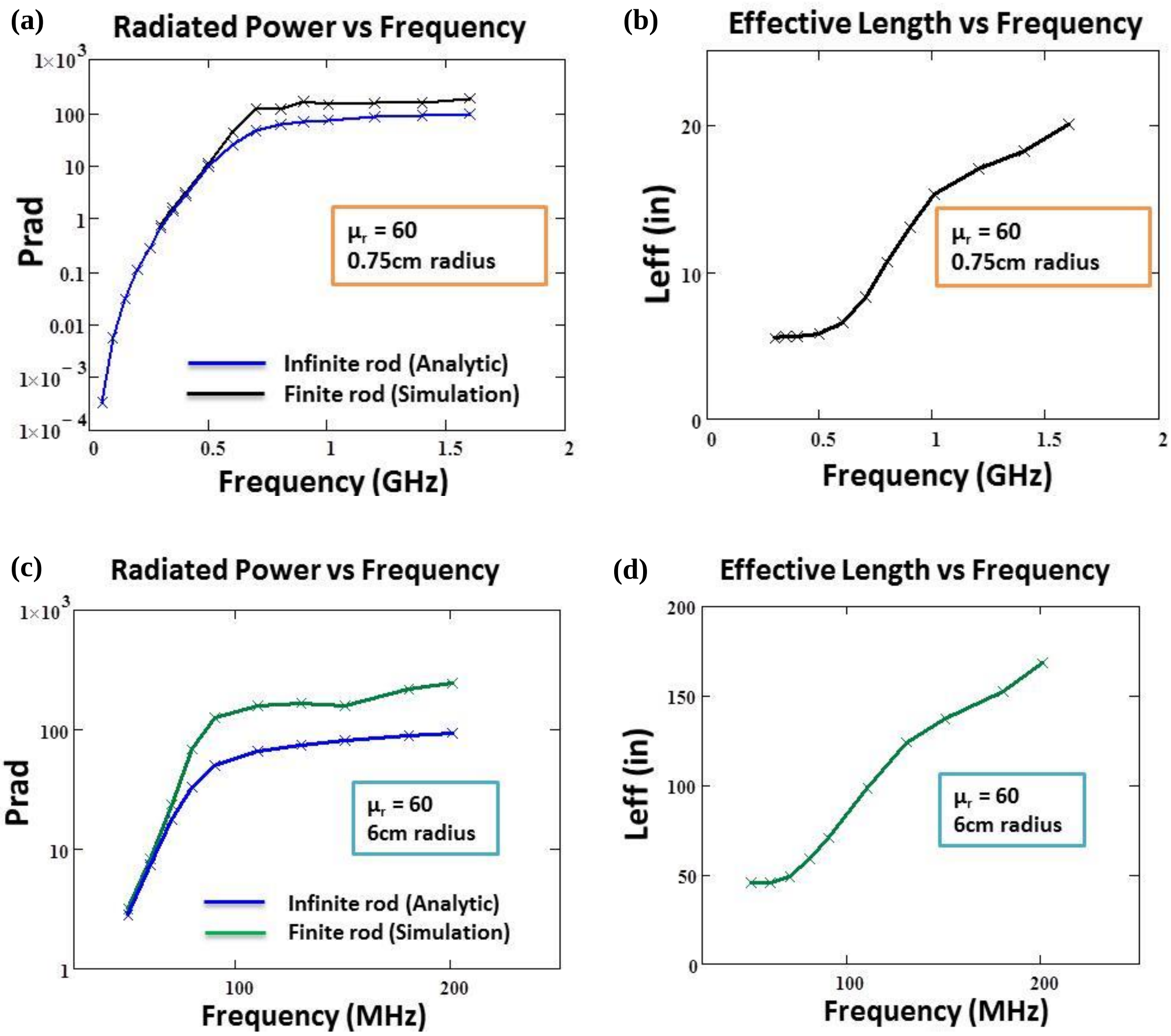

Fig. 7-13 a) Radiated power, (b) Effective (Half) Length of finite 0.75cm radius magneto-dielectric cylinder vs Frequency and (c) Radiated power, (d) Effective (Half) Length of finite 6cm radius magneto-dielectric cylinder vs Frequency.

The Prad curves in these two cases behave the same as Fig. 7-12. The radiated power is same as the analytic case at lower frequencies and deviates to about twice the amount as cut-off frequency is approached due to increase in radiation from the ends of the finite magneto-dielectric antenna. The three curves can be put together and plotted w.r.t k_0 $(= \omega/c_0)$ times the radius 'a' of the cylinder as shown below in Fig. 7-14. $k_0 a = 0.31$ is the cut-off value of the TE01 mode.

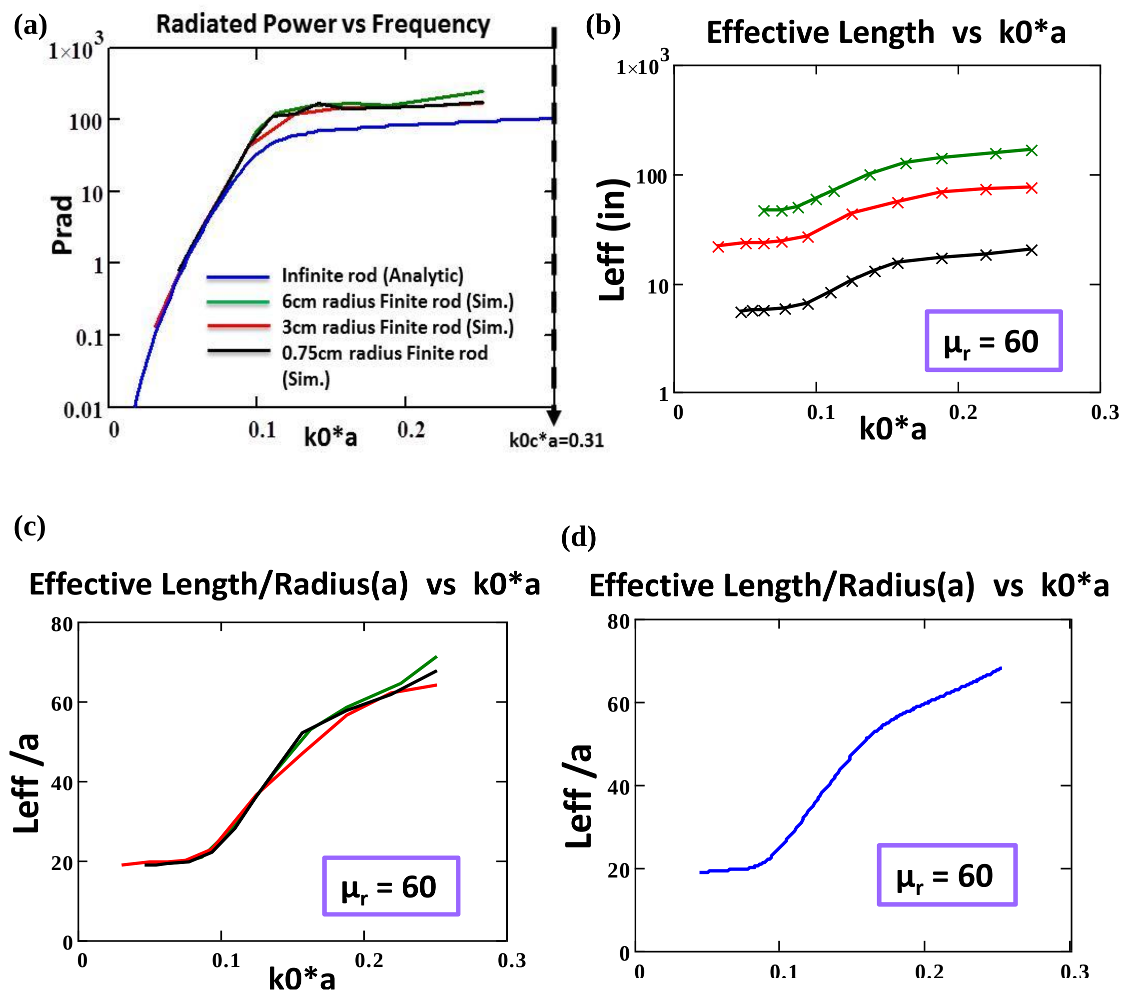

Fig. 7-14 (a) Radiated power, (b) Effective (Half) Length (c) Effective (Half) Length / Radius of a magneto-dielectric Antenna versus k0*a for a permeability $\mu_r = 60$ (d) Average of the three curves in (c)

Fig. 7-14 (a) shows that the three Simulated ‘Prad’ curves lie on top of each other when plotted w.r.t k_0a. Similarly, the effective length curves of the finite magneto-dielectric antenna when normalized by the cross-section of the antennas lie on top of each other. Therefore, we have reduced our complete analysis to a single curve (Fig. 7-14(c)), i.e. given a magneto-dielectric materials permeability we can find the effective length of a finite magneto-dielectric antenna for any cross-section that gives the same amount of radiated power as an infinite magneto-dielectric rod at low frequency ($k_0a < 0.09$ for $\mu_r = 60$) and about twice the amount of power as we approach the TE01 cut-off frequency ($0.09 < k_0a < 0.3$).

7.4. Summary, Conclusions and Future Work

The green function problem of the cylindrical permeable rod excited by a electric current loop was presented in this chapter. The current wave in a magneto-dielectric infinite rod is shown to go through a succession of fast wave-slow wave transitions. Below the first mode and in between modes the fast wave regions exhibit leaky wave behavior with decaying amplitude and waves travelling faster than speed of light. Every time we approach the onset of guidance of a mode, there is a band of frequencies over which the magneto-dielectric rod behaves very much like a PMC metal rod. Then as the mode gets more trapped the magnetic current and the radiated power eventually drop because this magnetic current cannot be excited from the surface. Eventually, as frequency increases, the mode reverts to a fast wave leaky mode that corresponds to the next higher order mode.

The exponential decay of the current during the leaky wave periods reduces the effective electrical length of the antenna. This reduced aperture size contributes to the lower gain bandwidth product when compared to a similarly sized metal dipole in free space.

We also established a method to estimate the minimum length required for a magneto-dielectric antenna to give the same (or slightly greater) radiated power than an infinite length magneto-dielectric rod of the same cross-section and permeability when operating in the leaky domain. It is first shown that this length is directly proportional to the value of permeability of the rod for a fixed frequency and radius of the rod. When analyzed w.r.t frequency for a single permeability of $\mu_r = 60$, it was observed that the effective length is a function of frequency as well. Finally, the complete analysis versus frequency was reduced to a single curve of 'Effective length/a versus $k_0 a$' (Figure 2.14) from which it is possible to determine the effective length required to radiate more power than an infinite μ_r=60 magneto-dielectric rod for a given cross-section. In the future, this analysis can be repeated for different μ's to obtain a family of effective length curves.

So far we have discussed the case of loading a loop antenna with a cylinder of infinite length. Since an infinite cylinder is never realizable in reality, the next step in our effort to understand a pragmatic antenna is to obtain a rigorous model of a finite magneto-dielectric antenna. Because of the complexities involved in the analysis of the ends of a finite cylindrical magneto-dielectric rod we will assume a prolate spheroidal shape antenna. A long and thin prolate spheroid is a good approximation to a finite cylinder. We propose to solve this problem in a similar way as the infinite case, by solving the inhomogeneous wave equation using the appropriate boundary condition, however, this time due to the spheroidal geometry, a spheroidal coordinate system will be used. This analysis is done in Chapter 5.

The most useful application of magneto-dielectric dipoles is in conformal antenna applications where it is placed tangential to a metallic ground plane. There are cases, where even this might be unacceptable for example on a UAV where any protrusion would increase the drag force and increase fuel consumption. Thus ideally we want to an antenna which can be buried in the ground plane. The use of permeable materials does enable us to do so. The magneto-dielectric antenna can be buried inside a metallic trough in the ground plane and thus be truly conformal. The analysis of such a trough structure is planned for the future.

Chapter 8

FINITE MAGNETO-DIELECTRIC PROLATE SPHEROIDAL ANTENNA ANALYSIS

8.1 Introduction

In Chapter 7, we analyzed an infinite magneto-dielectric cylinder and saw the guided and partially guided (leaky) wave propagation along the structure as a function of frequency and material properties. The infinite magneto-dielectric cylinder antenna problem was first tackled because the solution of the wave equation for a finite cylinder is not trivial due of the finite ends of the cylinder. Another workaround for that problem is to assume that the finite magneto-dielectric cylinder wire antenna to be analyzed is thin enough and long enough to be approximated by a large aspect prolate spheroid. The same argument was used in Chapter 6, where the cylindrical magneto-dielectric dipole was assumed to be a prolate spheroid since the polarizability has a closed form solution. Therefore, in this chapter we examine a finite magneto-dielectric prolate spheroid antenna which is analyzed by solving the wave equation and applying the appropriate boundary conditions in the prolate spheroidal coordinate system.

A large aspect ratio (AR=major axis/minor axis) prolate mimics a long slender cylindrical dipole. Under quasi-static assumptions, the wave equation solution of a magneto-dielectric prolate spheroidal antenna fed by a single loop was analyzed by Islam [44]. In the last decade, using similar quasi-static assumptions, Simpson et al. analyzed solenoid fed prolate spheroidal [45] and hollow prolate spheroidal material antennas [46].

The quasi-static assumptions ensured that the solution of the wave equation is a sum of Legendre polynomials which are orthogonal functions. Hence the algebra involved in matching boundary conditions to find the coefficients of the wave function solution was simplified. But , clearly the quasi-static analysis in [44] [45] [46] is applicable only for low frequencies. In [45], the validity is shown from 1MHz to 10MHz.

In this chapter, the wave equation is solved in the prolate spheroidal coordinate system (ξ, η, φ). The derivation of the wave equation in this system is shown in Appendix C. The solution takes the form of a sum of angular spheroidal functions $S_{1n}(h,\eta)$ and radial spheroidal functions $je_{1n}(h,\xi)$ and $he_{1n}(h,\xi)$ where, $h = fk = f\omega\sqrt{\mu\varepsilon}$ and 'f' is the focus of the spheroid. The angular spheroidal functions are related to associated Legendre functions and the radial spheroidal functions are related to the spherical Bessel and Hankel functions.

In Section 8.2, a brief description of the prolate spheroidal coordinate system is given along with the statement of the problem at hand. In Section 8.3, the solution of the wave equation is derived, the coefficients of which are found by applying appropriate boundary conditions. Section 8.4 contains the comparison with full-wave solutions and finally Section 8.5 contains a summary and a look at future work.

8.2 Prolate Spheroidal Antenna Problem Statement

A set of prolate spheroids is obtained by revolution about the major axis of a family of confocal ellipses. Let ‘a’ be the major radius, ‘b’ the minor radius of the ellipse and ‘f’ the focus $f = \sqrt{a^2 - b^2}$. If x,y, and ‘z’ are Cartesian coordinates with $\rho = \sqrt{x^2 + y^2}$, then the prolate spheroidal coordinates (ξ, η, φ) are obtained by applying a hyperbolic cosine conformal transformation as shown below:

$$z + j\rho = f * \cosh(u + iv) \tag{8-1}$$

$$\xi = \cosh(u)\ ,\ \ \eta = \cos(v) \text{ and } \varphi = \tan^{-1}(y/x) \tag{8-2}$$

The range of each coordinate are : $1 \to \infty$; $-1 \le \eta \le 1$ and $\varphi\!: 0\ to\ 2\pi$. The coordinate system is shown in Fig. 8-1.

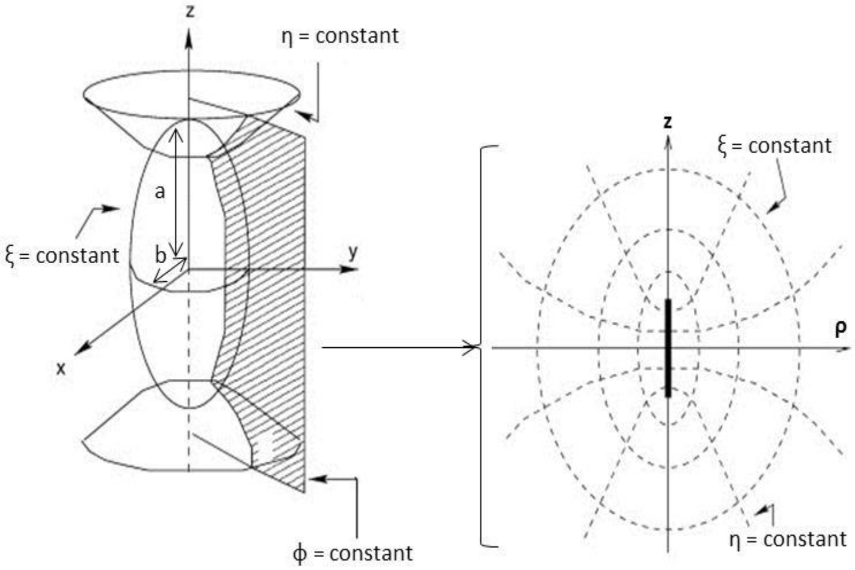

Fig. 8-1 Prolate spheroidal coordinate system (ξ, η, φ)

The goal is to find the electric and magnetic fields at a point in space (ξ, η, φ) in the prolate spheroidal coordinate system in the presence of a finite magneto-dielectric

$(\mu_r, \varepsilon_r > 1\ with\ \mu_r >> \varepsilon_r)$ prolate spheroidal antenna fed by a circular current loop with a uniform electric current distribution located at $(\xi_0, \eta_0 = 0, \varphi\colon 0\ to\ 2\pi)$ as shown in Fig. 8-2

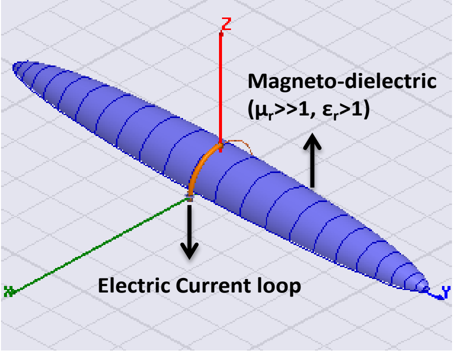

Figure 1:

Fig. 8-2 Magneto-Dielectric finite prolate spheroidal antenna fed by anate spheroidal antenna fed by a circular electric current loop at $\xi_0, \eta_0 = 0, \varphi\colon 0\ to\ 2\pi$

8.3 Solution of the Wave Equation

The field equations are derived by solving the Helmholtz vector wave equation subject to the appropriate boundary conditions.

$$\nabla^2 A + k^2 A = 0 \tag{8-3}$$

$$\nabla(\nabla. A) - \nabla \times \nabla \times A + k^2 A = 0 \tag{8-4}$$

where, A: magnetic vector potential and ‘k’ is the wave number. The first step is to express the vector wave equation (1) in prolate spheroidal coordinate system. Due to circular symmetry, only the ‘φ’ component of the magnetic vector potential will exist and ∂/∂φ=0. As shown in Appendix A, Helmholtz vector wave equation in spheroidal coordinates under circular ‘φ’ symmetry is:

$$\frac{\partial}{\partial\xi}\left[(\xi^2-1)\frac{\partial A_\varphi}{\partial\xi}\right]-\frac{1}{\xi^2-1}A_\varphi+\frac{\partial}{\partial\eta}\left[(1-\eta^2)\frac{\partial A_\varphi}{\partial\eta}\right]-\frac{1}{1-\eta^2}A_\varphi$$
$$+f^2k^2(\xi^2-\eta^2)A_\varphi=0 \tag{8-5}$$

Now let us separate the variables by assuming $A_\varphi = U(\xi)V(\eta)$

Then,

$$\frac{\partial}{\partial\xi}\left[(\xi^2-1)\frac{\partial(UV)}{\partial\xi}\right]-\frac{1}{\xi^2-1}(UV)+\frac{\partial}{\partial\eta}\left[(1-\eta^2)\frac{\partial(UV)}{\partial\eta}\right]-\frac{1}{1-\eta^2}(UV)$$
$$+f^2k^2(\xi^2-\eta^2)(UV)=0 \tag{8-6}$$

$$V\frac{\partial}{\partial\xi}\left[(\xi^2-1)\frac{\partial(V)}{\partial\xi}\right]-\frac{1}{\xi^2-1}(UV)+U\frac{\partial}{\partial\eta}\left[(1-\eta^2)\frac{\partial(V)}{\partial\eta}\right]-\frac{1}{1-\eta^2}(UV)$$
$$+f^2k^2(\xi^2-\eta^2)(UV)=0 \tag{8-7}$$

Diving throughout by UV we get,

$$\frac{1}{U}\frac{\partial}{\partial\xi}\left[(\xi^2-1)\frac{\partial(U)}{\partial\xi}\right]-\frac{1}{\xi^2-1}+\frac{1}{V}\frac{\partial}{\partial\eta}\left[(1-\eta^2)\frac{\partial(V)}{\partial\eta}\right]-\frac{1}{1-\eta^2}+f^2k^2(\xi^2-\eta^2)$$
$$=0$$

Let $h = fk$,

$$\frac{-1}{U}\frac{\partial}{\partial\xi}\left[(\xi^2-1)\frac{\partial(U)}{\partial\xi}\right]-\frac{1}{1-\xi^2}-h^2\xi^2$$
$$=\frac{1}{V}\frac{\partial}{\partial\eta}\left[(1-\eta^2)\frac{\partial(V)}{\partial\eta}\right]-\frac{1}{1-\eta^2}+h^2\eta^2 \tag{8-8}$$

Since the left side of the above equation is a function of ξ only, the right side of the equation is a function of η only and that the equation must be valid for the left and the right hand side can be equated to a constant say -B. Therefore the left hand side is:

$$\frac{-1}{U}\frac{\partial}{\partial\xi}\left[(\xi^2-1)\frac{\partial(U)}{\partial\xi}\right]-\frac{1}{1-\xi^2}-h^2\xi^2=-B$$

$$\frac{1}{U}\frac{\partial}{\partial \xi}\left[(1-\xi^2)\frac{\partial(U)}{\partial \xi}\ \right]+B-\frac{1}{1-\xi^2}-h^2\xi^2=0 \tag{8-9}$$

Similarly the right hand side,

$$\frac{1}{V}\frac{\partial}{\partial \eta}\left[(1-\eta^2)\frac{\partial(V)}{\partial \eta}\right]+B-\frac{1}{1-\eta^2}+h^2\eta^2=0 \tag{8-10}$$

The solution for U involves its behavior in the range: 1 to ∞ and the solution for V involves behavior between singular points -1 & +1. The current source as mentioned before is at $\xi=\xi_0$.

The solution of (A) and (B) is of the form:

$$A_\varphi^{[1]}=\sum_n C_n S_{1n}(h,\eta) je_{1n}(h,\xi) \quad ;for\ \ \xi\le\xi_0 \tag{8-11}$$

$$A_\varphi^{[2]}=\sum_n D_n S_{1n}(h_0,\eta) he_{1n}(h_0,\xi) \quad ;for\ \ \xi\ge\xi_0 \tag{8-12}$$

where, $h_0=fk_0=f\omega\sqrt{\mu_0\varepsilon_0}$ and C_n and D_n are constants to be determined by applying the proper boundary conditions, $S_{1n}(h,\eta)$ are angular spheroidal functions and $he_{1n}(h_0,\xi)$ and $je_{1n}(h,\xi)$ are radial spheroidal functions.

Now at the boundary between the two regions I and II ($\xi=\xi_0$), the boundary condition on the E-field is:-

$$\hat{n}\times(E_2-E_1)=0 \Rightarrow A_\varphi^{[1]}=A_\varphi^{[2]}$$

Therefore,

$$\sum_n C_n S_{1n}(h,\eta) je_{1n}(h,\xi_0)=\sum_n D_n S_{1n}(h_0,\eta) he_{1n}(h_0,\xi_0) \tag{8-13}$$

The boundary condition on the H-field is

$$\hat{n}\times(H_2-H_1)=true\ surface\ current$$

The “true surface current” which in this case is the loop current I at $\eta = \eta_0$ can be represented as

$$true\ surface\ current = \frac{I}{e_\eta}\delta(\eta - \eta_0) \tag{8-14}$$

Therefore, the boundary condition on the H-field can be written as

$$\frac{1}{e_\xi e_\varphi}\left[\frac{1}{\mu_r\mu_0}\frac{\partial\left(e_\varphi A_\varphi^{[1]}\right)}{\partial\eta} - \frac{1}{\mu_0}\frac{\partial\left(e_\varphi A_\varphi^{[2]}\right)}{\partial\eta}\right]\Bigg|_{\xi=\xi_0} = \frac{I}{e_\eta}\delta(\eta - \eta_0) \tag{8-15}$$

e_ξ, e_η, e_φ are the scale factors of the prolate spheroidal system defined as

$$e_\xi = f\sqrt{\frac{\xi^2 - \eta^2}{\xi^2 - 1}} \quad ; \quad e_\eta = f\sqrt{\frac{\xi^2 - \eta^2}{1 - \eta^2}} \quad ; \quad e_\varphi = f\sqrt{\xi^2 - 1}\sqrt{1 - \eta^2} \tag{8-16}$$

Substituting (8-16) in (8-15), the boundary condition on the H-field can be expanded as,

$$\frac{1}{f\sqrt{\frac{\xi_0^2 - \eta^2}{\xi_0^2 - 1}}\, f\sqrt{\xi_0^2 - 1}\sqrt{1 - \eta^2}}\left[\frac{1}{\mu_r\mu_0}\frac{\partial\left(f\sqrt{\xi^2 - 1}\sqrt{1 - \eta^2}A_\varphi^{[1]}\right)}{\partial\xi}\right.$$

$$\left. - \frac{1}{\mu_0}\frac{\partial\left(f\sqrt{\xi^2 - 1}\sqrt{1 - \eta^2}A_\varphi^{[2]}\right)}{\partial\xi}\right]\Bigg|_{\xi=\xi_0} = \frac{I}{f\sqrt{\frac{\xi_0^2 - \eta^2}{1 - \eta^2}}}\delta(\eta - \eta_0)$$

$$\frac{1}{f\sqrt{1 - \eta^2}}\left[\frac{1}{\mu_r\mu_0}\frac{\partial\left(f\sqrt{\xi^2 - 1}\sqrt{1 - \eta^2}\sum_n C_n S_{1n}(h, \eta) je_{1n}(h, \xi)\right)}{\partial\xi}\right.$$

$$\left. - \frac{1}{\mu_0}\frac{\partial\left(f\sqrt{\xi^2 - 1}\sqrt{1 - \eta^2}\sum_n D_n S_{1n}(h_0, \eta) he_{1n}(h_0, \xi)\right)}{\partial\xi}\right]\Bigg|_{\xi=\xi_0}$$

$$= I\sqrt{1 - \eta^2}\delta(\eta - \eta_0)$$

$$\frac{1}{f\sqrt{1-\eta^2}}\left[\frac{f\sqrt{1-\eta^2}}{\mu_r\mu_0}\sum_n C_n S_{1n}(h,\eta)\frac{\partial\left(\sqrt{\xi^2-1}\,je_{1n}(h,\xi)\right)}{\partial\xi}\right.$$

$$\left.\left.-\frac{f\sqrt{1-\eta^2}}{\mu_0}\sum_n D_n S_{1n}(h_0,\eta)\frac{\partial\left(\sqrt{\xi^2-1}he_{1n}(h_0,\xi)\right)}{\partial\xi}\right]\right|_{\xi=\xi_0}$$

$$=I\sqrt{1-\eta^2}\delta(\eta-\eta_0)$$

$$\left[\frac{1}{\mu_r\mu_0}\sum_n C_n S_{1n}(h,\eta)\left[\frac{\xi}{\sqrt{\xi^2-1}}je_{1n}(h,\xi)+\sqrt{\xi^2-1}\frac{\partial}{\partial\xi}je_{1n}(h,\xi)\right]\right.$$

$$-\frac{1}{\mu_0}\sum_n D_n S_{1n}(h_0,\eta)\left[\frac{\xi}{\sqrt{\xi^2-1}}he_{1n}(h_0,\xi)\right.$$

$$\left.\left.\left.+\sqrt{\xi^2-1}\frac{\partial}{\partial\xi}he_{1n}(h_0,\xi)\right]\right]\right|_{\xi=\xi_0}=I\sqrt{1-\eta^2}\delta(\eta-\eta_0)$$

$$\sum_n C_n S_{1n}(h,\eta)\frac{\sqrt{\xi_0^2-1}}{\mu_r\mu_0}\left[\frac{\xi_0}{\xi_0^2-1}je_{1n}(h,\xi_0)+je'_{1n}(h,\xi_0)\right]$$

$$-\sum_n D_n S_{1n}(h_0,\eta)\frac{\sqrt{\xi_0^2-1}}{\mu_0}\left[\frac{\xi_0}{\xi_0^2-1}he_{1n}(h_0,\xi_0)\right. \tag{8-17}$$

$$\left.+he'_{1n}(h_0,\xi_0)\right]=I\sqrt{1-\eta^2}\delta(\eta-\eta_0)$$

The Dirac delta function can be expanded as,

$$\delta(\eta-\eta_0)=\sum_n\frac{1}{\Lambda_{1n}(h_0)}S_{1n}(h_0,\eta)S_{1n}(h_0,\eta_0) \tag{8-18}$$

where, $\Lambda_{1n}(h_0)=\int_{-1}^{1}|S_{1n}|d\eta$

Substituting (8-18) in (8-17) we get,

$$\sum_n C_n S_{1n}(h,\eta)\frac{\sqrt{\xi_0^2-1}}{\mu_r\mu_0}\left[\frac{\xi_0}{\xi_0^2-1}je_{1n}(h,\xi_0)+je'_{1n}(h,\xi_0)\right]$$

$$-\sum_n D_n S_{1n}(h_0,\eta)\frac{\sqrt{\xi_0^2-1}}{\mu_0}\left[\frac{\xi_0}{\xi_0^2-1}he_{1n}(h_0,\xi_0)\right. \tag{8-19}$$

$$\left.+he'_{1n}(h_0,\xi_0)\right]=I\sqrt{1-\eta_0^2}\sum_n\frac{1}{\Lambda_{1n}(h_0)}S_{1n}(h_0,\eta)S_{1n}(h_0,\eta_0)$$

(Note that RHS=0 for all $\eta \neq \eta_0$). Therefore, the term $\sqrt{1-\eta^2}$ can be replaced by $\sqrt{1-\eta_0^2}$.

In (8-13) and (8-19), $S_{1n}(h,\eta)$and$S_{1n}(h_0,\eta)$are two different terms that are not orthogonal to each other. Therefore strictly speaking we cannot compare terms. But, we can represent $S_{1n}(h,\eta)$as:

$$S_{1n}(h,\eta)=\sum_r d_r^{1,n}(h)P_{1+r}^1(\eta) \tag{8-20}$$

$$S_{1n}(h_0,\eta)=\sum_r d_r^{1,n}(h_0)P_{1+r}^1(\eta) \tag{8-21}$$

where the coefficients $d_r^{1,n}(h)$ are non-zero when r is even (odd) and n is odd (even). $P_{1+r}^1(\eta)$ is the associated Legendre function. Since $P_{1+r}^1(\eta)$ exists on both sides of the equations now, it is possible to make use of the orthogonality of Legendre polynomials or to compare both sides of the equations using the coefficients of $P_{1+r}^1(\eta)$. Therefore, (8-13) can be rewritten as;

$$\sum_n C_n\sum_r d_r^{1,n}(h)P_{1+r}^1(\eta)\,je_{1n}(h,\xi_0)$$

$$=\sum_n D_n\sum_r d_r^{1,n}(h_0)P_{1+r}^1(\eta)\,he_{1n}(h_0,\xi_0) \tag{8-22}$$

And (8-19) can be rewritten as:

$$\sum_n C_n \sum_r d_r^{1,n}(h) P_{1+r}^1(\eta) \frac{\sqrt{\xi_0^2 - 1}}{\mu_r \mu_0} \left[\frac{\xi_0}{\xi_0^2 - 1} je_{1n}(h, \xi_0) + je'_{1n}(h, \xi_0) \right]$$

$$- \sum_n D_n \sum_r d_r^{1,n}(h_0) P_{1+r}^1(\eta) \frac{\sqrt{\xi_0^2 - 1}}{\mu_0} \left[\frac{\xi_0}{\xi_0^2 - 1} he_{1n}(h_0, \xi_0) \right.$$

$$\left. + he'_{1n}(h_0, \xi_0) \right] \tag{8-23}$$

$$= \sum_n \frac{I\sqrt{1 - \eta^2}}{\Lambda_{1n}(h_0)} \sum_r d_r^{1,n}(h_0) P_{1+r}^1(\eta)\, S_{1n}(h_0, \eta_0)$$

Since these two equations are valid for each ‘r’ sufficient equations can be generated depending on the number of coefficients required. Since $d_r^{1,n}$ is non-zero only when n is odd(even) and r is even(odd), the equations involving the odd ordered functions are completely decoupled from those of even order. This implies that the problem can be broken into two parts: solving for even ordered coefficients and solving for the odd ordered coefficients.

Equations (8-22) and (8-23) can be re-written as

$$\sum_n E(r,n) C_n - \sum_n F(r,n) D_n = 0 \tag{8-24}$$

$$\sum_n G(r,n) C_n - \sum_n H(r,n) D_n = \sum_n K(r,n) \tag{8-25}$$

where,

$$E(r,n) = d_r^{1,n}(h) je_{1n}(h, \xi_0) \tag{8-26}$$

$$F(r,n) = d_r^{1,n}(h_0) he_{1n}(h_0, \xi_0) \tag{8-27}$$

$$G(r,n) = d_r^{1,n}(h)\frac{\sqrt{\xi_0^2-1}}{\mu_r\mu_0}\left[\frac{\xi_0}{\xi_0^2-1}je_{1n}(h,\xi_0) + je'_{1n}(h,\xi_0)\right] \tag{8-28}$$

$$H(r,n) = d_r^{1,n}(h_0)\frac{\sqrt{\xi_0^2-1}}{\mu_0}\left[\frac{\xi_0}{\xi_0^2-1}he_{1n}(h_0,\xi_0) + he'_{1n}(h_0,\xi_0)\right] \tag{8-29}$$

$$K(r,n) = d_r^{1,n}(h_0)\frac{I\sqrt{1-\eta_0^2}}{\Lambda_{1n}(h_0)}S_{1n}(h_0,\eta_0) \tag{8-30}$$

Therefore, (8-24) and (8-25) are system of equations that can be solved for Cn and Dn. In the matrix form

$$\begin{bmatrix} (E) & -(F) \\ (G) & -(H) \end{bmatrix}\begin{bmatrix} (C) \\ (D) \end{bmatrix} = \begin{bmatrix} 0 \\ (K) \end{bmatrix} \tag{8-31}$$

where, E,F,G and H can be written as (X), (the first subscript is for ‘r’ and the second subscript for ‘n’)

$$(X) = \begin{cases} \begin{pmatrix} X_{01} & X_{03} & X_{05} & \cdots \\ X_{21} & X_{23} & X_{25} & \cdots \\ \cdots & \cdots & \cdots & \cdots \end{pmatrix} & for\ odd\ 'n' \\ \begin{pmatrix} X_{12} & X_{14} & X_{16} & \cdots \\ X_{32} & X_{34} & X_{36} & \cdots \\ \cdots & \cdots & \cdots & \cdots \end{pmatrix} & for\ even\ 'n' \end{cases} \tag{8-32}$$

And C or D can be represented as (Y):

$$(Y) = \begin{cases} \begin{pmatrix} Y_1 \\ Y_3 \\ Y_5 \\ \vdots \\ \vdots \end{pmatrix} & for\ odd\ 'n' \\ \begin{pmatrix} Y_2 \\ Y_4 \\ Y_6 \\ \vdots \\ \vdots \end{pmatrix} & for\ even\ 'n' \end{cases} \tag{8-33}$$

And (K) can be written as

$$(K) = \begin{cases} \begin{pmatrix} \sum_n K_{0n} \\ \sum_n K_{2n} \\ \sum_n K_{4n} \\ \vdots \\ \vdots \end{pmatrix} & for\ odd\ 'n' \\ \begin{pmatrix} \sum_n K_{1n} \\ \sum_n K_{3n} \\ \sum_n K_{5n} \\ \vdots \\ \vdots \end{pmatrix} & for\ even\ 'n' \end{cases} \tag{8-34}$$

Note that the function $S_{1n}(h_0, \eta_0) = 0$ when $\eta_0 = 0$ i.e when the feed loop is at the center of the spheroid. Hence D_n and C_n coefficients are equal to zero when ‘n’ is even. Therefore in summary, given the coefficients we can find the magnetic vector potential A_φ at an point (ξ, η, φ) in space using (8-11) and (8-12).

The individual field components can be determined as follows: Under circular symmetry,

$$E_\varphi = -j\omega A_\varphi \tag{8-35}$$

The H-field components can be obtained by taking the curl of the vector potential as

$$H = \frac{1}{\mu_0} \nabla \times A_\varphi \tag{8-36}$$

In the far field, in the prolate spheroidal coordinate system,

$$H_\xi \hat{\xi} + H_\eta \hat{\eta} = \frac{1}{\mu_0}\left[\frac{\hat{\xi}}{e_\eta e_\varphi}\left\{\frac{\partial}{\partial \eta}\left(e_\varphi A_\varphi^{[2]}\right)\right\} - \frac{\hat{\eta}}{e_\xi e_\varphi}\left\{\frac{\partial}{\partial \xi}\left(e_\varphi A_\varphi^{[2]}\right)\right\}\right] \tag{8-37}$$

Therefore,

$$H_\xi^{[2]} = \frac{1}{\mu_0}\left[\frac{1}{e_\eta e_\varphi}\left\{e_\varphi \sum_n D_n S'_{1n}(h_0,\eta) he_{1n}(h_0,\xi) + \frac{\partial e_\varphi}{\partial \eta}\sum_n D_n S_{1n}(h_0,\eta) he_{1n}(h_0,\xi)\right\}\right] \tag{8-38}$$

Now equation (8-38) can be further simplified by first finding the derivative of the scaling factor,

$$\frac{\partial e_\varphi}{\partial \eta} = \frac{\partial}{\partial \eta}\left(f\sqrt{\xi^2-1}\sqrt{1-\eta^2}\right) = -\frac{f\eta\sqrt{\xi^2-1}}{\sqrt{1-\eta^2}} = -\frac{f\eta\sqrt{\xi^2-1}\sqrt{1-\eta^2}}{(1-\eta^2)^2}$$

$$= -\frac{\eta}{1-\eta^2} e_\varphi$$

Substituting in (8-38),

$$=> \quad H_\xi^{[2]} = \frac{1}{\mu_0}\left[\frac{1}{e_\eta e_\varphi}\left\{e_\varphi \sum_n D_n S'_{1n}(h_0,\eta) he_{1n}(h_0,\xi) - \frac{\eta}{1-\eta^2} e_\varphi \sum_n D_n S_{1n}(h_0,\eta) he_{1n}(h_0,\xi)\right\}\right]$$

$$=> \quad H_\xi^{[2]} = \frac{1}{\mu_0 e_\eta}\left[\sum_n D_n S'_{1n}(h_0,\eta) he_{1n}(h_0,\xi) - \frac{\eta}{1-\eta^2}\sum_n D_n S_{1n}(h_0,\eta) he_{1n}(h_0,\xi)\right]$$

$$=> \quad H_\xi^{[2]} = \frac{1}{\mu_0 e_\eta}\left[\sum_n D_n he_{1n}(h_0,\xi)\left(S'_{1n}(h_0,\eta) - \frac{\eta}{1-\eta^2} S_{1n}(h_0,\eta)\right)\right] \tag{8-39}$$

Similarly from (8-37),

$$H_\eta^{[2]} = \frac{1}{\mu_0}\left[\frac{-1}{e_\xi e_\varphi}\left\{e_\varphi \sum_n D_n S_{1n}(h_0,\eta) he'_{1n}(h_0,\xi) + \frac{\partial e_\varphi}{\partial \xi}\sum_n D_n S_{1n}(h_0,\eta) he_{1n}(h_0,\xi)\right\}\right] \tag{8-40}$$

Equation (8-40) can be further simplified as,

$$\frac{\partial e_\varphi}{\partial \xi} = \frac{\partial}{\partial \xi}\left(f\sqrt{\xi^2-1}\sqrt{1-\eta^2}\right) = \frac{f\xi\sqrt{1-\eta^2}}{\sqrt{\xi^2-1}} = \frac{f\xi\sqrt{\xi^2-1}\sqrt{1-\eta^2}}{\xi^2-1} = \frac{\xi}{\xi^2-1}e_\varphi$$

$$=> \quad H_\eta^{[2]} = \frac{1}{\mu_0}\left[\frac{-1}{e_\xi e_\varphi}\left\{e_\varphi \sum_n D_n S_{1n}(h_0,\eta) he'_{1n}(h_0,\xi) + \frac{\xi}{\xi^2-1}e_\varphi\sum_n D_n S_{1n}(h_0,\eta) he_{1n}(h_0,\xi)\right\}\right]$$

$$=> \quad H_\eta^{[2]} = \frac{-1}{\mu_0 e_\xi}\left[\sum_n D_n S_{1n}(h_0,\eta) he'_{1n}(h_0,\xi) + \frac{\xi}{\xi^2-1}\sum_n D_n S_{1n}(h_0,\eta) he_{1n}(h_0,\xi)\right]$$

$$H_\eta^{[2]} = \frac{-1}{\mu_0 e_\xi}\left[\sum_n D_n S_{1n}(h_0,\eta)\left(\frac{\xi}{\xi^2-1}he_{1n}(h_0,\xi) + he'_{1n}(h_0,\xi)\right)\right] \tag{8-41}$$

The complex Poynting vector is then,

$$P = \frac{1}{2}E \times H^* = \frac{1}{2}\hat{\xi}\{-E_\varphi(H_\eta^*)\} - \frac{1}{2}\hat{\eta}\{-E_\varphi(H_\xi^*)\} = \hat{\xi}P_\xi + \hat{\eta}P_\eta \tag{8-42}$$

The radiated power ‘Prad’ can be calculated by integrating the complex Poynting vector over a closed surface enclosing the antenna for a large $\xi > \xi_0$. That is,

$$Prad = \oiint Re(P).ds_{\eta\varphi} = \oiint Re\big(\hat{\xi}P_{\xi} + \hat{\eta}P_{\eta}\big).(\hat{\xi}e_{\eta}e_{\varphi}d\varphi d\eta)$$

$$= \oiint \frac{1}{2}Re\big\{-E_{\varphi}\big(H_{\eta}^{*}\big)\big\}(e_{\eta}e_{\varphi})d\varphi d\eta$$

$$Prad = \frac{1}{2}\oiint e_{\eta}e_{\varphi}Re\big\{-E_{\varphi}H_{\eta}^{*}\big\}d\varphi d\eta = \pi\int_{-1}^{1}e_{\eta}e_{\varphi}Re\big\{-E_{\varphi}H_{\eta}^{*}\big\}d\eta \tag{8-43}$$

All the field components outside the antenna (region 2) and the radiated power equation are summarized below:

$$E_{\varphi}^{[2]} = -j\omega\sum_{n}D_{n}S_{1n}(h_{0},\eta)he_{1n}(h_{0},\xi)$$

$$H_{\xi}^{[2]} = \frac{1}{\mu_{0}e_{\eta}}\left[\sum_{n}D_{n}he_{1n}(h_{0},\xi)\left(S_{1n}'(h_{0},\eta) - \frac{\eta}{1-\eta^{2}}S_{1n}(h_{0},\eta)\right)\right]$$

$$H_{\eta}^{[2]} = \frac{-1}{\mu_{0}e_{\xi}}\left[\sum_{n}D_{n}S_{1n}(h_{0},\eta)\left(\frac{\xi}{\xi^{2}-1}he_{1n}(h_{0},\xi) + he_{1n}'(h_{0},\xi)\right)\right]$$

$$Prad = \frac{1}{2}\oiint e_{\eta}e_{\varphi}Re\big\{-E_{\varphi}H_{\eta}^{*}\big\}d\varphi d\eta = \pi\int_{-1}^{1}e_{\eta}e_{\varphi}Re\big\{-E_{\varphi}H_{\eta}^{*}\big\}d\eta$$

8.4 Comparison with Full-Wave Simulations

In this section, the closed form equations derived in Section 8.4 are compared with full-wave HFSS simulations. The simulation geometry is shown in Fig. 8-2. The magneto-dielectric material used was $\mu_r = 60$ and $\varepsilon_r = 1$. The feed loop radius is same as the minor radius ‘b’ of the spheroid (It is slightly greater than ‘b’ to account for the finite wire thickness). The antenna is placed above a ground plane. Two cases were considered (A) a=8” and b=0.5” i.e. a 16 inch long antenna of 0.5” inch cross-sectional radius & (B) a=12” and b=1.5” i.e. a 24 inch long antenna with a radius of cross-section of 1.5”. The first set of comparisons was done for E_φ (8-35) versus η for a fixed value of ξ as shown in Fig. 8-3.

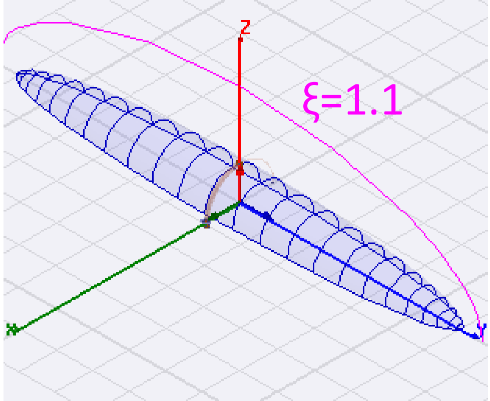

Fig. 8-3 Prolate spheroidal antenna with a=8” and b=0.5” showing the line ξ=1.1.

The electric feed current was first measured in the full-wave simulator. The plot of feed electric current versus angle (alpha ‘α’) on the feed loop is shown in Fig. 8-4.

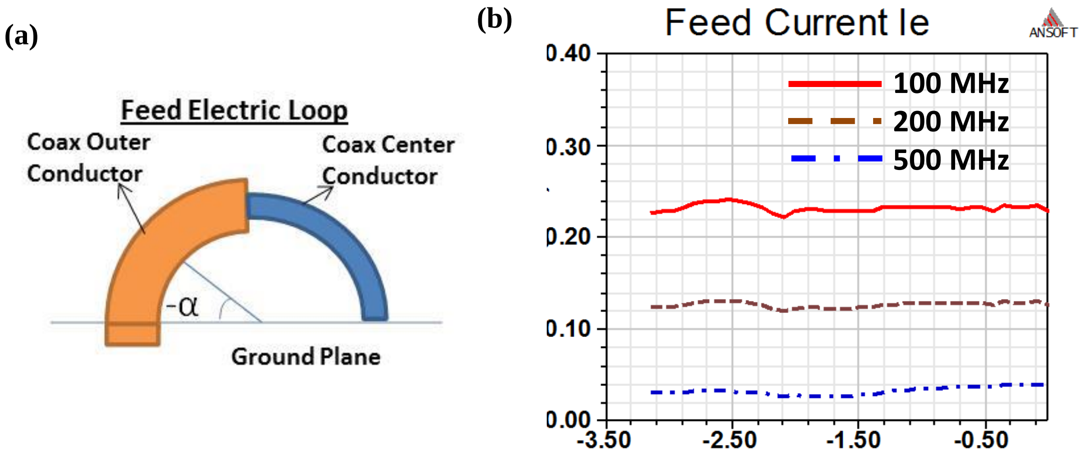

Fig. 8-4 (a)The electric feed loop used in the full-wave simulator. Note that the outer conductor was extended to the center to maintain symmetry w.r.t to the ground plane. (b) Measured feed current ‘Ie’ for different frequencies for case(A)

The average of the feed current in Fig. 8-4(b) was used for feed current 'I_0' in the analytical equation (8-35). The comparison between the simulated E_φ and the calculated Eφ for three different frequencies for ξ=1.1 and ξ=5 for case (A) is shown in Fig. 8-5.

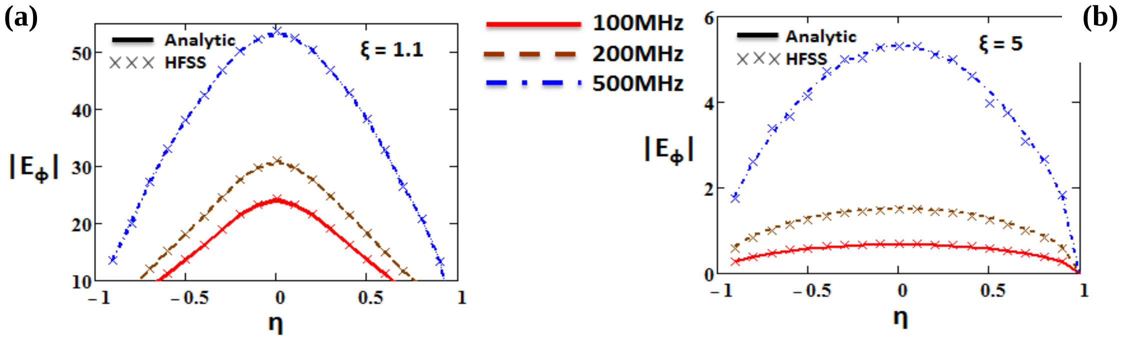

Fig. 8-5 Comparison of $|E_\varphi|$ of the analytical equation and the simulated result for case (A) at (a) $\xi = 1.1$ path in the near field and (b) $\xi = 5$ path which is in the far field.

The agreement between the analytical equation and the simulation is excellent for near field (ξ=1.1) and far-field (ξ=5) at these frequencies. Note that as frequency increases the feed current starts becoming less and less uniform in the simulation. The feed loop becomes large w.r.t to the wavelength at these frequencies. This effect is more pronounced for a fatter dipole (and therefore a bigger feed loop since rad=b) as seen in Fig. 8-6 which shows the feed current for case (B) with a=12" and b=1.5".

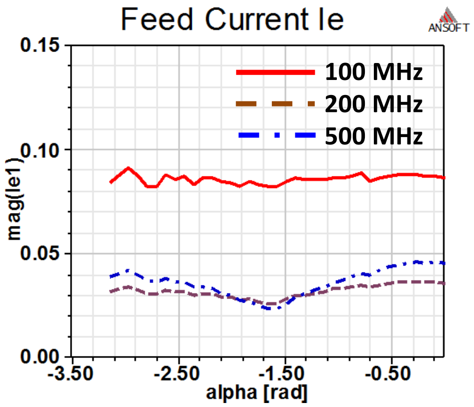

Fig. 8-6 Measured electric feed current at different frequencies vs. angle 'α' for case (B)

As seen in Fig. 8-6, the feed current at 500MHz can no longer be called uniform throughout the loop which is one of the first assumptions made in deriving the analytical equations. Nevertheless E_φ is compared to simulation for the fat prolate spheroid case (B) in Fig. 8-7 by taking the average of the electric feed current versus 'α' in Fig. 8-6.

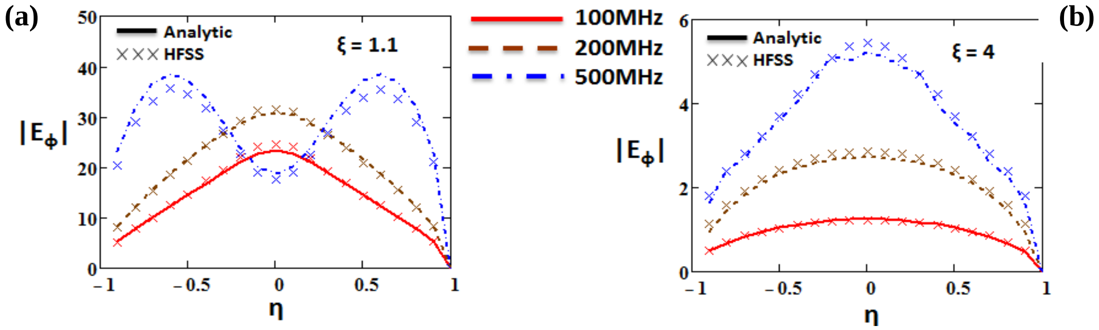

Fig. 8-7 Comparison of $|E_\varphi|$ of the analytical equation and the simulated result for case (B) at (a) $\xi = 1.1$ and (b) $\xi = 4$.

The agreement between the simulation and analytical equation is excellent at low frequencies and starts deviating slightly at higher frequencies due to the non-uniform electric feed current. Next, the radiated power calculated analytically in (8-43) is compared with full-wave simulations for both case (A) and case (B) versus frequency in Fig. 8-8.

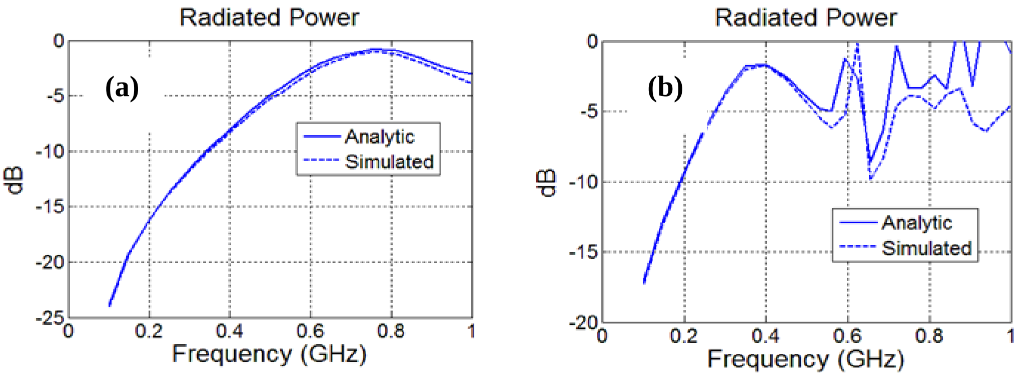

Fig. 8-8 Comparison between analytic and simulated radiated power 'Prad' for the (A) a=8" & b=0.5" and (B) a=12" and b=1.5".

Again, the agreement is excellent at low frequencies but it starts to deviate at higher frequencies and again the reason being that the electric feed current is no longer uniform due to the large size of the feed loop. This is clearly seen in the measured electric feed current in the HFSS simulator (Fig. 8-9).

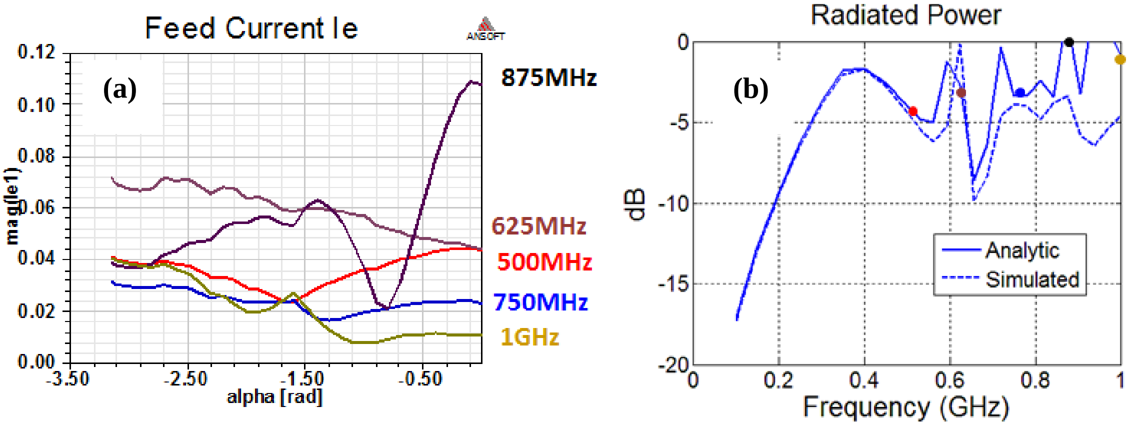

Fig. 8-9 (a) Non-uniform Electric feed current for higher frequencies computed in HFSS (b) Radiated power at those frequencies indicated by the circle markers.

8.5 Summary and Future Work

The closed form equations for the electric and magnetic fields in the near and far field of a finite prolate spheroidal magneto-dielectric antenna are derived in this chapter. The analytical equations agreed well with simulations. The power radiated by the antenna was also calculated. The equations are shown to be accurate as long as the electric feed current distribution is uniform.

The magneto-dielectric material in this chapter was assumed to be lossless. Thus, a possible future work in this topic will be to derive the field equations for lossy magneto-dielectric prolate spheroidal dipole antenna.

REFERENCES

[1] S. Schelkunoff and H. Friis, Antenna theory and practice, Wiley, 1952.

[2] H. Wheeler, "Fundamental limitations of small antennas," *Proc. IRE,* vol. 35, pp. 1479-1484, Jul. 1947.

[3] H. Wheeler, "Small Antennas," *IEEE Trans. Antennas Propag.*, vol. 23, no. 4, pp. 462-469, Jul.1975.

[4] M. Smith, "Properties of dielecrically loaded antennas," *Proc. IEE Electronics,* vol. 124, no. 10, pp. 837-839, Oct. 1977.

[5] R. Richtmeyer, "Dielectric Resonators," *J. Appl. Phys.*, vol. 10, pp. 391-398, Jun. 1939.

[6] S. Long, M. McAllister and L. Shen, "The resonant cylindrical dielectric cavity antenna," *IEEE Trans. on Antennas Propag.*, vol. 31, pp. 406-412, Mar. 1983.

[7] Petosa, "Dielectric reosnator antennas: A historical review and the current state of the art," *IEEE Trans. Antennas Propag.*, vol. 52, no. 5, pp. 91-116, Oct. 2010.

[8] S. R. Best and A. D. Yaghjian, "Impedance, bandwidth and Q of antennas," *IEEE Trans. Antennas Propag.,* vol. 44, no. 5, pp. 672-676, May 1996.

[9] H. A. Wheeler, "The radian sphere around a small antenna," *Proc. IRE,* vol. 47, pp. 1325-1331, Aug. 1959.

[10] E. D. Palik, Handbook of Optical Constants of Solids, Elsevier, 1998.

[11] V. Rumsey and W. Weeks, "Electrically small ferrite loaded loop antennas," *IRE Nat. Conv. Rec.,* vol. 4, no. 1, pp. 165-170, 1956.

[12] V. Rumsey, "Reaction concept in electromagnetic theory," *Phys. Rev.,* vol. 94, no. 6, pp. 1483-1491, Jun. 1954.

[13] R. DeVore and P. Bohley, "The electrically small magnetically loaded multiturn loop antenna," *IEEE Trans. Antennas Propag.,* vol. 25, pp. 496-505, 1977.

[14] H. Stuart and A. Yaghjian, "Approaching the lower bounds on Q for electrically small electric dipole antennas using high permeability shells," *IEEE Trans. Antennas Propag.*, vol. 58, no. 12, pp. 3865-3872, Dec. 2010.

[15] S. Best, "A low Q electrically small magnetic (TE mode) dipole," *IEEE Antennas Wireless Propag. Lett.*, vol. 8, pp. 572-575, 2009.

[16] J. McLean, H. Foltz and R. Sutton, "Electrically small TE01 mode spherical wire antennas employing lossy magnetodielectric materials," in *International Workshop on Antenna Technology Proceedings*, Lisbon, Portugal, Mar. 2010.

[17] T. Hansen, O. Kim and O. Breinbjerg, "Electrical properties of spherical dipole antennas with lossy material cores," in *6th European conference on Antennas and Propag.*, Prague, Czech Republic, Mar. 2012.

[18] J. McLean and R. Sutton, "An efficienct low profile antenna employing lossy magneto-dielectric materials," in *IEEE International worskshop on antenna technology*, Tucson,AZ., 2012.

[19] L. J. Chu, "Physical limitations of omni-directional antennas," *J. Appl. Phys.*, vol. 35, pp. 1479-1484, 1948.

[20] W. Geyi, "Optimization of the Ratio of Gain to Q," *IEEE Trans. Antennas Propag.*, vol. 61, no. 4, pp. 1916-1922, 2013.

[21] J. S. McLean, "A Re-examination of the Fundamental Limits on the Radiation Q of Electrically Small Antennas," *IEEE Trans. Antennas Propag.*, vol. 44, no. 5, pp. 672-676, May, 1996.

[22] H. L. Thal, "New Radiation Q Limits for Spherical Wire Antennas," *IEEE Trans. Antennas Propag.*, vol. 54, no. 10, pp. 2757-2763, Oct. 2006.

[23] R. Hansen, "Q and Mu," in *IEEE Sym. Antennas Propag. (APSURI)*, Spokane,WA, July 2011.

[24] J. L. Snoek, "Dispersion and Absorption in Magnetic Ferrites at Frequencies Above 1 Mc/s," *Physica*, vol. 14, no. 4, pp. 207-217, 1948.

[25] J. Smit and H. Wijn, Ferrites, New York: Wiley, 1959.

[26] J. Toll, "Causality and the Dispersion Relation: Logical Foundations," *Phys. Rev.,* vol. 104, pp. 1760-1770, 1956.

[27] F. Grant, "Use of Complex Conductivity in the Representation of Dielectric Phenomena," *J. Appl. Phys.,* vol. 29, pp. 76-80, 1958.

[28] R. Diaz and N. Alexopoulos, "An Analytic Contiuation Method for the Analysis and Design of Dispersive Materials," *IEEE Trans. Antennas Propag.,* vol. 45, no. 11, pp. 602-610, Nov. 1997.

[29] H. J. Josephs, "The Heaviside Papers Found at Paignton in 1957," *IEE Monograph,* vol. 319, pp. 70-76, 1959.

[30] Fair-Rite Products Corp, [Online]. Available: http://www.fair-rite.com/cgibin/catalog.pgm#select:freq1.

[31] E. Louis, I. Jeong and R. Walser, "Magnetization distribution in nearly isotropic ultra-soft magnetic CoB amorphous thin films," *IEEE Trans. Magn,* vol. 25, no. 5, pp. 3366-3368, 1989.

[32] W. Weeks, Electromagnetic Theory for Engineering Applications, Wiley, 1964.

[33] H. Fricke, "A mathematical treatment of the electric conductivity and capacity of disperse systems: I. The electric conductivity of a suspension of homogenous spheroids," *Phys. Rev.,* vol. 24, no. 5, pp. 575-587, 1924.

[34] O. Jeffimenko, Electricity and Magnetism, Start city, WVa: Meredith, 1989.

[35] S. A. Schelkunoff and H. Friis, Antenna theory and practice, Wiley, 1952.

[36] R. Diaz, W. Merrill and N. Alexopoulos, "Analytic framework for the modeling of effective media," *Journal of Appl. Phys.,* vol. 84, no. 12, pp. 6815-6826, 1998.

[37] M. Islam, "A theoretical treatment of low frequency loop antennas with ferrite cores," *IEEE Trans. Antennas Propag.,* vol. 11, no. 3, pp. 162-169, Mar. 1963.

[38] M. Islam, "Mathematical Analysis on the Effect of a Prolate Spheroidal Core in a Magnetic Dipole field," *J. Math Phys.,* vol. 4, no. 9, pp. 1205-1212, 1963.

[39] T. Simpson and Y. Zhu, "The electrically small multi-turn loop antenna with a spheroidal core," *IEEE Antennas Propag. Mag.,* vol. 48, no. 5, pp. 54-66, Oct. 2006.

[40] T. Simpson, "Electrically Small Spheroidal loops wound on a hollow ferrite core," *IEEE Antennas Propag. Mag.,* vol. 50, no. 3, pp. 88-94, Jun 2008.

[41] D. Halliday and D. Kiely, "Dielectric rod aerials," *Proc. IEE Part IIIA: Radio Comm.,* vol. 94, no. 16, pp. 610-618, Mar. 1947.

[42] J. James, "Theoretical investigation of cylindrical dielectric rod antennas," *Proc. IEE,* vol. 114, no. 3, pp. 672-676, May 1996.

[43] G. Mueller and W. Tyrell, "Polyrod Antennas," *Bell Sys. Tech. J.,* vol. 26, pp. 837-851, 1947.

[44] O. Kim and O. Breinbjerg, "Lower bound for the radiation Q of electrically small magnetic dipole antenna with solid magnetodielectric core," *IEEE Trans. Antennas Propag.,* vol. 59, no. 2, pp. 679-681, 2011.

[45] O. Kim, O. Breinbjerg and A. Yaghjian, "Electrically small magnetic dipole antennas with quality factors approaching the Chu lower bound," *IEEE Antennas Propag.,* vol. 58, no. 6, pp. 1898-1906, 2010.

[46] R. Hansen and M. Burke, "Antennas with magneto-dielectrics," *Microwave Opt. Tech. Lett.,* vol. 26, no. 2, pp. 75-78, 2000.

[47] D. V. Giri, "Electrically small loop antenna loaded by a homogenous and isotropic ferrite cylinder-part I," Harvard University, Cambridge, Mass., Jul. 1973.

[48] A. Karilainen, P. Ikonen, C. Simovski and S. Tretyakov, "Choosing dielectric or magnetic material to optimize the bandwidth of miniaturized resoannt antennas," *IEEE Trans. Antennas Propag.,* vol. 59, no. 11, pp. 3991-3998, Nov. 2011.

[49] P. Ikonen, K. Rozanov, A. Osipov, P. Alitalo and S. Tretyakov, "Magnetodielectric substrates in antenna miniaturization: potential and limitations," *IEEE Trans. Antennas Propag.,* vol. 54, no. 11, pp. 3391-3998, Nov. 2006.

[50] J. McLean and R. S. a. H. Foltz, "Broadband, electrically small spherical wire and generalized loop antennas exploting inhomogenous magnetic cores," in *20th International Conference on applied electromagnetics and communications proceedings*, Dubrovnik, Croatia, Sept. 2010.

[51] T. Sebastian, S. Clavijo and R. Diaz, "Small Material Dipole Antenna Analysis: I. Dielectric Dipole," *IEEE Trans. on Antennas Propag.,* submitted for publication.

APPENDIX A

DERIVATION OF THE INTERNAL FIELD SHAPE CORRECTION FACTOR TO ACCOUNT FOR THE EFFECT OF SKIN DEPTH

The energy stored by an inductor ‘L’ is the amount of work done to establish a current ‘I’ through the inductor. That is,

$$EnergyL = \frac{1}{2}LI^2 \tag{A-1}$$

Now, the assumed TM internal magnetic field (H_φ) of a magneto-dielectric cylinder ($\varepsilon = \varepsilon_0\varepsilon_r$ & $\mu = \mu_0\mu_r$) of radius ‘ρ’ with the skin depth ‘δ’ < ρ as shown in Fig. 3-2 is:

$$H_\varphi = \frac{I}{2\pi\rho}\frac{r-(\rho-\delta)}{\delta} \tag{A-2}$$

The internal magnetic energy (IME) of this magneto-dielectric cylinder assuming a uniform field along the length ‘l’ of the cylinder is therefore given by

$$IME = \frac{1}{2}\iiint \mu H^2 dVol = \frac{1}{2}\int_{-l/2}^{l/2}\int_0^{2\pi}\int_{\rho-\delta}^{\rho} \mu H_\varphi^2 \, rdzd\varphi dr \tag{A-3}$$

(A-1) and (A-3) must be identical. Therefore

$$\frac{1}{2}L_{uni}I^2 = \frac{1}{2}l\int_0^{2\pi} d\varphi \int_{\rho-\delta}^{\rho} \mu\left(\frac{I}{2\pi\rho}\frac{r-(\rho-\delta)}{\delta}\right)^2 rdr \tag{A-4}$$

$$L_{uni} = l\left(\frac{2\pi\mu}{4\pi^2\rho^2\delta^2}\right)\int_{\rho-\delta}^{\rho} r\big(r^2+(\rho-\delta)^2-2r(\rho-\delta)\big)dr = \frac{\mu l}{8\pi}FSF \tag{A-5}$$

where,

$$FSF = \frac{1}{\left(\frac{\delta}{\rho}\right)^2}\left[1-\frac{8}{3}\left(1-\frac{\delta}{\rho}\right)+2\left(1-\frac{\delta}{\rho}\right)^2-\frac{1}{3}\left(1-\frac{\delta}{\rho}\right)^4\right] \tag{A-6}$$

When skin depth can be neglected i.e. when δ>ρ, then δ is set equal to ρ and therefore FSF is unity which gives us

$$L = \frac{\mu l}{8\pi} \tag{A-7}$$

This is the internal inductance of a wire of length 'l'. Now if the current distribution and therefore the magnetic field across the length of the wire is not uniform but triangular, then the current 'I' for a wire should be replaced by

$$I = I_0\left(1 - \frac{z}{l/2}\right) \tag{A-8}$$

where, I_0 is the maximum value of current seen at the origin(or feed point) with the wire extending from $-l/2$ to $l/2$. Therefore on solving the integral in (A-4) with the current in (A-4) we get

$$L_{\Delta lar} = \frac{1}{3}\frac{\mu l}{8\pi}FSF \tag{A-9}$$

which is the same as (3-26).

APPENDIX B

DERIVATION OF EFFICIENCY OF A PERMEABLE DIPOLE FOLLOWING THE APPROACH BY DEVORE ET. AL. [15]

Consider a multi-turn loop antenna of 'n' turns radius 'ρ' of total length 'l' carrying a constant current 'I_0'. Let it be loaded by an ellipsoidal permeable material (μ_r) of length 'l'. The internal magnetic field of an ellipsoidal core in terms of the an unperturbed static field 'H_0' is given by

$$H_F = \frac{H_0}{1 + D(\mu_r - 1)} \tag{B-1}$$

where, D: is the demagnetization factor. The uniform field of the ellipsoidal winding is equated to the unperturbed field:

$$H_0 \approx H_w = \frac{n}{l}(1 - D)I_0 \tag{B-2}$$

If A_i is the cross-sectional area and L_i is the self-inductance of the ith winding then the self-inductance of the ith winding is given by

$$L_i = \frac{\varphi}{I_0} = \frac{BA_i}{I_0} = \mu_0\mu_r\frac{H_FA_i}{I_0} \tag{B-3}$$

Therefore, the total inductance of the loaded multi-turn loop antenna by superposition over 'n' turns is given by

$$L = nL_i = \mu_0\mu_r\frac{n\frac{H_0}{1 + D(\mu_r - 1)}A_i}{I_0} = \mu_0\mu_r\frac{\frac{n^2}{l}(1 - D)}{1 + D(\mu_r - 1)}(\pi\rho^2) \tag{B-4}$$

Since the permeability μ_r is complex ($\mu_r = \mu' - j\mu"$), to account for the energy lost in the permeable material we introduce a loss resistance R_{loss}.

$$R_{Loss} = -Im(\omega L) \tag{B-5}$$

From (B-4),

$$L = \mu_0\frac{n^2}{l}(\pi\rho^2)(1 - D)\left[\frac{\mu' - j\mu"}{1 + D(\mu' - 1) - jD\mu"}\right] \tag{B-6}$$

From (B-4), the imaginary part of the inductance 'L' can be expanded as

$$Im(L) = \mu_0 \frac{n^2}{l}(\pi\rho^2)(1-D)^2 \frac{-\mu"}{\{1+D(\mu'-1)\}^2 + \{D\mu"\}^2} \tag{B-7}$$

From (B-4) and (B-4), the loss resistance R_{loss} is given by:

$$R_{Loss} = \omega\mu_0 \frac{n^2}{l}(\pi\rho^2)(1-D)^2 \frac{\mu"}{\{1+D(\mu'-1)\}^2 + \{D\mu"\}^2} \tag{B-8}$$

Now, the radiation resistance of an electrically small loop antenna is given by

$$Rrad = 20k^4 \frac{|m|^2}{|I_0|^2} \tag{B-9}$$

where, 'm' is the magnetic dipole moment. The magnetic dipole moment of the antenna m is the magnetic moment of the core is given by

$$m = (\mu_r - 1)H_F(\pi\rho^2 l) \tag{B-10}$$

The magnetic moment of the winding is given by

$$m_W = nI_0(\pi\rho^2) \tag{B-11}$$

Substituting (B-4) and (B-4) into (B-4) and we get,

$$Rrad = \frac{20k^4}{I_0^2}\left|\frac{(\mu_r-1)\frac{n}{l}(1-D)I_0}{\{1+D(\mu_r-1)\}}\pi\rho^2 l\right|^2 \tag{B-12}$$

Assuming that the flux is well contained that there is no demagnetization i.e. D~0. Now from (B-4)

$$R_{loss} = \omega\mu_0 \frac{n^2}{l}(\pi\rho^2)\mu" \tag{B-13}$$

And (B-4) becomes

$$Rrad = 20k^4 n^2 |(\mu_r - 1)\pi\rho^2|^2 \tag{B-14}$$

Dividing (B-4) by (B-4) and expanding we get

$$\frac{R_{Loss}}{R_{rad}} = \frac{6}{(kl)^3 \left(\frac{\rho}{l}\right)^2} \frac{\mu"}{|\mu_r - 1|^2} \tag{B-15}$$

Therefore the radiation efficiency upon <u>not</u> assuming that $\mu" \ll \mu'$ is given by

$$Eff_{Bohley} = \frac{1}{1 + \frac{R_{loss}}{R_{rad}}} = \frac{1}{1 + \frac{6}{(kl)^3 \left(\frac{\rho}{l}\right)^2} \frac{\mu"}{|\mu_r - 1|^2}} \tag{B-16}$$

APPENDIX C

HELMHOLTZ VECTOR WAVE EQUATION IN PROLATE SPHEROIDAL COORDINATES UNDER CIRCULAR (φ) SYMMETRY.

The electric and magnetic field equations of a finite prolate spheroid magneto-dielectric antenna are derived by solving the Helmholtz vector wave equation subject to the appropriate boundary conditions.

$$\nabla^2 A + k^2 A = 0 \tag{C-1}$$

$$\nabla(\nabla . A) - \nabla \times \nabla \times A + k^2 A = 0 \tag{C-2}$$

The first step is to express the vector wave equation (C-1) in prolate spheroidal coordinate system. Due to circular symmetry, only the 'φ' component of the magnetic vector potential will exist and $\partial/\partial\varphi = 0$. Under these conditions, $\nabla . A = 0$ and $-\nabla \times \nabla \times A$ can be expanded as

$$-(\nabla \times \nabla \times A) = \hat{\varphi}\left[\frac{1}{e_\xi e_\eta}\frac{\partial}{\partial \xi}\left\{\frac{e_\eta}{e_\xi e_\varphi}\frac{\partial}{\partial \xi}\left(e_\varphi A_\varphi\right)\right\} + \frac{1}{e_\xi e_\eta}\frac{\partial}{\partial \eta}\left\{\frac{e_\xi}{e_\eta e_\varphi}\frac{\partial}{\partial \eta}\left(e_\varphi A_\varphi\right)\right\}\right] \tag{C-3}$$

$$= \hat{\varphi}[P + Q]$$

where, e_ξ, e_η and e_φ are the scale factors of the prolate spheroidal system defined as

$$e_\xi = f\sqrt{\frac{\xi^2 - \eta^2}{\xi^2 - 1}} \quad ; \quad e_\eta = f\sqrt{\frac{\xi^2 - \eta^2}{1 - \eta^2}} \quad ; \quad e_\varphi = f\sqrt{\xi^2 - 1}\sqrt{1 - \eta^2} \tag{C-4}$$

And, $P = \frac{1}{e_\xi e_\eta}\frac{\partial}{\partial \xi}\left\{\frac{e_\eta}{e_\xi e_\varphi}\frac{\partial}{\partial \xi}\left(e_\varphi A_\varphi\right)\right\}$ & $Q = \frac{1}{e_\xi e_\eta}\frac{\partial}{\partial \eta}\left\{\frac{e_\xi}{e_\eta e_\varphi}\frac{\partial}{\partial \eta}\left(e_\varphi A_\varphi\right)\right\}$

Now,

$$P = \frac{1}{e_\xi e_\eta}\frac{\partial}{\partial \xi}\left\{\frac{e_\eta}{e_\xi e_\varphi}\frac{\partial}{\partial \xi}\left(e_\varphi A_\varphi\right)\right\} = \frac{1}{e_\xi e_\eta}\frac{\partial}{\partial \xi}\left\{\frac{e_\eta}{e_\xi e_\varphi}\left(e_\varphi\frac{\partial A_\varphi}{\partial \xi} + \frac{\partial e_\varphi}{\partial \xi}A_\varphi\right)\right\}$$

$$P = \frac{1}{e_\xi e_\eta}\left\{\frac{\partial}{\partial \xi}\left(\frac{\frac{e_\eta e_\varphi}{e_\xi}\frac{\partial A_\varphi}{\partial \xi}}{e_\varphi}\right) + \frac{\partial}{\partial \xi}\left(\frac{e_\eta}{e_\xi e_\varphi}\frac{\partial e_\varphi}{\partial \xi}A_\varphi\right)\right\}$$

$$P = \frac{1}{e_\xi e_\eta}\left\{\left(\frac{e_\varphi \frac{\partial}{\partial \xi}\left(\frac{e_\eta e_\varphi}{e_\xi}\frac{\partial A_\varphi}{\partial \xi}\right) - \frac{e_\eta e_\varphi}{e_\xi}\frac{\partial A_\varphi}{\partial \xi}\frac{\partial e_\varphi}{\partial \xi}}{e_\varphi^2}\right) + \frac{\partial}{\partial \xi}\left(\frac{e_\eta}{e_\xi e_\varphi}\frac{\partial e_\varphi}{\partial \xi}A_\varphi\right)\right\}$$

$$P = \frac{1}{e_\xi e_\eta\, e_\varphi}\frac{\partial}{\partial \xi}\left(\frac{e_\eta e_\varphi}{e_\xi}\frac{\partial A_\varphi}{\partial \xi}\right) + \frac{A_\varphi}{e_\xi e_\eta}\frac{\partial}{\partial \xi}\left(\frac{e_\eta}{e_\xi e_\varphi}\frac{\partial e_\varphi}{\partial \xi}\right) \tag{C-5}$$

Now,

$$\frac{\partial e_\varphi}{\partial \xi} = \frac{\partial}{\partial \xi}\left(f\sqrt{\xi^2 - 1}\sqrt{1 - \eta^2}\right) = \frac{f\xi\sqrt{1 - \eta^2}}{\sqrt{\xi^2 - 1}} \tag{C-6}$$

And

$$\frac{e_\eta e_\varphi}{e_\xi} = f(\xi^2 - 1) \tag{C-7}$$

Substituting (C-7) and (C-6) in (C-5) we get,

$$P = \frac{f}{e_\xi e_\eta\, e_\varphi}\frac{\partial}{\partial \xi}\left((\xi^2 - 1)\frac{\partial A_\varphi}{\partial \xi}\right) + \frac{A_\varphi}{e_\xi e_\eta}\frac{\partial}{\partial \xi}\left(\frac{\xi}{\sqrt{\xi^2 - 1}\sqrt{1 - \eta^2}}\right)$$

$$P = \frac{f}{e_\xi e_\eta\, e_\varphi}\frac{\partial}{\partial \xi}\left((\xi^2 - 1)\frac{\partial A_\varphi}{\partial \xi}\right) + \frac{A_\varphi}{e_\xi e_\eta\sqrt{1 - \eta^2}}\left(\frac{\sqrt{\xi^2 - 1} - \frac{\xi^2}{\sqrt{\xi^2 - 1}}}{\xi^2 - 1}\right)$$

$$P = \frac{f}{e_\xi e_\eta\, e_\varphi}\frac{\partial}{\partial \xi}\left((\xi^2 - 1)\frac{\partial A_\varphi}{\partial \xi}\right) + \frac{A_\varphi}{e_\xi e_\eta\sqrt{1 - \eta^2}}\left(\frac{-1}{(\xi^2 - 1)\sqrt{\xi^2 - 1}}\right)$$

$$P = \frac{f}{e_\xi e_\eta\, e_\varphi}\frac{\partial}{\partial \xi}\left((\xi^2 - 1)\frac{\partial A_\varphi}{\partial \xi}\right) - \frac{f}{e_\xi e_\eta\, e_\varphi}\frac{A_\varphi}{(\xi^2 - 1)} \tag{C-8}$$

Now, similarly from (C-3)

$$Q = \frac{1}{e_\xi e_\eta}\frac{\partial}{\partial \eta}\left\{\frac{e_\xi e_\varphi}{e_\eta e_\varphi}\frac{\partial A_\varphi}{\partial \eta} + \frac{e_\xi}{e_\eta e_\varphi}\frac{\partial e_\varphi}{\partial \eta}\right\}$$

$$Q = \frac{1}{e_\xi e_\eta}\left\{\frac{e_\varphi \frac{\partial}{\partial\eta}\left(\frac{e_\xi e_\varphi}{e_\eta}\frac{\partial A_\varphi}{\partial\eta}\right) - \frac{e_\xi e_\varphi}{e_\eta}\frac{\partial A_\varphi}{\partial\eta}\frac{\partial e_\varphi}{\partial\eta}}{e_\varphi^2} + \frac{\partial}{\partial\eta}\left(\frac{e_\xi}{e_\eta e_\varphi}\frac{\partial e_\varphi}{\partial\eta}\right)\right\}$$

$$Q = \frac{1}{e_\xi e_\eta e_\varphi}\left\{\frac{\partial}{\partial\eta}\left(\frac{e_\xi e_\varphi}{e_\eta}\frac{\partial A_\varphi}{\partial\eta}\right) + \frac{A_\varphi}{e_\xi e_\eta}\frac{\partial}{\partial\eta}\left(\frac{e_\xi}{e_\eta e_\varphi}\frac{\partial e_\varphi}{\partial\eta}\right)\right\} \tag{C-9}$$

Now,

$$\frac{\partial e_\varphi}{\partial\eta} = \frac{\partial}{\partial\eta}\left(f\sqrt{\xi^2-1}\sqrt{1-\eta^2}\right) = -\frac{f\eta\sqrt{\xi^2-1}}{\sqrt{1-\eta^2}} \tag{C-10}$$

And

$$\frac{e_\xi e_\varphi}{e_\eta} = f(1-\eta^2) \tag{C-11}$$

Substituting (C-11) and (C-10) in (C-9) we get,

$$Q = \frac{f}{e_\xi e_\eta e_\varphi}\frac{\partial}{\partial\eta}\left((1-\eta^2)\frac{\partial A_\varphi}{\partial\eta}\right) + \frac{A_\varphi}{e_\xi e_\eta}\frac{\partial}{\partial\eta}\left(\frac{-\eta}{\sqrt{\xi^2-1}\sqrt{1-\eta^2}}\right)$$

$$Q = \frac{f}{e_\xi e_\eta e_\varphi}\frac{\partial}{\partial\eta}\left((1-\eta^2)\frac{\partial A_\varphi}{\partial\eta}\right) - \frac{A_\varphi}{e_\xi e_\eta\sqrt{\xi^2-1}}\left(\frac{\sqrt{1-\eta^2} + \frac{\eta^2}{\sqrt{1-\eta^2}}}{1-\eta^2}\right)$$

$$Q = \frac{f}{e_\xi e_\eta e_\varphi}\frac{\partial}{\partial\eta}\left((1-\eta^2)\frac{\partial A_\varphi}{\partial\eta}\right) - \frac{A_\varphi}{e_\xi e_\eta\sqrt{\xi^2-1}}\left(\frac{1}{(1-\eta^2)\sqrt{1-\eta^2}}\right)$$

$$Q = \frac{f}{e_\xi e_\eta e_\varphi}\frac{\partial}{\partial\eta}\left((1-\eta^2)\frac{\partial A_\varphi}{\partial\eta}\right) - \frac{f}{e_\xi e_\eta\, e_\varphi}\frac{A_\varphi}{(1-\eta^2)} \tag{C-12}$$

From (C-8) and (C-12)

$$P + Q = \frac{f}{e_\xi e_\eta\, e_\varphi}\left[\frac{\partial}{\partial\xi}\left((\xi^2-1)\frac{\partial A_\varphi}{\partial\xi}\right) + \frac{\partial}{\partial\eta}\left((1-\eta^2)\frac{\partial A_\varphi}{\partial\eta}\right) - \frac{A_\varphi}{(\xi^2-1)} - \frac{A_\varphi}{(1-\eta^2)}\right]$$

Now,

$$\frac{f}{e_\xi e_\eta \, e_\varphi} = \frac{1}{f^2(\xi^2 - \eta^2)}$$

Therefore,

$$P + Q = \frac{1}{f^2(\xi^2 - \eta^2)}\left[\frac{\partial}{\partial \xi}\left((\xi^2 - 1)\frac{\partial A_\varphi}{\partial \xi}\right) + \frac{\partial}{\partial \eta}\left((1 - \eta^2)\frac{\partial A_\varphi}{\partial \eta}\right) - \frac{A_\varphi}{(\xi^2 - 1)} - \frac{A_\varphi}{(1 - \eta^2)}\right] \tag{C-13}$$

Substituting (C-13) in (C-3) and then in (C-2), under circular symmetry,

$$\frac{1}{f^2(\xi^2 - \eta^2)}\left[\frac{\partial}{\partial \xi}\left((\xi^2 - 1)\frac{\partial A_\varphi}{\partial \xi}\right) + \frac{\partial}{\partial \eta}\left((1 - \eta^2)\frac{\partial A_\varphi}{\partial \eta}\right) - \frac{A_\varphi}{(\xi^2 - 1)} - \frac{A_\varphi}{(1 - \eta^2)}\right] + k^2 A_\varphi = 0$$

$$\frac{\partial}{\partial \xi}\left((\xi^2 - 1)\frac{\partial A_\varphi}{\partial \xi}\right) + \frac{\partial}{\partial \eta}\left((1 - \eta^2)\frac{\partial A_\varphi}{\partial \eta}\right) - \frac{A_\varphi}{(\xi^2 - 1)} - \frac{A_\varphi}{(1 - \eta^2)} + f^2 k^2 (\xi^2 - \eta^2) A_\varphi = 0 \tag{C-14}$$

Equation (C-14) is the Helmholtz vector wave equation in spheroidal coordinates under circular 'φ' symmetry.